UNIVERSITY OF SOUTHAMPTON

FACULTY OF ENGINEERING AND PHYSICAL SCIENCES

Physical Sciences

Unraveling the mysteries of spacetime: holographic codes and gravitational lensing

by

Charlie Woodward

Supervisors: Marika Taylor

Thesis for the degree of Doctor of Philosophy

12th January 2023

UNIVERSITY OF SOUTHAMPTON

ABSTRACT

FACULTY OF ENGINEERING AND PHYSICAL SCIENCES

Physical Sciences

Thesis for the degree of Doctor of Philosophy

UNRAVELING THE MYSTERIES OF SPACETIME: HOLOGRAPHIC CODES AND GRAVITATIONAL LENSING

by Charlie Woodward

The fabric of spacetime is the underlying structure embedding the entirety of the observable phenomena in our universe and though it has been studied in significant detail, many mysteries remain. This thesis is dedicated to studying two particular topics that arose from explorations into the nature of spacetime and is correspondingly separated into two distinct parts, namely holographic quantum error-correcting codes and gravitational microlensing.

The first part of this thesis concerns itself with the suggestion that spacetime is not fundamental but rather an emergent concept. According to the holographic principle, the fundamental degrees of freedom of a bulk spacetime are encoded on its boundary surface, which is of one dimension lower than the bulk. The AdS/CFT correspondence is the most explicit realisation of the holographic principle, forming a unique framework in which one can use concepts and techniques arising in quantum information theory to study quantum gravity. Holographic properties have been vastly explored through the novel use of tensor networks, which can be interpreted as encoders for quantum error-correcting codes. We focus our attention on the study of codes associated with holographic geometries living in higher dimensions, constructing stabiliser codes that are analogues of the famous HaPPY code [1]. We do so by considering both absolutely maximally entangled (AME) and non-AME codes noting that discrete symmetries of the polytope are always broken for AME codes in dimensions higher than two. We also explore alternate constructions of stabiliser codes for hyperbolic spaces in which the we associate the logical information with the boundary.

The second part of this thesis involves gravitational lensing, the observed astrophysical phenomena involving the propagation of light through a specific background spacetime, governed by its null geodesic equations. Utilising the expansions presented in [2], we consider gravitational lensing by a rotating, compact object (i.e an object described by the Kerr metric) in the weak deflection limit, thus assuming large astrophysical separations. We present magnification curves using point-source models for numerous geometrical configurations involving different inclinations and spins. Throughout this analysis, we discuss the plethora of applications that arise in both astrophysics and fundamental theory before introducing a more realistic model adjusted for the inclusion of extended sources with limb-darkening effects.

Table of Contents

List of Figures

Declaration of Authorship

I, Charlie Woodward, declare that the thesis entitled *Unraveling the mysteries of spacetime: holographic codes and gravitational lensing* and the work presented in the thesis are both my own, and have been generated by me as the result of my own original research. I confirm that:

- this work was done wholly or mainly while in candidature for a research degree at this University;
- where any part of this thesis has previously been submitted for a degree or any other qualification at this University or any other institution, this has been clearly stated;
- where I have consulted the published work of others, this is always clearly attributed;
- where I have quoted form the work of others, the source is always given. With the exception of such quotations, this thesis is entirely my own work;
- I have acknowledged all main sources of help;
- where the thesis is based on work done by myself jointly with others, I have made clear exactly what was done by others and what I have contributed myself;
- parts of this work have been published as:
  - M. Taylor and C. Woodward, *Holography, cellulations and error correcting codes*, 2112.12468.
  - M. Middleton, M. Taylor and C. Woodward, *Gravitational microlensing in Kerr spacetime*, (to appear).

Signed: .....

Date: .....

Acknowledgements

First and foremost I would like to express my deepest gratitude to my primary supervisor, Prof. Marika Taylor, without whom none of this would be possible. She has provided invaluable guidance and insights into the world of theoretical physics, as well as both her support and patience during my candidature. Her extensive knowledge and expertise has immensely influenced my understanding and passion for the subject from my earliest of days at undergraduate level, and I will carry the problem solving skills developed under her supervision with me for the rest of my days.

I would also like to give my utmost appreciation to many other members of the STAG group that I had the pleasure of interacting with. Namely, I would like to thank Dr. Matthew Middleton for providing valuable intuition and enthusiasm with regards to the stimulating discussions we had concerning the various astrophysical phenomena in gravitational lensing. Other notable staff members who have shaped my development, both directly and indirectly, through weekly seminars, progression reviews, informal discussions and more include Kostas Skenderis, David Turton, Nick Evans, Carlos Mafra, Andrew O'Bannon, Oscar Dias, Nansen Petrosyan, Inês Aniceto, James Drummond, Tim Morris and Mark Sullivan.

I also benefitted from numerous interactions with a wonderful network of fellow PhD students over the last 4 years, who have made my candidature significantly more enjoyable and academically satisfying. Honourable mentions should be given to Ross Glew and Arran Freegard for partaking in many profound mathematics and physics oriented conversations while being fantastic companions to share this journey with. Similarly, I extend a more broad thanks to the other STAG and DISCnet students that impacted my studies, namely Michele Santagata, Matthew Russell, Alex Mitchell, Sam Rowley, Billy Ford, Ben Kitching-Morley, Ciara Byers, Adam Forster, James Richings,

Davide Bufalini, Ernesto Bianchi, Sami Rawash, Daniel Hasenbichler, Vlad Mandric, Jack Mitchell, Dalius Stulga, Rajnandini Mukherjee, Callum Radley-Scott, Norman Khan, Matthew Grayling, Jakub Orwat-Kapola, James Keeble, Aran Borkum, Brett Mayes, Connor McIsaac, Joe Davies, Josh Wilde, Jussi Kuusisto, Lewis Hill, Maria del Carmen Campos Varillas and Meirin Evans.

To my closest friends for which I am enormously grateful, I thank you for helping to alleviate the stresses associated with this academic milestone, whilst forever keeping me grounded. Thus, I would like to show appreciation to Gareth Dyer, Joe Broadway, Alec Knott, Jenny Manley, Kathryn Card, Dan Gallagher, Eloise Robbins, Tara Kelley and Miniver Mortimer. Your support and encouragement is truly treasured and I hold my friendship with each of you to the highest regard.

I extend my thanks to my immediate family for building the underlying foundations allowing me to chase my dreams and teaching me the utmost importance of education. To my parents, Andrew and Julie, my sister Laura and my cousin Luci, thank you for your undying patience and unconditional support, despite all the hardships the last few years have brought.

Last, but certainly not least, I owe my eternal gratitude to my dearest, Lucy. Throughout this process, you have shown unwavering support and wholehearted belief in me, providing reassurance every step of the way. If things were ever bleak, your love, understanding and rationale provided me the strength and motivation I needed to prevail in this endeavour.

Preface

Introduction

At its heart, theoretical physics is the elegant blend of the lucrative fields of mathematics and physics, perfectly epitomised by the following two quotes:

'*The most beautiful thing we can experience is the mysterious. It is the source of all true art and science.*' - Albert Einstein

'*Scientists have become the bearers of the torch of discovery in our quest for knowledge.*' - Stephen W. Hawking

Understanding our universe at the most fundamental level and uncovering all of its subtleties and secrets, stands at the forefront of every physicist's aspirations. The last decade has been particularly fruitful, constituting the discovery of the Higgs boson [4, 5], the first detection of gravitational waves [6] and the emergence of the first images of the event horizon of a black hole [7–12]. Indeed, it truly is a compelling time to be working in the discipline.

This thesis is divided into two parts. In the first part we concern ourselves with a particularly fascinating avenue of the holographic principle, elucidating its confluence with ideas in quantum information theory, namely its natural interpretation in the language of quantum error correcting codes. In the second part, we describe the curious phenomena of gravitational lensing, incorporating rotating celestial objects such as Kerr black holes, analysing the null geodesics from both an astrophysical perspective and the viewpoint of a

fundamental theorist. The underlying connection uniting these two exhilarating concepts stems from the fundamental nature of spacetime itself, together with its many mystifying properties and unique mathematical structure.

One of the considerable, outstanding problems in theoretical physics stems from the incompatibility of gravity and the realm of quantum mechanics. Unifying the strong and weak nuclear forces, electromagnetism and gravity into one consistent 'theory of everything' remains an elusive dream, due to the persistence of the latter resisting quantisation. Pursuits of achieving this unprecedented goal has led to the development of numerous postulations that combine the four fundamental forces of our universe into a single consistent theory, the leading candidate being string theory [13–15].

Due to the meticulous study of black holes, one of natures most mysterious objects, throughout the 1970s [16–22], new insight was drawn from their quantum properties. The interpretation of these findings led to the more radical prospect that spacetime itself is not fundamental but rather that it emerges from quantum physics. The radical conjecture that arose, appropriately deemed *the holographic principle* [23, 24], stated that the world is in fact a hologram with the fundamental description living at its boundary. The holographic principle was first realised Maldacena in the form of the AdS/CFT correspondence [25] within string theory, providing a duality between a particular class of spacetimes and conformal field theories.

The emergence of the bulk geometry from a field theory living at its boundary is an astonishing aspect of the AdS/CFT correspondence, and over time, studying the various aspects of entanglement entropy became an encouraging candidate to probe the bulk [26–31]. The seminal work [32] sought to understand the emergence of locality in the bulk, uncovering a new affinity in which the AdS/CFT correspondence can be interpreted as a quantum error correcting code. This stimulating relationship was only established recently, thus the field is subject to much ongoing work, however there have been numerous innovative constructions of holographic codes [1, 33–38]; toy-models that realise the AdS/CFT correspondence.

The perplexing phenomena describing the deflection of light rays in the presence of a gravitational field, was first formally addressed by Einstein [39], prior to the development of the full theory of general relativity [40]. Implementing the acclaimed equivalence principle, he explicitly calculated the deflection angle, reproducing the formula from Newtonian physics [41] which was later shown to be in quantitative agreement with the experimental measurement [42]. While occasional research papers made reference to gravitational lensing in the decades that followed [43–47], the field became somewhat dormant, only receiving substantial attention in the 1960s [48–53]. Most notably, in the invigorating studies [51, 52], the underlying equations describing gravitational lensing

were derived and it was shown how one could utilise gravitational lensing in order to determine Hubble's constant.

However until 1979, gravitational lensing was viewed as an obscure subject to pursue with no substantial experimental evidence. This outlook was altered dramatically when the quasi-stellar object (or quasar) QSO 0957+561 became the first observed source to exhibit gravitational lensing [54]. The two corresponding optical images A and B, with redshift $z \sim 1.4$, had an angular separation of around 6 arcseconds. This observation sparked a new era in the gravitational lensing community and many further lensing systems were consequently observed, kindling tremendous excitement in the research area, inspiring a plethora of remarkable works [55–65].

Outline

Before beginning the discussion at a higher level of technicality, we briefly summarise the organisation of the material within this thesis. In chapter 1, we begin by establishing the holographic principle [23, 24], providing the motivation for its most well understood realisation, the AdS/CFT conjecture [25], the central focus of this chapter. We discuss the correspondence in both its original and most general form, constructing a precise holographic dictionary [66,67] via the field-operator map, before articulating the key ideas behind holographic renormalisation [68–71].

In chapter 2, we present all of the essential ingredients making up quantum information theory [72] that have significant value in subsequent chapters. We illustrate the concepts related to the unique phenomenon of quantum entanglement [73], providing essential elaboration on the representation of quantum systems using tensor networks [74, 75]. Further, we introduce the notion of quantum error correcting codes [72, 76, 77], discussing their key properties, prior to introducing a particular class of codes known as stabiliser codes [78].

Chapter 3 is devoted to bringing together the two major concepts introduced in the first two chapters. This fascinating confluence between the AdS/CFT correspondence and those appropriate branches of quantum information theory, encompass fresh concepts such as holographic entanglement entropy [30, 31], the Ryu-Takayanagi conjecture [26, 27] and holographic quantum error correcting codes [1, 32, 79].

Chapter 4 of this thesis consists of the original research published in [80]. Here, we initiate a systematic study of codes associated with holographic geometries in higher dimensions, relating cellulations of the spatial sections of the geometries to stabiliser codes. We construct analogues of the HaPPY code [1] for three-dimensional hyperbolic space (AdS_4), using both absolutely maximally entangled (AME) and non-AME codes.

These codes are based on uniform regular tessellations of hyperbolic space but we note that AME codes that preserve the discrete symmetry of the polytope of the tessellation do not exist above two dimensions. We also explore different constructions of stabiliser codes for hyperbolic spaces in which the logical information is associated with the boundary and discuss their potential interpretation. We explain how our codes could be applied to interesting classes of holographic dualities based on gravity-scalar theories (such as JT gravity [81, 82]) through toroidal reductions of hyperbolic spaces.

In chapter 5, we provide a comprehensive literature review of the various aspects of gravitational lensing subsequently used in chapter 6. A general overview of lensing in the Schwarzschild regime introduces this chapter, outlining the fundamental aspects of this phenomena. This involves defining the lens equations [51, 83], deriving the deflection angle [39] and summarising the notion of microlensing [84]. We then extend to a more general situation, encapsulating the addition of spin, so that we have a rotating lens by considering null geodesics in Kerr spacetime [2, 85–92]. We close this chapter by commenting on how our work may relate to two extremely fascinating concepts with regards to the fundamentals of spacetime, namely the fuzzball proposal [93–96] and the Kerr/CFT correspondence [97, 98].

Chapter 6 of this work consists of further original research that has yet to be submitted for publication. After reviewing the parameter space constituting the weak deflection limit and the introducing the analytic expansions first presented in [2, 88], we investigate the importance of the spin asymmetry that arises in Kerr lensing for large astrophysical separations. These effects are initially illustrated through study of the point source magnification curves for various different spin and inclination configurations and by drawing comparisons with the analogous Schwarzschild magnification curves. Our analysis is then extended by considering spherical (finite) sources of uniform brightness as well as cases involving limb darkening effects. We explain how our initial model paves the way for future research that has rather interesting consequences, with vast applications in both astrophysics and fundamental theory.

Part I

Holographic quantum error correcting codes

CHAPTER 1

The AdS/CFT correspondence

1.1 The holographic principle

The vital ingredient, underpinning many of the proposals within this work, is the highly acclaimed *anti-de Sitter/conformal field theory correspondence*, commonly referred to as the AdS/CFT correspondence [25]. This duality has shown concrete success in pursuits to realise the *holographic principle*, a concept arising from the countless endeavours to quantise gravity. The following section is dedicated to introducing the holographic principle, discussing its origin and thus motivating the AdS/CFT correspondence. The original arguments were presented by 't Hooft [23] and Susskind [24], before the enlightening review [99] was produced, covering the topic in remarkable depth whilst providing a full list of references.

1.1.1 Black holes: The emergence of the holographic principle

Quantising gravity remains one of the great outstanding problems in theoretical physics. However, attempts to understand this elusive puzzle, have proved useful nonetheless. In most physical circumstances gravitational fields are weak, so a lack of understanding of quantum gravity is not essential, however should one truly wish to reveal the characteristics of quantum gravity, the natural place to investigate are situations where gravity proves

to be strong. Strong gravity is known to prevail in circumstances where matter becomes sufficiently dense resulting in the gravitational collapse of an astronomical object. As is well known, black hole formation is a result of complete gravitational collapse, making the study of black holes a prime candidate to uncover the mysteries of quantum gravity.

One of the most remarkable results in modern physics was uncovered in the 1970s, when physicists began investigating these quantum properties of black holes. Black holes were realised to be thermodynamical objects that both radiate thermally at a well-defined temperature and carry entropy.

This discovery arose with Hawking's area theorem, which illustrated that the area of a black hole's event horizon can never decrease, in analogy to the second law of thermodynamics [16];

$$\delta S_{\text{matter}} \geq 0 \quad \longleftrightarrow \quad \delta A_{\text{horizon}} \geq 0. \tag{1.1.1}$$

Pushing this realisation further, four laws of black hole thermodynamics were hypothesised [17] which consequently were speculated to be purely mathematical since black holes were truly thought to be black (hence having no entropy or temperature). However a concern arose: launching a thermodynamical system into the black hole would destroy entropy, violating the second law of thermodynamics. Thus, Bekenstein [18–21] proposed that black holes have an entropy, S_{BH}, that is directly proportional to the area, A_{horizon}, of the event horizon,

$$S_{BH} = \frac{k_B A_{\text{horizon}}}{4 l_P^{d-2}} = \frac{k_B c^3 A_{\text{horizon}}}{4\hbar G^{(d)}}, \tag{1.1.2}$$

where k_B is the Boltzmann constant, $l_P = (\hbar G^{(d)}/c^3)^{\frac{1}{d-2}}$ is the d-dimensional Planck length and $G^{(d)}$ is the Newtonian gravitational constant, differing according to the dimension of the spacetime d. This entropy is famously known as the *Bekenstein-Hawking entropy*. Furthermore, this led to the suggestion that S_{BH} truly is a thermodynamic quantity, leading to the emergence of the generalised second law of black hole thermodynamics [18–20]: the sum of the entropy from other fields of matter S_{matter} and the black hole entropy S_{BH} can never decrease,

$$\delta S_{\text{total}} = \delta(S_{BH} + S_{\text{matter}}) \geq 0. \tag{1.1.3}$$

The thermodynamic characterisation of these extreme objects was clarified when Hawking considered quantised fields in a classical black hole background. Describing black holes in this semi-classical regime, it was discovered that black holes slowly emit thermal radiation. Thus, they were not truly black at all [22]. In fact, the laws of black hole mechanics were not solely a mathematical analogy to the laws of thermodynamics, black holes were true thermodynamic systems. This emitted thermal radiation is

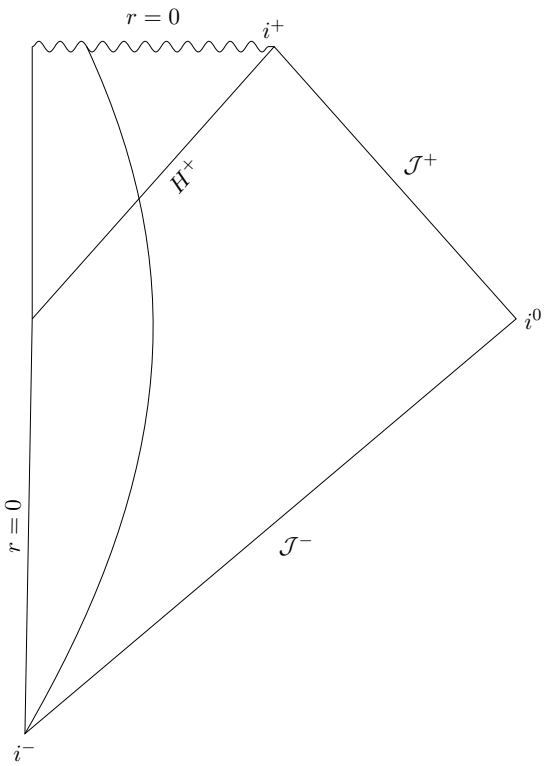

Figure 1.1.1: The Carter-Penrose diagram depicting the formation of a black hole due to the gravitational collapse of some spherically symmetric shell, with the future event horizon denoted H^+.

associated with the temperature

$$T_H = \frac{\hbar\kappa}{2\pi k_B c}, \tag{1.1.4}$$

known as the *Hawking temperature* of a black hole, where κ is the surface gravity of the horizon. For instance, the radiation emitted from a $d = 4$ Schwarzschild black hole has Hawking temperature

$$T_H = \frac{\hbar c^3}{8\pi k_B G M}. \tag{1.1.5}$$

These astounding results inspired numerous proposals and insights into quantum gravity. Firstly, the Bekenstein-Hawking entropy formula (1.1.2) can be used to argue that, for some volume V with surface area A, the maximally entropic system is that of a black hole. Consider a system undergoing gravitational collapse, evolving via an adiabatic process, resulting in the formation of a black hole. For instance, consider some spherical shell with area A collapsing into a black hole with horizon area A such as in figure 1.1.1. Of course, since black holes are the densest objects in the universe and the area bounding the object remains constant, the initial object must necessarily contain less energy than that of the black hole. So by simply adding matter to this initial system, one achieves gravitational collapse and the volume becomes filled by the black hole. Hence, in order to preserve the

generalised second law, one must satisfy the *spherical entropy bound* [24]

$$S_{\text{matter}} \leq S_{BH} = \frac{A}{4G}. \tag{1.1.6}$$

In other words, there are underlying constraints on how densely information can be packed within an object [1]. Compressing too much entropy into a sufficiently small region would result in the system collapsing into a black hole. Therefore, (1.1.2) yields the surprising yet crucial result; the maximal entropy of any static object is not related to the volume as one may expect, but instead is related with the surface area. While (1.1.6) has several shortcomings, such as the requirement the initial system is initially nearly spherically symmetric, the more rigorous *covariant entropy bound* [100] rectifies these issues. Moreover, it has been extensively proved valid in numerous instances and can be used to derive the Bekenstein bound [101] in any isolated, weakly gravitating system [102].

When considering quantum systems, it is well-known that the thermodynamic entropy, S, of an isolated system and the dimension of the Hilbert space of the system, $\mathcal{N}$, have the following relation:

$$\mathcal{N} = e^S. \tag{1.1.7}$$

Likewise, for any quantum mechanical system, the total number of degrees of freedom N is defined to be the logarithm of the Hilbert space's dimension,

$$N = \log \mathcal{N}. \tag{1.1.8}$$

Since quantum field theory (QFT) is a local theory, a justifiable assumption is that the number of degrees of freedom of a system scale with the volume of the system, $N \sim V$, or in other words, the Hilbert space of the system will consist of $\mathcal{N} = e^V$ states.

Return to the aforementioned example in which we considered some system undergoing evolution resulting in black hole formation. According to (1.1.2), the total number of degrees of freedom for the final black hole system, bounded by some area A and filling a volume V, is $N = A/4G$ while the total number of states is $\mathcal{N} = e^{A/4G}$. Consequently, the initial system will have a much larger Hilbert space (of dimension $\sim e^V$) prior to the collapse, leading to the total number of states being reduced, meaning any recovery of the initial state will have been made impossible - undoubtedly a violation of unitarity. Thus, insisting on preserving unitarity, one is left with the startling outcome that the dimension of the Hilbert space was $e^{A/4G}$ from the very beginning.

[1] Note, to make the variables of interest more apparent, in (1.1.6) one uses units such that $c = \hbar = k_B = 1$, which will now be adopted for the remainder of this thesis.

This intriguing phenomenon led to the proposal of the *holographic principle* by Susskind and 't Hooft [23,24]: Any theory of quantum gravity in a given region of spacetime should be exactly equivalent to another theory living at the boundary of this region, since the maximum entropy is proportional to the boundary area, as opposed to the volume. In other words, any volume V bounded by some area A, is completely described by the $N = A/4G$ fundamental degrees of freedom encoded on the boundary surface A.

The holographic principle is frequently declared as a duality. In this language, the holographic principle states:

> Any quantum theory of gravity in a $(d+1)$-dimensional spacetime is dual (mathematically equivalent) to another theory without gravity, in a spacetime with one less, non-compact dimension d.

This 'holographic' interpretation of gravitational theories indeed has a resemblance to the concept of a hologram with regards to visual perception. There, the image is encoded in some 2-dimensional surface, projected to appear in 3-dimensions. Before continuing to the next section where we describe the most prevalent realisation of the holographic principle, the AdS/CFT correspondence, we briefly describe some of the other implications of black hole thermodynamics.

Firstly, due to the no-hair theorem, which states black holes are uniquely characterised by their mass, charge and angular momentum, they cannot have classical microstates. Therefore these microstates (1.1.7) that are closely associated with the Bekenstein-Hawking entropy must stem from the full quantum theory of gravity. Descriptions of certain classes of black holes viewed from a microscopic, unitary quantum perspective have been provided from string theory. Further, Strominger and Vafa [103] were able to successfully reproduce the Bekenstein-Hawking entropy for a particular extremal, maximally supersymmetric black hole configuration. Though numerous other classes of black holes have since been explicitly shown to satisfy the Bekenstein-Hawking entropy, understanding the microstate structure of the Schwarzschild black hole remains elusive.

The thermal radiation emitted by the black hole in the semiclassical regime arises from the pair production and annihilation of virtual particles that populate the vacuum outside the event horizon and is known as *Hawking radiation* [21, 22]. A heuristic description of Hawking radiation is the view that one member of the entangled pair produced from vacuum fluctuations falls into the black hole, while the other member escapes to infinity. The existence of Hawking radiation results in the astonishing puzzle that is the black hole information paradox [104]. From a quantum perspective this corresponds to a violation of

unitarity, since an initial infalling pure state will be converted into a mixed (thermal) state. Furthermore, when black hole evaporation eventually occurs, the information associated to the infalling particles will be lost. A solution the black hole information paradox may provide information about the underlying theory of quantum gravity. While there is no general consensus for a resolution to this startling paradox, several different approaches have been proposed. The most widely acknowledged include the fuzzball proposal [93–96], the island proposal [105–109], as well as the concept of soft hair on black holes [110].

1.2 The AdS/CFT conjecture

As previously described, the most concrete realisation of the holographic principle arose from string theory, first explored by Maldacena in his profoundly influential study [25]. In this section, after introducing anti-de Sitter spacetimes, we review the $\mathrm{AdS}_5/\mathrm{CFT}_4$ conjecture, the most studied example of the correspondence, which is a duality relating a four-dimensional conformal field theory (CFT) and anti-de Sitter spacetime in five dimensions. We then introduce the more general statement of the AdS/CFT conjecture, outlining other key examples originating from various different string theory configurations. To close the chapter, we summarise the numerous applications of the conjecture as well as depicting a handful of further interesting features.

1.2.1 Anti-de Sitter spacetime

The Lorentzian analogue of Euclidean hyperbolic spacetime, anti-de Sitter spacetime (AdS) is the maximally symmetric solution of Einstein's equations with constant negative curvature. That is, it is the maximally symmetric spacetime satisfying

$$R_{\mu\nu} - \frac{1}{2}Rg_{\mu\nu} + \Lambda g_{\mu\nu} = 8\pi T_{\mu\nu}, \tag{1.2.1}$$

where one has negative cosmological constant $\Lambda < 0$. In what follows, we will only discuss vacuum solutions, i.e. $T_{\mu\nu} = 0$, though generalisations are straightforward. Thus, the Riemann curvature tensor for exact AdS may be expressed as

$$R_{\mu\nu\rho\gamma} = \frac{1}{L^2}(g_{\rho\mu}g_{\nu\gamma} - g_{\mu\gamma}g_{\nu\rho}). \tag{1.2.2}$$

The $(d+1)$-dimensional spacetime AdS_{d+1} can be exprssed with the metric in global coordinates

$$ds^2 = -\Big(1 + \frac{r^2}{L^2}\Big)dt^2 + \frac{dr^2}{1 + \frac{r^2}{L^2}} + r^2 d\Omega_{d-1}^2, \tag{1.2.3}$$

where we have denoted the *AdS radius* of the spacetime as $L = \sqrt{-d(d-1)/2\Lambda}$. Here, $r \in [0, \infty)$, $t \in (-\infty, \infty)$ and Ω_{d-1} are the angular coordinates parametrising the sphere S^{d-1}.

Arguably the most noteworthy feature of AdS spacetime is the existence of the *conformal boundary*[2] at $r = \infty$. Moreover, this boundary has the topology $\mathbb{R} \times S^{d-1}$, matching that of conformally compactified Minkowski Space on $\mathbb{R}^{1,d-1}$. This boundary plays an important role in the AdS/CFT correspondence as we will see in section 1.2.2. One defines *asymptotically locally AdS spacetimes* (AlAdS) as Einstein metrics with a negative Λ that can be conformally compactified to have the same conformal structure as AdS. We will return to the discussion of these spacetimes in section 1.4, where we provide further mathematical insight by explicitly assigning them a metric.

Another convenient parametrisation of the embedding of AdS spacetime is provided using the Poincaré patch coordinates. In these coordinates, the AdS_{d+1} metric becomes

$$ds^2 = \frac{L^2}{r^2} dr^2 + \frac{r^2}{L^2} \eta_{\mu\nu} dx^\mu dx^\nu, \tag{1.2.4}$$

where the spacetime is foliated over r with $r \in (0, \infty)$ and $\eta_{\mu\nu} = \mathrm{diag}(-1, +1, \ldots, +1)$ denoting the usual Minkowski metric. In these new coordinates, the conformal boundary can clearly be noticed to be present at $r = \infty$, where the metric diverges due to the second order pole $r \to \infty$. One may also notice that in the opposing limit, $r \to 0$, there is a degenerate Killing horizon known as the Poincaré horizon. This singularity is not a curvature singularity and simply arises due to the choice of coordinates.

Similarly, the AdS metric is often expressed in the Poincaré coordinates[3], which is achievable by introducing the inverse radial coordinate $z = L^2/r$. Then

$$ds^2 = \frac{L^2}{z^2} (dz^2 + \eta_{\mu\nu} dx^\mu dx^\nu), \tag{1.2.5}$$

where $z \in (0, \infty)$. In this new set of coordinates, the conformal boundary lies at $z = 0$ while the Poincaré horizon is located at $z \to \infty$.

Now we have outlined the basic structure of AdS spacetime and its features, we proceed to present the remarkable AdS/CFT correspondence itself.

[2] See appendix A.1.1 for concrete mathematical definitions on the conformal boundary and conformal compactifications.

[3] This coordinate system only strictly covers half of the AdS_{d+1} spacetime.

1.2.2 The AdS_5/CFT_4 conjecture

The original and most studied account of the AdS/CFT correspondence encompasses type IIB string theory on $AdS_5 \times S^5$ and the superconformal theory, four-dimensional $\mathcal{N} = 4$ supersymmetric Yang-Mills (SYM) theory, living at the boundary of AdS_5. For our purposes here, we will not explicitly show the derivation of the duality, but the motivation arises when examining a stack of N coincident $D3$-branes from both the open ($g_sN \ll 1$) and closed ($g_sN \gg 1$) string perspectives. In the near-horizon or Maldacena limit, $\alpha' \to 0$ with r/α' fixed, the quantum field theory emerges as the gauge theory living on the $D3$-brane worldvolume associated with the conformal boundary, ∂M, of the AdS_5 component.

The AdS_5/CFT_4 conjecture can be stated as:

> $\mathcal{N} = 4$ SYM theory in four spacetime dimensions, with gauge group $SU(N)$ and Yang-Mills coupling constant g_{YM} is dual to ten-dimensional type IIB string theory on $AdS_5 \times S^5$ consisting of N units of five-form flux (F_5) and curvature radius L.

Each side of the duality has two key free parameters. Firstly, on the CFT side of the theory, one has the rank of the gauge group N and the Yang-Mills coupling constant g_{YM}. Similarly, investigating the AdS side of the map, there are two dimensionless parameters. Firstly, we have the string coupling g_s. The second parameter is the shared radius L of both the five-dimensional AdS_5 space and the five dimensional sphere S^5 expressed in units of string length $L/\sqrt{\alpha'}$, with $\alpha' = l_s^2$ as usual. According to the AdS_5/CFT_4 correspondence, these parameters are related as

$$g_{YM}^2 = 2\pi g_s, \qquad 2g_{YM}^2 N = \frac{L^4}{\alpha'^2}. \tag{1.2.6}$$

While this form of the conjecture is most precise, the correspondence is often studied in numerous different parameter regimes. The duality is particularly interesting when the string coupling is considered in the weak coupling perturbative limit $g_s \ll 1$, whilst keeping $L/\sqrt{\alpha'}$ constant. Should one insist that the 't Hooft coupling, $\lambda \equiv g_{YM}^2 N$ remains fixed, then the duality can be understood to be an exact equivalence between classical string theory and a gauge theory in the large-N limit ('t Hooft limit), i.e. when $N \to \infty$.

Further, taking the limit $\lambda \to \infty$, and consequently $L/\sqrt{\alpha'} \to \infty$, implies that the radius of curvature is significantly larger than the length of a string $L \gg l_s$, thus the AdS side of the duality is in the low-energy limit of IIB string theory - a supergravity regime (so $AdS_5 \times S^5$ has weak curvature). Hence, we are left with a duality between type IIB supergravity on $AdS_5 \times S^5$ and strongly-coupled $\mathcal{N} = 4$ SYM theory in four spacetime dimensions. In this sense, the AdS/CFT duality is a *strong/weak duality*. The various

different forms of the AdS/CFT correspondence, depending on which limit we are in, are listed in table 1.2.1.

Since these two theories are mathematically equivalent, then the global symmetries on both sides of the duality should concur. To exemplify this, consider the subgroup generating the bosonic symmetries, $SO(4,2) \times SO(6)$. From the boundary field theory perspective, $SO(4,2)$ corresponds to the conformal group, while rotating supercharges under R-symmetry provides the $SU(4) \sim SO(6)$. From the gravity theory perspective, these symmetry groups arise from the isometry groups of the AdS_5 and S^5 components respectively. Indeed, one can show the full superconformal group $PSU(2,2|4)$ will also be preserved by each side of the correspondence.

Note, with the current interpretation, the four-dimensional CFT is then seemingly encoded at the boundary of the ten-dimensional string theory. However, after Kaluza-Klein compactification on the five dimensions encompassed by the sphere S^5, we immediately notice that this duality is a manifestation of the holographic principle since the five-dimensional string theory on the AdS_5 geometry is then mathematically equivalent to the four-dimensional $\mathcal{N} = 4$ SYM theory living on the conformal boundary of AdS_5.

Various forms of the AdS/CFT correspondence		
	Conformal Field Theory	IIB string theory
Strongest	General $\mathcal{N} = 4$ SYM theory.	Quantum string theory on $AdS_5 \times S^5$.
	$\downarrow N \to \infty$, λ =const.	$\downarrow g_s \to 0$, $\alpha'/L^2 =$ const.
Strong	Large N $\mathcal{N} = 4$ SYM theory.	Classical string theory on $AdS_5 \times S^5$.
	$\downarrow \lambda \to \infty$	$\downarrow \alpha'/L^2 \to 0$
Weak	Strongly coupled, large N $\mathcal{N} = 4$ SYM theory.	Classical supergravity theory on $AdS_5 \times S^5$.

Table 1.2.1: The multiple different forms of the AdS/CFT correspondence.

1.2.3 The general $\mathrm{AdS}_{d+1}/\mathrm{CFT}_d$ conjecture

In the previous section we briefly mentioned that the $\mathrm{AdS}_5/\mathrm{CFT}_4$ correspondence emerged as a realisation of the holographic principle from a particular string theory configuration involving $D3$-branes. This concept of beginning with a full string theory or supergravity solution and compactifying on the internal space is known as a *top-down* approach.

While we have restricted our focus to just the $\mathrm{AdS}_5/\mathrm{CFT}_4$ correspondence here, many other instances of the more general AdS/CFT correspondence exist, stemming from various different string theory configurations, following a top-down approach. The product spaces between various asymptotically locally AdS spacetimes and some compact geometry are known to realise the holographic principle. For example, in [25], spheres with different but appropriate dimensionality (with respect to the AdS space) such as $\mathrm{AdS}_4 \times S^7$ and $\mathrm{AdS}_7 \times S^4$ are shown to be appropriate configurations for $\mathrm{AdS}_4/\mathrm{CFT}_3$ and $\mathrm{AdS}_7/\mathrm{CFT}_6$. Correspondingly, the superconformal field theories making up these dualities are the ABJM [111] and $\mathcal{N} = (2, 0)$ [112] gauge theories respectively. There is no requirement, however, that these compact spaces are spheres and such configurations have been shown to realise the AdS/CFT correspondence [113].

Another interesting case is the $\mathrm{AdS}_3/\mathrm{CFT}_2$ correspondence in which the $D1$-$D5$ brane solution of string theory is considered on $\mathrm{AdS}_3 \times S^3 \times M_4$, where M_4 is some compact manifold. As discovered by Brown and Henneaux [114], the isometry group of AdS_3 is $SO(2, 2) \cong SL(2, \mathbb{R}) \times SL(2, \mathbb{R})$, with algebra $\mathfrak{sl}(2, \mathbb{R}) \times \mathfrak{sl}(2, \mathbb{R})$, which is enhanced to the infinite-dimensional Virasoro algebra $\mathfrak{vir} \times \bar{\mathfrak{vir}}$. Further, the corresponding central charge of the conformal field theory is given by

$$c = \frac{3L}{2G^{(3)}}. \tag{1.2.7}$$

Study of the $\mathrm{AdS}_3/\mathrm{CFT}_2$ duality can also provide interesting insights to the so-called Banados-Teitelboim-Zanelli (BTZ) asymptotically AdS_3 black hole [115], which we will discuss in section 3.1.2.

These various examples led to the more general AdS/CFT conjecture:

> Any quantum theory of gravity in a $(d + 1)$-dimensional asymptotically locally anti-de Sitter spacetime is dual (mathematically equivalent) to a conformal field theory of dimension d.

This duality can also be extended to include non-conformal field theories, however these theories cannot simply be dual to asymptotically AdS gravity. As demonstrated

in [116, 117], one can construct relevant Dp-brane solutions ($p \neq 3$) such that in the near-horizon limit, conformal symmetry is broken. This is since the dilaton admitted is not constant, or correspondingly, in the dual field theory these constructions inherit a gauge coupling that runs with energy scale. This class of dual theories is then said to possess a generalised conformal structure [118]. Configurations of this type were studied in greater depth in [119] to understand the precise holographic map between the *bulk* gravity theory and the *boundary* field theory.

Traditionally, when discussing the so-called bulk theory, we mean the gravity theory (i.e. AdS_{d+1} spacetime), while reference to the boundary theory indicates the asymptotic boundary of the spacetime (i.e. the flat $\mathbb{R}^{1,d-1}$). The relation between these is depicted in figure 1.2.2 for $\mathrm{AdS}_3/\mathrm{CFT}_2$. We note here, that from this instance forwards, when discussing an AdS gravity theory, one really means an asymptotically locally AdS gravity theory.

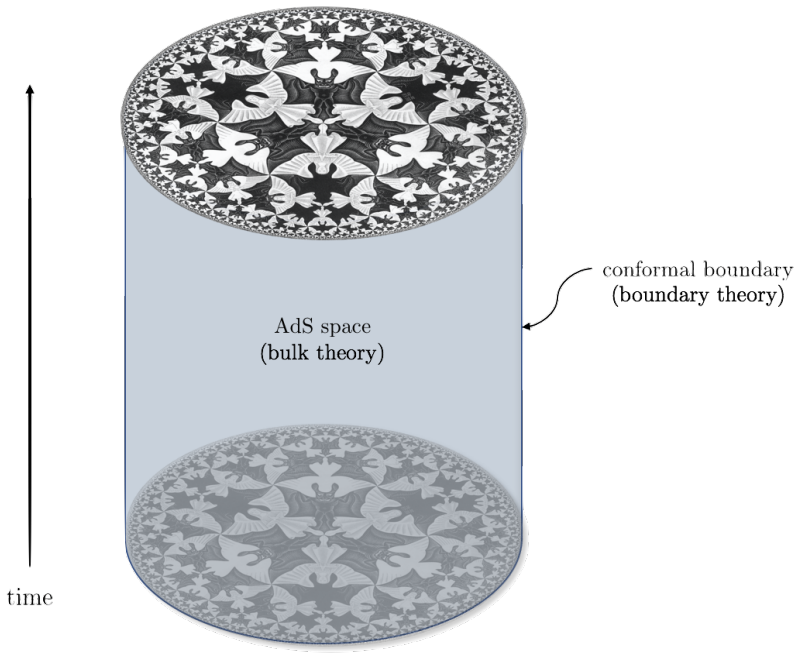

Figure 1.2.2: A representation of the bulk/boundary correspondence in AdS_3 spacetime. Fixed time slices t = const are represented by the Poincaré disk, thus generating the shaded cylinder to depict the full AdS_3 spacetime. At spatial infinity of the bulk AdS_3 spacetime, there is a conformal boundary where the boundary theory lives.

This enormous landscape of *gauge/gravity* dualities that has been unveiled, including those considering non-conformal field theories in addition to non-relativistic quantum field theories [120], continue to provide new and curious insights into the world of quantum gravity. For phenomenological purposes, these holographic dualities have been investigated in great depth. In order to describe strongly coupled field theories that exhibit interesting phenomena, one aims to construct bulk gravity theories with appropriate symmetries in

order to match that of the field theory of interest. Of course, many of these dualities require lower degrees of conformal symmetry and supersymmetry in the field theory than the cases presented so far. Due to this adversity, in practice, one often uses a *bottom-up* approach.

As opposed to the top-down approach, the bottom up approach involves fashioning an effective gravitational theory with appropriate field content to that of the case of phenomenological interest. While the actions of these theories are necessarily ad-hoc, they still possess the ability to capture the essential physics of the problem. These approaches have led to numerous applications of holography being developed, with notable utilisations in quantum chromodynamics (AdS/QCD) [121–124], condensed matter systems (AdS/CMT) [125–128] and hydrodynamics [129–131].

For example, in hydrodynamics, the exotic state of matter observed in heavy-ion collisions known as quark-gluon plasma can be well described by a strongly coupled relativistic fluid. The universal values of certain transport coefficients in strongly coupled fluids have been predicted using the gauge/gravity duality. Most illustriously, the ratio of shear viscosity η over entropy density s was found to be [132, 133]

$$\frac{\eta}{s} = \frac{1}{4\pi}, \tag{1.2.8}$$

a result that is consistent with the particularly small values of η/s which can be inferred from RHIC/LHC experiments for quark-gluon plasma. This has led to the development of the *fluid/gravity* correspondence [129]: the duality between long wavelength solutions of the Einstein equations in $(d+1)$-dimensions and solutions of nonlinear boundary fluid dynamics described by the generalised d-dimensional Navier-Stokes equations.

1.3 The holographic dictionary

The gauge/gravity duality has provided a clear relation between two theories: a gravitational theory on asymptotically locally AdS spacetimes and a quantum field theory (without gravity) living on its boundary. In this section, one explicitly illustrates these details by introducing the precise one-to-one mapping established in [66, 67]. The existence of such a map paves the way for the establishment of a full holographic dictionary between the two sides of the correspondence. We will also briefly encounter Witten diagrams and the required AdS propagators, the latter of which we will re-encounter later when demonstrating how bulk reconstruction justifies the existence of holographic codes.

1.3.1 The field-operator map

The conjectured correspondence [25] was further clarified and more rigorous rules identifying the dynamical equivalence between the bulk and boundary theories were developed independently by both Witten [67] and Gubser, Klebanov and Polyakov [66]. By equating the generating functionals, a precise computational dictionary can be established between the two sides of the correspondence. For any CFT, the generating functional $W_{CFT}[\phi_{(0)}]$ may be expressed as

$$W_{CFT}[\phi_0] := \log Z_{CFT}[\phi_{(0)}] = \log \left\langle e^{-\int d^d x \phi_{(0)}(x)\mathcal{O}(x)} \right\rangle_{CFT}, \tag{1.3.1}$$

where $\mathcal{O}$ are field theory operators and the source fields are denoted by $\phi_{(0)}$. Then, the *master formula* capturing the correspondence lies in the quintessential relation equating the gravitational partition function, Z_{grav}, and the CFT partition function Z_{CFT}:

$$Z_{grav}[\phi_{(0)}] = Z_{CFT}[\phi_{(0)}], \tag{1.3.2}$$

where the bulk fields ϕ have boundary asymptotics $\phi_{(0)} = \phi|_{\partial_{AdS}}$. More explicitly, on the gravity side, one computes the path integral across all bulk field configurations ϕ satisfying these boundary conditions. Thus,

$$Z_{grav}[\phi_{(0)}] = \int_{\phi|_{\partial_{AdS}}=\phi_{(0)}} \mathcal{D}\phi e^{-S[\phi]} = \left\langle e^{-\int d^d x \phi_{(0)}(x)\mathcal{O}(x)} \right\rangle_{CFT} \tag{1.3.3}$$

where the action functional for the bulk theory is denoted $S[\phi]$. Then, we have a correspondence; there is a one-to-one map between bulk field ϕ in the gravitational theory and the field theory operators $\mathcal{O}$ in the boundary theory. Specifically,

$$\phi_{(m)} \leftrightarrow \mathcal{O}_{(\Delta)}, \tag{1.3.4}$$

where m indicates the mass of $\phi_{(m)}$ and Δ is the scaling dimension of $\mathcal{O}_{(\Delta)}$. Subsequently, a relationship between m and Δ can also established. For example, should ϕ be a massive scalar we have

$$m^2 L^2 = \Delta(\Delta - d). \tag{1.3.5}$$

While fields of different spins satisfy different relations, the fundamental one-to-one mapping holds true. This is often called the *field/operator* correspondence.

In general, it is often extremely difficult to calculate the full partition function on the gravity side (Z_{grav}) of the correspondence. Typically, we restrict our interest to the leading term in the saddle-point approximation during the evaluation of Z_{grav}, or in other words, focusing on the partition function in the low-energy limit. In doing so, we are localising

the path integral on the classical solution to the equations of motion, ϕ_{cl}, so

$$Z_{grav}[\phi_{(0)}] = e^{-S_{on-shell}[\phi_{cl}]}, \tag{1.3.6}$$

where $S_{on-shell}$ denotes the on-shell supergravity action and the classical solutions satisfy the boundary conditions $\phi_{cl}|_{\partial AdS} = \phi_{(0)}$. Therefore,

$$S_{on-shell}[\phi_{cl}] = -W_{CFT}[\phi_{(0)}]. \tag{1.3.7}$$

Now we have a clear understanding of the map between generating functionals, connected correlation functions can now be computed holographically. This is implemented by taking derivatives of the generating functional with respect to the sources, evaluated by setting these sources to vanish, e.g. we have the one-point correlation function

$$\langle \mathcal{O}(x) \rangle = \frac{\delta S_{on-shell}}{\delta \phi_{(0)}(x)}\bigg|_{\phi_{(0)}=0}, \tag{1.3.8}$$

the two-point correlation function

$$\langle \mathcal{O}(x_1)\mathcal{O}(x_2) \rangle = \frac{\delta^2 S_{on-shell}}{\delta \phi_{(0)}(x_1)\delta \phi_{(0)}(x_2)}\bigg|_{\phi_{(0)}=0}, \tag{1.3.9}$$

and the more general n-point correlation function

$$\langle \mathcal{O}(x_1)\mathcal{O}(x_2)\dots\mathcal{O}(x_n) \rangle = \frac{\delta^n S_{on-shell}}{\delta \phi_{(0)}(x_1)\delta \phi_{(0)}(x_2)\dots\delta \phi_{(0)}(x_n)}\bigg|_{\phi_{(0)}=0}. \tag{1.3.10}$$

1.3.2 Propagators in anti-de Sitter spacetime

An alternative language to use when discussing the field/operator correspondence is that of AdS propagators. From the gravity perspective, computing correlation functions from 1.3.7 is equivalent to calculating the tree-level diagrams in AdS space, known as *Witten diagrams*. We will not discuss these diagrams in depth here, but they are analogous to Feynman diagrams and are supplemented by a set of rules comparable to the Feynman rules.

In Witten diagrams, there are two propagators to consider, the *bulk-to-boundary propagator* and the *bulk-to-bulk propagator*. As their names may indicate, the bulk-to-boundary operator connects a source at the boundary ∂AdS to an interaction point in the bulk (or another source at the boundary) while the bulk-to-bulk propagator connects two interaction points within the bulk. Various examples of Witten diagrams can be seen in figure 1.3.1.

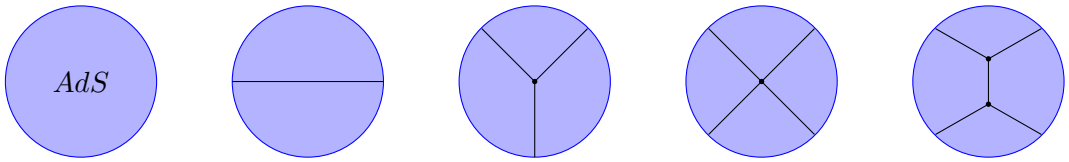

(a) boundary AdS (b) 2-pt (c) 3-pt (d) 4-pt type-I (e) 4-pt type-II

Figure 1.3.1: Examples of Witten diagrams in AdS. Diagram (a) shows an empty diagram used to denote the general structure. The interior of the circle denotes the bulk of the AdS space while the circle itself corresponds to the boundary ∂AdS. Diagrams (b)-(d) indicate various n-point diagrams with only bulk-to-boundary propagators while (e) also includes a bulk-to-bulk propagator.

As usual, the objective is to solve the bulk equations of motion for some bulk field ϕ, subject to the boundary conditions $\phi|_{\partial AdS_{d+1}} \sim z^{d-\Delta}\phi_{(0)}$, where one identifies Δ as the conformal dimension of the dual field theory operator $\mathcal{O}_\Delta$ and $\phi_{(0)}$ as the source for this operator. The problem can be reformulated as an integral equation involving the bulk-to-boundary propagator K, expressing the bulk field as

$$\phi(x) = \int_{\partial_{AdS}} d^d X K(x;X)\phi_{(0)}(X). \tag{1.3.11}$$

This propagator acts as an integration kernel, responsible for applying the boundary conditions as well as implementing the dynamics from the bulk equations of motion. For clarity, we have used coordinates X and x here, such that in this notation, these coordinates are abbreviations i.e. in global coordinates $X = (t', \Omega')$ is a boundary point and $x = (t, r, \Omega)$ is a bulk point. We note that the bulk-to-boundary propagator is most often expressed in Poincaré coordinates[4] in the literature, in which it explicitly takes the form

$$K(z, x; y) = C_\Delta \left(\frac{z}{z^2 + (x-y)^2} \right)^\Delta, \tag{1.3.12}$$

where

$$C_\Delta = \frac{\Gamma(\Delta)}{\pi^{d/2}\Gamma(\Delta - \frac{d}{2})}, \tag{1.3.13}$$

however our more general notation is a natural choice for the purposes of this thesis, as shall be made clear in section 3.2. The bulk-to-bulk propagator G is similarly defined,

$$\phi(x) = \int_{AdS} d^{d+1}y \, \sqrt{g} \, G(x;y)J(y), \tag{1.3.14}$$

equivalent to solving the equations of motion in the presence of some source $J(y)$ where $y = (t', r', \Omega')$ is another point in the bulk. The bulk-to-bulk propagator may similarly

[4]For the bulk-to-boundary propagator, the choice of Poincaré coordinates are such that (z, x) denotes a point with bulk coordinate z and boundary coordinates x^μ while y^μ denotes the coordinates of the boundary variable.

be expressed using Poincaré coordinates[5], where it takes the form of a hypergeometric function;

$$G(z,x;w,y) = \frac{C_\Delta}{2^\Delta(2\Delta-d)}\xi^\Delta \cdot \ {}_2F_1\Big(\frac{\Delta}{2},\frac{\Delta+1}{2};\Delta-\frac{d}{2}+1;\xi^2\Big), \tag{1.3.15}$$

where

$$\xi = \frac{2zw}{z^2+w^2+(x-y)^2}. \tag{1.3.16}$$

While we do not use the bulk-to-bulk propagator in much that follows though the bulk-to-boundary operator will resurface in section 3.2.

1.4 Holographic renormalisation

One of the crucial identifications in the AdS/CFT correspondence is that in the supergravity solution, the radial coordinate can be associated with the renormalisation (energy) scale in the dual conformal field theory. Recall, the AdS_{d+1} metric in Poincaré coordinates,

$$ds^2 = \frac{L^2}{z^2}(dz^2+\eta_{\mu\nu}dx^\mu dx^\nu). \tag{1.4.1}$$

Scale invariance in the boundary CFT implies the dilatation $x_\mu \to a x_\mu$ along with $\mu \to \mu/a$ is a symmetry, where μ is the energy scale. Analogously, the corresponding transformation in AdS_{d+1} is generated by the $SO(d,2)$ isometry

$$x_\mu \to a x_\mu, \qquad z \to az. \tag{1.4.2}$$

One may then naturally identify the radial coordinate $r = 1/z$ with the energy scale μ, i.e. $r \sim \mu$. The boundary $z \to 0$ then corresponds to the ultraviolet (UV) regime of the boundary field theory, while in the limit $z \to \infty$ implies we are in the infrared (IR) regime of boundary field theory. Alternatively, at the boundary region of AdS, $z \to 0$ implies $r \to \infty$ and so we are in the IR regime in the gravitational theory while towards the Poincaré horizon, $z \to \infty$ means we are in the UV regime in the bulk theory. This phenomenon is a general property of the gauge/gravity duality often called the UV/IR connection.

According to this UV/IR connection, since one expects UV divergences to arise from correlations functions in quantum field theory, as a consequence, it should be expected that the bulk theory suffers from IR divergences. These UV divergences are familiarly dealt with in quantum field theory by performing the procedure of renormalisation. Hence,

[5]For the bulk-to-bulk propagator, the choice of Poincaré coordinates are such that (z,x) denotes a point with bulk coordinate z and boundary coordinates x^μ while (w,y) denotes a point with bulk coordinate w and boundary coordinates y^μ.

in order to eliminate the IR divergences in the bulk theory (these divergences at the boundary), one expects holographically that solely from a near-boundary analysis, one will be able renormalise the bulk theory. Addressing these concerns is the procedure of *holographic renormalisation* [68–71].

We begin this section by outlining the general process of holographic renormalisation, creating a clear framework to follow. We then consider the case of pure gravity (i.e. the situation where the metric is the only bulk field), illustrating this method and stating some of the most recognised ramifications. For further details, the reader is suggested to study the original papers [68–70], together with the enlightening review [71].

1.4.1 The general procedure

The general procedure of holographic renormalisation may be summarised as follows:

1. Firstly, the Einstein field equations must be solved in full generality enforcing the prescribed boundary conditions. These field equations are solved iteratively using a near-boundary expansion and arbitrary Dirichlet boundary conditions, thus the resultant solution will take on an asymptotic form.

2. We proceed by substituting this asymptotic solution to the field equations back into the original action, evaluating it on-shell. During this computation, one introduces a *regulator*, ϵ, restricting the integration range, and calculates all arising divergences. We denote the regulated on-shell action $S_{reg}[f_{(0)};\epsilon]$ where $f_{(0)}$ represents the value an arbitrary bulk field takes at the boundary (i.e. the field theory source). The divergences are isolated such that $S_{reg} = S_{div} + S_{fin}$.

3. A new covariant counter-term action is then defined in terms of the diverging pieces of $S_{reg}[f_{(0)}]$,
$$S_{ct}[\mathcal{F}(x,\epsilon);\epsilon] = -S_{div}[f_{(0)}[\mathcal{F}(x,\epsilon)];\epsilon]. \tag{1.4.3}$$
Here we have explicitly shown that $f_{(0)}$ must be properly defined on the full asymptotic bulk field solution, which we denoted as $\mathcal{F}(x,\epsilon)$. This requirement arises since one must invert the series $\mathcal{F}(x,\epsilon)$ order by order since one needs to express the divergent pieces in terms of the induced metric on the regulated boundary.

4. The subtracted action at the cut-off, defined as the summation
$$S_{sub}[\mathcal{F}(x,\epsilon);\epsilon] = S_{reg}[f_{(0)};\epsilon] + S_{ct}[\mathcal{F}(x,\epsilon);\epsilon], \tag{1.4.4}$$
is then noticeably finite as one considers the limit $\epsilon \to 0$. The renormalised on-shell

action can then be defined as

$$S_{ren}[f_{(0)}] = \lim_{\epsilon \to 0} S_{sub}[\mathcal{F}(x, \epsilon); \epsilon]. \tag{1.4.5}$$

Here we have outlined the general procedure of holographic renormalisation. It is worth noting while it is conceptually simple, due to the inversion within step 3, applying this procedure can become computationally challenging and cumbersome. Alternative approaches have been considered based off of Hamiltonian and Hamilton-Jacobi techniques [134, 135].

1.4.2 Asymptotically locally AdS spacetimes

It is now natural to investigate holographic renormalisation by studying the asymptotics in a purely gravitational environment. Should we enforce conformal structure at spatial infinity and find the the most general asymptotic solution of the Einstein field equations 1.2.1, one will obtain an asymptotically locally AdS spacetime, as we previously alluded to in section 1.2.1. In the works of Fefferman and Graham [136], this spacetime was shown to possess the metric

$$ds^2 = g_{\mu\nu} dx^\mu dx^\nu = L^2 \left(\frac{d\rho^2}{4\rho^2} + \frac{1}{\rho} \tilde{g}_{ij}(\rho, x) dx^i dx^j \right), \tag{1.4.6}$$

where in odd boundary dimensions d, $g_{ij}(\rho, x)$ is given by the expansion

$$\tilde{g}(\rho, x) = g_{(0)} + \rho g_{(2)} + \cdots + \rho^{(d-1)/2} g_{(d-1)} + \rho^{d/2} g_{(d)} + \ldots \tag{1.4.7}$$

and in even boundary dimensions d, $g_{ij}(\rho, x)$ is given by the expansion

$$\tilde{g}(\rho, x) = g_{(0)} + \rho g_{(2)} + \cdots + \rho^{d/2} g_{(d)} + h_{(d)} \rho^{d/2} \log \rho + \ldots \tag{1.4.8}$$

Similarly to the ordinary AdS metric in Poincaré coordinates, the coordinates used here are (ρ, x^i), with $\rho \in (0, \infty)$ corresponding to the radial direction of the extra holographic dimension[6]. Hence, the conformal boundary is located at $\rho = 0$. Similarly, we use the notation of lower case Roman indices (i, j) to indicate the remaining d directions as opposed to the Greek indices (μ, ν) which denote all $d + 1$ directions. As before, the AdS radius of the spacetime is $L = \sqrt{-d(d-1)/2\Lambda}$.

[6]The radial coordinate was changed from z to $\rho = z^2$ for convenience when explicitly solving the equations of motion

For the bulk spacetime (M, g) with boundary ∂M, the Einstein-Hilbert action is

$$S[g] = \frac{1}{16\pi G}\Big[\int_M d^{d+1}x\sqrt{g}(R[g] - 2\Lambda) + \int_{\partial M} d^d x\, 2\sqrt{\gamma}K\Big], \tag{1.4.9}$$

such that the second term is the Gibbons-Hawking-York term [137,138]. The action should always be supplemented by this term for spacetime manifolds possessing a boundary in order to remove second-order derivatives. Denoting n^i as the outward-pointing normal unit vector, we use $K = \nabla_i n^i$ to represent the trace of the extrinsic curvature (second fundamental form) of ∂M and γ_{ij} as the induced metric on ∂M.

As mentioned previously, this action will contain a divergence upon its evaluation on-shell, originating from a second order pole at $\rho = 0$. Following the second stage of holographic renormalisation, one introduces a regulator, $\epsilon > 0$, in turn restricting the range of integration to be over the bulk region $\rho \geq \epsilon$. Further, the boundary term is evaluated on the hypersurface $\rho = \epsilon$, so the new regulated action is

$$S_{reg}[g] = \frac{1}{16\pi G}\Big[\int_{\rho\geq\epsilon} d^{d+1}x\sqrt{g}(R[g] - 2\Lambda) + \int_{\rho=\epsilon} d^d x\, 2\sqrt{\gamma}K\Big]. \tag{1.4.10}$$

The induced metric on $\rho = \epsilon$ is given by $\gamma_{ij} = (L^2\tilde{g}_{ij})/\epsilon$. One computes this action using the Fefferman-Graham gauge 1.4.6 by first realising that on-shell, we have the relationship

$$R[g] - 2\Lambda = -\frac{2d}{L^2}. \tag{1.4.11}$$

Similarly, the trace of the second fundamental form on the hypersurface $\rho = \epsilon$ can be expressed as

$$K = \frac{1}{L^2}(d - \rho \mathrm{Tr} g^{-1}\partial_\rho g). \tag{1.4.12}$$

Hence substituting these expressions into the regulated action 1.4.10, the on-shell regulated action becomes[7]

$$S_{reg}[g] = -\frac{L^{d-1}}{16\pi G}\int d^d x\, \Big[\int_\epsilon d\rho \frac{d}{\rho^{d/2+1}}\sqrt{\det\,\tilde{g}} + \frac{1}{\rho^{d/2}}(-2d\sqrt{\det\,\tilde{g}} + 4\rho\partial_\rho\sqrt{\det\,\tilde{g}})|_{\rho=\epsilon}\Big]. \tag{1.4.13}$$

In this new form, the divergences in the regulated action arise in the limit $\epsilon \to 0$. As described in step 2 of the procedure, we isolate these terms by expressing the S_{reg} as an expansion about the divergences by using the asymptotic solution: i.e. 1.4.7 for odd d and 1.4.8 for even d. Thus, for odd d, the expansion becomes

$$S_{reg} = -\frac{L^{d-1}}{16\pi G}\int d^d x\sqrt{g_{(0)}}\Big(\epsilon^{-d/2}a_{(0)} + \epsilon^{-d/2+1}a_{(2)} + \ldots \epsilon^{-1/2}a_{(d-1)}\Big) + \mathcal{O}(\epsilon^0), \tag{1.4.14}$$

[7]Here we manipulate the algebra using the well-known relationship between the trace and determinant $\mathrm{Tr} g^{-1}\partial_\rho g = \mathrm{Tr}\partial_\rho g/g = (\partial_\rho \det\, g)/\det\, g$, as well as the chain rule; $\partial_\rho\sqrt{\det\, g} = \partial_\rho \det\, g/2\sqrt{\det\, g}$.

where each of the coefficients a_k are local covariant terms of the boundary metric $g_{(0)}$. The full explicit values of these expressions may be found in [69]. For even d, we have

$$S_{reg} = -\frac{L^{d-1}}{16\pi G}\int d^dx\sqrt{g_{(0)}}\Big(\epsilon^{-d/2}a_{(0)} + \epsilon^{-d/2+1}a_{(2)} + \dots \epsilon^{-1}a_{(d-2)} - \log\epsilon a_{(d)}\Big) + \mathcal{O}(\epsilon^0), \tag{1.4.15}$$

with the notable difference stemming from the additional divergent logarithmic piece $\log\epsilon$. From step 3, one can then form expressions for the counter-term action. For odd d,

$$S_{ct} = \frac{L^{d-1}}{16\pi G}\int d^dx\sqrt{g_{(0)}}\Big(\epsilon^{-d/2}a_{(0)} + \epsilon^{-d/2+1}a_{(2)} + \dots \epsilon^{-1/2}a_{(d-1)}\Big), \tag{1.4.16}$$

while for even d,

$$S_{ct} = \frac{L^{d-1}}{16\pi G}\int d^dx\sqrt{g_{(0)}}\Big(\epsilon^{-d/2}a_{(0)} + \epsilon^{-d/2+1}a_{(2)} + \dots \epsilon^{-1}a_{(d-2)} - \log\epsilon a_{(d)}\Big). \tag{1.4.17}$$

Then, in order to finally remove the divergences from the system, as described in step 4, one sums the counter-term action, S_{ct}, with the regulated action, S_{reg}. Then the regulator, ϵ, is removed by taking the limit in which it vanishes, leaving the renormalised on-shell action

$$S_{ren} = \lim_{\epsilon\to 0}(S_{reg} + S_{ct}). \tag{1.4.18}$$

The procedure of holographic renormalisation is critical in any discussion of the AdS/CFT correspondence and now we have outlined how one implements it in practice, we briefly close this chapter with some interesting results that arose due to this technique.

The first of these is known as the *holographic Weyl anomaly*, a discovery first appearing in [68]. Here, consider the finite portion of the action, S_{fin}, defined as before as $S_{fin} = S_{reg} - S_{div}$. Should we want to consider a different representation of the boundary metric with the same conformal structure, or in other words, vary the boundary metric under a Weyl transformation as

$$\delta g^{ij}_{(0)} = 2\delta\sigma g^{ij}_{(0)}, \tag{1.4.19}$$

this manifests as

$$\delta S_{fin} = \frac{L^{d-1}}{16\pi G}\int d^dx\ \sqrt{g_{(0)}}\delta\sigma\mathcal{A}, \tag{1.4.20}$$

where $\mathcal{A}$ is the Weyl anomaly. It is worth noting that in the case of odd d, in order to ensure the vanishing of the variation $\delta S_{reg} = 0$ to consequently obtain $\delta S_{fin} = \delta S_{ct}$, we must consider the combined transformation of (1.4.19) together with $\delta\epsilon = \delta\sigma\epsilon$. In [68] it was shown that the anomaly vanishes in odd dimensions, $\mathcal{A}_{odd} = 0$, while in even dimensions it is given by the coefficient of the divergent logarithmic counter-term

$$\mathcal{A}_{even} = -a_{(d)}. \tag{1.4.21}$$

In dimensions $d = 2$ and $d = 4$, the holographic Weyl anomaly calculated in the bulk exactly matches the corresponding anomaly arising in the dual CFT. In the case of $d = 2$, this of course coincides with the central charge 1.2.7 previously described (calculated using the asymptotic symmetry algebra of AdS_3 [114]), while in the case of $d = 4$, it agrees with the large-N limit of $\mathcal{N} = 4$ SYM with gauge group $SU(N)$. Further, for $d = 6$, the Weyl anomaly was computed holographically, providing new information about the dual (0,2) theory.

The next interesting case to consider is that of the holographic energy-momentum tensor T_{ij}, with the following arguments first described in [69]. As mentioned earlier, the one-point correlation function of some operator $\mathcal{O}$ may be calculated according to (1.3.8). Then the expectation value of T_{ij} in the context of holographic renormalisation is given by

$$\langle T_{ij}(x)\rangle = \frac{2}{\sqrt{g_{(0)}}}\frac{\delta S_{ren}}{\delta g^{ij}_{(0)}}, \tag{1.4.22}$$

since it is sourced by the representative of the conformal structure $g^{ij}_{(0)}(x)$ on boundary ∂M. Under the limit where the regulator vanishes, $\epsilon \to 0$, this gives

$$\langle T_{ij}(x)\rangle = \lim_{\epsilon\to 0}\left(\frac{2}{\sqrt{\tilde{g}(\epsilon,x)}}\frac{\delta S_{fin}}{\delta \tilde{g}^{ij}(\epsilon,x)}\right) = \lim_{\epsilon\to 0}\left(\frac{L^{d-2}}{\epsilon^{d/2-1}}T_{ij}[\gamma]\right), \tag{1.4.23}$$

where

$$T_{ij}[\gamma] = \frac{2}{\sqrt{\gamma}}\frac{\delta S_{fin}}{\delta \gamma^{ij}} = T^{reg}_{ij}[\gamma] + T^{ct}_{ij}[\gamma] \tag{1.4.24}$$

is the energy-momentum tensor defined on the induced metric γ_{ij} at the cut-off $\rho = \epsilon$ and we have made use of $\gamma_{ij} = (L^2\tilde{g}_{ij})/\epsilon$. Naturally, T^{reg}_{ij} arises from the regulated action S_{reg} while T^{ct}_{ij} comes from the counter-terms. In [69], $\langle T_{ij}\rangle$ is shown to be covariantly conserved with respect to $g^{ij}_{(0)}$ and is explicitly calculated as

$$\langle T_{ij}\rangle = \frac{dL^{d-1}}{16\pi G}g_{(d)ij} + X_{ij}[g_{(0)ij}], \qquad X_{ij} \equiv 0 \text{ if } d \text{ is odd.} \tag{1.4.25}$$

The contact terms X_{ij} are tensors with dependence upon $g_{(0)ij}$ as well as the relevant spacetime dimension. In particular, they share a relation with the conformal anomaly in the boundary field theory. For further details and specific values of X_{ij}, see [69].

Should one wish to study the trace of $\langle T_{ij}\rangle$, then consider the Weyl rescaling (1.4.19) in the form of the following variation:

$$\delta S_{ren} = \lim_{\epsilon\to 0}\delta S_{fin} = -\int d^dx\,\sqrt{g_{(0)}}\Big(\frac{1}{2}\,\langle T_{ij}\rangle\,\delta g^{ij}_{(0)}\Big). \tag{1.4.26}$$

Now, one can clearly understand the importance of the dimension d, or more precisely, whether it is odd or even. Should one consider the case of odd d, then we have vanishing

Weyl anomaly $\mathcal{A}_{odd} = 0$ and so δS_{fin} will also vanish. Thus, on one hand, we obtain the relation

$$\left\langle T_i^i \right\rangle = 0. \tag{1.4.27}$$

On the other hand, for the case of even d, since the Weyl anomaly is non-zero and has the form (1.4.21), then

$$\left\langle T_i^i \right\rangle = \frac{L^{d-1}}{16\pi G} a_{(d)}. \tag{1.4.28}$$

Then we immediately see the relationship between the holographic energy-momentum tensor and the Weyl anomaly (1.4.21).

CHAPTER 2

Quantum information and quantum error correcting codes

2.1 Quantum entanglement and tensor networks

In this section, two of the motivating factors for holographic codes are introduced, quantum entanglement and tensor network theory. Quantum entanglement is a unique phenomenon, stemming from quantum mechanics, in which the quantum states of two or more objects must be described in reference to one another even if these objects are spatially separated. Further details on entanglement and its applications in quantum information theory are presented more broadly in [73] and [72] respectively.

Tensor networks may be thought of as a mechanism capable of describing wave functions of quantum many-body systems that see later use when discussing holographic codes. This topic is rather extensive so only the most relevant details have been procured in this thesis but for a more in depth review, the reader is suggested to study the following monograph [74, 75].

2.1.1 Quantum entanglement

Quantum entanglement is a crucial characteristic of quantum systems, arising from the superposition principle, therefore being a feature that is not exhibited in classical systems.

States existing in a quantum system that is composed of two subsystems, A and B, associated with Hilbert spaces $\mathcal{H}_A$ and $\mathcal{H}_B$ respectively, will live in the Hilbert space $\mathcal{H} = \mathcal{H}_A \otimes \mathcal{H}_B$. Should the bipartite state be decomposed as

$$|\psi\rangle = |\phi\rangle_A \otimes |\phi'\rangle_B \tag{2.1.1}$$

then it is deemed separable. Should the state not be separable, it is *entangled*. Of course, for a multipartite system consisting of n parties, the analogue definition of a separable state is

$$|\psi\rangle = |\phi\rangle_1 \otimes \cdots \otimes |\phi'\rangle_n \tag{2.1.2}$$

and it is entangled if it cannot be decomposed as in (2.1.2). The canonical example of entangled states are the Bell states (also known as EPR pairs):

$$|\psi^{\pm}\rangle = \frac{1}{\sqrt{2}}(|00\rangle \pm |11\rangle), \qquad |\Phi^{\pm}\rangle = \frac{1}{\sqrt{2}}(|01\rangle \pm |10\rangle), \tag{2.1.3}$$

where the notation $|ij\rangle := |i\rangle \otimes |j\rangle$. These states are the essential components at the centre of many quantum protocols such as quantum teleportation [139], superdense coding [140] and quantum key distribution [141].

In order to quantify entanglement, we introduce two concepts, the Schmidt decomposition and entanglement entropy. Firstly, it is useful to describe quantum systems using the density operator

$$\rho = \sum_i \lambda_i \, |\psi_i\rangle \, \langle\psi_i| \, , \tag{2.1.4}$$

for some ensemble of pure states $\{\lambda_i, |\psi_i\rangle\}$, where λ_i are the probabilities associated with the states $|\psi_i\rangle$. Now for the pure state $|\psi\rangle$ of the bipartite system consisting of subsystems A and B, with orthonormal sets $\{u_i\} \in \mathcal{H}_A$ and $\{v_i\} \in \mathcal{H}_B$, the Schmidt decomposition [142, 143] is

$$|\psi\rangle = \sum_{i=1}^{d} \lambda_i^{1/2} \, |u_i\rangle \, |v_i\rangle \, . \tag{2.1.5}$$

Here, $d = \min(d_A, d_B)$ where $(d_A, d_B) = (\dim(\mathcal{H}_A), \dim(\mathcal{H}_B))$ and λ_i are non-negative real numbers. Each value $\lambda_i^{1/2}$ is called a Schmidt coefficient and satisfies $\sum_{i=1}^{d} \lambda_i = 1$. An important consequence of the Schmidt decomposition is that for a pure state $|\psi\rangle$ in a bipartite system, one immediately has $\rho_A = \sum_i \lambda_i \, |u_i\rangle \, \langle u_i|$ and $\rho_B = \sum_i \lambda_i \, |v_i\rangle \, \langle v_i|$. Hence, the eigenvalues λ_i are the square of the Schmidt coefficients and more remarkably, are identical for both density operators ρ_A and ρ_B.

A basic way to 'measure' entanglement is through the Schmidt rank (Schmidt number); the number of non-zero Schmidt coefficients $\lambda_i^{1/2}$. Should the Schmidt rank be 1, then the state $|\psi\rangle$ is a product state and is therefore separable. However, if the Schmidt rank is

strictly larger than 1, the state is entangled.

There is, however, a finer way to measure entanglement, using the notion of entanglement entropy. Once again, suppose the total quantum state of the system is described by the pure density matrix, ρ_{AB}, and the Hilbert space can be bipartitioned as before as $\mathcal{H} = \mathcal{H}_A \otimes \mathcal{H}_B$, for two subsystems A and B. The reduced density matrix associated to subsystem A is

$$\rho_A \equiv \mathrm{Tr}_B(\rho_{AB}), \tag{2.1.6}$$

where Tr_B is the partial trace over subsystem B. The reduced density matrix ρ_A can be interpreted as a way to describe the statistical outcomes of subsystem A when averaging out the measurement outcomes of subsystem B. So, ρ_A is then of course a very useful object if we are only interested in the development of subsystem A (and similarly ρ_B if we are only interested in subsystem B).

For any density matrix ρ_A, the pure state ρ_{AB} that satisfies (2.1.6) is referred to as the *purification* of ρ_A. In general, the reduced density matrix ρ_A will be a mixed state since the two subsystems are likely to be entangled, though should the pure state ρ_{AB} not be entangled then the reduced states will also be pure.

This entanglement between various mixed subsystems leading to a pure state ρ can be quantified using the entanglement entropy. The *von-Neumann entropy* [144] of the subsystem A measures the total amount of quantum entanglement between A and its complement A^C in ρ:

$$S(\rho_A) = -\mathrm{Tr}(\rho_A \log \rho_A). \tag{2.1.7}$$

Of course should the quantum system be bipartitioned into subsystems A and B, the entanglement entropy would simply measure the entanglement between A and B. The von-Neumann entropy can also be expressed in terms of the eigenvalues λ_i of ρ_A as

$$S(\rho_A) = -\sum_i \lambda_i \log \lambda_i, \tag{2.1.8}$$

noting that logarithms are taken to be base two and by convention we define $0 \log 0 \equiv 0$ (justified by the limit $\lim_{x \to 0} x \log x = 0$). Should ρ_A be a pure state, then it follows that the von-Neumann entropy vanishes as expected, i.e. $S(\rho_A) = 0$.

To provide a simple yet effective example, consider the Bell state $|\psi^+\rangle$ on a bipartite Hilbert space, $\mathcal{H}_A \otimes \mathcal{H}_B$, where A and B are single qubits corresponding to the first and second qubits respectively. The total density matrix can be described by

$$\rho_{AB} = |\psi^+\rangle \langle\psi^+| = \frac{1}{2}(|00\rangle \langle 00| + |11\rangle \langle 00| + |00\rangle \langle 11| + |11\rangle \langle 11|), \tag{2.1.9}$$

and so the reduced density matrix ρ_A is given by

$$\rho_A \equiv \mathrm{Tr}_B(\rho_{AB}) = \frac{1}{2}(\,|0\rangle\langle 0| + |1\rangle\langle 1|\,) = \frac{1}{2}I_A. \tag{2.1.10}$$

Thus should one want to measure the entanglement entropy of a single qubit (taken here to be the first qubit) in the Bell state $|\psi^+\rangle$, a simple computation reveals

$$S(\rho_A) = -\mathrm{Tr}(\rho_A \log \rho_A) = -\frac{1}{2}\sum_{i=0,j=0}^{1} \langle i_A| \log\left(\frac{1}{2}|j_A\rangle\langle j_A|\right)|i_A\rangle = \log 2. \tag{2.1.11}$$

Since ρ_A is diagonal here, the entanglement entropy is maximal or in other words, the states ρ_A and ρ_B are maximally entangled. Obviously, the entanglement entropy for B returns the same result, $S(\rho_B) = \log 2$. This is a general feature of any bipartite system. Since the Schmidt decomposition implies that the two density operators ρ_A and ρ_B share the same eigenvalues λ_i, then provided ρ_{AB} is in a pure state, the von-Neumann entropies will always equate; $S(\rho_A) = S(\rho_B)$. Further, since the EPR pair display maximal entanglement, one can clearly state that for any two qubit system, the entanglement entropy must satisfy $S(\rho_A) \leq \log 2$. For a quantum state consisting of N qubits, with Hilbert space $\mathcal{H}_A$, then $\dim(\mathcal{H}_A) = 2^N$. Thus maximal entanglement corresponds to entropy

$$S(\rho_A) = N \log 2 = \log[\dim(\mathcal{H}_A)] \tag{2.1.12}$$

and in general entanglement entropy is bound by

$$S(\rho_A) \leq \log[\dim(\mathcal{H}_A)]. \tag{2.1.13}$$

2.1.2 Tensor networks

Finite-dimensional tensors are multilinear maps often represented as a multi-dimensional array. Thus, a rank-r tensor is an element of $\mathbb{C}^{d_1\times\cdots\times d_r}$ with dimension $d_1 \times \cdots \times d_r$ and scalars, vectors and matrices are simply rank-0, rank-1 and rank-2 tensors respectively. Often, tensors are represented diagrammatically by some solid shape associated with numerous legs, with each of these legs being given a corresponding index such that the total number of legs provides the order of the tensor. For example, figure 2.1.1 depicts a fourth order tensor T with elements (or amplitudes when discussing quantum states) $T_{i,j,k,l}$ that has been graphically shown as a circle and its four free legs. Networks consisting of multiple tensors may also be constructed by contracting over legs with shared indices, resulting in a single composite tensor. Suppose we wish to contract two tensors A and B, with amplitudes $A_{i,j}$ and $B_{j,k}$, over the shared index j, as depicted by

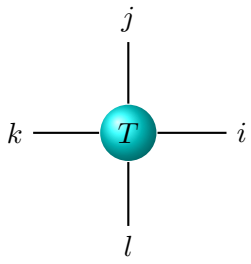

Figure 2.1.1: A single tensor T depicted as a circular node while its uncontracted indices i, j, k, l correspond to the four free legs.

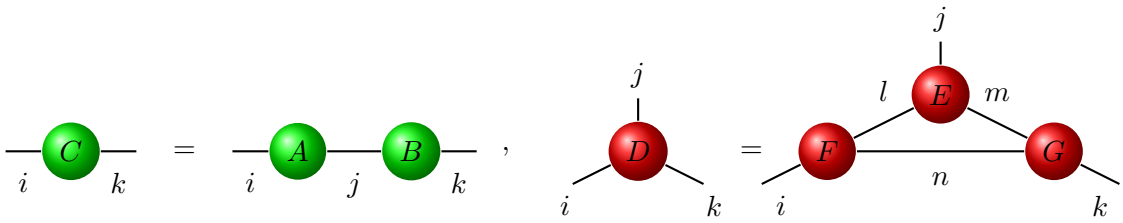

Figure 2.1.2: Two examples of tensor networks built from contractions of various smaller tensors. On the left, two tensors with amplitudes $A_{i,j}$ and $B_{j,k}$ are contracted over shared indices to form a new tensor C with amplitude $C_{i,k}$. On the right, three tensors with amplitudes $E_{l,j,m}$, $F_{i,l,n}$ and $G_{n,m,k}$ are contracted over shared indices to give a new tensor D with amplitude $D_{i,j,k}$.

the first network in figure 2.1.2. The resulting tensor C can thus be expressed as

$$C_{i,k} = \sum_j A_{i,j} B_{j,k}. \tag{2.1.14}$$

Graphically, this has been demonstrated by interpreting legs connecting two tensors as contracted indices between those tensors while indices not summed over remain as free legs. Similarly, consider the second tensor network in figure 2.1.2. Here one contracts three tensors across their shared edges in a similar fashion resulting in a rank-3 tensor

$$D_{i,j,k} = \sum_{l,m,n} E_{l,j,m} F_{i,l,n} G_{n,m,k}. \tag{2.1.15}$$

Now, one can use the language of tensor networks to interpret quantum many-body systems. As is well known, a quantum system with local dimension D (i.e. a qudit system) has a D-dimensional Hilbert space and some pure state $|\phi\rangle$ of the system can be specified as a weighted superposition of the D orthogonal basis states: $|\phi\rangle = \sum_{k=1}^{D} T_k |k\rangle$ with $T_k \in \mathbb{C}$ corresponding to a set of D complex amplitudes. Diagrammatically, this could be drawn as a rank-1 tensor T with one leg indexed by k. For a quantum many-body system consisting of N degrees of freedom, the pure state wavefunction ψ

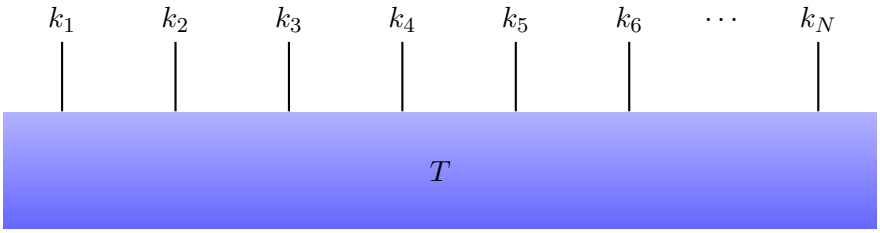

Figure 2.1.3: The rank-N tensor T with complex amplitudes $T_{k_1,k_2\ldots k_N}$ describing an N-qudit quantum many-body system with wavefunction ψ and state (2.1.16). Internally this large tensor consists of a network of tensors interconnected by contracted indices. The N degrees of freedom of the system corresponding to the N uncontracted indices $k_1, k_2 \ldots k_N$ are represented by free legs.

can be described as

$$|\psi\rangle = \sum_{k_1,k_2\ldots k_N}^{D} T_{k_1,k_2\ldots k_N} |k_1, k_2 \ldots k_N\rangle \,, \tag{2.1.16}$$

where $T_{k_1,k_2\ldots k_N} \in \mathbb{C}$ are the set of D^N complex amplitudes and consequently T can be regarded as a rank-N tensor. The dimension of each of the indices $k_1, k_2 \ldots k_N$ is commonly known as the *bond dimension* χ, given here as $\chi = D$. Figure 2.1.3 depicts the tensor network diagram describing the wavefunction ψ, consisting of the rank-N tensor T and the N free legs corresponding to the N uncontracted indices.

Accordingly, a natural mechanism when considering some wavefunction ψ of a quantum many-body system is to model this large tensor T, corresponding to the entire Hilbert space $\mathcal{H}$, as a tensor network consisting of contractions of various smaller tensors P_i, corresponding to some smaller subset of $\mathcal{H}$.

Suppose we wish to consider a many-body quantum state described by a tensor network, subdivided into two disjoint regions, A and its complement A^C. Then, there will be some cut $\hat{\gamma}_A$ through the network segregating it into two smaller tensor networks, each one associated with one of the two subsystems A or A^C. The contracted legs that are intersected by the cut results in entanglement between A and A^C. An example of a tensor network partitioned in this way is demonstrated in figure 2.1.4. One could then calculate the associated entanglement entropy between the two regions using the Schmidt decomposition (2.1.5) and evaluating (2.1.8). For an arbitrary tensor network, an upper bound emerges:

$$S(\rho_A) \leq |\gamma_A| \log \chi_j, \tag{2.1.17}$$

assuming a common bond dimension χ_j for all internal legs and where γ_A is the minimal cut (i.e. the cut through the fewest legs) through the network ending on the boundary ∂A that separates A and A^C. Note, $|\gamma_A|$ indicates the total number of cut internal legs: the length of γ_A. If the bond dimension is not consistent throughout the internal legs of the

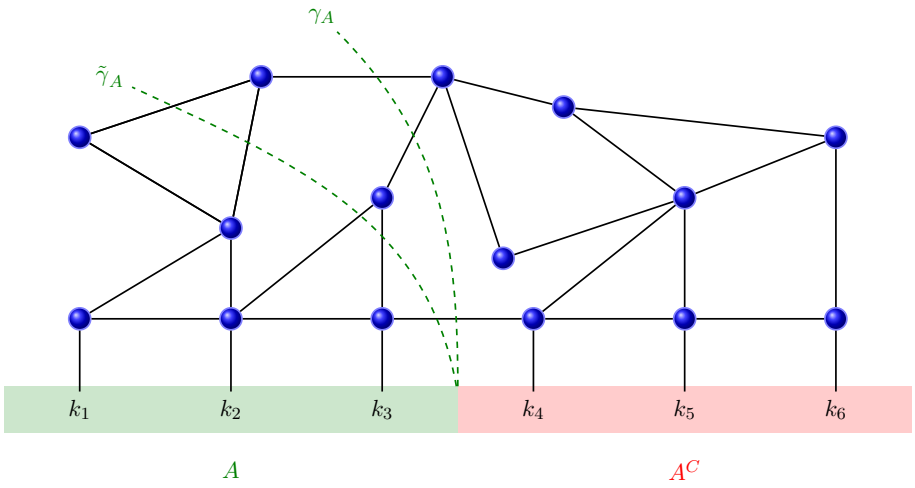

Figure 2.1.4: Multiple cuts γ_A and $\tilde{\gamma}_A$ through a tensor network representation of a quantum many-body system that has been divided into two sub-regions A and A^C. Endpoints of the cuts lie on the boundary ∂A between the two subsystems and γ_A is the minimal cut through the network.

network, then the generalised result is

$$S(\rho_A) \leq \min\{\sum_{b\in\hat{\gamma}_A} \log d_b\}, \tag{2.1.18}$$

with d_b the dimension of each corresponding bond b cut by $\hat{\gamma}_A$.

There are several different architectures for tensor networks that are commonly employed to reproduce the entanglement structure of different wave functions, the most prevalent being matrix product states (MPS) [145, 146], projected entangled pairs (PEPS) [147], tree tensor networks (TTN) [148] and the multi-scale entanglement renormalization ansatz (MERA) [149]. These different representations are each better suited to different types of states.

Firstly MPS, which correspond to a one-dimensional chain or ring of tensors (as depicted in figure 2.1.5), are commonly employed to characterise ground and low energy eigenstates of local and gapped one-dimensional Hamiltonians [150, 151] efficiently. In fact, for these tensor networks, the entanglement entropy $S(\rho_A)$ satisfies an area law [152] i.e. the entanglement entropy is proportional to the boundary ∂A of the region A, $S(\rho_A) \propto |\partial A|$.

One can straightforwardly think of PEPS as the higher-dimensional generalisation of MPS, where we now consider an array of tensors in spatial dimensions $d > 1$. If $d = 2$, one could have the particular case of a 3×3 square lattice as shown in figure 2.1.6. Two-dimensional PEPS tensor networks are suited to simulate the low-energy eigenstates of a two-dimensional local Hamiltonian that satisfies the two-dimensional area law [150, 151]

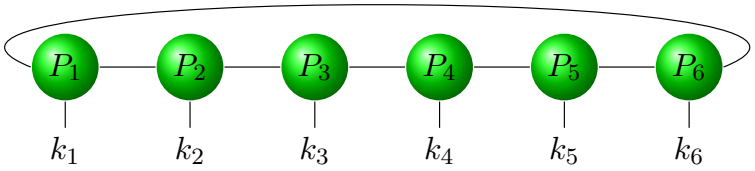

Figure 2.1.5: An example of a matrix product state (MPS) structure of a tensor network consisting of six tensors $P_1, \dots P_6$ with the loop indicating periodic boundary conditions.

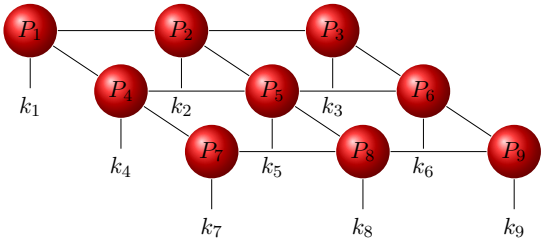

Figure 2.1.6: An example of a projected entangled pair state (PEPS) structure of a tensor network consisting of nine tensors $P_1, \dots P_9$ with open boundary conditions.

and two-dimensional thermal states [153].

The final tensor network architecture we will briefly describe is MERA, perhaps the most relevant when considering holographic codes. The tree-like structure of MERA is composed of two specific tensors, isometries and disentanglers, visualised in figure 2.1.7. These disentanglers are chosen to be unitary and account for short-range entanglement amongst neighbouring sites, thus making it a favourable configuration when approximating states possessing long-range entanglement.

Further, the geometry of MERA exhibits a logarithmic entanglement entropy between subsystems and is thus capable of approximating critical (gapless) systems i.e. conformal field theories. For example, the entanglement entropy of a subsystem A in a $(1+1)$-dimensional conformal field theory [154–156]

$$S(\rho_A) = \frac{c}{3} \log \frac{l}{a}, \tag{2.1.19}$$

where c is the central charge of the CFT and a is the lattice spacing (ultraviolet cutoff), scales logarithmically with linear length $l = |A|$.

While MERA represents a d-dimensional quantum many-body system living on the bottom row of the diagram, the MERA network itself can be seen as a $d+1$-dimensional object. This additional holographic dimension is associated with a renormalisation scale, so that each layer in the MERA network corresponds to some length or energy scale, generating a coarse-graining transformation from a coarse-grained state to a fine-grained state (or vice-versa). Thus, MERA can be understood as an *entanglement*

renormalisation [157]. For example, in figure 2.1.7, one considers a course-grained state $|\psi_0\rangle$ for some one-dimensional critical system, such that the vertical axis corresponds to this extra holographic dimension encoding the renormalisation scale.

One may begin to notice numerous similarities between MERA and the AdS/CFT correspondence, with MERA capturing many of the geometric properties of AdS, leading to proposals of a correspondence between the MERA and AdS [158,159]. This idea generated considerable interest from both the AdS/CFT and tensor network communities [160–162]. We will not explicitly review the specifics of AdS/MERA itself here, though the implications that follow and ultimately understanding this relationship between tensor networks and AdS/CFT, is the catalyst to much of the work in this thesis and will play a crucial role in the discussion that follows.

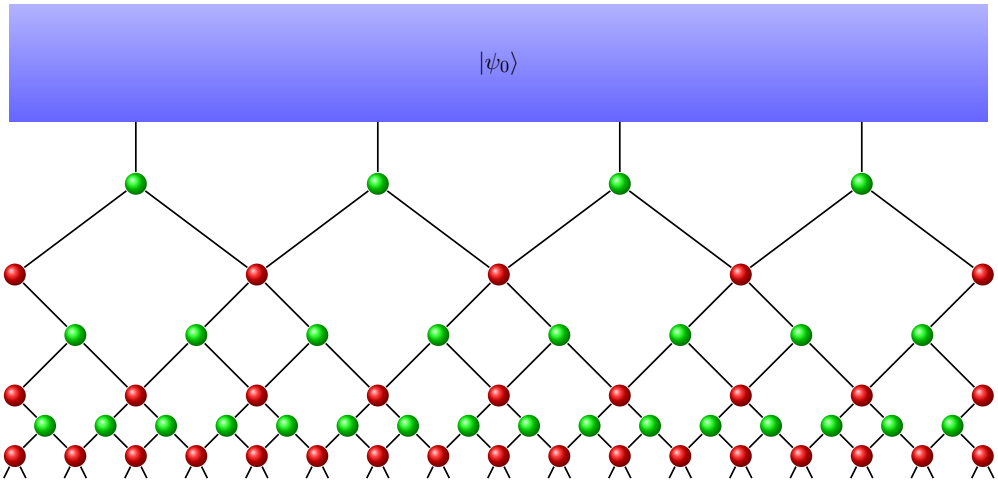

Figure 2.1.7: An example of a multi-scale entanglement renormalization ansatz (MERA) tensor network acting on an initial coarse-grained state vector $|\psi_0\rangle$. Green circles depict isometries while red circles identify the unitary disentanglers.

2.2 Quantum error correcting codes

In the following section we introduce the extensive topic of quantum error correcting codes, discussing the fundamental principles and theories of error correction. Firstly, we lay the foundations by reviewing the underlying ideas associated with quantum error correction, before diving further into the mathematical set up behind general quantum codes, adopting features from classical linear codes. For comprehensive reviews on the topic, the reader is referred to the following monographs [72, 76, 77].

2.2.1 Fundamentals of quantum error correction

Quantum computers are extremely powerful devices, with the potential to significantly outperform classical computers and perform simulations classical computers simply cannot [163]. One of the greatest challenges facing quantum computers is the protection of quantum information from errors, arising from their high susceptibility to interference of noise. Quantum computers inevitably interact with the environment surrounding them, hence suffering from decoherence. Quantum error correction is a procedure implemented in an attempt to suppress the noise of this effect.

A quantum error correcting code (QECC) may be viewed as a mapping where one encodes k *logical qudits* (those we wish to protect), into n *physical qudits*, such that $n > k$. In the case of qubits, this is then a mapping from a Hilbert space of dimension 2^k to one of dimension 2^n. The encoded information is less likely to be corrupted since one has $n-k$ additional qudits storing the k logical qudits redundantly.

The essence of quantum error correction can be captured by considering a simple QECC, the Shor code [164]. Suppose we wish to protect a single logical qubit as it is sent through some quantum channel, assuming this channel only causes an error on a single qubit at any particular instance. Then, one encodes the logical qubit into nine physical qubits in the following manner;

$$|0\rangle \to |\bar{0}\rangle = \frac{1}{2\sqrt{2}}(|000\rangle + |111\rangle)(|000\rangle + |111\rangle)(|000\rangle + |111\rangle), \tag{2.2.1}$$

$$|1\rangle \to |\bar{1}\rangle = \frac{1}{2\sqrt{2}}(|000\rangle - |111\rangle)(|000\rangle - |111\rangle)(|000\rangle - |111\rangle), \tag{2.2.2}$$

where the notation $|\bar{0}\rangle$ and $|\bar{1}\rangle$ indicates that these are the basis states of the logical $|0\rangle$ and logical $|1\rangle$ states. Of course, superpositions of the basis states can then be expressed from the corresponding superposition of these encoded states.

We consider two possible quantum channels, the bit flip channel and the phase flip channel. The bit flip channel flips a single qubit with probability p or leaves the qubit untouched with probability $1-p$. That is, there is a probability p chance that one applies the Pauli operator X to the state $|\psi\rangle$ resulting in the new state $X|\psi\rangle$. The phase flip channel is such that there is a q chance of flipping the relative phase of the $|0\rangle$ and $|1\rangle$ states and a $1-q$ chance the qubit is untouched. Specifically, there is a probability q chance that the Pauli operator Z is applied to the state $|\psi\rangle = \alpha|0\rangle + \beta|1\rangle$, leaving the new state $Z|\psi\rangle = \alpha|0\rangle - \beta|1\rangle$. The Pauli operators X and Z are defined as

$$X = \begin{pmatrix} 0 & 1 \\ 1 & 0 \end{pmatrix}, \qquad Z = \begin{pmatrix} 1 & 0 \\ 0 & -1 \end{pmatrix}, \tag{2.2.3}$$

and are often referred to as the bit flip operator and the phase flip operator respectively.

Now, one prepares and encodes an intial quantum state, $|\psi\rangle = \alpha\,|\bar{0}\rangle + \beta\,|\bar{1}\rangle$. Suppose the quantum channel causes a single bit flip, for instance by the application of X_1, where we use subscript to denote which qubit the operator is acting upon. In order to determine the location of the bit flip, it is sufficient to measure the operators Z_1Z_2 and Z_2Z_3. The eigenstates of these operators are the logical basis states $|\bar{0}\rangle$ and $|\bar{1}\rangle$ with eigenvalue $+1$. However, should a qubit have been flipped, performing this measurement can be used to determine which qubit has been flipped. For our case, one would find $Z_1Z_2 = -1$ and $Z_2Z_3 = 1$ hence deducing the first qubit has been flipped. One can then recover the original state by simply flipping the qubit back, in our case applying X_1. Similarly, $Z_1Z_2 = 1$ and $Z_2Z_3 = -1$ would indicate the third qubit has been flipped, $Z_1Z_2 = -1$ and $Z_2Z_3 = -1$ that the second qubit has been flipped and $Z_1Z_2 = 1$ and $Z_2Z_3 = 1$ that no qubits have been flipped. Of course we can perform similar analysis on the other two clusters to diagnose bit flip errors there.

We can perform a similar method to correct for errors that occur in the phase flip channel. Here, we measure the operators $X_1X_2X_3X_4X_5X_6$ and $X_4X_5X_6X_7X_8X_9$. Once again, the eigenstates of these operators are the logical basis states $|\bar{0}\rangle$ and $|\bar{1}\rangle$ with eigenvalue $+1$. Should a phase flip error occur on any qubits in a particular cluster, it would alter the value of $X_iX_jX_k$ in that cluster. Thus by measuring these operators, we can deduce which cluster had been affected by the phase flip and recover the original state by applying the relevant Z operator.

Of course, it is possible that there are other possible single qubit errors that could occur. For example, in a certain quantum channel, the state may undergo a simultaneous bit flip and phase flip on the same qubit, corresponding to the Pauli operator

$$Y = iXZ = \begin{pmatrix} 0 & -i \\ i & 0 \end{pmatrix}. \tag{2.2.4}$$

The Shor code will in fact correct this error in a similar manner - one first fixes the bit flip followed by the phase flip. In fact it turns out that the Shor code can protect the logical qubit state against arbitrary errors provided they only act upon a single qubit.

2.2.2 Classical linear codes

Quantum Calderbank-Shor-Steane (CSS) codes are constructed from classical linear codes, and it is useful to summarise here the defining properties of the latter. More details may be found in [72]. A linear code which encodes k bits of information within an n bit code space, i.e. an $[n, k]$ code, may be specified by an $(n \times k)$ generator matrix G whose elements are zeroes and ones. This matrix maps the message to the coded equivalent i.e. a message

x is encoded as $y = G \cdot x$. The set of possible codewords for the code is the space spanned by the columns of the generator matrix G. For example, take a simple $[3, 1]$ code that maps one bit into three repetitions. i.e.

$$0 \to 000, \qquad 1 \to 111. \tag{2.2.5}$$

Then the corresponding generator matrix is

$$G = \begin{bmatrix} 1 \\ 1 \\ 1 \end{bmatrix}, \tag{2.2.6}$$

such that $G[0] = (0, 0, 0)$ and $G[1] = (1, 1, 1)$.

Alternatively, error correction for linear codes may be captured by the parity check matrix, an $(n-k) \times n$ matrix H. An $[n, k]$ code consists of all n element vectors y such that $H \cdot y = 0$; the code is the kernel of H, which is k dimensional. Using matrix manipulations one can bring the parity check matrix into the standard form $[A_{(n-k)\times k}|I_{(n-k)\times(n-k)}]$ where A is an $(n-k) \times k$ matrix. The parity check matrix for the $[3, 1]$ repetition code can be defined as

$$H = \begin{bmatrix} 1 & 1 & 0 \\ 0 & 1 & 1 \end{bmatrix}. \tag{2.2.7}$$

Clearly, $H \cdot y = 0$ is only satisfied for the codewords $y = (0, 0, 0)$ and $y = (1, 1, 1)$. Suppose that the code y is corrupted, so that the received message is y', then

$$y' = y + e \tag{2.2.8}$$

where e is the error. Then by construction $H \cdot y' = H \cdot e$ captures the error (i.e. the error syndrome is $H \cdot y'$) since

$$H \cdot y' = H \cdot (y + e) = H \cdot y + H \cdot e \tag{2.2.9}$$

and $H \cdot y = 0$ for all codewords.

The (Hamming) *distance* between code words counts the number of places at which the n bit code words differ. The distance of a code d is defined to be the minimum distance between any two (distinct) codewords, and classical codes are often referred to as $[n, k, d]$, i.e. specifying this distance. If $d \geq 2t + 1$ for some integer t then one can correct errors on up to t bits. The distance is bounded from above according to the Singleton bound

$$d - 1 \leq (n - k). \tag{2.2.10}$$

2.2.3 General quantum error correcting codes

Now we consider more general QECCs, together with their most notable properties. While the Shor code is very useful to understand the main concepts of a QECC, it is not a realistic model. It is therefore important to understand how the general theory of quantum error correction operates and how it should be implemented in the most general framework. Any interaction between n qubits plus another quantum system (for instance their environment) may be expressed as

$$|\psi\rangle \otimes |0\rangle_E \to \sum_a E_a |\psi\rangle \otimes |e_a\rangle_E , \tag{2.2.11}$$

where $|\psi\rangle$ is some initial arbitrary state of the qubits, $|0\rangle_E$ is the initial (pure) state of the environment and $|e_a\rangle_E$ are states of the environment that are not necessarily mutually orthogonal or normalised. The error operators $\{E_a\}$ are unitary operators that act on the n qubits. More explicitly, they are the linearly independent Pauli operators,

$$\{E_a\} = \{I, X, Y, Z\}^{\otimes n}, \tag{2.2.12}$$

where index a is used to range over the 2^{2n} operators. We now wish to construct a QECC that is able to correct a subset $\mathcal{E} \subseteq \{E_a\}$. In order to distinguish which error $E_a \in \mathcal{E}$ has taken place, the idea is to perform one collective measurement on the n physical qubits. Performing the measurement will result in knowing the outcome of a and the preparation of a state $E_a |\psi\rangle \otimes |e_a\rangle_E$. Now, since E_a is unitary, in order to recover the undamaged state $|\psi\rangle$, one simply needs to apply $E_a^\dagger$ to the code block.

In order for any QECC to correct some set of errors $\mathcal{E}$, it must be able to distinguish every pair of errors $E_a, E_b \in \mathcal{E}$ on the codespace. This is only possible if $E_a |\psi_i\rangle$ and $E_b |\psi_j\rangle$ are mutually orthogonal, where $|\psi_i\rangle$, $|\psi_j\rangle$ are different basis codewords. Therefore,

$$\langle\psi_i| E_a^\dagger E_b |\psi_j\rangle = 0, \tag{2.2.13}$$

where $i \neq j$ and E_a, E_b are correctable errors. Information about the error is learnt by measuring $\langle\psi_i| E_a^\dagger E_b |\psi_j\rangle$ for all possible E_a, E_b. Since we must learn nothing about the coding space, all basis codewords produce the same value when evaluating this quantity:

$$\langle\psi_i| E_a^\dagger E_b |\psi_i\rangle = \langle\psi_j| E_a^\dagger E_b |\psi_j\rangle . \tag{2.2.14}$$

Combining the two expressions provides the Knill-Laflamme condition [165, 166]:

$$\langle\psi_i| E_a^\dagger E_b |\psi_j\rangle = C_{ab}\delta_{ij}, \qquad \forall E_a, E_b \in \mathcal{E}, \tag{2.2.15}$$

such that $|\psi_i\rangle$ and $|\psi_j\rangle$ run over all possible basis codewords and $C_{ab} = \langle\psi_i| E_a^\dagger E_b |\psi_i\rangle$ is Hermitian. This is the necessary and sufficient condition required to ensure recovery of the

original state. Should C_{ab} have maximum rank, the code is referred to as a *non-degenerate code*. This means that there exists a particular measurement that can unambiguously diagnose $E_a \in \mathcal{E}$. Alternatively, should C_{ab} be singular, then it is known as a *degenerate code*. Shor's code is an example of a degenerate code.

Pauli operators can also be assigned a *weight*, defined to be the number of qubits that the operator acts non-trivially upon. Thus the weight of a Pauli operator is an integer t, such that $0 \leq t \leq n$, for an n qubit system. Similarly to the definition of distance for a classical linear code, the *distance* of a QECC is the minimum weight of a Pauli operator $E = E_a^\dagger E_b$ for which the Knill-Laflamme condition (2.2.15) fails to hold. QECCs that encode k logical qubits as n physical qubits with distance d, are described as $[[n, k, d]]$ quantum codes, with the double square bracket indicating the code is quantum as opposed to classical. Should the set of errors $\mathcal{E}$ consist of error operators E_a that are all of weight t or less, the QECC can correct up to t errors, provided the distance of the code satisfies $d \geq 2t + 1$. Thus, a QECC that has distance $d = 2t + 1$ is able to correct t errors.

There are two important bounds that give further insight into the general properties possessed by QECCs. The first constraint is known as the *quantum Hamming bound*. Suppose one wishes to encode k logical qubits into n physical qubits in a non-degenerate fashion, where j errors occur. Of course $j \leq t$ in order for the code to be able to correct all the errors. There are $\binom{n}{j}$ distinct sets of locations where the j errors may occur and three possible errors (the X, Y, Z Pauli operators) that can occur on each qubit, meaning in total there are 3^j possible errors. Thus, the total number of errors of weight up to t may be expressed as

$$\sum_{j=0}^{t} \binom{n}{j} 3^j \tag{2.2.16}$$

Now, for k logical qubits, each error must correspond to a 2^k-dimensional subspace. In order to accommodate all of these subspaces, the 2^ndimensional Hilbert space consisting of n physical qubits must therefore satisfy

$$\sum_{j=0}^{t} \binom{n}{j} 3^j 2^k \leq 2^n, \tag{2.2.17}$$

an inequality known as the quantum Hamming bound [167]. In the special case where the QECC encodes a single qubit ($k = 1$) tolerating errors on one qubit only ($t = 1$), the quantum Hamming bound reduces to

$$1 + 3n \leq 2^{n-1} \tag{2.2.18}$$

and is only satisfied when there are five or more physical qubits ($n = 5$). In fact, should a non-degenerate code encoding $k = 1$ logical qubits into $n = 5$ physical qubits exist, i.e. the

$[[5, 1, 3]]$ quantum code, the quantum Hamming bound is saturated. A second interesting bound to note is the *quantum Singleton bound* [168], the quantum analogue of (2.2.10);

$$2(d-1) \leq (n-k), \tag{2.2.19}$$

imposing constraints on the distance of the code.

2.3 Stabiliser codes

In the final section of this chapter, we focus our attention on a particular subclass of quantum error correcting codes whose construction surfaced from group theory. The formalism of these stabiliser codes is an obvious starting point, reflecting on their formulation and various properties. Then, we will utilise classical linear codes to summarise the main features of the CSS construction of stabiliser codes before ending with examples of stabiliser codes and a particularly fascinating application. For those unfamiliar with the topic, further exploration of stabiliser codes can be studied using the following resources [72, 76–78].

2.3.1 General formulation of stabiliser codes

We next review the basic properties of stabiliser quantum codes, a particular class of QECCs that arise by exploiting group theory. The essential group needed for this formulation is the Pauli group $\mathcal{P}_n$ where the subscript indicates the number of physical qubits acted upon. The Pauli group acting on n qubits is

$$\mathcal{P}_n := \langle i, X_j, Z_j \rangle = \{\phi \otimes_{j=1}^{n} P_j\} \tag{2.3.1}$$

where $j = \{1, \cdots, n\}$, $\phi \in \{\pm 1, \pm i\}$ and $P_j \in \{I, X, Y, Z\}$ with X, Y, Z the Pauli matrices. The Pauli group has $(2n+1)$ generators and its order is 4^{n+1}. It also has numerous key properties:

1. All elements $s \in \mathcal{P}_n$ are unitary, i.e. $s^{-1} = s^{\dagger}$,

2. Every element $s \in \mathcal{P}_n$ squares to the identity: $s^2 = \pm I$. If $s^2 = I$, then s is Hermitian ($s = s^{\dagger}$) however if $s^2 = -I$, then s is anti-Hermitian ($s = -s^{\dagger}$).

3. Since X, Y, Z all commute when acting upon different qubits and all anticommute when acting on the same qubit, two elements of the set $s_1, s_2 \in \mathcal{P}_n$ only ever commute or anticommute: $s_1 s_2 = \pm s_2 s_1$.

The stabiliser approach uses properties of the Pauli group to define subspaces of the Hilbert space. A stabiliser group S is a subgroup of the Pauli group which is abelian and does not contain $-I$. Elements of S are called stabilisers and usually the stabiliser group has a distinguished set of generators, whose properties will be defined below. All stabilisers have the eigenvalue 1 and stabilisers are independent if the group they generate becomes smaller if any of them are omitted.

A *stabiliser code* C is the eigenspace of all elements of a stabiliser group S

$$C = \{|\psi\rangle|\ s|\psi\rangle = |\psi\rangle\ \forall s \in S\}. \tag{2.3.2}$$

The dimension of the code space is 2^{n-r} where there are r independent generators of S. Accordingly C encodes k logical qubits where

$$k = (n - r). \tag{2.3.3}$$

S has a minimal representation in terms of the r independent generators $s_1, s_2, ...$, each of which functions in the same way as a parity check does on a classical linear code. So, consider some $s \in S$, a particular error operator $E = E_a^\dagger E_b$ and some state $|\psi_i\rangle \in C$. Should E and s commute, $[E, s] = 0$, then

$$sE\,|\psi_i\rangle = Es\,|\psi_i\rangle = E\,|\psi_i\rangle\,, \tag{2.3.4}$$

thus the error will remain undetected by the stabiliser generator since $E\,|\psi_i\rangle$ will be an eigenvector of s with eigenvalue $+1$. However, should E and s anti-commute, $\{E, s\} = 0$, then

$$sE\,|\psi_i\rangle = -Es\,|\psi_i\rangle = -E\,|\psi_i\rangle \tag{2.3.5}$$

and the eigenvalue corresponding to s is flipped to -1. Therefore, the error can be detected by measuring s

$$\langle\psi_i|\,E\,|\psi_j\rangle = \langle\psi_i|\,sE\,|\psi_j\rangle = -\,\langle\psi_i|\,E\,|\psi_j\rangle = 0, \tag{2.3.6}$$

so the QECC satisfies (2.2.13) when E and $s \in S$ anticommute. Since both $\langle\psi_i|\,E\,|\psi_i\rangle$ and $\langle\psi_j|\,E\,|\psi_j\rangle$ will be null in this instance, (2.2.14) will also be satisfied, hence the Knill-Laflamme condition (2.2.15) will also be fulfilled. Thus, for all errors $E_a, E_b \in \mathcal{E}$, provided $\{E, s\} = 0$ for some element of the stabiliser $s \in S$, with $E = E_a^\dagger E_b$, the set of errors will be be correctable by the code.

Additionally the Knill-Laflamme condition (2.2.15) may also be satisifed in another way, that is, if $E \in S$. Trivially,

$$\langle\psi_i|\,E\,|\psi_j\rangle = \langle\psi_i|\psi_j\rangle = \delta_{ij}. \tag{2.3.7}$$

Thus the code will also be able to correct any set of errors $\{\mathcal{E}\}$ if $E = E_a^\dagger E_b \in S$.

So, a stabiliser code C with stabiliser S can correct $\{\mathcal{E}\}$ provided either:

a.) $E_a^\dagger E_b \in S$,

b.) There exists at least one generator $s \in S$, such that $\{s, E_a^\dagger E_b\} = 0$,

$\forall E_a, E_b \in \mathcal{E}$. The stabiliser code will be non-degenerate if there are no $E_a^\dagger E_b$ operators satisfy the first condition.

There are however, a set of operators that will remain undetectable by this code: operators that commute with all elements of the stabiliser S however are not themselves in S. For example, consider (2.3.4). Here, E and s commute implying $E|\psi_i\rangle \in C$. But if $E \notin S$ then there will be a state in C that will not be fixed by E. In other words, the *logical operators* are those elements of the Pauli group that act non-trivially on the code space but leave the code space as a whole invariant. One defines the normaliser of the stabiliser group in the Pauli group as

$$N(S) = \{g \in P_n |\ gsg^\dagger \in S \ \ \forall s \in S\}. \tag{2.3.8}$$

Clearly $S \subseteq N(S)$ and, since all elements of S have trivial action on the code space, the elements of $N(S)\backslash S$ form the logical operators. The group of logical operators is isomorphic to the Pauli group on k qubits, up to phases, and it is therefore usual to represent the generators of the logical group as $\bar{X}_1, \cdots \bar{X}_k$ and $\bar{Z}_1 \cdots \bar{Z}_k$. It is trivial to see that $\bar{X}$ and $\bar{Z}$ have the following commutation relations:

$$[\bar{X}_i, \bar{X}_j] = 0, \tag{2.3.9}$$

$$[\bar{Z}_i, \bar{Z}_j] = 0, \tag{2.3.10}$$

$$[\bar{X}_i, \bar{Z}_j] = 0 \quad i \neq j, \tag{2.3.11}$$

$$\{\bar{X}_i, \bar{Z}_i\} = 0. \tag{2.3.12}$$

The distance d of a stabiliser code is the minimum weight of a logical operator

$$d = \min_{g \in N(S)\backslash S} \mathrm{wt}(g), \tag{2.3.13}$$

where the weight $\mathrm{wt}(g)$ of a Pauli group element is the number of qubits on which it acts non-trivially. The distance can be thought of as a measure of how well the code can protect against qubit errors. Similarly to standard QECCs, stabiliser codes are often denoted as $[[n, k, d]]$ where n is the number of physical qubits, k is the number of logical qubits and d is the distance.

2.3.2 CSS construction

In this section we summarise the main features of the CSS (Calderbank and Shor [169], and Steane [170]) construction of codes using classical linear codes. The CSS construction begins with two classical linear codes, W_1 ($[n, k_1]$) and W_2 ($[n, k_2]$), such that all elements of W_1 and W_2 are orthogonal i.e. $\langle a, b\rangle = 0$ for all $a = (a_1, \cdots, a_n) \in W_1$ and $b = (b_1, \cdots, b_n) \in W_2$. A stabiliser group can then be constructed as

$$S = \langle X^a, Z^b \mid a \in W_1, b \in W_2 \rangle \tag{2.3.14}$$

where

$$X^a = X^{a_1} \otimes \cdots \otimes X^{a_n} \qquad Z^b = Z^{b_1} \otimes \cdots \otimes Z^{b_n} \tag{2.3.15}$$

The group S is Abelian, since X^a and Z^b commute; the latter follows from the orthogonality of W_1 and W_2. The number of independent generators of S is given by

$$R = \dim(W_1) + \dim(W_2). \tag{2.3.16}$$

The distance is the minimum weight Pauli operator that commutes with all elements in S. The check matrix for a CSS code may be expressed in the form

$$\begin{bmatrix} H(W_1) & 0 \\ 0 & H(W_2^{\perp}) \end{bmatrix} \tag{2.3.17}$$

where $H(W_1)$ and $H(W_2^{\perp})$ are the check matrices of the associated classical codes.

For any stabiliser code (i.e. not necessarily CSS) we can express the check matrix as an $l \times 2n$ matrix, where there are $l = (n - k)$ independent generators of the stabiliser group. The left hand side of the matrix (i.e. an $l \times n$ matrix) contains ones to indicate which generators contain X matrices, and zero otherwise. Similarly, the right hand side of the matrix shows ones for generators containing Z matrices and zero otherwise. If there is a one in the same position on both sides, then there is a Y in the generator as the product of X and Z gives Y.

By matrix manipulations, the check matrix for any stabiliser code can be brought into a standard form:

$$\left[\begin{array}{ccc|ccc} I_{r\times r} & A_{r\times(n-k-r)} & B_{r\times k} & C_{r\times r} & 0_{r\times(n-k-r)} & D_{r\times k} \\ 0_{(n-k-r)\times r} & 0_{(n-k-r)\times(n-k-r)} & 0_{(n-k-r)\times r} & E_{(n-k-r)\times r} & I_{(n-k-r)\times(n-k-r)} & F_{(n-k-r)\times k} \end{array}\right], \tag{2.3.18}$$

where r is the rank of left hand side of the check matrix. In the case of a CSS code, this standard form simplifies further, with the matrices C and D being zero.

A well known example of a CSS code is the Steane $[[7,1,3]]$ code [170], which is constructed from $[7,4]$ and $[7,3]$ classical codes. The standard form for the check matrix for this code is discussed in detail in [72],

$$\left[\begin{array}{ccccccc|ccccccc} 1&0&0&0&1&1&1&0&0&0&0&0&0&0\\ 0&1&0&1&0&1&1&0&0&0&0&0&0&0\\ 0&0&1&1&1&1&0&0&0&0&0&0&0&0\\ 0&0&0&0&0&0&0&1&0&1&1&0&0&1\\ 0&0&0&0&0&0&0&0&1&1&0&1&0&1\\ 0&0&0&0&0&0&0&1&1&1&0&0&1&0 \end{array}\right]. \tag{2.3.19}$$

This can be represented in a Tanner graph as shown in Figure 4.5.1.

2.3.3 Examples of stabiliser codes

We now proceed by presenting two examples of stabiliser codes that are commonly featured in the literature. Firstly, the Shor code presented in section 2.2.1 is a $[[9,1,3]]$ stabiliser code. The eight stabiliser generators are shown in table 2.3.1.

Name	Operator								
s_1	Z	Z	I	I	I	I	I	I	I
s_2	I	Z	Z	I	I	I	I	I	I
s_3	I	I	I	Z	Z	I	I	I	I
s_4	I	I	I	I	Z	Z	I	I	I
s_5	I	I	I	I	I	I	Z	Z	I
s_6	I	I	I	I	I	I	I	Z	Z
s_7	X	X	X	X	X	X	I	I	I
s_8	I	I	I	X	X	X	X	X	X
$\bar{X}$	X	X	X	X	X	X	X	X	X
$\bar{Z}$	Z	Z	Z	Z	Z	Z	Z	Z	Z

Table 2.3.1: The stabiliser generators of the $[[9,1,3]]$ Shor code.

One can easily check that all single qubit operators are either in the stabiliser S or anticommute with at least one generator in S, hence not being an element of the normaliser $N(S)$. For example, consider the single qubit operators X_1 and Z_4. The product of these operators X_1Z_4 obviously commutes with Z_1Z_2. One could perform this analysis for every combination of possible operators so consequently, the Shor code is able to correct an arbitrary, single qubit operator.

The second example of a stabiliser code which is presented here, is the $[[5,1,3]]$ quantum code. As mentioned in 2.2.3, this code saturates the quantum Hamming bound (2.2.17). Further, as a result it is the smallest possible QECC that encodes a single qubit, being

able to detect and correct any error in the encoded state on a single qubit. The stabiliser generators of the $[[5, 1, 3]]$ code are given in table 2.3.2.

Name	Operator				
s_1	X	Z	Z	X	I
s_2	I	X	Z	Z	X
s_3	X	I	X	Z	Z
s_4	Z	X	I	X	Z
$\bar{X}$	X	X	X	X	X
$\bar{Z}$	Z	Z	Z	Z	Z

Table 2.3.2: The stabiliser generators of the $[[5, 1, 3]]$ code.

Again, one can easily check that each weight-1 or weight-2 Pauli operator anti-commutes with at least one generator, so the code has distance 3. It is possible to construct an orthonormal basis of codewords. Begin with some initial state $|\psi_0\rangle$ such that one has the encoding

$$|\Psi_0\rangle = \sum_{s\in S} s\,|\psi_0\rangle\,. \tag{2.3.20}$$

So the logical codewords can be taken to be

$$|\bar{0}\rangle = \sum_{s\in S} s\,|00000\rangle\,, \qquad |\bar{1}\rangle = \bar{X}\,|\bar{0}\rangle\,. \tag{2.3.21}$$

Then by expanding the sum we obtain

$$\begin{aligned}|\bar{0}\rangle = |00000\rangle &+ s_1\,|00000\rangle + s_2\,|00000\rangle + s_3\,|00000\rangle + s_4\,|00000\rangle + s_1s_2\,|00000\rangle + s_1s_3\,|00000\rangle \\ &+ s_1s_4\,|00000\rangle + s_2s_3\,|00000\rangle + s_2s_4\,|00000\rangle + s_3s_4\,|00000\rangle + s_1s_2s_3\,|00000\rangle \\ &+ s_1s_2s_4\,|00000\rangle + s_1s_3s_4\,|00000\rangle + s_2s_3s_4\,|00000\rangle + s_1s_2s_3s_4\,|00000\rangle\end{aligned}$$

$$\begin{aligned}= |00000\rangle &+ |10010\rangle + |01001\rangle + |10100\rangle + |01010\rangle - |11011\rangle - |00110\rangle - |11000\rangle - |11101\rangle \\ &- |00011\rangle - |11110\rangle - |01111\rangle - |10001\rangle - |01100\rangle - |10111\rangle + |00101\rangle\end{aligned} \tag{2.3.22}$$

and subsequently

$$\begin{aligned}|\bar{1}\rangle &= \bar{X}\,|\bar{0}\rangle \\ &= |11111\rangle + |01101\rangle + |10110\rangle + |01011\rangle + |10101\rangle - |00100\rangle - |11001\rangle - |00111\rangle - |00010\rangle \\ &\quad - |11100\rangle - |00001\rangle - |10000\rangle - |01110\rangle - |10011\rangle - |01000\rangle + |11010\rangle\,.\end{aligned} \tag{2.3.23}$$

Trivially both $|\bar{0}\rangle$ and $|\bar{1}\rangle$ are states within C. The $[[5, 1, 3]]$ code is just one example of a *perfect code*, i.e. a code that saturates the quantum Hamming bound and numerous others exist [171, 172].

The $[[5, 1, 3]]$ code also uniquely captures the essence of quantum secret sharing [173], forming the basis of a $((3, 5))$ quantum threshold scheme. An $((m, n))$ quantum threshold scheme may be thought of in the following way. Suppose one wished to divide up some top secret information between n parties. No information can be learnt about the secret from $m - 1$ shares, however with m shares it is possible to reconstruct the secret in its entirety. This can be interpreted in the language of quantum codes, with the secret being the k logical qubits, encoded and divided such that each party receives one of $n = 2m - 1$ physical qubits. Thus having m shares of the physical qubits allows total reconstruction of the logical information since the code can correct for the remaining $m - 1$ erasures.

In theory, any QECC of the form $[[2m - 1, k, m]]_D$ (with D representing the quantum system is D-dimensional) can demonstrate quantum secret sharing in the form of an $((m, n))$ threshold scheme such that there is at least one logical qudit $k \geq 1$. However, in the case of qubits ($D = 2$), the $[[3, 1, 2]]$ and $[[7, 1, 4]]$ codes do not exist and codes with $m > 3$ cannot exist due to the more stringent conditions (e.g. the stronger bound obtained by Rains presented in [76]). Hence for qubits, the $[[5, 1, 3]]$ code is the only quantum threshold scheme that exists.

CHAPTER 3

Holography and quantum information

3.1 Holographic entanglement entropy

In this section we begin to combine the two major concepts from the preceding chapters emphasising the significance of quantum information theory in holography. The AdS/CFT correspondence can be understood more deeply as a result, particularly in the realm of entanglement. We will firstly review the notion of *holographic entanglement entropy*, for which there are numerous extensive resources available [30, 31]. This includes discussion of entanglement first in a more general QFT setting as well as an introduction to the renowned Ryu-Takayanagi formula [26]. We will then briefly touch upon the relation between quantum entanglement and the emergent geometry in the bulk spacetime, exemplified by the thermofield double state in the CFT and its holographic dual, the eternal AdS black hole.

3.1.1 Entanglement in QFT and the Ryu-Takayanagi conjecture

Just as in quantum mechanics, one can similarly understand entanglement in the language of quantum field theories. Suppose we have a d-dimensional QFT defined on some manifold $\mathbb{R}\times N^{d-1}$, denoting the time direction as $\mathbb{R}$ and the $(d-1)$-dimensional space-like manifold as N^{d-1}. Then at some fixed time $t = t_0$, we can partition N^{d-1} into two regions, $A \subset$

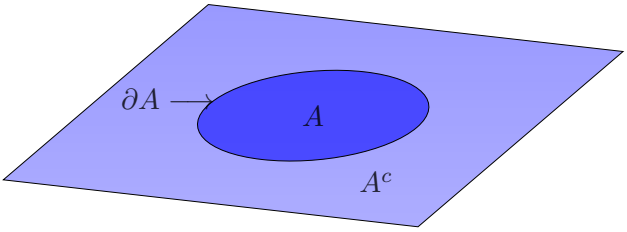

Figure 3.1.1: A particular choice of bipartition of space into two regions $A \subset N^{d-1}$ and its complement $A^c \subset N^{d-1}$. Correspondingly the total Hilbert space is decomposed as $\mathcal{H} = \mathcal{H}_A \otimes \mathcal{H}_{A^c}$. The surface separating the two regions (the entangling surface) is the boundary of region A, denoted ∂A.

N^{d-1} and its complement $A^c \subset N^{d-1}$, separated by the boundary ∂A. This decomposition is depicted in figure 3.1.1. Then, analogous to quantum mechanics, theoretically one can use the von-Neumann entropy (2.1.7) to define the entanglement entropy of subsystem A.

While entanglement is easily understood for pure states in quantum mechanics, fresh complications arise when studying quantum field theory. Since the Hilbert spaces in a QFT typically have infinite dimensionality, when calculating von-Neumann entropies of the form (2.1.7), there are an infinite number of degrees of freedom that must be traced out. Though there are cases where sensible entropies can be computed for systems with infinite-dimensional Hilbert spaces (e.g. quantum harmonic oscillators), this hints at the likelihood of $S(\rho_A)$ diverging in QFT. In fact, in the continuum limit, the entanglement entropy between adjoining spacetime regions is indeed UV divergent. Thus, in lattice simulations, it is natural to introduce a UV cutoff to regulate the theory.

As alluded to, explicitly calculating these entanglement entropies can be difficult. Significant progress was achieved due the development of the replica trick technique [156, 174]. This provided a systematic approach to compute entanglement entropies in lattice regularised QFTs, involving the evaluation of partition functions on an n-sheeted Riemannian surface, initially realised in the case of (1+1)-dimensional CFTs [156, 174]. As previously discussed, in these systems $S(\rho_A)$ scales logarithmically with respect to the linear length l (2.1.19) and is well approximated by MERA.

It was identified in [155, 175, 176] that for a subsystem A, one always anticipates that the divergence in $S(\rho_A)$ is proportional to the boundary ∂A of A:

$$S(\rho_A) = \gamma \frac{\text{Area}(\partial A)}{a^{d-2}} + \dots, \tag{3.1.1}$$

where a is the lattice spacing (UV cut-off) and γ is some constant dependent upon the theory of the system. Notice that in the case of (1+1)-dimensional CFTs, the entanglement entropy satisfies a slightly different relation. This is since here there is only one spatial dimension and so the power law divergence $a^{-(d-2)}$ reduces to a logarithmic divergence.

One may promptly notice the similarity between this law and that of the Bekenstein-Hawking entropy (1.1.2). The two can be hypothesised to be related with the following logic: On the one hand, we have an observer that only has access to one particular subsystem in a quantum system, say subsystem A, such that they are unable to receive information from A^c. On the other hand, consider an observer in spacetime A outside a black hole horizon. They similarly cannot access information beyond the horizon and so the black hole interior can be thought to be analogous to A^c. Thus, one could interpret these entropies to be analogous to one another. This ideology is not totally accurate but it does motivate the possible existence of a holographic duality.

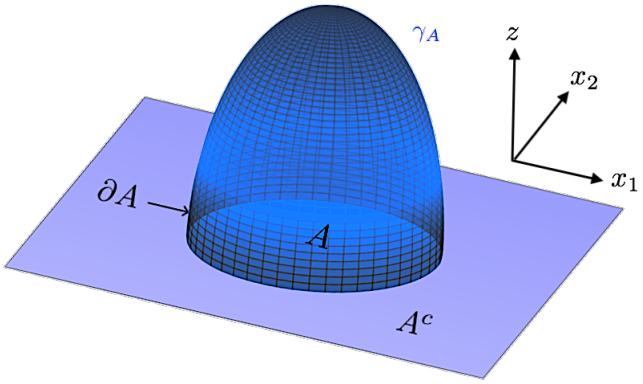

Figure 3.1.2: Visualisation of the Ryu-Takayanagi formula (3.1.2) quantifying the entanglement entropy of a subregion A in the boundary CFT. The extremal surface γ_A in the bulk is homologous to A, i.e. $\partial\gamma_A = \partial A$.

The true holographic description relating entanglement entropy and the geometry in the bulk was first proposed by Ryu and Takayanagi [26]. This conjecture states that the entanglement entropy for some spatial subregion A in the d-dimensional CFT is dual to the area of an extremal space-like surface γ_A in the bulk spacetime AdS_{d+1} that is homologous to A. In particular, the entanglement entropy of A can be calculated via the *Ryu-Takayanagi (RT) formula*,

$$S(\rho_A) = \frac{\mathrm{Area}(\gamma_A)}{4G^{(d+1)}}, \tag{3.1.2}$$

where the $(d-1)$-dimensional minimal surface is denoted by γ_A and has $(d-2)$-dimensional boundary satisfying $\partial\gamma_A = \partial A$. Figure 3.1.2 offers a visualisation of this notion.

Curiously, the RT formula can be thought of as a generalisation of the Bekenstein-Hawking formula (1.1.2), thus the heavy similarities we have touched upon. Should we consider some subregion A of the boundary CFT and allow it to grow until it encompasses the entire boundary, one immediately notices that the bulk extremal surface γ_A is without boundary. Though from a topology perspective, due to the

imposed constraint on the homology in our definition, one requires that the only permitted surfaces are those wrapping the black hole horizon in the bulk. Then if the area spanned by the minimal surface is exactly the horizon, the entanglement entropy given in the RT formula (3.1.2) is precisely the Bekenstein-Hawking entropy (1.1.2).

This geometric relation has been shown to satisfy numerous crucial properties of entanglement entropy, most notably consistency with subadditivity and strong subadditivity [29], given by

$$S(\rho_{AB}) \leq S(\rho_A) + S(\rho_B) \tag{3.1.3}$$

and

$$S(\rho_B) + S(\rho_{ABC}) \leq S(\rho_{AB}) + S(\rho_{BC}) \tag{3.1.4}$$

respectively. The proof of strong subadditivity in holography is relatively straightforward and can be summarised diagrammatically as shown in figure 3.1.3. Additionally, the new inequality constraining the entanglement between three regions [177],

$$S(\rho_A) + S(\rho_B) + S(\rho_C) + S(\rho_{ABC}) \leq S(\rho_{AB}) + S(\rho_{AC}) + S(\rho_{BC}), \tag{3.1.5}$$

is often called the *monogamy of mutual information* (MMI) and was shown to exist through the study of entanglement entropies of QFTs with holographic duals. Finding and characterising the complete list of the extra satisfied conditions of the holographic entanglement entropy is still a topic on ongoing research [178, 179].

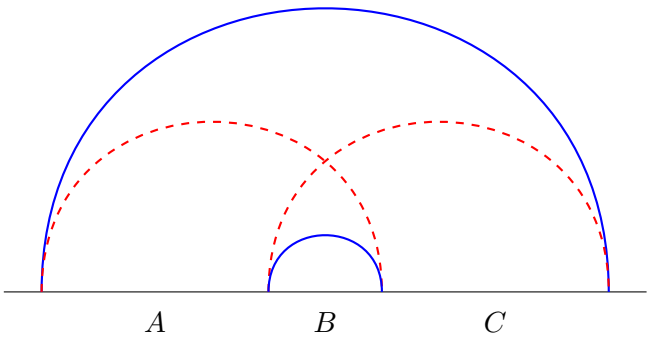

Figure 3.1.3: A configuration in AdS_3 exemplifying the strong subadditivity of holographic entanglement entropy. Entanglement entropies $S(\rho_{AB})$ and $S(\rho_{BC})$ are computed according to 3.1.2 through the red, dashed geodesics while entanglement entropies $S(\rho_B)$ and $S(\rho_{ABC})$ are computed with the solid, blue geodesics. One can alternatively interpret the red geodesics as two separate lines, with one homologous to ABC (larger exterior 'M' shape) and one homologous to B (interior 'n' shape). Since neither of these lines are geodesics, their total length must exceed that of their counterparts, thus $S(\rho_B) + S(\rho_{ABC}) \leq S(\rho_{AB}) + S(\rho_{BC})$.

Another good consistency check for the RT formula is to study the familiar (1+1)-dimensional CFT and reproduce results using the AdS_3/CFT_2 correspondence. Introducing a suitable regulator ϵ, one may fairly trivially check that we obtain the expected result (2.1.19), identifying c as the Brown-Henneaux central charge (1.2.7).

Ryu and Takayanagi's original proposal, as we have discussed here, provides a prescription for calculating the entanglement entropy of a boundary subregion A in a time-independent environment. In order to describe a dynamical system one must invoke the *Hubeny-Ryu-Takayanagi* (HRT) formula [27], the covariant generalisation of (3.1.2), capable of capturing time-dependent effects.

3.1.2 Geometry, gravity and entanglement

One of the most fascinating implications arising from studying holographic entanglement entropy is the relation between geometry and entanglement. Due to the presence of the extremal surface, a geometrical object in the bulk, we are left with the impression that quantum entanglement at the boundary may have a deeper connection with the geometry. In order to truly understand the AdS/CFT correspondence, it is desirable to identify the circumstances for which a QFT state is holographically dual to a smooth semi-classical gravity geometry. It has been suggested that gravity should not be viewed as a fundamental force and that it emerges holographically due to quantum degrees of freedom. From this viewpoint it has been argued that the quantum entanglement between these degrees of freedom plays a fundamental role in the emergence of the geometry [180, 181].

A prevalent example is that of the thermofield double (TFD) state, where we introduce a CFT comprised of two copies of the same CFT (say CFT_L and CFT_R), with the Hilbert space $\mathcal{H} = \mathcal{H}_L \otimes \mathcal{H}_R$. Then, the TFD state is defined as the unique pure state

$$|\text{TFD}\rangle = \frac{1}{Z(\beta)} \sum_n e^{-\beta E_n/2} |n\rangle_L \otimes |n\rangle_R \,. \tag{3.1.6}$$

Here $Z(\beta)$ is the canonical partition function and β^{-1} is the temperature. The two copies of the CFT are labelled L and R and their energy eigenstates are given by $|n\rangle_L$ and $|n\rangle_R$ respectively. This pure state can then be thought of as an entangling state of these eigenstates weighted by a Boltzmann factor. The corresponding density matrix of the doubled QFT can be expressed as

$$\rho_{tot} = |\text{TFD}\rangle \langle \text{TFD}| \,. \tag{3.1.7}$$

By construction, the reduced density matrix of either system L or R always amounts to a thermal state. Consider the reduced density matrix of system R, found by tracing out

the L degrees of freedom:

$$\rho_R = \frac{1}{Z(\beta)} \sum_n e^{-\beta E_n} |n\rangle_R \langle n|_R = e^{-\beta H}. \tag{3.1.8}$$

Indeed this is the thermal state in $\mathcal{H}_R$. Notice how the inverse temperature β controls to what extent entanglement between the CFTs plays a role, exemplified in two intriguing temperature limits. When we consider low temperatures, $\beta \gg 1$, the ground state dominates and entanglement is heavily suppressed while at high temperatures, $\beta \ll 1$, the state becomes highly entangled. As may be expected since the ground state in a CFT is holographically dual to AdS_{d+1}, at low temperatures, the holographic dual of the TFD state can be viewed as thermal AdS. In particular it can be described by two disconnected copies of AdS spacetime. Alternatively, the dual description of the TFD state at high temperatures in the bulk is the Hartle-Hawking state $|HH\rangle$ describing an AdS-Schwarzschild black hole [182].

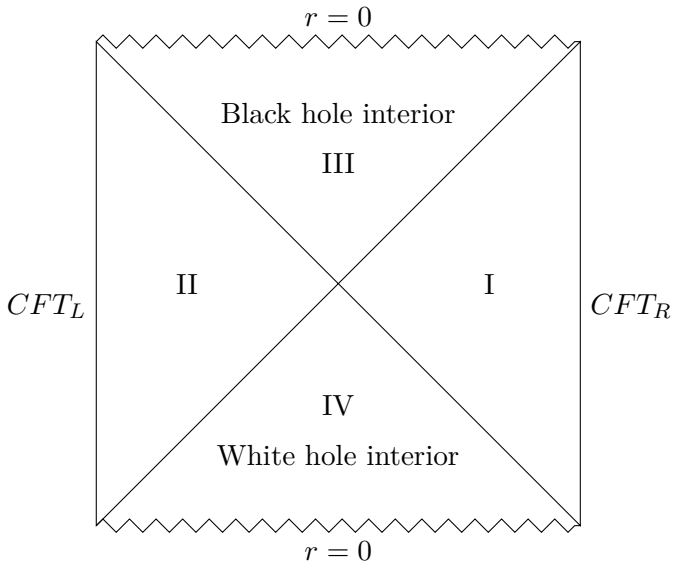

Figure 3.1.4: The Carter-Penrose diagram depicting an eternal black hole (the extended AdS-Schwarzschild spacetime). The two asymptotically AdS regions I and II are dual to the two copies of the CFT (CFT_R and CFT_L respectively) living at the time-like boundaries at spatial infinity. Regions III and IV lie inside the black hole and white hole horizons respectively where the corresponding space-like singularities are contained.

These eternal AdS black hole (maximally extended AdS-Schwarzschild) solutions have a particularly interesting structure, consisting of two asymptotically AdS regions associated to one another via a spatial Einstein-Rosen (ER) bridge. They also possess two time-like boundaries located at spatial infinity as illustrated in figure 3.1.4. The simplest asymptotically AdS black hole arises in AdS_3 and has the metric

$$ds^2 = -\frac{(r^2 - r_+^2)(r^2 - r_-^2)}{r^2} dt^2 + \frac{dr^2}{(r^2 - r_+^2)(r^2 - r_-^2)} + r^2 (dy + \frac{r_+ r_-}{r^2} dt)^2. \tag{3.1.9}$$

This solution is known as a BTZ black hole [115], a namesake to its founders. It has been suggested that the macroscopic entanglement present in the TFD state is characterised as holographically dual to the wormhole connecting the asymptotic regions. This is the underlying argument relating geometry and entanglement first posed by Maldacena and Susskind in the so-called 'ER = EPR' conjecture [183]; Einstein-Rosen bridges (or highly quantum wormholes) connecting two qubits and entanglement between an EPR pair (maximally entangled pair of qubits) are fundamentally equivalent. Further, this hypothesis was initially proposed as a solution to the black hole firewall problem [184].

3.2 Holographic quantum error correcting codes

The following section is dedicated to understanding the relationship between quantum error correcting codes and the emergence of bulk locality in the AdS/CFT correspondence. Our focus initially is to introduce the concept of bulk reconstruction, which fundamentally aims to complete the dictionary between bulk and boundary. Then, following [32], we make the connection to quantum codes demonstrated using the 3-qutrit code [173]. An enriched overview of the material presented in this section can be found in the lecture notes [79].

3.2.1 Bulk locality and bulk reconstruction

One extremely significant conundrum in the AdS/CFT correspondence is that locality in the bulk is not manifestly respected by the boundary CFT. Of course, no problem arises when considering a usual 'scattering experiment' where local boundary operators are initially acted upon, allowed to interact in the bulk, and then later measured as boundary operators with the result contained in a CFT correlator e.g. $\langle \mathcal{O}(X_1)\mathcal{O}(X_2)\mathcal{O}(X_3)\mathcal{O}(X_4)\rangle$ as depicted on the left in figure 3.2.1. This is since the CFT innately respects locality in the the d-dimensions present at the boundary. However, should we be interested in a case such as the one depicted on the right in figure 3.2.1, then this causes some concern. These arguments are answered by holographic bulk reconstruction, where one investigates to what extent bulk locality is respected by CFT.

Recall from section 1.3.2 that the solution to the bulk equations of motion for some bulk field ϕ is always subject to specific boundary conditions. More explicitly, near the boundary of AdS, the fields are considered to have non-normalisable fall-off;

$$\phi(z, x) \sim z^{d-\Delta}\phi_{(0)}(x), \tag{3.2.1}$$

identifying the non-normalisable modes $\phi_{(0)}$ as the source for the dual field theory operator $\mathcal{O}_\Delta$ with conformal dimension Δ. As described in section 1.3.2, we can equivalently use

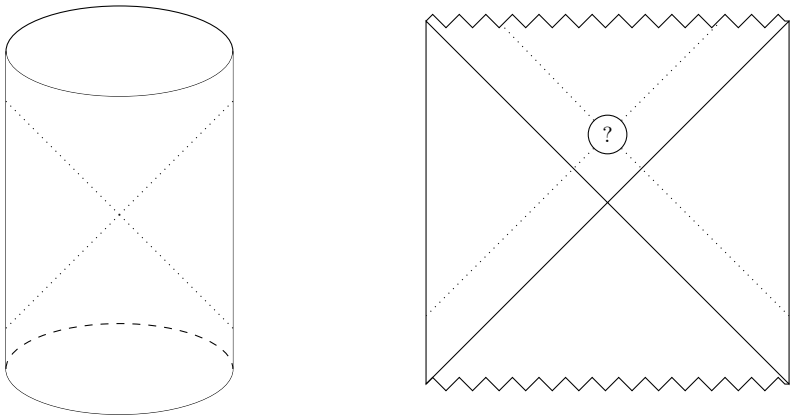

Figure 3.2.1: Left: A bulk scattering experiment in pure AdS_3, described the by the correlation function $\langle \mathcal{O}(X_1)\mathcal{O}(X_2)\mathcal{O}(X_3)\mathcal{O}(X_4)\rangle$. Right: The Carter-Penrose diagram of the AdS-Schwarzschild spacetime consisting of an experiment in the bulk between two incoming particles that have been prepared in some initial state. The extrapolate dictionary does not inform us how the region behind the horizon will be encoded in the CFT description.

the the integration kernel known as the bulk-to-boundary propagator K to express the bulk field as

$$\phi(x) = \int_{\partial_{AdS}} d^d X K(x;X)\phi_{(0)}(X). \tag{3.2.2}$$

A comment of importance is that this equation has no explicit mention of operators in the dual CFT and solely describes bulk fields along with their asymptotics. From the field-operator correspondence, one may be motivated to uncover a similar relation consisting purely of CFT operators. Then, for some local operator $\mathcal{O}(X)$ in the CFT,

$$\mathcal{O}_{\text{Bulk}}(x) = \int_{\partial_{AdS}} d^d X \mathcal{K}(x;X)\mathcal{O}(X), \tag{3.2.3}$$

where the local bulk operator $\mathcal{O}_{\text{Bulk}}(x)$ is manifestly non-local in the CFT. Hence, we deduce local bulk fields are holographically dual to CFT boundary operators that are non-local [185, 186]. In this context, $\mathcal{K}(x;X)$ is often referred to as *smearing function* and while it shares similarities with the the bulk-to-boundary propagator, it is clear that these are distinctly different functions. To see this more explicitly, further details on the smearing function can be found in appendix A.1.2, while the bulk-to-boundary propagator has the form stated in (1.3.12). For the sake of brevity, if we wish to consider cases beyond free field theory and introduce interactions, one can find similar motivation utilising the bulk-to-bulk propagator (1.3.14) though we do not consider this here. Returning to (3.2.3) we can specify the range of integration to be over X that are space-like separated from the bulk point x. Choosing this as the support for $\mathcal{K}(x;X)$ in (3.2.3) is often referred to as the *global reconstruction* of $\mathcal{O}_{\text{Bulk}}(x)$ [185], since the bulk field has support on the entire boundary of Cauchy slice Σ.

There are however, alternative choices for the support of the smearing function $\mathcal{K}(x;X)$. One can further restrict the spatial support to a proper subregion A of the CFT at the boundary of Σ. Consideration of bulk reconstruction in this sense leads to the idea of the *subregion duality* [187–189]: the notion that should we only have access to subregion A in the CFT, this subregion will provide us with complete information for some subregion in the bulk.

One of the most compelling forms of bulk reconstruction amalgamating this concept using boundary subregions is the AdS-Rindler reconstruction [190, 191]. Considering AdS_{d+1} and adopting a particular parametrisation of the embedding in new bulk coordinates, the metric becomes

$$ds^2 = -(\rho^2-1)d\tau^2 + \frac{d\rho^2}{\rho^2-1} + \rho^2(dx^2 + \sinh^2 x\, d\Omega_{d-2}^2), \tag{3.2.4}$$

with coordinate ranges $\rho > 1$, $x \geq 0$ and $-\infty < \tau < \infty$. One may also identify that the final term enclosed by parentheses corresponds to the metric on the $(d-1)$-dimensional hyperbolic ball. Thus we are parametrising a subregion of AdS_{d+1}, illustrated in AdS_3 in figure 3.2.2, named the AdS-Rindler wedge.

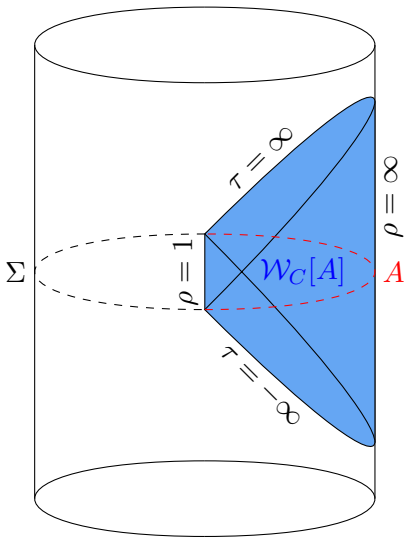

Figure 3.2.2: The AdS-Rindler wedge $\mathcal{W}_C[A]$ (shaded blue region) depicted in AdS_3 spacetime used to reconstruct local bulk operators in some boundary subregion A.

Now, consider some spatial subregion A of the boundary of an asymptotically AdS geometry. The set of all boundary points that can be reached via an inextendible null or timelike curve intersecting A is called the *boundary domain of dependence* $D[A]$. Then, the causal wedge of A [187, 188, 192], denoted $\mathcal{W}_C[A]$, is the set of bulk spacetime events intersected by a causal curve both originating from and evolving to $D[A]$. Hence,

$$\mathcal{W}_C[A] \equiv \mathcal{J}^+[D[A]] \cap \mathcal{J}^-[D[A]], \tag{3.2.5}$$

where $\mathcal{J}^{\pm}$ represent the bulk causal future/past domains of influence as usual. There is then an isomorphism between the bulk region of any AdS causal wedge and the AdS-Rindler wedge. Thus, the idea of bulk reconstruction using the smearing function can be realised using the causal wedge and due to relations through bulk isometries (or the boundary conformal transformations in the CFT), this amounts to employing the AdS-Rindler wedge to do so. Further, this illustrates the concept of subregion duality through the *causal wedge reconstruction conjecture*: in asymptotically AdS spacetime, any bulk field located within the causal wedge of the boundary subregion A can be successfully reconstructed on the boundary region $D[R]$.

However, one may then notice, there is a clear redundancy to the encoding of the non-local bulk operators when implementing (3.2.3). Since we can theoretically have infinite boundary subregions then the same bulk field operator $\mathcal{O}_{\text{Bulk}}(x)$ can lie in multiple of these regions. The naive interpretation of this would be that a local bulk operator reconstructed in any wedge corresponds to the same CFT operator. However, this approach cannot be correct. Consider two causal wedges, $\mathcal{W}_C[A]$ and $\mathcal{W}_C[B]$, both containing the bulk point x, as shown in figure 3.2.3. In order to obtain a CFT operator with support in both regions A and B to truly reconstruct the bulk field $\mathcal{O}_{\text{Bulk}}(x)$, the only possible solution is that it has support on $A \cap B$. However this is not the case, as x has been chosen to lie outside of $\mathcal{W}_C[A \cap B]$, so the operator cannot possess this representation.

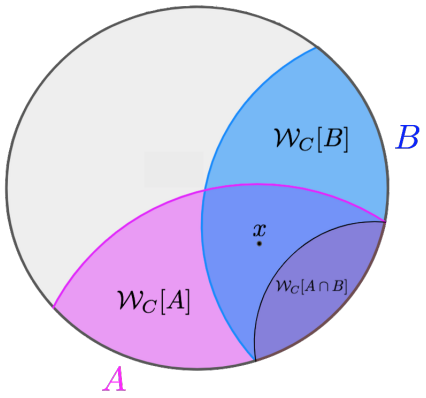

Figure 3.2.3: A Cauchy slice Σ of AdS_3, consisting of two overlapping causal wedges $\mathcal{W}_C[A]$ and $\mathcal{W}_C[B]$ associated to the subregions A and B lying at the boundary of slice. Both wedges contain the bulk point x yet the wedge $\mathcal{W}_C[A \cap B]$ associated with the intersection of A and B does not contain x, leading to a paradox.

Further enlightenment is provided, with regards to this contradiction, by considering the example depicted in figure 3.2.4. In this instance, there are three separate causal wedges $\mathcal{W}_C[A], \mathcal{W}_C[B]$ and $\mathcal{W}_C[C]$, each associated to a subregion of the boundary CFT A, B and C respectively. The bulk operator $\mathcal{O}_{\text{Bulk}}(x)$ is defined at a point x in the bulk that lies outside of all three causal wedges and so cannot be reconstructed on any individual subregion. However, considering the union of any two of these regions (i.e. $A \cup B, A \cup C$ or

$B \cup C$), one is able to fully reconstruct the bulk operator. Clearly, these three reconstructed operators cannot truly be the same.

The resolution to this paradox was suggested in [32]. The statement is that for each subregion A in which the bulk field $\mathcal{O}_{\text{Bulk}}(x)$ can be reconstructed, it then must have a different representation in the boundary CFT. One may notice many parallels between the redundancy of the encoding of $\mathcal{O}_{\text{Bulk}}(x)$ and the language of quantum error correcting codes, motivating the discussion in the next section. We note at this point that a different bulk region may also be chosen for some boundary subregion A, as opposed to the causal wedge, known as the *entanglement wedge* $\mathcal{W}_E[A]$ [193]. We define this wedge to be the bulk region confined between A, the minimal surface γ_A (that appears in the HRT formula generalising (3.1.2)) and its bulk domain of dependence. Under reasonable assumptions, the causal wedge is actually contained within the entanglement wedge $\mathcal{W}_C[A] \subset \mathcal{W}_E[A]$ [28, 194].

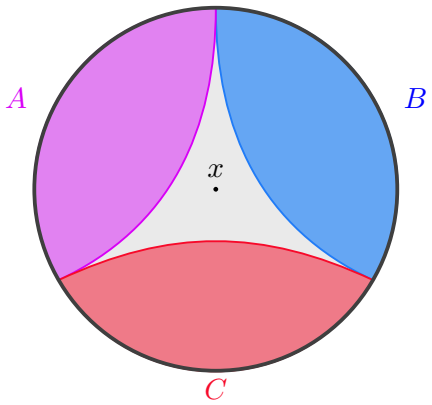

Figure 3.2.4: The boundary of the CFT for Cauchy slice Σ has been split into three subregions A, B and C. The bulk point x does not lie in any of the subregions causal wedge however does lie in the causal wedge of the union of any two of the subregions. This exhibits a redundant encoding since one can reconstruct the bulk operator $\mathcal{O}_{\text{Bulk}}(x)$ on in any of the causal wedges $\mathcal{W}_C[A \cup B], \mathcal{W}_C[A \cup C]$ or $\mathcal{W}_C[B \cup C]$.

3.2.2 Holography and quantum error correction

The thorough description of quantum error correcting codes discussed in section 2.2 can be summarised as the redundant encoding of quantum information from one system (consisting of k logical qudits) into another system (consisting of n physical qudits) with a much larger Hilbert space in order to protect the information from noise induced by the environment. Since there is a redundancy in how $\mathcal{O}_{\text{Bulk}}(x)$ is encoded in the CFT at a sub-algebra level, we realise that this phenomena exhibits the same nature as that of a QECC. Recovery of the information in the bulk (operators localised in the bulk) for one subregion against particular erasures in the boundary CFT is independent to the same erasures in the boundary CFT on different boundary subregions. Then we realise a

QECC through an encoding map storing bulk information (from the k logical qudits) in the degrees of freedom (n physical qudits) at the boundary. For example, reconstruction for operators supported at bulk point x at CFT subregion A would then not be possible if the complement CFT subregion A^c with causal wedge containing bulk point x was erased.

The degree of sensitivity to which the bulk operator $\mathcal{O}_{\text{Bulk}}(x)$ is to boundary erasures is necessarily dependent upon its depth into the bulk. Bulk operators that live close to the asymptotic boundary are extremely sensitive to small erasures since the information will be totally lost if the CFT subregion, with wedge containing it, is erased. Alternatively, as one probes deeper into the bulk, the bulk information becomes increasingly protected against boundary erasures. Figure 3.2.5 emphasises this behaviour visually.

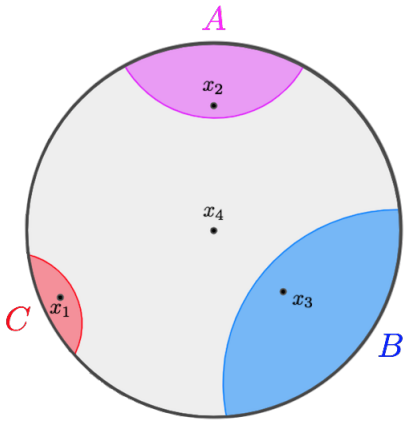

Figure 3.2.5: Three boundary subregions A, B and C such that each of their corresponding causal wedges contain a bulk point. Erasure of any these subregions causes reconstruction of the respective bulk point within them to become impossible. As we move deeper into the bulk, bulk operators are more protected against erasures since larger regions of erasure are needed to stop reconstruction. The bulk point x_4 at the centre of the Cauchy slice is protected from the erasure of all three subregions.

The understanding of these holographic codes can be enhanced by considering the simple toy-model proposed in [32] which was further elucidated in [195]. In this model, one employs the 3-qutrit code [173], thus protecting a single logical qutrit by encoding it into 3 physical qutrits by means of the map

$$|\bar{0}\rangle = \frac{|000\rangle + |111\rangle + |222\rangle}{\sqrt{3}}, \tag{3.2.6}$$

$$|\bar{1}\rangle = \frac{|012\rangle + |120\rangle + |201\rangle}{\sqrt{3}}, \tag{3.2.7}$$

$$|\bar{2}\rangle = \frac{|021\rangle + |210\rangle + |102\rangle}{\sqrt{3}}. \tag{3.2.8}$$

Similarly to the $[[5, 1, 3]]$ code discussed in section 2.3.3, this quantum code exhibits the unique feature that it is a quantum secret sharing scheme.

From the holographic perspective, the three physical qutrits living at the boundary are associated with the local degrees of freedom at the boundary CFT while the logical qutrit living in the bulk is the local degree of freedom in the bulk theory. At the particular point where the logical qutrit lives, the local bulk operators can be understood as logical operations on that encoded subspace. In this sense, these bulk operators commute with all local boundary operators in the CFT. Further, one can represent the bulk operators as operators that act upon only two physical qutrits, establishing a subregion duality between these boundary qutrits and the information in the bulk.

It is clear that this toy-model is not satisfactory to truly illustrate many of the technicalities of the AdS/CFT correspondence, especially the intricacies of the geometry in the bulk. However, the fundamental ideas underlined by this model set the stage for numerous eloquent constructions that shortly followed. Much of the focus of our work in this thesis regards the highly influential HaPPY code, a discrete toy-model adopting tensor network theory, developed by Pastawski, Yoshida Harlow, Preskill [1].

CHAPTER 4

Holography, cellulations and error correcting codes

4.1 Introduction

In recent years there has been increasing interest in relations between quantum information and holography. A key connection is the relationship between the hyperbolic plane, viewed as the spatial slice of AdS_3, and quantum error correction codes. AdS/CFT is usually discussed in continuum language but the quantum code picture of holography relies on discretisations of the hyperbolic plane with which simple quantum error correcting codes can be associated.

The best known class of such codes is the HaPPY codes [1]. These are based on regular uniform tessellations of the hyperbolic plane, with a corresponding graph state respecting the maximal discrete symmetry group of the tessellation. The codes are related to perfect tensors and absolutely maximally entangled (AME) states [196], properties which immediately give rise to Ryu-Takayanagi behaviour [30] for the entanglement i.e. the entanglement of a boundary region scales with the length of the associated discrete geodesic through the bulk.

While perfect tensors have elegant properties that facilitate the analysis of the code properties, the properties of AME/perfect tensor codes do not reflect the expected behaviour of the dual conformal field theory. For example, correlation functions in a

conformal field theory have power law fall-off but the correlation functions induced by AME states do not admit such behaviour. However, there are various ways to adapt the HaPPY construction to give rise to the expected two-dimensional CFT behaviour, ranging from using random tensors to almost perfect tensors [33, 34, 36, 37]. Thus for many purposes the HaPPY construction is viewed as a useful toy model for physical behaviour.

Despite the considerable study of codes, there are still many important conceptual questions about quantum error correction codes for holographic spacetimes. Most of the code constructions are based around two-dimensional spatial slices of static (or stationary) three-dimensional geometries. Dynamics has been explored in [197–199] but is primarily restricted to evolutions that respect constant curvature. The code constructions are associated with discretisations of the spacetime, and the relation to continuum geometry is not well understood. (See however [200, 201] for discussions of taking the continuum limit in the context of tensor networks and entanglement.)

While AdS_3 gravity is often used as a toy model for holography, it misses important features of generic holographic dualities. Three-dimensional gravity is not dynamical and negative Einstein curvature implies constant negative Riemann curvature. In higher-dimensional gravity dynamics would change the Riemann curvature and any discrete approach/code mapping should incorporate this feature. Holographic dualities involve additional fields (scalars, gauge fields, fermions) and the quantum error correction codes should be able to capture these additional degrees of freedom. There have been some previous attempts to explore these issues. For example, by generalising the tensors to represent a Bacon-Shor code, one can include gauge fields in quantum error correcting codes (in two spatial dimensions) [202, 203]. The construction of codes in dimensions higher than two has been considered in [199]; this approach uses so-called perturbation gadgets to construct codes associated with discretisations of higher dimensional spaces. A recent review of holographic quantum error correction can be found in [204].

The main goal of this work is to initiate the systematic construction of codes associated with AdS spacetimes in general dimensions. As we discuss in section 4.2, AdS codes are relevant not only in the context of the standard conformal AdS/CFT dualities. Reduction of AdS spacetimes on tori gives rise to scalar/gravity theories for which the holographic duals are theories with dimensionally running couplings. A specific example of considerable current interest is the reduction of AdS_3 on a circle to give JT gravity, for which the details of the holographic dictionary were studied in [205, 206]. However, the relation between these bulk scalar/gravity theories and dual quantum field theories with generalized conformal structure holds much more broadly [119] and it was shown in [207] that all such dualities could be understood in terms of toroidal reductions of AdS (with

the torus not necessarily having an integer dimension).

In section 4.2 we discuss how one would carry out a toroidal reduction of a hyperbolic tessellation, illustrating our discussions with the example of the hyperbolic plane reduced on a circle, which is relevant for the AdS_3/JT gravity case. This discussion shows how one would obtain codes associated with the lower-dimensional scalar/gravity theories from higher dimensional hyperbolic codes.

In sections 4.3 and 4.4 we develop the construction of codes associated with regular uniform tessellations of hyperbolic geometries in three and higher dimensions. The reason for beginning with a HaPPY type approach based on regular uniform tessellations is the desirable properties captured by such codes e.g. Ryu-Takayanagi entanglement, pushing behaviour, greedy algorithm. While one would anticipate the need to adapt the construction to obtain CFT entanglement and correlation function behaviour, the two-dimensional HaPPY code is a useful starting point for more realistic constructions.

One of the key aspects of the HaPPY construction is the relationship between perfect tensors and absolutely maximally entangled states and we review this in detail in section 4.3. For higher dimensional hyperbolic space a number of subtleties are encountered in using regular uniform tessellations and perfect tensors to construct codes. Firstly, the number of regular uniform tessellations decreases with dimension e.g. there are only four such tessellations for three dimensional hyperbolic space. This contrasts with the infinite number of such tessellations in two dimensions.

Secondly, one cannot assign qudits to the polytope of the tessellation in a way that the assignment both preserves the discrete symmetry of the polytope and corresponds to a perfect tensor/absolutely maximally entangled state. The prototype HaPPY code is based on pentagons and the physical qubits associated to each side of the pentagon are equivalent to each other in the corresponding graph state. Standard classifications of absolutely maximally entangled (AME) states [208–211] imply that one cannot, for example, have the qudits associated with each face of a three-dimensional polytope of a regular hyperbolic tessellation being equivalent in the corresponding graph state.

This might sound surprising but in fact many hyperbolic plane tessellations are also incompatible with simultaneously preserving the discrete symmetry of the polygon cell and corresponding to an AME state. The new issue in higher dimensions is that the number of regular uniform tessellations is sparse, and all the polytopes corresponding to these tessellations are not compatible with maximal discrete symmetry and AME states. In section 4.4 we present two alternative ways of addressing this issue. The first is to relax the requirement of AME/perfect tensor; we construct codes that respect the discrete symmetry of each polytope cell of the tessellation but are not AME. The second approach

is to work with AME codes, but now the assignment of the qudits to polytope cell faces does not respect the discrete symmetry of the polytope. The latter implies that one has to be careful with the concatenation of cells and we give an example of how this can be done consistently. There are many future directions to develop these codes further, which we discuss in section 4.6.

The underlying principle of the HaPPY code is that logical qubit information is encoded in each cell of the tessellation with this information pushed to the boundary via physical qubits. HaPPY and related codes have natural interpretations in terms of spacetime reconstruction: one can ask questions about which parts of the boundary are necessary for reconstruction of a given region in the bulk.

While most holographic constructions of hyperbolic codes are based on the principle of encoding logical information into each cell, this is not the only possible way to construct codes for hyperbolic spaces. It is known that one can map cellulations of spaces into other types of quantum error correction codes, namely CSS codes. As we discuss in section 4.5 the logical information in such codes is associated both with the asymptotic boundary of the space as well as with internal boundaries/defects.

CSS codes associated with the hyperbolic plane have been constructed in earlier literature. In section 4.5 we review such constructions and explain how CSS codes associated with higher dimensional hyperbolic spaces can be constructed. We note that these codes could potentially be used in two distinct ways. Firstly, if the code is associated with the entire (regulated) hyperbolic space, then the logical information at the boundary would be interpretable in the dual conformal field theory. One could think of these codes as in some sense reversing the logic of HaPPY: in these codes, one can ask questions about how logical information in the boundary is encoded through a physical qubit network in the bulk.

The second potential use of the CSS code construction is as a way to implement local holography. Suppose one considers a region of a hyperbolic space with a boundary at finite distance, and associates a CSS code to a tessellation of this region with logical information being encoded at the boundary of the region. Each region is thus locally holographic, with logical information associated with the boundary. One could then envisage concatenating codes associated with neighbouring regions, pushing the logical information all the way out to the asymptotic boundary. This approach could be a natural starting point for incorporating dynamics, with the curvature and encoding in each region potentially evolving with time.

The outline of this thesis chapter is as follows. In section 4.2 we discuss tessellations and cellulations for geometries that arise in holographic correspondences. In section 4.3

we explore in detail the construction of quantum error correction codes associated with two-dimensional tessellations, focusing particularly on AME states and the concatenation of codes between cells. In section 4.4 we construct codes associated with hyperbolic geometries in three and higher dimensions, giving examples of both AME and non-AME codes. In section 4.5 we discuss alternative constructions of codes associated with hyperbolic tessellations, CSS codes in which the logical qubits are encoded through global properties of the tessellation. We conclude and explore directions for future research in section 4.6.

4.2 Holographic geometries, polytopes and tessellations

Throughout this paper we will be exploring cellulations of holographic geometries and associated codes using several classes of representative examples. Our examples are primarily based on maximally symmetric geometries as these are both the best understood holographic geometries and furthermore their cellulations are well studied by mathematicians.

Our main example of holographic geometry is perhaps unsurprisingly Anti-de Sitter for which spatial slices are hyperboloids, as this is the basis for the best understood holographic correspondence. Earlier literature on holographic codes has been primarily based around AdS_3 whose spatial slices are hyperbolic planes. In this section we will discuss cellulations of hyperbolic spaces in general dimensions as a first step towards generalising AdS_3 constructions to higher dimensions.

We will also be interested in holographic geometries with compact directions, focussing on two distinct representative classes of examples. The first class of examples is products of AdS with spheres which of course arise frequently in holographic dualities. For example, AdS_3 spacetimes often occur as products with two and three dimensional spheres:

$$ds^2 = \frac{1}{z^2}\left(dz^2 + dx^2 - dt^2\right) + \mathcal{R}^2 d\Omega_n^2 \tag{4.2.1}$$

where $d\Omega_n^2$ is the metric on S^n with $n = 2$ or 3. Here we represent the anti-de Sitter spacetime in Poincaré coordinates to contrast against the case discussed below but the spacetime is regular and global coordinates would cover the entire spacetime. The simplest prototype for compact additional dimensions of this type would be $\mathrm{AdS}_3 \times \mathrm{S}^1$, for which we can express the metric as

$$ds^2 = \frac{1}{z^2}\left(dz^2 + dx^2 - dt^2\right) + \mathcal{R}^2 dy^2, \tag{4.2.2}$$

where the anti-de Sitter space has unit radius and $\mathcal{R}$ is the radius of the circle direction y. We will discuss tessellation of this prototypical example below.

Our second class of examples relates to toroidal compactifications of higher dimensional AdS spacetimes. These examples are interesting as from the lower dimensional perspective they give rise to holographic dualities with running couplings: reducing the CFT on a torus, the dual field theory is from the lower dimensional perspective a theory with generalised conformal structure i.e. conformal invariance broken only by a single running coupling.

Such dualities are amongst the simplest prototypes for non-conformal gauge/gravity dualities and arise in the context of dualities associated with D-branes and fundamental strings in [117]. The detailed holographic dictionary for non-conformal branes and the associated generalized conformal structure was studied in [119]. It was shown in [207] that generic dualities with generalized conformal structure could be interpreted in terms of compactifications of AdS on tori, with the dimension of the torus not necessarily being integral.

As an illustrative case, we can express the metric for $\mathrm{AdS}_{(\sigma+3)}$ in the form

$$ds^2 = \frac{1}{z^2}\left(dz^2 + dx^2 - dt^2 + d\mathbf{y}\cdot d\mathbf{y}_\sigma\right) \tag{4.2.3}$$

where $\mathbf{y}$ denotes σ coordinates. When the y coordinates are not periodic the metric simply describes the Poincaré patch of anti-de Sitter space in $(\sigma+3)$ dimensions, with the Poincaré horizon being at $z \to \infty$.

If the coordinates $\mathbf{y}$ are periodically identified, and thus parameterise a torus T^σ, the metric above has a conical singularity as $z \to \infty$; one cannot view the metric above as covering part of a regular manifold. Nonetheless this situation is of physical interest: it corresponds to the dual CFT being compactified on a torus T^σ and the conical singularity can be cloaked by a horizon at finite temperature.

In this setup we can relate negative curvature geometries in $(\sigma + 3)$ dimensions to solutions of three dimensional Einstein-scalar gravity as follows. Pure gravity solutions in $(\sigma + 3)$ dimensions satisfy the equations of motion following from the action

$$S = L\int d^{\sigma+3}x\sqrt{-G}\,(R(G) + (\sigma+1)(\sigma+2)) \tag{4.2.4}$$

where

$$L = \frac{l^{\sigma+1}}{16\pi G_{\sigma+3}} \tag{4.2.5}$$

with l the AdS radius and $G_{\sigma+3}$ the Newton constant.

Now consider a diagonal reduction ansatz for the metric G:

$$ds^2 = ds_3^2 + e^{\frac{2\phi}{\sigma}} d\mathbf{y} \cdot d\mathbf{y}_\sigma \tag{4.2.6}$$

The three dimensional metric and scalar field ϕ satisfy the equations of motion following from the reduced action

$$S = LV_\sigma \int d^3x \sqrt{-g} e^\phi \left(R(g) + \left(\frac{\sigma - 1}{\sigma} \right) (\partial\phi)^2 + (\sigma + 1)(\sigma + 2) \right), \tag{4.2.7}$$

where V_σ is the volume of the compactified directions $\mathbf{y}$. One particular solution of these reduced equations is

$$ds^2 = \frac{1}{z^2} \left(dz^2 + dx^2 - dt^2 \right) \qquad e^\phi = \frac{1}{z^\sigma}, \tag{4.2.8}$$

i.e. the reduction of the higher dimensional AdS solution. The key conceptual difference relative to (4.2.2) is that the radii of the circle directions scale with the AdS radius, rather than being fixed.

The above example relates to three dimensional Einstein scalar theories. However, the general picture holds in generic dimensions providing a generic class of non-conformal holographic dualities. A particularly interesting case of considerable recent interest is the circle reduction of AdS_3 itself i.e. in the metric

$$ds^2 = \frac{1}{z^2} \left(dz^2 + dx^2 - dt^2 \right) \tag{4.2.9}$$

the x direction is taken to be periodic with radius R_x. Reduction of AdS_3 gravity on a circle results in a two-dimensional theory that is equivalent to JT gravity [119, 205], which is again dual to a (one-dimensional) theory with a dimensionally running coupling. Such two-dimensional backgrounds have been discussed extensively in the context of SYK dualities following the well-known work of [212, 213]. In later sections we will discuss tessellations for these backgrounds and how these may relate to quantum codes.

4.2.1 Tessellations of hyperbolic spaces

In this section will review how classes of holographic geometries can be tessellated and cellulated by polytopes, beginning with the very familiar case of two dimensional tessellations. We start with the definition of a tessellation for a two-dimensional (Riemannian) manifold. A tessellation consists of a covering of the manifold $\mathcal{M}$ by a set of polygons $\{P_j\}$, each of which is associated with a distance preserving function $\phi_j : P_j \to \mathcal{M}$. This implies that any two points on a polygon which are associated with (a, b) satisfy

$$D_{P_j}(a, b) = d_{\mathcal{M}}(\phi_j(a), \phi_j(b)) \tag{4.2.10}$$

where D_{P_j} and $d_{\mathcal{M}}$ are distances in the polygon and manifold, respectively. In two dimensions tessellations are commonly referred to as tilings.

Turning to holographic applications, in the context of AdS_3, the spatial section is the hyperbolic plane H_2, tessellations of which are very well studied within the mathematics literature. From the perspective of physical applications it is often natural to focus on tessellations that respect discrete symmetry groups that are subgroups of the continuous symmetry group of hyperbolic space. The most symmetric tessellations are based on regular uniform tilings.

It is a well known result in mathematics, following the famous work of Coxeter [214], that the hyperbolic plane admits an infinite number of regular tilings. *Regular* tilings can be characterised by the Schläfli pair $\{p, q\}$, where p is the p-gonal regular polygon and q denotes the number of line segments associated with each vertex of the polygon (or equivalently the number of p-gons at each vertex). Every positive integer pair such that

$$\frac{1}{p} + \frac{1}{q} < \frac{1}{2} \tag{4.2.11}$$

gives a hyperbolic tiling. The specific tilings used in the context of the original HaPPY code [1] are $\{5, 4\}$ (and dual, see below), which is an example of tiling which is both regular and uniform.

A *uniform* tiling is a tiling that has regular polygons as faces and is vertex transitive so there is an isometry mapping any vertex onto any other. Uniform tilings can be described by their vertex configuration, a notation for representing the sequence of faces around the vertex. The vertex configuration gives the number of sides of faces going around the vertex. For example $a.b.c$ denotes a vertex that has three faces around it, faces with sides a, b and c. With this notation the regular pentagonal tiling is denoted 5.5.5.5.

Uniform tilings may be regular, if also face and edge transitive, but can also be quasi regular (edge transitive but not face transitive) or semi-regular (if neither edge nor face transitive). In the context of holography it is most natural to work with uniform regular tilings, as one would expect transitivity of faces, edges and vertices. All uniform tilings generate *dual* uniform tilings; in the context of two-dimensional tessellations, duality relates the vertices of one tessellation to the edges of the dual. For the uniform regular tilings, each tiling $\{p, q\}$ has a dual tiling $\{q, p\}$. For example, the dual of the pentagonal tiling with four pentagons meeting at each vertex, $\{5, 4\}$, is a square tiling with five squares meeting at each vertex $\{4, 5\}$.

The main focus of this paper is generalising codes based on tessellations to spatial dimensions higher than two. To describe higher dimensional tessellations we first need to

define the relevant polytopes. A d-dimensional (Euclidean) polytope P is a compact subset of d dimensional Euclidean space bounded by a finite number k of $(d-1)$ dimensional hyperplanes; compactness implies that $k > d$. A d dimensional polytope has facets which are $(d-1)$ dimensional polytopes; these facets themselves have facets that are $(d-2)$ dimensional polytopes and so on. The set of all the i dimensional sub-polytopes are referred to as i cells.

A tessellation of a d-dimensional Riemannian manifold $\mathcal{M}$ formally consists of a set of d-dimensional polytopes $\{P_j\}$ embedded via isometries $\phi_j : P_j \to \mathcal{M}$. The images of the i cells under the mapping are also i cells. Tessellations for which the isometric maps are replaced by injective homeomorphisms are called cellulations; a cellulation does not respect distances (and therefore $\mathcal{M}$ need not necessarily admit a metric) but a cellulation does respect the topology of the manifold.

Given this general definition of tessellations, let us now consider higher dimensional AdS spacetimes whose spatial sections are hyperbolic. We begin with AdS_4, with spatial section H^3. Again, from a physical perspective, it is natural to look first at tessellations that respect discrete subgroups of the continuous symmetry group, i.e. regular and uniform tessellations. These are well studied within the mathematics literature.

Three-dimensional hyperbolic space may be tessellated with regular polytopes that are regular polyhedra and are characterised by Schläfli symbols $\{p, q\}$. Here p refers to the face type of the regular polyhedron while q is the vertex figure, which is the polygon obtained by connecting vertices that are one edge away from a given vertex. For a regular polyhedron the vertex figure is always a regular polygon. An example is $\{5, 3\}$, the regular dodecahedron with pentagonal faces and three edges around each vertex. Hyperbolic geometry is obtained, as in the two dimensional case, when

$$\frac{1}{p} + \frac{1}{q} < \frac{1}{2}. \tag{4.2.12}$$

Topologically a regular two-dimensional tessellation may be viewed as a polyhedron such that the angular defect at the vertex is zero and this is why the Schläfli $\{p, q\}$ symbols arise in both contexts.

The polytope clearly does not uniquely define how the three-dimensional hyperbolic space is tessellated. For regular tessellations (also called honeycombs), the tessellation is defined by the polytope $\{p, q\}$ together with the edge figure $\{r\}$, i.e. the number of polyhedra around each edge. This information may be summarised in the Schläfli symbol $\{p, q, r\}$.

A key difference relative to two dimensions is that the number of regular uniform tessellations is finite. Indeed, the only four regular compact three-dimensional hyperbolic honeycombs are shown in Table 4.2.1.

Name	Schläfli symbol	Polytope	Edge figure
Icosahedral honeycomb	$\{3,5,3\}$	Icosahedron $\{3,5\}$	$\{3\}$
Order 5 cubic honeycomb	$\{4,3,5\}$	Cube $\{4,3\}$	$\{5\}$
Order 4 dodecahedral honeycomb	$\{5,3,4\}$	Dodecahedron $\{5,3\}$	$\{4\}$
Order 5 dodecahedral honeycomb	$\{5,3,5\}$	Dodecahedron $\{5,3\}$	$\{5\}$

Table 4.2.1: The four regular compact hyperbolic honeycombs of H^3.

Under duality operations, the cells and vertices are interchanged, and the faces and edges. We illustrate the corresponding Schläfli symbols for these dual honeycombs in Table 4.2.2.

Name	Schläfli symbol	Dual
Icosahedral honeycomb	$\{3,5,3\}$	$\{3,5,3\}$
Order 5 cubic honeycomb	$\{4,3,5\}$	$\{5,3,4\}$
Order 4 dodecahedral honeycomb	$\{5,3,4\}$	$\{4,3,5\}$
Order 5 dodecahedral honeycomb	$\{5,3,5\}$	$\{5,3,5\}$

Table 4.2.2: Dual honeycombs of H^3.

Hyperbolic honeycombs in higher dimensions can similarly be classified [214]. For tessellations of spatial slices of AdS_5, the regular compact honeycombs of H^4 are

$$\{3,3,3,5\} \qquad \{4,3,3,5\} \qquad \{5,3,3,5\} \qquad \{5,3,3,4\} \qquad \{5,3,3,3\}. \tag{4.2.13}$$

Analogously to the 3d honeycombs, the Schläfli symbol $\{p,q,r,s\}$ captures the four-dimensional polytope $\{p,q,r\}$ and via s the structure of the honeycomb i.e. how the polytopes fit together.

The relevant 4d regular polytopes are $\{3,3,3\}$ (5-cell with tetrahedron 3d projection); $\{4,3,3\}$ (tesseract, with cubic 3d projection) and $\{5,3,3\}$ (120-cell, with tricontahedron 3d projection). Note that the canonical honeycomb for R^4 is $\{4,3,3,4\}$. For five dimensional hyperbolic space H^5 there is only one regular honeycomb ($\{3,4,3,3,3\}$). Interestingly, for hyperbolic spaces in dimensions greater than five there are no regular compact honeycombs.

4.2.1.1 Tessellations of $\mathbf{AdS}_3\times\ \mathbf{S}^n$

In this section we will consider possible tessellations for holographic geometries involving compact spheres, using the example of (4.2.1) to illustrate the discussions. The spatial

sections of $AdS_3 \times S^n$ are $H^2 \times S^n$. Consider first the prototype case of $n = 1$. Clearly since the space is a direct product we can take direct products of tessellations for each component. For S^1 the relevant polytopes are closed line segments; these are regular and are represented by the Schläfli symbol $\{\}$. Uniform regular tessellations of $H^2 \times S^1$ can thus be characterised as $\{p, q\} \times \{\}$. A special case of this is where the circle is covered by one single segment.

Now consider the case of $n = 2$, i.e. the two sphere. Uniform tessellations of the sphere are well documented and in particular the regular uniform tessellations include $\{p, q\}$ where

$$\frac{1}{p} + \frac{1}{q} > \frac{1}{2}. \tag{4.2.14}$$

There are a finite number of such regular uniform tessellations with $p > 2$, and the total number of polygons required to cover the sphere is in each case finite. One can also consider tessellations of the form $\{2, m\}$ as this manifestly satisfies the requirement above for any value of m. Here the sphere is divided into m equivalent segments; for such tessellations one can take $m \to \infty$ i.e. there are an infinite number of possible tessellations.

Having discussed the possible regular tessellations, let us now turn to what would be the most natural approach in the context of holographic codes. In holographic dualities of the type (4.2.1) the compact space plays a qualitatively different role to the non-compact hyperbolic space: the radius of the compact space is fixed and does not depend on the hyperbolic radial coordinate i.e. the renormalization group scale. As we review later, the basic idea of the encoding map of a code is to represent interior regions of the hyperbolic space by logical qubits: the tessellation captures the increase in the number of qubits required as one approaches the conformal boundary.

As the radius of the compact space is fixed, it is not clear tessellating the compact space non-trivially would be the natural choice for the encoding map approach to holography, rather than working with the trivial tessellation which is the compact space itself (tessellations are $\{p, q\} \times S^2$). The latter manifestly preserves the full symmetry group of the compact space, while any non-trivial tessellation breaks the symmetry group to a discrete subgroup.

Thus, for holographic geometries in which the compact part has a fixed radius, tessellations and associated codes are perhaps most naturally constructed by treating the code qubits to transform in appropriate representations of the compact space symmetry group. We will however use non-trivial tessellations of spheres in section 4.5, in the context of the topologically spherical regulated boundary of hyperbolic space itself.

4.2.1.2 Toroidal compactification of hyperbolic spaces

Now let us turn to toroidal compactifications of hyperbolic spaces. In this set up the compact direction has a radius that depends on the holographic scale; toroidal identifications have fixed points and thus the holographic geometries are not regular manifolds. Mathematics literature focuses on tessellations and cellulations of regular manifolds and such irregular toroidal compactifications do not fall within the usual classifications. Nevertheless, as discussed above, such geometries arise rather generically in holography and it is interesting to explore how one could relate these to quantum codes.

We will explore two qualitatively different ways to cellulate a toroidal compactification which are distinguished by whether they preserve a discrete subgroup of the toroidal symmetry. Let us illustrate this discussion using the example given in (4.2.3). One can manifestly cellulate the space locally with cells of the type $\{p, q\} \times T^\sigma$. The torus itself can also be non-trivially cellulated by breaking each circle direction into segments. In both approaches the cellulation will break down as $z \to \infty$, reflecting the conical singularity. This can be addressed by excising this region i.e. considering a cellulation with a boundary near to $z \to \infty$.

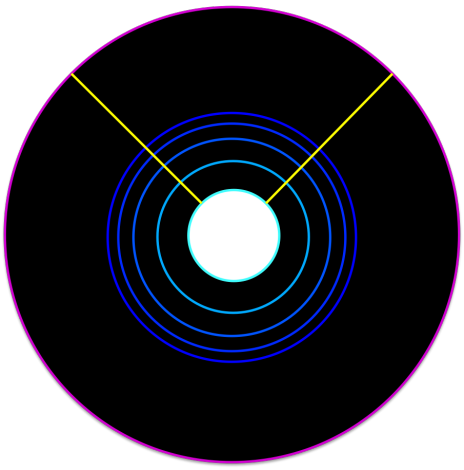

Figure 4.2.3: Compactified hyperbolic plane, tiled by annuli of equal area. The yellow lines are identified to compactify the plane, creating a conical singularity which is shown as excised (white region).

This type of cellulation is similar to those discussed in the previous subsection. However, in the situation described in the previous subsection the scale of the compact geometry is fixed. For toroidally compactified hyperbolic spaces the scale of the torus is not constant but varies with z. To capture this feature the volumes of the toroidal components of the cells T^σ cannot be constant but should increase as cells approach the boundary. The constant negative curvature therefore has to be built in by hand through the volumes of the cells.

The simplest example to visualise is the case of the hyperbolic plane itself, with the x direction periodic; this is relevant for the relationship between AdS_3 reduced on a circle to give JT gravity. The associated tiling is shown in Figure 4.2.3. Each annulus is of equal proper area, and accordingly the width of the annulus decreases along the radial direction. One can implement any radius of the x direction by identifications, but these result in a conical singularity that needs to be excised from the tiling. The identifications are shown in yellow, and the excised region is shown in white.

A second approach to cellulating a toroidal compactification involves the use of local regular tessellations such as those described in section 4.2.1 with appropriate identifications. In this case the cells are of constant proper volume, with the negative curvature captured by the structure of the cellulation. Again one will need to excise a hole in the centre of the space, reflecting the singularity as $z \to \infty$.

The simplest class of examples relate to circular reduction of the hyperbolic plane. Consider a generic hyperbolic $\{p, q\}$ tessellation, with a regular p-gon at the centre. Such a tessellation has a discrete rotational symmetry Z_p associated with the symmetry group of the p-gon. We can construct from this a cellulation of a negative curvature space with conical singularity, by removing the central p-gon. One then identifies two of the vertices of the missing pentagon, which will necessarily be related by a certain Z_p transformation. One then continues to remove pentagons and identify vertices related by the same Z_p transformation.

An example based on a $\{5, 4\}$ tessellation is shown in Figure 4.2.4. The tessellation preserves a discrete Z_5 symmetry group. The numbered vertices and associated edges are related by a Z_5 transformation and are identified. This identification is clearly only possible if the central pentagon is removed. The resulting tiling describes a space that is locally hyperbolic but which has an excised conical singularity. By suitable choice of $\{p, q\}$ and discrete symmetry group, one can realise different radii of the x direction.

The generalisation to higher dimensions would work similarly. Tilings based on regular polytopes have discrete symmetry groups, which are subgroups of the continuous rotation group of the hyperbolic space. An analogous process of removing the central cell and identifying faces/edges etc that are related by a discrete symmetry transformation will result in a tessellation of a space in which one direction is compact and there is an excised conical singularity.

The two approaches have complementary advantages. The first approach preserves the continuous symmetry group of the toroidal directions and therefore compactification and restriction to zero modes on the compact space are straightforward. However, the tiling is not based on a regular tessellation and therefore does not directly inherit standard

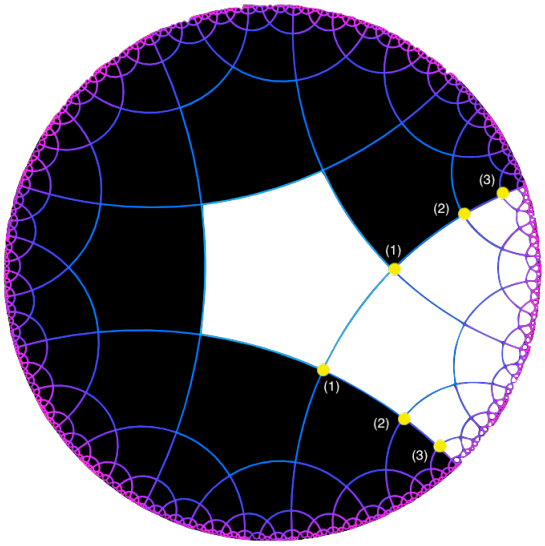

Figure 4.2.4: $\{5, 4\}$ tessellation, with central pentagon removed. Numbered vertices, and the edges that link them, which are all related by Z_5 transformations, are identified.

geometric properties associated with tessellations.

The second approach breaks the continuous symmetry group of the toroidal directions but is obtained from regular tessellations via quotienting and therefore inherits properties from the original tessellation. However, as the symmetry in the compact directions is broken, one cannot straightforwardly describe the tiling using only the lower-dimensional perspective. Dynamically, one often focuses on the zero mode sector of a toroidal reduction, but in this setup it would not be straightforward to identify and retain only zero modes. We will comment on the features of codes associated with both classes of tilings in our conclusions.

4.2.2 Cellulations and graphs

In the final part of this section we review how cellulations of manifolds can be described by graphs known as Hasse diagrams. These graphs are useful in relating cellulations to certain classes of quantum error correcting codes, as we discuss in section 4.5.

In a tessellation the polytopes are embedded via isometries as described in section 4.2.1. If we are primarily interested in embeddings in which the cells do not intersect and the overlap between the cells is invariant, embedding via isometries may be an unnecessarily strong condition. The term cellulation refers to embedding of polytopes via (injective) homeomorphisms. In a cellulation the topology of the manifold is respected but the manifold does not necessarily have a metric i.e. a notion of distance.

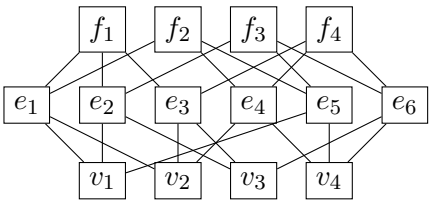

Figure 4.2.5: Hasse diagram for the tetrahedron.

Hasse diagrams are multipartite graphs that show how cells within a cellulation are connected. Each node in the diagram represents a cell in the cellulation. Two nodes can be connected to each other only if

1. The cell corresponding to one node is contained in the cell corresponding to the other.

2. In addition, the difference of dimensionalities of these cells is one.

Each level in the Hasse diagram thus corresponds to the set of all i-dimensional subpolytopes (i cells) and the total number of levels for a D-dimensional cellulation is D: the polytope itself is usually not included as part of the Hasse diagram, so the levels range from 0 (vertices) to $(D-1)$.

A simple example of a Hasse diagram is a tetrahedron, shown in Figure 4.2.5. Suppose that the faces of the tetrahedron are labelled as (f_1, f_2, f_3, f_4) and its six edges are labelled as $(e_1, e_2, e_3, e_4, e_5, e_6)$, with the four vertices being (v_1, v_2, v_3, v_4). The Hasse diagram shows the connections between faces, edges and vertices. Note that this diagram omits the single 3-cell itself i.e. the tetrahedron.

To connect with quantum codes, we will need to use the following property of cellulations:

- If c_{i+1} and c_{i-1} are nodes at levels $(i+1)$ and $(i-1)$, respectively, then the number of cells at level i that are connected to both c_{i+1} and c_{i-1} is either zero or two.

The significance of this property is that, as reviewed in [215], it relates to the existence of a map between three consecutive levels of a cellulation and a CSS (Calderbank, Shor and Steane) code:

- Any subgraph of a Hasse diagram consisting of three consecutive levels defines the Tanner graph of a CSS code.

The key properties of CSS stabiliser codes are summarised in section 2.3.2, and we will explain Tanner graphs further in section 4.5.

4.3 Connecting tessellations with error correcting codes

In this section we will discuss how tessellations of hyperbolic spaces can be related to quantum error correcting codes, explaining the approach of HaPPY [1], focusing on aspects of the construction that are key in generalising to higher dimensions. Throughout this section we will reference various well known properties of quantum error correcting codes, all of which were previously described in chapter 2. To generalise the construction to higher dimensions we will in particular need to explore in detail the properties of absolutely maximally entangled states and how these relate to the tessellation used.

4.3.1 Stabiliser construction of HaPPY codes in two spatial dimensions

Perhaps the best known example of a holographic code is the HaPPY code proposed in [1]. This code is based on a regular $\{p, q\}$ tessellation of hyperbolic space viewed as a spatial section of AdS_3. The basic premiss of the code is the following. Each of the polygons is associated with a certain *perfect tensor* structure. Perfect tensors have an even number of indices and symmetry properties that relate to the entanglement structure of the associated quantum state/code. The main example used in [1] is a $[[5, 1, 3]]$ stabilizer code, encoding one logical qubit into five physical qubits with code distance three.

Before we describe the HaPPY construction in detail, let us summarise the main geometric features. The realisation is based on a $\{5, 4\}$ tessellation, shown in Figure 4.3.1. For every pentagon there is a "logical" qubit associated with the entire pentagon while edges connecting vertices are associated with five "physical" qubits. The conformal boundary of the spatial section is regulated and the edges intersecting the regulated boundary are associated with the physical qubits in a discretisation of the boundary theory.

There is a rank six perfect tensor describing the code and this is shown in the dual $\{4, 5\}$ tessellation, shown in Figure 4.3.2. Each node in the $\{4, 5\}$ tessellation is associated with an uncontracted leg of the tensor (the logical qubit). The legs of the tensor associated with the physical qubits are contracted against the corresponding legs in the neighbouring pentagon; in the $\{4, 5\}$ tessellation these are the edges linking nodes.

We next explore in detail the construction presented in [1] from first principles; the details of this construction are required in developing higher dimensional generalisations

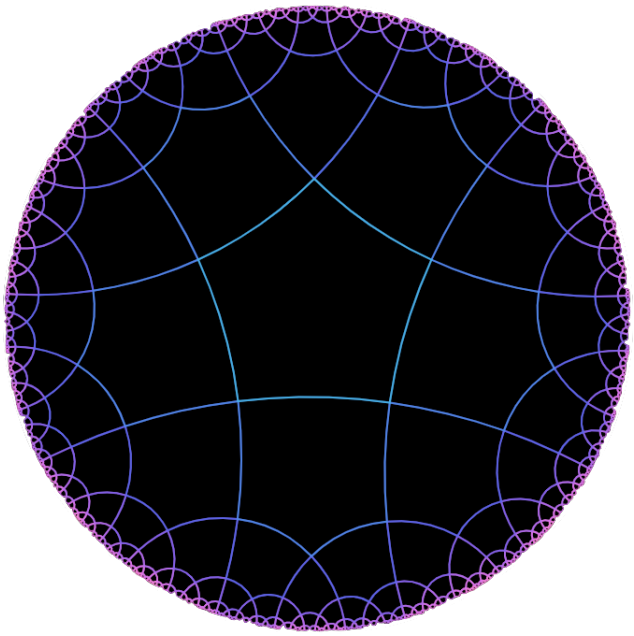

Figure 4.3.1: $\{5, 4\}$ Tessellation of hyperbolic plane. Associated with each pentagon there is one logical qubit and five physical qubits, each of which is associated with an edge.

in the following section. We consider fixed time slices of the bulk space AdS_3 corresponding to the two-dimensional hyperbolic plane H^2. The models presented are then realisations of regular, uniform hyperbolic tessellations that discretise H^2 in a maximally symmetric fashion. The HaPPY construction utilises the pentagonal tiling of two-dimensional hyperbolic space, given by Schläfi symbol $\{5, 4\}$. For each pentagon, one places a single physical qubit on each edge. A final qubit is placed in the centre of the pentagon which can later be shown to have the interpretation of a logical qubit, see Figure 4.3.3.

More generally, for each such system of this type, one associates a graph $G = (V, E)$, where $V = \{1, \ldots, n\}$ is a finite set of vertices and E are the corresponding edges such that $n = 5$ for the pentagon. The vertices of this graph are chosen to be the qubits in the system. In order to preserve maximal symmetry, the graph is chosen such that neighbouring qubits on the pentagon are connected via an edge. The central qubit of the pentagon is chosen to be connected to every other qubit in the pentagon. Hence our graph looks as shown in Figure 4.3.4.

4.3.2 Graph States and AME states

In this section we discuss the relation between graphs and absolutely maximally entangled states. Given a graph $G = (V, E)$ representing the system, one can define a graph state $|G\rangle$. One will first construct this in terms of the controlled-Z gate operator CZ_{ij}, defined

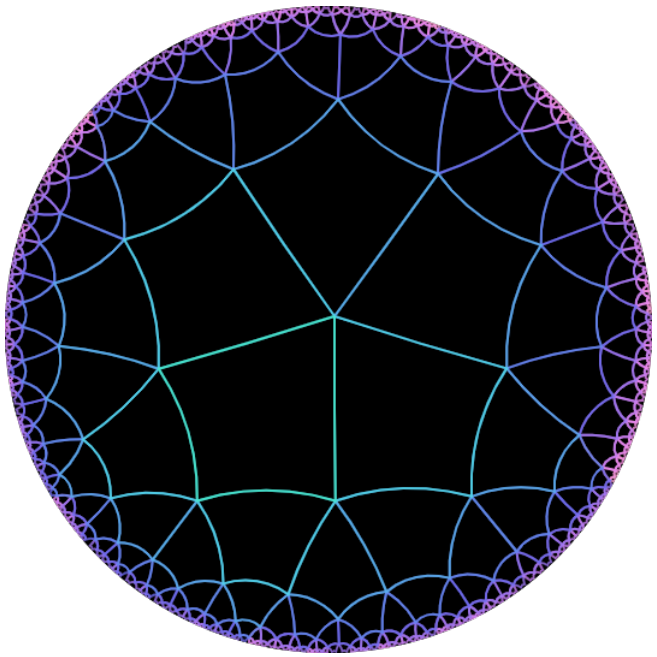

Figure 4.3.2: $\{4,5\}$ Tessellation of hyperbolic plane. In the HaPPY code each node represents the uncontracted logical qubit leg of the perfect tensor, and each edge represents the contraction of physical qubit tensor legs.

in A.1.27, before noticing it can be extended to have an interpretation in the stabiliser formalism. For any graph G consisting of n vertices (system of n qudits), the corresponding graph state $|G\rangle \in \mathcal{H}^{\otimes n}$ is defined by

$$|G\rangle := \prod_{i>j} CZ_{ij}^{A_{ij}} |+\rangle^{\otimes n} \tag{4.3.1}$$

where $A_{ij} \in \mathbb{Z}_p$ are called weights and form the $n \times n$ adjacency matrix $A \in \mathbb{Z}_p^{n\times n}$. Here, p is prime and the Hilbert space $\mathcal{H} \cong \mathbb{C}_p$. The adjacency matrix encapsulates all the relevant information about the connectivity of the graph, such that a weight zero operator represents no edge joining the vertices i and j and weight one operators represent a single edge connecting them and so on. The initial prepared state $|+\rangle^{\otimes n}$ represents joint $+1$ eigenstate of X_i arising from the X-eigenbasis

$$|+\rangle = F^\dagger |0\rangle = \frac{1}{\sqrt{D}} \sum_{l=0}^{D-1} \omega^{-0l} |l\rangle \,, \tag{4.3.2}$$

where F is the Fourier gate. For example in the most simple case, where one considers qubits; $|+\rangle = (|0\rangle + |1\rangle)/\sqrt{2}$, the Fourier gate reduces to the Hadamard gate

$$H = \frac{1}{\sqrt{2}} \begin{bmatrix} 1 & 1 \\ 1 & -1 \end{bmatrix} \tag{4.3.3}$$

and the controlled-Z operator is $CZ = |00\rangle\langle 00| + |01\rangle\langle 01| + |10\rangle\langle 10| - |11\rangle\langle 11|$.

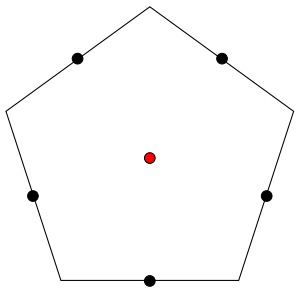

Figure 4.3.3: A single pentagon constructed using the HaPPY approach associated with a single logical qubit (that one diagrammatically represents by placing in it's centre) and five physical qubits (one associated with each edge).

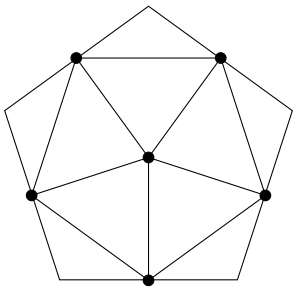

Figure 4.3.4: The maximally symmetric construction of graph G for a single pentagon.

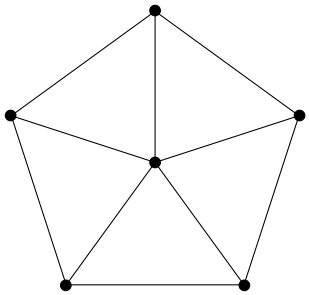

Figure 4.3.5: The resulting graph (state) to which G stabilisers are assigned.

Since graph states are just a special class of stabiliser states, an alternative but equivalent way of defining a graph state is possible using the generators of the stabiliser group. Any n-qudit graph state may be represented as n operators,

$$g_i = X_i \prod_{j=1}^{n} Z_j^{A_{ij}}, \tag{4.3.4}$$

which provide the minimal set of generators of the stabiliser group. The graph state can then be thought of as the common $+1$ eigenspace of these generators;

$$g_i \left|G\right\rangle = \left|G\right\rangle, \text{ for } i = 1, \ldots, n. \tag{4.3.5}$$

One should note that for the case of qubits, graphs can only have edges of weight 0 or 1. This is because if one imposes a weight 2 edge, $Z^2 = Z^0 = \mathbb{1}$ and is the same as a weight zero operator. When extending to qudits of a more general dimension D, one now has $Z^D = \mathbb{1}$ and so one can have weights A_{ij} from 0 to $D-1$. This allows for graphs to have multiple edges between vertices as indicated in Figures 4.3.6 and 4.3.7. The only constraints on each adjacency matrix element A_{ij} are that these weights are symmetric (i.e. $A_{ij} = A_{ji}$) and that there are no weights connecting a vertex to itself A_{ii} or in other words, there are no loops present in G.

Figure 4.3.6: A single Z operator between 2 nodes corresponds to a single edge in the graph state.

Figure 4.3.7: Z^2 operator between two nodes. For qubits $Z^2 = \mathbb{1}$ this is the same as the two nodes being disconnected.

The generalised Clifford group $\mathcal{C}_n$ is the (group-theoretic) normaliser of the Pauli group $\mathcal{P}_n$. In other words it is the group of unitary operators U which map the Pauli group onto itself: $U\mathcal{P}_n U^\dagger = \mathcal{P}_n$. Further, the local Clifford group $\mathcal{C}_n^l \subseteq \mathcal{C}_n$ is the n-fold tensor product of the Clifford group of order one ($\mathcal{C} = \mathcal{C}_1$). When considering the Pauli group acting on qubits, the Clifford group is simply generated by the Hadamard gate H, the phase gate P and the CNOT gate U_{CNOT}. One also notes that under conjugation, a unitary operator U that fixes the stabiliser group S of a quantum error correcting code is an encoded operation. Hence, $S' = USU^\dagger$ implies that $|c'\rangle = U|c\rangle$ is a codeword stabilised by every stabiliser element in S', where $|c\rangle$ is stabilised by every element in S.

As proven in [216], two stabiliser states with generator matrices A and B are equivalent under the action of the local Clifford group if and only if there exist invertible matrices U and Y such that $B = UAY$ and where Y can be represented as

$$Y = \begin{pmatrix} E & F \\ E' & F' \end{pmatrix} \tag{4.3.6}$$

where

$$E = \mathrm{diag}(e_1, \ldots, e_n), \quad F = \mathrm{diag}(f_1, \ldots, f_n), \tag{4.3.7}$$

$$E' = \mathrm{diag}(e'_1, \ldots, e'_n), \quad F' = \mathrm{diag}(f'_1, \ldots, f'_n), \tag{4.3.8}$$

and $e_i f'_i - f_i e'_i = 1 \ \forall i$. Another important result of [216] is that every stabiliser state is equivalent under the action of the local Clifford group to a graph state. This means that one only needs to consider graph states when considering entanglement properties of stabiliser states since for any stabiliser state there will exist an equivalent graph state that shares the same entanglement properties.

Since graph states are a subclass of the stabiliser states, then these arguments trivially hold for all graph states. Diagrammatically, one can claim that two graph states are equivalent under local Clifford transformations if and only if one there exists a sequence consisting of the following operations on a vertex v, such that one can obtain one graph state from the other;

(i) One multiplies the weight of each edge connected to vertex v by $b \in \mathbb{Z}_p$ and $b \neq 0$.

(ii) One transforms the elements of the adjacency matrix as $A_{jk} \to A_{jk} + aA_{vj}A_{vk}$ where

$a \in \mathbb{Z}_p$ and $j \neq k$.

When considering qubits, operation (i) is always just the identity. For $a = 1$, the second operation (ii) is known as local complementation and has been extensively studied [217, 218]. An example of a local complementation of a graph state is shown in Figure 4.3.8. Here the previous graph state, locally Clifford equivalent to AME(6,2) is considered (left graph in Figure 4.3.8) and after applying a local complementation, one obtains a new graph state (right graph in Figure 4.3.8). This new graph state is then still locally Clifford equivalent to AME(6,2) as can be checked using its stabiliser generators.

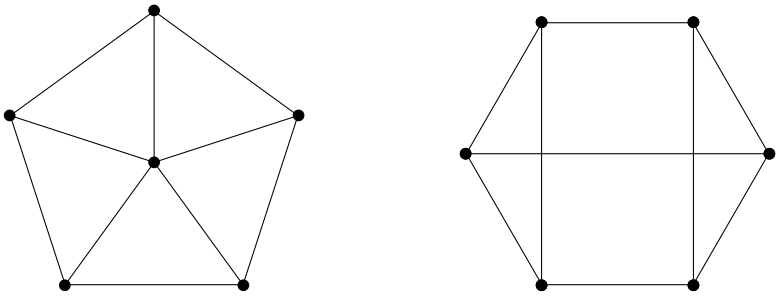

Figure 4.3.8: Two possible graph states that are locally Clifford equivalent to AME(6,2). The two are related by a local complementation.

Key features of the $\{5, 4\}$ tessellation relate to the graph state given in Figure 4.3.5 being an absolutely maximally entangled state represented by the notation AME$(6, 2)$. For those unfamiliar with absolutely maximally entangled (AME) states, a brief review is detailed in section 4.3.3 or, for more detailed discussions, see the expansive literature [208–211, 219]. There are a number of known AME states that have been shown to be locally Clifford equivalent to graph states. A mechanism was developed in [209] for determining bipartite entanglement in graph states and hence being able to determine whether a graph state corresponds to an AME state.

4.3.3 Absolutely Maximally Entangled States

In this section we define an absolutely maximally entangled (AME) state through several equivalent definitions and we summarise a method for testing whether a graph state is AME. Our discussion provides a concise summary of the key results in [209, 219] and more details can be found in these works.

Definition: *An absolutely maximally entangled state $|\Phi\rangle \in \mathcal{H}$ is a pure state consisting of N qudits of local dimension D, with the total Hilbert space $\mathcal{H} \cong (\mathbb{C}^D)^{\otimes N}$. Therefore, $|\Phi\rangle \in \mathcal{H}_1 \otimes \mathcal{H}_2 \otimes \cdots \otimes \mathcal{H}_N$ where $\mathcal{H}_i \cong \mathbb{C}^D$, such that it satisfies the following equivalent properties.*

1. *For any possible bipartition of* $P = \{1, \ldots, N\}$ *into disjoint sets* A *and* B *such that* $A \cup B = P$, $|\Phi\rangle$ *is maximally entangled. That is,* $|\Phi\rangle$ *can be expressed as*

$$|\Phi\rangle = \frac{1}{\sqrt{D^m}} \sum_{k \in \mathbb{Z}_D^m} |k_1\rangle_{B_1} \cdots |k_m\rangle_{B_m} |\phi(k)\rangle_A \,, \tag{4.3.9}$$

where one has assumed $m = |B| \leq |A| = N - m$ *without loss of generality and* $\langle \phi(k) | \phi(k') \rangle = \delta_{kk'}$.

2. *Every possible subset of parties* $A \subset P$ *with* $|A| = \lfloor \frac{N}{2} \rfloor$ *gives rise to a reduced density matrix that is totally mixed;* $\rho_A = D^{-\lfloor \frac{N}{2} \rfloor} \mathbb{1}_{D^{\lfloor \frac{N}{2} \rfloor}}$.

3. *Every possible subset of parties* $A \subset P$ *with* $|A| \leq \frac{N}{2}$ *gives rise to a reduced density matrix that is totally mixed.*

4. *Every possible subset of parties* $A \subset P$ *with* $|A| = \lfloor \frac{N}{2} \rfloor$ *gives rise to a von Neumann entropy that is maximal,* $S(A) = \lfloor \frac{N}{2} \rfloor \log D$.

5. *Every possible subset of parties* $A \subset P$ *with* $|A| \leq \frac{N}{2}$ *gives rise to a von Neumann entropy that is maximal,* $S(A) = |A| \log D$.

   One represents absolutely maximally entangled states defined in this way using the notation AME(N, D).

The method used to distinguish whether a graph state is AME can be explained in the following way. This method was presented in [209]; for a more detailed discussion, we refer the reader to the original paper. In order to proceed, we need to make use of the following definitions:

Definition: *Consider the graph state* $|G\rangle \in \mathcal{H}^{\otimes n}$ *shared between a set of parties* P. *Then for some subset* $K \subset P$, *the state represented by the graph* G *such that all vertices in* K, *and all edges that are connected to the parties in* K, *are removed, define the truncated graph state* $|G^{\setminus K}\rangle$.

Definition: *The i-th row of the* $n \times n$ *adjacency matrix* $A \in \mathbb{Z}_p^{n \times n}$ *can be denoted* $A_i = (A_{i1} \ldots A_{in})$. *One defines the quantity* $A_i \backslash K$ *to be the row vector* A_i *with entries* $\{A_{ik_1} \ldots A_{ik_m}\}$ *removed such that the elements of the subset* $K = \{k_1, k_2, \ldots k_m\}$ *are between* 1 *and* n.

Now suppose we have a graph state $|G\rangle$ with adjacency matrix A and the party subsets $K = \{k_1, k_2, \ldots k_m\}$ with $m = \lfloor \frac{n}{2} \rfloor$. Representing $A_{k_i} \backslash K$ as the k_i-th row of the adjacency matrix with elements $\{A_{k_i k_1} \ldots A_{k_i k_m}\}$ removed, we can show the graph state is absolutely

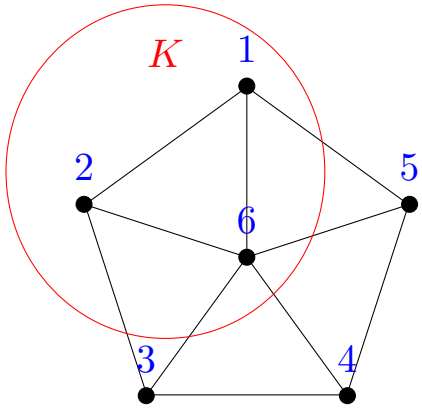

Figure 4.3.9: Bipartition of AME(6,2) into $K = \{1, 2, 6\}$ and $L = \{3, 4, 5\}$.

maximally entangled if and only if the vector quantity $A_{k_i} \backslash K$ are linearly independent in $\mathbb{Z}_p^{n-m}$.

We now turn to the AME(6,2) state and use its corresponding graph state, given in Figure 4.3.5, to show that this state is absolutely maximally entangled. This serves as a concrete example of how one can check whether a graph state is AME and develop understanding of the method involved.

The first question to ask is which bipartitions must be considered. Bipartitions for which one set has just a single node are trivial and will clearly provide linearly independent $A_{k_i} \backslash K$. Hence the only bipartitions that need to be considered are all possible combinations of sets of two nodes (corresponding to four nodes in the other set in the bipartition) and sets of three nodes (corresponding to another three nodes in the other set in the bipartition). One must consider every possible combination of nodes for each of these cases; however using the symmetries in the geometry it is obvious that many of these cases are analogous to each other. For brevity, we only give the example of a single one of these bipartitions visually here to outline the method; similar graphs may be drawn for all other possible bipartitions with $m = \lfloor \frac{n}{2} \rfloor$.

Consider the graph state given in Figure 4.3.5. Here we choose to bipartition the sets into $K = \{1, 2, 6\}$ and $L = \{3, 4, 5\}$, where K has been explicitly drawn in Figure 4.3.9. Calculating the relevant vectors from the edges connecting nodes in K and those in L

$$A_1 \backslash \{1, 2, 6\} = (0, 0, 1) \tag{4.3.10}$$

$$A_2 \backslash \{1, 2, 6\} = (1, 0, 0) \tag{4.3.11}$$

$$A_6 \backslash \{1, 2, 6\} = (1, 1, 1). \tag{4.3.12}$$

These three vectors are clearly linearly independent of one another.

Due to the symmetries of the geometry, we would obtain this result for any bipartition consisting of two nodes that are next to each other on the outer pentagon and the centre node. There are obviously more possible bipartitions into two sets of three but these can all be reduced to one of the following due to the symmetry; $K = \{1, 2, 3\}$ and $L = \{4, 5, 6\}$, $K = \{1, 3, 6\}$ and $L = \{2, 4, 5\}$ or $K = \{1, 2, 4\}$ and $L = \{3, 5, 6\}$. The vectors obtained from these cases are given in Table 4.3.10, where we have grouped the three cases into the three columns of equations. Note that each column's vectors are linearly independent and so all bipartitions that split the graph into two sets of three give the correct result.

Case 1: $K = \{1, 2, 3\}$	Case 2: $K = \{1, 3, 6\}$	Case 3: $K = \{1, 2, 4\}$
$A_1 \backslash \{1, 2, 3\} = (0, 1, 1)$	$A_1 \backslash \{1, 3, 6\} = (1, 0, 1)$	$A_1 \backslash \{1, 2, 4\} = (0, 1, 1)$
$A_2 \backslash \{1, 2, 3\} = (0, 0, 1)$	$A_3 \backslash \{1, 3, 6\} = (1, 1, 0)$	$A_2 \backslash \{1, 2, 4\} = (1, 0, 1)$
$A_3 \backslash \{1, 2, 3\} = (1, 0, 1)$	$A_6 \backslash \{1, 3, 6\} = (1, 1, 1)$	$A_4 \backslash \{1, 2, 4\} = (1, 1, 1)$

Table 4.3.10: Remaining bipartitions of AME(6,2) where K and L both contain 3 elements.

Now we consider the case of bipartitions into one set of two elements and one set of four elements. All possible cases can once again be reduced due to symmetry, in this case, to three simple bipartitions; $K = \{1, 2\}$ and $L = \{3, 4, 5, 6\}$, $K = \{1, 3\}$ and $L = \{2, 4, 5, 6\}$ or $K = \{1, 6\}$ and $L = \{2, 3, 4, 5\}$. The vectors are presented in Table 4.3.11, where they have once again been placed in columns for each bipartition, and in each column we trivially have linearly independent vectors for each possible bipartition. Hence for all possible bipartitions of the AME(6,2) graph state given in Figure 4.3.5, each $A_{k_i} \backslash K$ is linearly independent for all choices of $K = \{k_1, \ldots, k_m\}$ with $m = \lfloor \frac{n}{2} \rfloor$. Therefore the state is indeed absolutely maximally entangled.

Case 1: $K = \{1, 2\}$	Case 2: $K = \{1, 3\}$	Case 3: $K = \{1, 6\}$
$A_1 \backslash \{1, 2\} = (0, 0, 1, 1)$	$A_1 \backslash \{1, 3\} = (1, 0, 1, 1)$	$A_1 \backslash \{1, 6\} = (1, 0, 0, 1)$
$A_2 \backslash \{1, 2\} = (1, 0, 0, 1)$	$A_3 \backslash \{1, 3\} = (1, 1, 0, 1)$	$A_6 \backslash \{1, 6\} = (1, 1, 1, 1)$

Table 4.3.11: Remaining bipartitions of AME(6,2) where K contains 2 elements and L contains 3 elements.

Given the graph state formulation of the AME(6,2) state, one may illustrate the importance of using AME states and connecting them with quantum error correcting codes. Firstly, it is well known that any AME state AME(N, D) is equivalent to a pure $[[N, 0, \lfloor N/2 \rfloor + 1]]_D$ quantum error correcting code [220]. Further, every pure $[[N, k, d]]$ code with $N, d \geq 2$ gives rise to a family of pure codes $[[N - i, k + i, d - i]]$ where $i = \{0, \ldots d - 1\}$ [221]. From the graph in Figure 4.3.5, one may describe the full

stabiliser group by a column vector of stabiliser generators found using 4.3.4;

$$\mathcal{S} = \begin{bmatrix} G_1 \\ G_2 \\ G_3 \\ G_4 \\ G_5 \\ G_6 \end{bmatrix} = \begin{bmatrix} X & Z & I & I & Z & Z \\ Z & X & Z & I & I & Z \\ I & Z & X & Z & I & Z \\ I & I & Z & X & Z & Z \\ Z & I & I & Z & X & Z \\ Z & Z & Z & Z & Z & X \end{bmatrix} \simeq \begin{bmatrix} X & Z & Z & X & I & I \\ I & X & Z & Z & X & I \\ X & I & X & Z & Z & I \\ Z & X & I & X & Z & I \\ X & X & X & X & X & X \\ Z & Z & Z & Z & Z & Z \end{bmatrix} = \mathcal{S}' \tag{4.3.13}$$

where in the second step one has used basic matrix manipulations including Gaussian elimination as well as performing a transformation under the action of the local Clifford group on the final qubit. This particular transformation came using the Hadamard gate which has the following effect on the Pauli matrices; $X \to HXH^\dagger = Z$, $Y \to HYH^\dagger = -Y$, $Z \to HZH^\dagger = X$.

The form given by $\mathcal{S}'$ in 4.3.13 is the most common presentation of the stabiliser generators for AME(6,2) in the literature and is the one presented in [1]. Thus, for clarity, the graph state in Figure 4.3.5 is locally Clifford equivalent to AME(6,2) as indicated by the use of the symbol '$\simeq$'. To make the connection with the perfect tensor construction in HaPPY, we rewrite $\mathcal{S}'$ in the following way;

$$\mathcal{S}' = \begin{bmatrix} -Y & Z & Y & I & I & Z \\ -Z & X & Z & I & I & X \\ Y & Y & Z & I & Z & I \\ Z & Z & X & I & X & I \\ -Z & Y & Y & Z & I & I \\ X & Z & Z & X & I & I \end{bmatrix}, \quad \begin{matrix} (3 \cdot 6) \\ (2 \cdot 3 \cdot 4 \cdot 5) \\ (1 \cdot 4) \\ (1 \cdot 2 \cdot 3 \cdot 4) \\ (1 \cdot 3 \cdot 4) \\ (1) \end{matrix} \tag{4.3.14}$$

where we have used row multiplication, indicated by the bracketed expression to the right of each stabiliser generator where each number denotes the original stabiliser generator multiplied. Note that due to the fact operators are implicitly connected via tensor products we have simply pulled any overall negative sign of each generator to the front.

The stabiliser matrix in the form (4.3.14) can be shown to correspond to a quantum error correcting code by removing the last qubit, as detailed in [78], converting an $[[n, k, d]]$ code into an $[[n-1, k+1, d-1]]$. In the specific example above this translates a $[[6, 0, 4]]$ state into a $[[5, 1, 3]]$ code. To summarise the construction, one chooses $n-k$ generators such that G_1 ends in Z and G_2 ends in X with the remaining generators $G_3, \ldots, G_{n-k}$ ending with the identity I. Dropping G_1 and G_2 allows a new stabiliser to form from the final $n-k-2$ generators. Now, restricting G_1 and G_2 to act only on the first $n-1$ qubits one can show these now become the logical operators $\bar{Z}$ and $\bar{X}$. The resulting $[[5, 1, 3]]$ code is expressed in Table 4.3.12.

G'_1	$YYZIZ$
G'_2	$ZZXIX$
G'_3	$-ZYYZI$
G'_4	$XZZXI$
$\bar{X}_1$	$-ZXZII$
$\bar{Z}_1$	$-YZYII$

Table 4.3.12: The $[[5,1,3]]_2$ code derived from the AME$(6,2)$ state.

G''_1	$-ZYYZ$
G''_2	$XZZX$
$\bar{X}'_1$	$-ZXZI$
$\bar{X}'_2$	$ZZXI$
$\bar{Z}'_1$	$-YZYI$
$\bar{Z}'_2$	$YYZI$

Table 4.3.13: The $[[4,2,2]]_2$ code derived from the $[[5,1,3]]_2$ code.

$\bar{X}''_1$	$-ZXZ$
$\bar{X}''_2$	ZZX
$\bar{X}''_3$	XZZ
$\bar{Z}''_1$	$-YZY$
$\bar{Z}''_2$	YYZ
$\bar{Z}''_3$	$-ZYY$

Table 4.3.14: The $[[3,3,1]]_2$ code derived from the $[[4,2,2]]_2$ code.

Trivially, from the form presented in (4.3.14), one could continue this process converting the $[[5,1,3]]$ code into a $[[4,2,2]]$ code (given in Table 4.3.13) and then even into a $[[3,3,1]]$ code (given in Table 4.3.14). Note that after the case of the $[[3,3,1]]$ code, one can not reduce this further since no stabiliser generators remain.

While any AME state AME(N,D) is equivalent to a pure $[[N,0,\lfloor N/2\rfloor+1]]_D$ quantum error correcting code, the concept of the resultant quantum error correcting code producing further codes was explored in [222]. The result is that, every N-qudit stabiliser AME state generates at least $\left\lfloor \frac{N}{2} \right\rfloor$ different stabiliser codes. In each of these codes, $m \in \{1,\ldots,\left\lfloor \frac{N}{2} \right\rfloor\}$ logical qudits are encoded into $N-m$ physical qudits.

4.3.4 Perfect Tensors

We now explain the relationship between AME states and perfect tensors, an important relation in the construction of the holographic codes presented in [1]. This provides the method used to concatenate AME states across the entire tessellation, forming a tensor network. This construction provides an isometric mapping from the uncontracted legs in the bulk to the uncontracted legs at the boundary of the geometric manifold and will be

explained further in Section 4.3.5. To begin we define a perfect tensor.

Perfect tensors naturally arise when considering AME states. One can always decompose an AME state into two subsystems $\mathcal{H}_A$ and $\mathcal{H}_B$ as

$$|\Phi\rangle = \sum_{a,b} T_{ab} |a\rangle |b\rangle , \tag{4.3.15}$$

such that $T : \mathcal{H}_A \to \mathcal{H}_B$ is a unique linear map between the two Hilbert spaces represented by a two-index tensor with

$$T : |a\rangle \to \sum_b |b\rangle T_{ba}. \tag{4.3.16}$$

Here one denotes the complete orthonormal basis $\{|a\rangle\}$ for $\mathcal{H}_A$ and similarly, $\{|b\rangle\}$ for $\mathcal{H}_B$. This map also preserves all inner products; i.e.

$$\sum_b T^\dagger_{a'b} T_{ba} = \delta_{a'a}. \tag{4.3.17}$$

Hence, each of these linear transformations applied to an AME state may be thought of as an isometry. Thus one defines the tensors associated with the isometry, isometric tensors. Similarly, the converse is true. Provided one has a perfect tensor, then one similarly has a corresponding AME state.

Definition: *Suppose one bipartitions the indices of a $2n$-index tensor $T_{a_1 a_2 \ldots a_{2n}}$ into one set A and its complementary set A^c with $|A| \leq |A^c|$. Then, T is a perfect tensor if it is proportional to an isometric tensor from A and A^c, i.e.*

$$\sum_{a_{n+1}\ldots a_{2n}} T^\dagger_{a_1 \ldots a_n a_{n+1} \ldots a_{2n}} T_{a_{n+1}\ldots a_{2n} b_1 \ldots b_n} = \delta_{a_1 b_1} \ldots \delta_{a_n b_n}, \tag{4.3.18}$$

where one may choose any of the $2n$ legs of the tensor to be $a_{n+1} \ldots a_{2n}$.

Since one can show that for every possible bipartition, one may use isometric tensors to define the transformations, then every AME state defines a perfect tensor. Each tensor can then be placed in each polytope of the tessellation, connected by the outgoing physical legs (across the facets) which represent the contraction of the tensor indices.

4.3.5 Concatenation and building a tensor network

Here we explain the concatenation process of AME states which results in an isometric mapping from the uncontracted legs in the bulk to the uncontracted legs at the boundary through a tensor network built from perfect tensors. We summarise here the case for two AME states but concatenations of one AME state and one not-necessarily AME state were explored in [222]. First we note that any AME state can always be expressed such that

for each of the final m columns, one only has a single X operator, a single Z operator and everywhere else is the identity [222]; relating to the statement at the end of Section 4.3.3. The two stabiliser generators that have the X and Z operators acting on a particular qudit, where all other generators act trivially are the logical operators encoding one qudit.

Now, consider two AME stabiliser states, denoted as left (L) and right (R) states defined on N_L and N_R qudits respectively. One can represent an L state as a tensor product of the form $L_i \otimes \sigma_i$, for $i = 1, \ldots, N_L$. Here L_i denotes a tensor product of Pauli operators on qudits l_1 to l_{N_L-1} and σ_i is the Pauli operator individual qudit l_{N_L}. One can similarly define the R state using the tensor product $\sigma_j \otimes R_j$ where $j = 1, \ldots, N_R$, with σ_j acting on qudit r_1 and R_j acting on qudits $r_2 \ldots r_{N_R}$. Then, concatenating these two states, the joint state $N_L + N_R$ can be expressed as the first matrix in 4.3.19.

$$\begin{pmatrix} & L_1 & I & I & \ldots & I \\ & L_2 & I & I & \ldots & I \\ & \vdots & \vdots & \vdots & \ddots & \vdots \\ & L_{N_L-2} & I & I & \ldots & I \\ & L_{N_L-1} & X & I & \ldots & I \\ & L_{N_L} & Z & I & \ldots & I \\ I & \ldots & I & Z & R_1 & \\ I & \ldots & I & X & R_2 & \\ I & \ldots & I & I & R_3 & \\ \vdots & \ddots & \vdots & \vdots & \vdots & \\ I & \ldots & I & I & R_{N_R-1} & \\ I & \ldots & I & I & R_{N_R} & \end{pmatrix} \xrightarrow{XX} \begin{pmatrix} & L_1 & I & I & \ldots & I \\ & L_2 & I & I & \ldots & I \\ & \vdots & \vdots & \vdots & \ddots & \vdots \\ & L_{N_L-2} & I & I & \ldots & I \\ & L_{N_L-1} & X & I & \ldots & I \\ & L_{N_L} & Z & Z & R_1 & \\ I & \ldots & X & X & \ldots & I \\ I & \ldots & I & X & R_2 & \\ I & \ldots & I & I & R_3 & \\ \vdots & \ddots & \vdots & \vdots & \vdots & \\ I & \ldots & I & I & R_{N_R-1} & \\ I & \ldots & I & I & R_{N_R} & \end{pmatrix} \xrightarrow{ZZ} \begin{pmatrix} & L_1 & I & I & \ldots & I \\ & L_2 & I & I & \ldots & I \\ & \vdots & \vdots & \vdots & \ddots & \vdots \\ & L_{N_L-2} & I & I & \ldots & I \\ & L_{N_L-1} & X & X & R_2 & \\ & L_{N_L} & Z & Z & R_1 & \\ I & \ldots & X & X & \ldots & I \\ I & \ldots & Z & Z & \ldots & I \\ I & \ldots & I & I & R_3 & \\ \vdots & \ddots & \vdots & \vdots & \vdots & \\ I & \ldots & I & I & R_{N_R-1} & \\ I & \ldots & I & I & R_{N_R} & \end{pmatrix}. \tag{4.3.19}$$

One then performs two different measurements to obtain the second and third matrices in (4.3.19). Recall that the process one undergoes after performing a measurement to update the list of generators of a stabiliser state is the following [72]:

- There is no need to update the list if the measured observable may be constructed from a product of the stabiliser generators.

- If the measured observable commutes with all the generators of the stabiliser, however cannot be constructed from these generators, one adds this observable to the list of generators (with a phase factor determined from the outcome of the measurement).

- If the measured observable does not commute with at least one stabiliser generator and cannot be constructed from these generators, one replaces one non-commuting generator with the measured observable (with a phase factor determined from the outcome of the measurement). One then multiplies all other generators that do not commute with the measured observable and multiply them with the generator that was removed from the list.

Now in (4.3.19) one first performs a measurement of the observable XX on qudits l_{N_L} and r_1 (assuming the outcome is $+1$). Clearly there are two generators that do not commute with this observable, those being the generators that have Z operators acting on either qudit l_{N_L} or r_1. Hence one updates the list using the above rules, replacing one of the non-commuting stabiliser generators by the measured observable before multiplying the other non-commuting generator by the one that was removed.

One then performs a similar measurement, this time measuring the observable ZZ, on the same pair of qudits. The result is indicated on the right hand side of (4.3.19). One can now see maximal entanglement between qudits l_{N_L} and r_1 with no relation to any of the other qudits present in the system. One therefore may trace these qudits out, removing the corresponding rows and columns from the matrix:

$$\rightarrow \left(\begin{array}{ccccc} L_1 & I & I & \dots & I \\ L_2 & I & I & \dots & I \\ \vdots & \vdots & \vdots & \ddots & \vdots \\ L_{N_L-2} & I & I & \dots & I \\ L_{N_L-1} & X & X & R_2 & \\ L_{N_L} & Z & Z & R_1 & \\ \cancel{I} & \cancel{\dots} & \cancel{X} & \cancel{X} & \cancel{\dots} \; \cancel{I} \\ \cancel{I} & \cancel{\dots} & \cancel{Z} & \cancel{Z} & \cancel{\dots} \; \cancel{I} \\ I & \dots & I & I & R_3 \\ \vdots & \ddots & \vdots & \vdots & \vdots \\ I & \dots & I & I & R_{N_R-1} \\ I & \dots & I & I & R_{N_R} \end{array}\right) \rightarrow \left(\begin{array}{ccccc} & L_1 & I & \dots & I \\ & L_2 & I & \dots & I \\ & \vdots & \vdots & \ddots & \vdots \\ & L_{N_L-2} & I & \dots & I \\ & L_{N_L-1} & R_2 & & \\ & L_{N_L} & R_1 & & \\ I & \dots \; I & R_3 & & \\ \vdots & \ddots \; \vdots & \vdots & & \\ I & \dots \; I & R_{N_R-1} & & \\ I & \dots \; I & R_{N_R} & & \end{array}\right). \quad (4.3.20)$$

In the case where the local dimension of the qudit is $D = 2$ (i.e. one is considering qubits), as in the HaPPY construction, these maximally entangled pairs correspond to EPR pairs. The final matrix on the right hand side of (4.3.20) is therefore the list of stabiliser generators created as a result of performing entanglement swapping on a pair of qudits shared between the two AME states L and R. Firstly, this consists of many of the original stabiliser generators of R and L that act non-trivially on qudits within their original domain, but have been extended to act trivially on those outside of their original domain. Secondly, one has two truncated rows, $(L_{N_L-1}R_2)$ and $(L_{N_L}R_1)$. Recall, that for the AME state R, a single qudit is encoded into $N_R - 1$ qudits by the logical X and Z operators, which are R_1 and R_2. Thus from (4.3.20), one can see that entanglement swapping across AME states is equivalent to concatenating the corresponding quantum error correcting codes that arise from these states.

Hence if we consider the full tessellation, we may use entanglement swapping between two AME states to concatenate the quantum codes described by them. Expanding the network by adding more AME states (or equivalently perfect tensors), filling the tessellation, builds the final holographic code by concatenating all of the codes that arise from each AME state.

We can also view this as concatenating perfect tensors resulting in a tensor network that builds an encoding isometry across the geometric manifold for the holographic code. In the perfect tensor language, isometries can be understood as follows. We simply choose which indices (legs) of the tensor are incoming and which are outgoing. Usually one interprets the logical qudit as an incoming leg as well as those legs that are output legs from previous tensors.

As an example, for the AME(6,2) state, one may have 0, 1, 2 or 3 incoming legs (including the uncontracted bulk leg corresponding to the logical qudit). Now, suppose one chooses that the only input leg is the logical qudit so there are five outgoing legs. This corresponds to the $[[5, 1, 3]]_2$ code encoding one logical qudit to five physical qudits. However if one considers two input legs, then one would have the stabilisers for the $[[4, 2, 2]]_2$ code. Thus, each encoding isometry corresponds to the number of logical qudits being encoded within each AME state.

Hence, by concatenating the AME states, one analogously contracts the perfect tensors building a tensor network. From the perfect tensor perspective, one is simply concatenating the isometries of each perfect tensor layer by layer. From the AME state point of view, one can see this is due to entanglement swapping between pairs of qudits, as this section has detailed. Clearly the product of isometries is simply an isometry itself. Hence the tensor network acts as a mapping from the logical qudits in the bulk to the physical qudits at the boundary. Similarly to the isometries for individual AME states, this isometry then corresponds to the encoding transformation of the holographic code.

4.4 The HaPPY Construction in higher dimensions

In section 4.3.1 we discussed how we can associate stabiliser generators to the $\{5, 4\}$ tessellation of the spatial slices of AdS_3. Then, one concatenates these AME states using EPR pairs building a tensor network (using perfect tensors) that acts as an exactly solvable toy model for AdS_3/CFT_2. To extend this construction to higher dimensions we need to consider in turn the following steps of the construction:

1. **Tessellation:** Find a tessellation for the spatial slices of AdS_{d+1} to discretise the hyperbolic geometry.

2. **Associate qudits to the geometry:** One should place both the logical and physical qudits onto the tessellated hyperbolic geometry. It should be noted that in the case of AdS_3, there are two possible choices for the physical qudits - either placed on the vertices or edges of the polygons. In HaPPY, one chooses to place them on edges in order to concatenate via EPR pairs. While there are more choices of cellulations as the dimension is increased (as can be visualised by the corresponding Hasse diagram), in order to maintain the concatenation principles in HaPPY, one should associate the logical qudit with the tessellated d-dimensional polytope itself and physical qudits with the $d-1$ dimensional facet. For example, when considering the spatial slices of AdS_4, one tessellates H^3 with three-dimensional polyhedra associating the logical qudit with the polyhedra and one physical qudit with each of its two-dimensional faces.

3. **Find the corresponding graph state:** Once the qudits have been associated to the geometry, one can build a graph state as explained in section 4.3.1. We will see that it is at this step that one is forced to drop one of the assumptions implicit in the two-dimensional HaPPY construction.

4. **Build the tensor network:** Provided the previous steps have been accomplished, one may straightforwardly build the tensor network using perfect tensors if AME states have been used.

In this section we explore whether and how this formulation generalises to higher dimensions and propose several possibilities of how to overcome potential obstructions. While we focus specifically on the HaPPY construction, analogous steps would need to be followed in generalising other approaches to holographic codes to higher dimensions and we will return to this point at the end of this section.

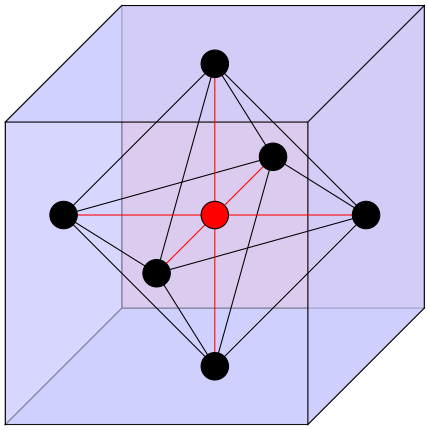

Figure 4.4.1: Qudits placed on a cube in H^3. Here, the one logical qudit associated to the cube is represented by being placed in it's centre and the six physical qudits are placed on faces.

4.4.1 AdS_4: Order-5 cubic honeycomb

A first step towards generalising the HaPPY approach to higher spacetime dimensions is the case of AdS_4. We begin by considering spatial slices given by hyperbolic 3-spaces H^3; regular tessellations of H^3 were summarised in Table 4.2.1. The simplest option to visualise would clearly be the order-5 cubic honeycomb with Schläfi symbol $\{4, 3, 5\}$ since the tessellated polyhedron is just the cube. We begin this section by trying to replicate the HaPPY approach of 4.4.1.1, before drawing the conclusion that the resultant graph state would not be AME. We then relax the assumption of preserving maximal discrete symmetry in 4.4.1.2 and force the graph state to be AME to provide an alternate construction.

4.4.1.1 Non-AME state

As noted in step 2 above, we can associate a single logical qudit to the centre of the cube and place physical qudits at each of the faces. To associate a graph state with this tessellation, it is natural to try to preserve maximal discrete symmetry as in the HaPPY approach. This means that if two faces are connected by an edge then the two physical qudits living on these faces should be considered as connected in the graph state. If faces are not connected by an edge, they are not connected. The logic of how the graph state is formed is illustrated diagrammatically in Figure 4.4.1. The graph drawn in three dimensions can then be compressed to two dimensions, as shown in Figure 4.4.2, so that it is in the standard representation of a graph state.

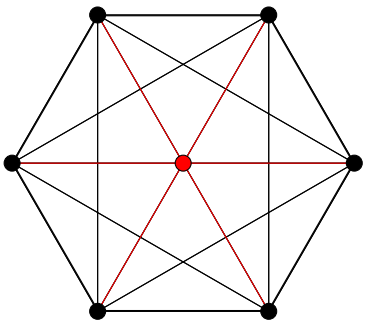

Figure 4.4.2: Resultant graph state for the cube, following the HaPPY approach, that preserves maximal discrete symmetry.

By construction, since any graph state is by definition a stabiliser state, then Figure 4.4.2 is a stabiliser state. Unfortunately, constructing the state in this way does not give rise to an AME state. This can be shown straightforwardly using the techniques explained in the previous section. We draw the graph state as before and choose the partition $\{0, 3, 6\}|\{1, 2, 4, 5\}$ as indicated in Figure 4.4.3.

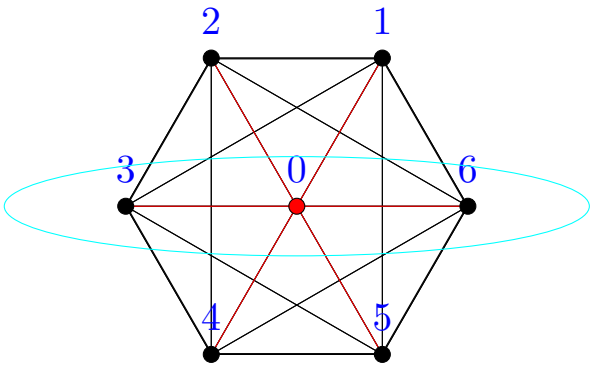

Figure 4.4.3: Bipartition of the graph state associated with the cube that preserves maximal discrete symmetry. Here the partition is chosen as $K = \{0, 3, 6\}$ and $L = \{1, 2, 4, 5\}$. The resultant equations are not linearly independent and thus this graph state is not AME.

Following the approach described in the previous section, one then obtains

$$A_0 \backslash \{0, 3, 6\} = (1, 1, 1, 1), \tag{4.4.1}$$
$$A_3 \backslash \{0, 3, 6\} = (1, 1, 1, 1), \tag{4.4.2}$$
$$A_6 \backslash \{0, 3, 6\} = (1, 1, 1, 1), \tag{4.4.3}$$

but these are not linearly independent and hence this graph state is not AME. In fact, this was to be expected since it has been shown in the literature that no AME state exists for 7 qubits or more [210]. This generic result indicates that extensions of the HaPPY construction to higher dimensions necessarily require a variation of the approach used in two dimensions.

The classifications of [210] show that one can have an AME state for 7 qudits or more for $D > 2$. This is possible since for $D > 2$ one can have multiple Z operators between qudits. The immediate issue in exploiting such AME states for our purposes is the difficulty in maintaining maximal discrete symmetry. To maintain the discrete symmetry, if one uses multiple Z operators between any pair of qudits, one has to do so everywhere. The immediate consequence of this is that none of these states can be AME since when considering $\lambda \in \{1, \ldots, D-1\}$ Z operators between D-dimensional qudits,

$$A_0 \backslash \{0, 3, 6\} = \lambda(1, 1, 1, 1), \tag{4.4.4}$$
$$A_3 \backslash \{0, 3, 6\} = \lambda(1, 1, 1, 1) \tag{4.4.5}$$
$$A_6 \backslash \{0, 3, 6\} = \lambda(1, 1, 1, 1) \tag{4.4.6}$$

which can never be linearly independent of one another. This of course generalises for $n \geq 7$ qudits: since no 7 qubit or higher AME state can exist, no maximally symmetric construction can be formed such that the graph state is AME. Hence, in dimensions $d > 2$,

one is either restricted to tessellations such that the d-dimensional polytope has $n < 7$ $(d-1)$-dimensional facets or one lifts one of the previous assumptions.

Since Figure 4.4.2 is not AME, there is now no longer a guarantee that it represents a quantum error correcting code. In order to check that this construction does indeed correspond to a graph code, we use the following theorem developed by Schlingermann and Werner [223]:

SW-theorem: *Consider a set of input vertices X and a set of output vertices Y. Then, given a finite abelian group G and the weighted graph with adjacency (coincidence) matrix Ξ, a quantum error correcting code v_Ξ is able to detect an error configuration $\mathcal{E} \subset Y$ iff*

$$\Xi^{I}_{X\cup\mathcal{E}} d^{X\cup\mathcal{E}} = 0 \tag{4.4.7}$$

with $I = Y\backslash\mathcal{E}$ implies

$$d^{X} = 0, \quad \textit{and} \quad \Xi^{X}_{\mathcal{E}} d^{\mathcal{E}} = 0. \tag{4.4.8}$$

Here, we focus on the simplest case with local dimension $D = 2$. The input vertices X refer to the single logical qubit in the centre of the polytope and the output vertices are the six physical qubits. The full 7×7 symmetric coincidence matrix Ξ [224], that describes the connectivity of the entire graph, inclusive of both input and output vertices is given by:

$$\Xi_{[[6,1,2]]} = \begin{bmatrix} 0 & 1 & 1 & 1 & 1 & 1 & 1 \\ 1 & 0 & 1 & 1 & 0 & 1 & 1 \\ 1 & 1 & 0 & 1 & 1 & 0 & 1 \\ 1 & 1 & 1 & 0 & 1 & 1 & 0 \\ 1 & 0 & 1 & 1 & 0 & 1 & 1 \\ 1 & 1 & 0 & 1 & 1 & 0 & 1 \\ 1 & 1 & 1 & 0 & 1 & 1 & 0 \end{bmatrix}, \tag{4.4.9}$$

and thus the 6×6 adjacency matrix Γ, describing the graph state of just the output vertices may be represented as

$$\Gamma = \begin{bmatrix} 0 & 1 & 1 & 0 & 1 & 1 \\ 1 & 0 & 1 & 1 & 0 & 1 \\ 1 & 1 & 0 & 1 & 1 & 0 \\ 0 & 1 & 1 & 0 & 1 & 1 \\ 1 & 0 & 1 & 1 & 0 & 1 \\ 1 & 1 & 0 & 1 & 1 & 0 \end{bmatrix}. \tag{4.4.10}$$

We can then write down the stabiliser generators associated with the graph state of the output vertices given in Figure 4.4.2, following the techniques previously introduced.

This gives

$$\mathcal{S} = \begin{bmatrix} G_0 \\ G_1 \\ G_2 \\ G_3 \\ G_4 \\ G_5 \\ G_6 \end{bmatrix} = \begin{bmatrix} X & Z & Z & Z & Z & Z & Z \\ Z & X & Z & Z & I & Z & Z \\ Z & Z & X & Z & Z & I & Z \\ Z & Z & Z & X & Z & Z & I \\ Z & I & Z & Z & X & Z & Z \\ Z & Z & I & Z & Z & X & Z \\ Z & Z & Z & I & Z & Z & X \end{bmatrix}. \tag{4.4.11}$$

Recall the following procedure to convert an $[[n, k, d]]$ code into an $[[n-1, k+1, d-1]]$ code: one performs standard matrix manipulations to obtain one stabiliser generator G_X ending with X, one stabiliser generator G_Z ending with Z and $n-k$ generators ending with the identity I. Then by dropping G_X and G_Z and removing the final qubit, we will be left with a stabiliser code formed from the remaining $n-k-2$ generators. The resultant code has distance $d-1$ and thus encodes $(n-1)-(n-k-2) = k+1$ qubits. Hence by performing this analysis on the stabiliser generators for the $[[7, 0]]$ state (4.4.11), we can show the stabiliser generators for the $[[6, 1]]$ code are:

$$\mathcal{S} = \begin{bmatrix} G'_0 \\ G'_1 \\ G'_2 \\ G'_3 \\ G'_4 \end{bmatrix} = \begin{bmatrix} X & I & I & X & I & I \\ I & X & I & I & X & I \\ I & I & X & I & I & X \\ Y & -Y & I & Z & Z & I \\ Y & I & -Y & Z & I & Z \end{bmatrix} \tag{4.4.12}$$

and the corresponding logical operators are given by $\bar{Z} = ZZZZZZ$, $\bar{X} = XZZIZZ$.

In order to see whether Figure 4.4.2 realises a one-error correcting code, with one input vertex and six output vertices, we apply error detection (correction) conditions given in the SW-theorem to the $\binom{6}{2} = 15$ two-error correction configurations. These are denoted $\mathcal{E}_j$ with $j \in \{1, \ldots, 15\}$ and are defined as

$$\mathcal{E}_1 = \{0,1,2\},\ \mathcal{E}_2 = \{0,1,3\},\ \mathcal{E}_3 = \{0,1,4\},\ \mathcal{E}_4 = \{0,1,5\},\ \mathcal{E}_5 = \{0,1,6\}, \tag{4.4.13}$$

$$\mathcal{E}_6 = \{0,2,3\},\ \mathcal{E}_7 = \{0,2,4\},\ \mathcal{E}_8 = \{0,2,5\},\ \mathcal{E}_9 = \{0,2,6\},\ \mathcal{E}_{10} = \{0,3,4\}, \tag{4.4.14}$$

$$\mathcal{E}_{11} = \{0,3,5\},\ \mathcal{E}_{12} = \{0,3,6\},\ \mathcal{E}_{13} = \{0,4,5\},\ \mathcal{E}_{14} = \{0,4,6\},\ \mathcal{E}_{15} = \{0,5,6\}. \tag{4.4.15}$$

For example, consider the error configuration $\mathcal{E}_1 = \{0,1,2\}$. The resulting set of equations from (4.4.7) are given in Table 4.4.4. Solving this set of relations results in $d_0 = d_1 = d_2 = d_3 = 0$ and thus by the SW-theorem, the error configuration $\mathcal{E}_1$ is a detectable error configuration. Following this logic, one can repeat this analysis for the remaining possible error configurations. The result of this calculation is that there are three problematic error configurations: $\mathcal{E}_3, \mathcal{E}_8$ and $\mathcal{E}_{12}$.

Vertex	Equation
3	$d_0 + d_1 + d_2 = 0$
4	$d_0 + d_2 = 0$
5	$d_0 + d_1 = 0$
6	$d_0 + d_1 + d_2 = 0$

Table 4.4.4: Set of equations for error configuration $\mathcal{E}_1$.

As in [78], a quantum code with stabiliser S will detect all errors $\mathcal{E}$ that are either in S or anticommute with at least one element in S (i.e. $\mathcal{E} \in S \cup (\mathcal{P}_n - N(S))$). For each of the problematic error configurations, three error operators exist that do not anticommute with at least one element in S, namely XX, YZ and ZY. Consider the first set of these operators; X_1X_4, X_2X_5 and X_3X_6, where the subscript refers to which qubit an operator acts upon. Each of these three operators is clearly an element of the stabiliser, as can be trivially read off from (4.4.12). Since these error operators belong to the stabiliser of the code; $X_1X_4, X_2X_5, X_3X_6 \in S$, they have no impact on the encoded state.

However, the remaining six two-error operators,

$$Y_1Z_4, \quad Z_1Y_4, \quad Y_2Z_5, \quad Z_2Y_5, \quad Y_3Z_6, \quad Z_3Y_6, \tag{4.4.16}$$

cannot be corrected for. Thus not all two-error configurations are either detectable or act trivially on the encoded state and so the graph state given in Figure 4.4.2 is a quantum error correcting code with distance $d = 2$, which we denote as $[[6, 1, 2]]_2$. Further evidence is provided by the Knill-Laflamme bound [165]

$$n \geq 2(d - 1) + k, \tag{4.4.17}$$

which in this instance reduces to the statement that the code distance must satisfy $d \leq 3$. We also note that for any quantum stabiliser code with distance d that if S contains elements of weight less than d, then it is a degenerate code. Since the minimum weight operator in S is a weight-2 operator (e.g. $X_1X_4 \in S$) and $d = 2$, the $[[6, 1, 2]]_2$ code presented here is non-degenerate.

The next step is to tessellate the full spatial slices of AdS_4 in the form of the order-5 cubic honeycomb, tessellating cubes by associating labels to each face and consistently gluing together them together. Since our code is not AME, we need to be careful to ensure that the concatenation is consistent. In [38], the authors create a consistent construction of the $\{7, 4\}$ tessellation of the spatial slice of AdS_3 using block-perfect tensors. Essentially the tessellation is constructed in levels, with the first level being some central heptagon, the second level being all adjacent heptagons to those in the first level and so on. We adapt this approach in the following construction of the concatenation of cells, so let us first describe how this works.

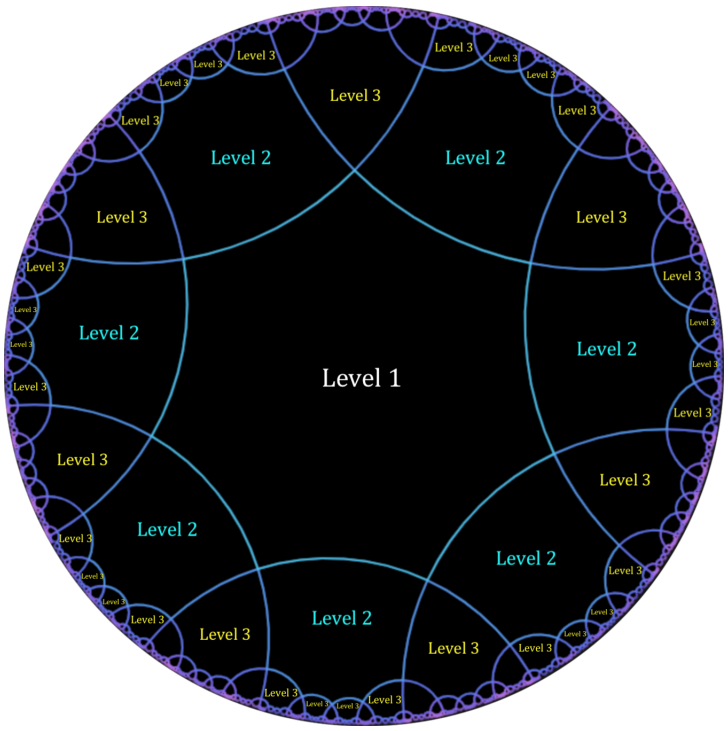

Figure 4.4.5: $\{7,4\}$ tessellation of hyperbolic plane H^2. One shows subsequent levels beginning from some central polytope defined to be at level $L = 1$ and adding a level for each polytope adjacent to a polytope at the previous level.

For every heptagon h_L at level L, one assigns the set of labels e_i with $i \in \{1, \ldots, 7\}$ to its edges. For every i, the labelled edge e_i at level L must then be glued to some other edge of a heptagon at level L'. In this instance, for each i, L' must be either level $L-1$ or $L+1$ but it cannot be both simultaneously. Thus all edges labelled e_i at level L are glued to the same level L'.

As an example, look at level $L = 2$ in [38]. Each edge e_6 is glued to an edge in level 1 $(L-1)$. Similarly, edges e_j with $j = \{1, 2, 3, 4, 5, 7\}$ at level $L = 2$ are always glued to an edge at level 3 $(L+1)$. A sketch depicting the levels in this example is shown in Figure 4.4.5.

Note, when one reaches level $L = 3$, one encounters an issue. There is an inconsistency of edges connecting to other levels. Some $L = 3$ heptagons are adjacent to two $L = 2$ heptagons and five $L = 4$ heptagons while others are only connected to one level $L = 2$ heptagons and six $L = 4$ heptagons. Fortunately, there is a simple fix for this. One simply treats the two cases to be distinct, as if they were there own levels (i.e. one could think of them as sub-levels $L = 3.\mathrm{A}$ and $L = 3.\mathrm{B}$), that collectively make up level $L = 3$. Due to the symmetry of tessellations with 4 edges meeting at each vertex ($q = 4$ in the Schläfi symbol), as one increases the level, there will always be two sub-levels for each level L from level $L = 3$ onwards.

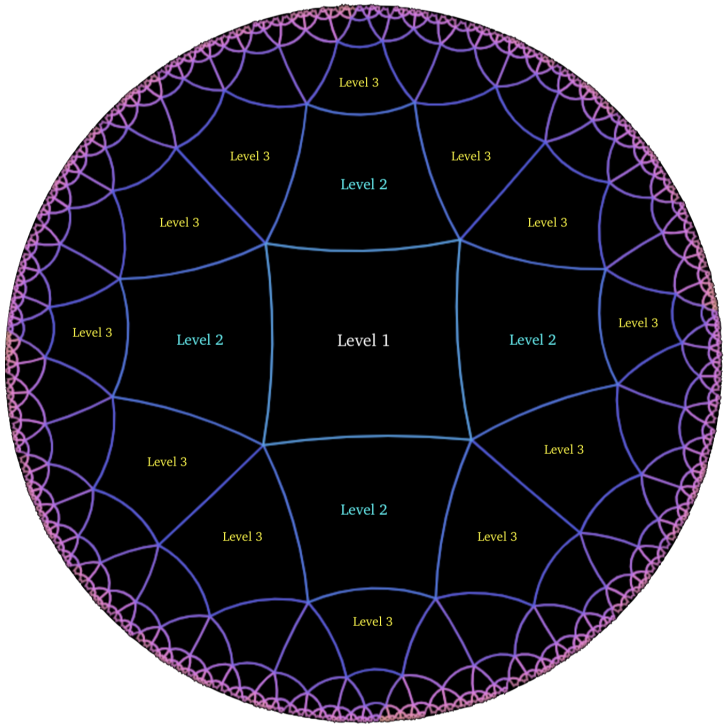

Figure 4.4.6: $\{4,5\}$ tessellation of hyperbolic plane H^2. One shows subsequent levels beginning from some central polytope defined to be at level $L = 1$ and adding a level for each polytope adjacent to a polytope at the previous level.

The ideas behind this construction can be generalised to concatenate the non-AME code across the cubic honeycomb on H^3. The construction is however more subtle than the two-dimensional case above. In order to visualise the 3d tessellation, we note that the structure is analogous to that of the $\{4,5\}$ tiling in H^2. We may proceed by labelling edges (corresponding to faces) and building the tessellation in levels as before. The result after three levels is shown in Figure 4.4.6.

The immediate issue arising is that one has inconsistencies, similar to that of the $\{7,4\}$ tiling when level $L = 3$ is reached. However, these are now more intricate than before due to the difference in symmetries between the two tilings. At $L = 3$, on one hand there are some polytopes where one edge will be glued to a polytope at level $L = 2$ and three edges will be glued to polytopes at level $L = 4$. On the other hand, there are some polytopes where one edge will be glued to level $L = 2$, one edge glued to another edge at level $L = 3$ and two edges that will be glued to a polytope at level $L = 4$. Hence, while one can choose one labelled edge to be glued to level $L = 2$ and two to be glued to level $L = 4$, one edge will sometimes be glued to level $L = 3$ and sometimes to level $L = 4$. Thus, one seems to have an inconsistent construction. Similarly, for the order-5 cubic honeycomb, one will analogous issues, where one face may be connected to level $L = 2$, and two faces to level $L = 4$ while one face will sometimes be glued to level $L = 3$ and sometimes to level $L = 4$.

The key issue arising is that one now has polytopes at level L adjacent to other polytopes at level L. In the $\{4,5\}$ tiling, this issue arises from the fact that the tessellation has an odd number of polytopes around each vertex (i.e. for Schläfi symbol $\{p,q\}$, one has q odd). Similarly, for the $\{4,3,5\}$ tiling this originates from the odd number of polytopes around each edge (i.e. for Schläfi symbol $\{p,q,r\}$, one has r odd).

Level L	Number of sub-levels
$L=1$	1
$L=2$	1
$L=3$	2
$L=4$	2
$L=5$	3
$L\geq 6$	3

Table 4.4.7: Number of sub-levels required at each level L in the $\{4,3,5\}$ order-5 cubic honeycomb to form a consistent construction.

It is possible to resolve these subtleties and obtain consistent concatenations of codes between cells. By dividing levels into sub-levels and treating each as if it were its own level, as previously explained, consistent constructions can be obtained. Table 4.4.7 shows the required number of sub-levels at each level L in order to maintain consistency, where we note that one sub-level simply means only the level L itself.

If we are using a tessellation with an even structure (q even in 2d or r even in 3d), we can obtain a consistent construction using a similar approach to that in [38]. We illustrate this for the order-4 dodecahedral honeycomb tessellation of H^3 with Schläfi symbol $\{5,3,4\}$ (noting here r is even) in section 4.4.2.

4.4.1.2 AME state

Now let us turn to an alternative approach to associating codes to H^3 spatial slices of AdS_4. If one lifts the assumption that the cells preserve maximal discrete symmetry, then graph states that are AME can be obtained. For example, for the case where the cube is the polyhedron tessellated (such as the order-5 cubic honeycomb tessellation of H^3), one requires a graph state consisting of six physical qudits and a single central logical qudit. The graph state given in Figure 4.4.8 satisfies this requirement while also being absolutely maximally entangled. Here the unit of quantum information used is the qutrit ($D=3$), allowing for up to two Z operators between pairs of qutrits.

While this graph state does not possess maximal symmetry, since it is AME, many of the arguments presented in [1] will still hold for this graph state. Importantly, this means this graph state still corresponds to a perfect tensor, and so when concatenated into a full tensor network, the bulk can be reconstructed using operator pushing. Now, suppose

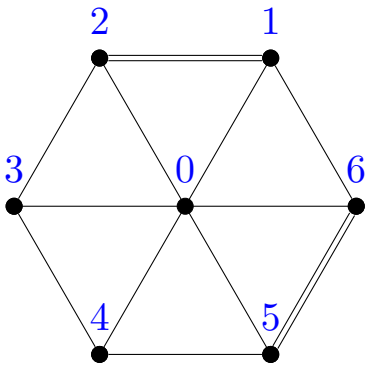

Figure 4.4.8: Graph state corresponding to the 7 qutrit AME state.

this suggestion can be implemented, representing the connectivity of the 6 physical qutrits that sit on each of the cube's faces and the single logical qutrit in its centre.

One can now try to consistently glue these cubes together when forming the full tessellation of H^3. For similar reasons to the logic presented in section 4.4.1.1, finding a consistent construction for the $\{4, 3, 5\}$ honeycomb is subtle due to there being an odd number of cubes around each edge (i.e r is odd). To begin this discussion, we will consider first the construction of the cubic honeycomb with Schläfi symbol $\{4, 3, 4\}$ that tessellates Euclidean 3-space $\mathbb{R}^3$, depicted in Figure 4.4.9, noting for this tiling that r is even. To our knowledge this construction has not been presented in any existing literature, and it will prove useful when considering the order-4 dodecahedral honeycomb in section 4.4.2. This tessellation belongs to a family of hypercube honeycombs with Schläfi symbols $\{4, 3, \ldots, 3, 4\}$ and so the following arguments should extend straightforwardly to higher dimensions.

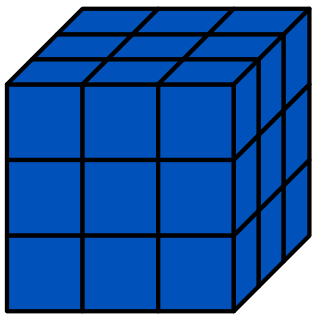

Figure 4.4.9: Visualisation of the cubic honeycomb with Schläfi symbol $\{4, 3, 4\}$ that tessellates $\mathbb{R}^3$.

When considering this tessellation, the first step is to find a representation of the graph state within the cube that preserves as much symmetry as possible. Clearly the logical qutrit (labelled '0') is maximally connected to all other qutrits so it is omitted from the following discussion. One can produce a construction that preserves as much symmetry as possible in the following way:

1. Consider the cyclically ordered set of all faces $\mathcal{F} = \{F_1, F_2, F_3, F_4, F_5, F_6\}$ and label a single vertex v_α for some $\alpha \in \{1, \ldots, 6\}$. Then label the adjacent faces $F_{\alpha-1}, F_\alpha, F_{\alpha+1}$. For example, label a single vertex v_1 and then label the adjacent faces F_6, F_1, F_2.

2. By construction, there will now be another vertex where both F_α and $F_{\alpha+1}$ meet. This vertex must then be labelled $v_{\alpha+1}$. There will also be one unlabelled face that is adjacent to both F_α and $F_{\alpha+1}$, which one labels $F_{\alpha+2}$. In the previous example one can hence label v_2 and F_3.

3. This process can be repeated until all faces are labelled together with the 6 vertices $v_1, \ldots v_6$. One can then place a single qutrit on each of these faces labelled $Q_1, \ldots, Q_6$ for faces $F_1, \ldots, F_6$ respectively. The resultant diagram representing the assignment of these qutrits is shown in Figure 4.4.10.

4. One can now connect qutrits $Q_1, \ldots, Q_6$ according to the graph state representation of the AME(7,3) state (Figure 4.4.8). The resulting graph state embedded in the cube is visualised in Figure 4.4.11.

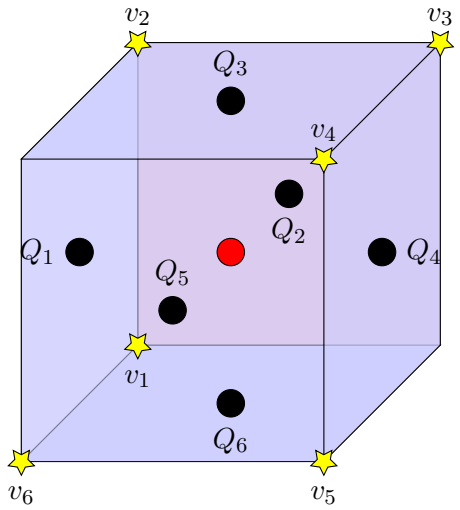

Figure 4.4.10: Assignment of qutrits to preserve the most symmetry when embedding the AME(7,3) state into a cube.

Now that we have a representation for the AME(7,3) state embedded on the cube, we can ask the question of how the qutrits living on the cube's faces can be concatenated. Consider two cubes C and C', with qutrits $Q_1, \ldots, Q_6$ and $Q'_1, \ldots, Q'_6$ living on each of the cube's faces respectively, assigned as depicted in Figure 4.4.11. We can concatenate C and C' by joining them facewise and since the graph states are AME, we can then maximally entangle the pair of qutrits (one from each face) using entanglement swapping as shown in section 4.3.5.

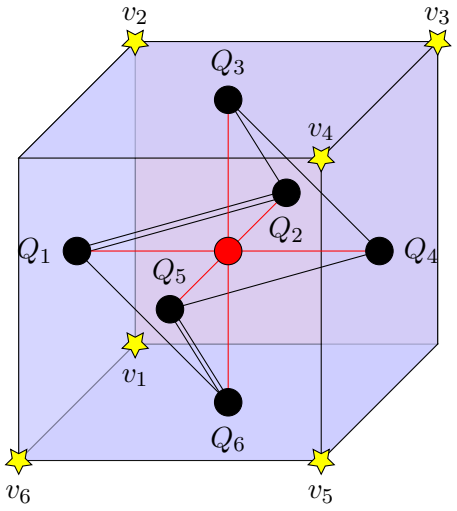

Figure 4.4.11: AME(7,3) graph state embedded on a cube C.

To maximise the symmetry of the resulting graph in the tessellation building H^3, one aims to consistently match pairs of qutrits. Qutrits can be categorised based on the weights of the incoming edges in the graph state, for example in Figure 4.4.11, qutrits Q_1, Q_2, Q_5 and Q_6 are associated to one weight-1 and one weight-2 operator, while qutrits Q_3 and Q_4 are associated with two weight-1 operators (in neither case including the one weight-1 operator connected with the logical qutrit).

The simplest way to match pairs based on this, is to match qutrits Q_i and Q_i', $i \in \{1, \ldots, 6\}$ when concatenating cubes C and C'. However, in order to successfully accomplish this, it is trivial to see that one cannot simply match the two cubes faces together without performing some operation on cube C' (e.g. rotating the cube about some central axis).

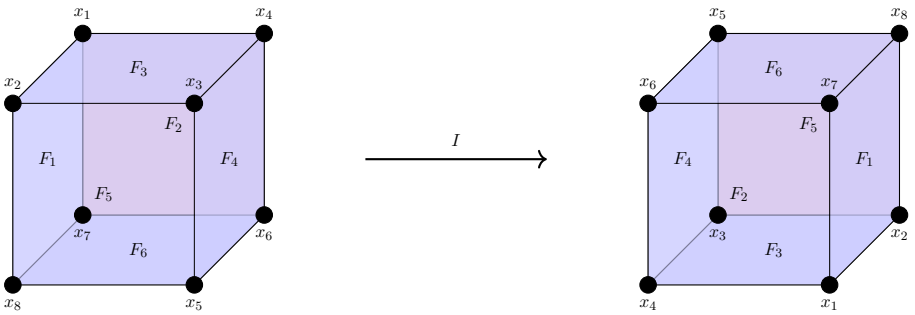

Figure 4.4.12: Inversion of C mapping to C'.

In order to preserve the internal structure of the graph state within the cube, one can attempt to choose a particular transformation mapping C to C' that exploits the innate symmetries of the cube. This transformation can be chosen to be an inversion, denoted $I : C \to C'$. Inversions in this context indicate mapping each vertex of the cube to the

opposing vertex, and similarly with mapping each face to its opposing face, such that the centre of the cube lies at the origin.

This is implemented by considering two cubes such that, the first, C, has the structure shown in Figure 4.4.11 and the second, C', is the inversion of C. This transformation can be visualised as shown in Figure 4.4.12. The left side represents the vertices of the original cube C, while the right side gives the cube's inversion C'. Using the particular choice of the labelling of vertices in C, as indicated on the left hand side of Figure 4.4.12, one may define the inversion operator as

$$I : C \to C' := \{I(x_i) = x_{i+4} \mid \forall x_i \in C\} \tag{4.4.18}$$

given x_i are the vertices of C, with $i \in \{1, \ldots, 8\}$ and such that the arithmetic is modulo 8 (i.e. the element $i + 4 \in \mathbb{Z}_8$). Clearly the faces bound by four vertices are also switched with their opposing face as a result.

Written in terms of the permutations of vertices, the inversion can be expressed as;

$$I(C) = (x_1x_5)(x_2x_6)(x_3x_7)(x_4x_8). \tag{4.4.19}$$

Note that an inversion can be completed from the combination of a rotation by an angle of 180° (π rad) about an axis defined to pass through the centre of a face and the opposing face, together with a reflection in the plane perpendicular to that axis. For example, define a set of axes such that the z-axis passes through the centre of faces F_3 and F_6 in C, as shown on the left hand side of Figure 4.4.13.

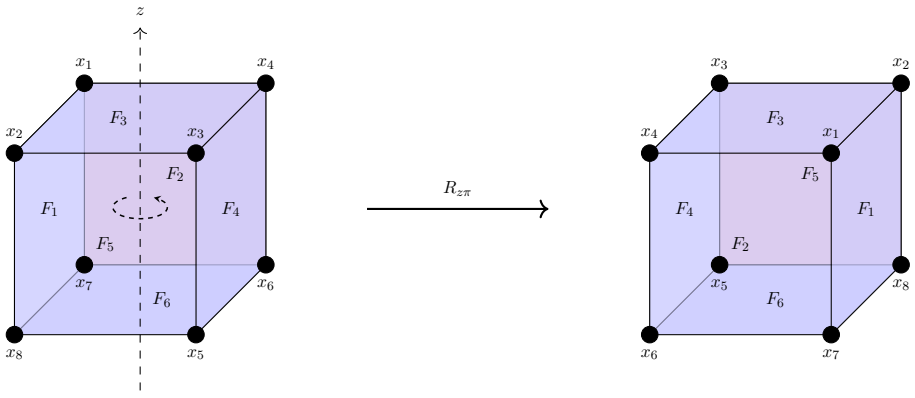

Figure 4.4.13: Rotation of vertices around the z-axis mapping C to $\tilde{C}$.

We define the operator $R_{z\pi} : C \to \tilde{C}$ as the rotation of each vertex in C, about the z-axis by π radians. Applying the rotation $R_{z\pi}$ to the cube C corresponds to the following permutations of vertices;

$$R_{z\pi}(C) = (x_1x_3)(x_2x_4)(x_5x_7)(x_6x_8), \tag{4.4.20}$$

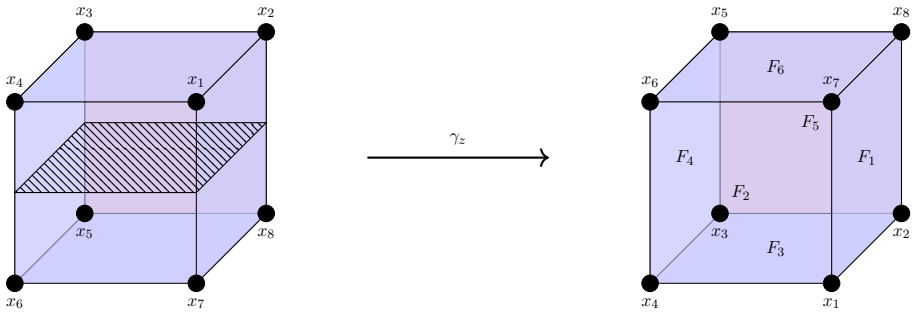

Figure 4.4.14: Reflection of vertices in the plane $z = 0$ mapping $\tilde{C}$ to C'.

mapping C to $\tilde{C}$. This mapping can be seen in Figure 4.4.13.

We can subsequently apply the reflection through the plane $z = 0$, denoted by γ_z, to the new cube $\tilde{C}$, with permutations

$$\gamma_z(\tilde{C}) = (x_1x_7)(x_2x_8)(x_3x_5)(x_4x_6), \tag{4.4.21}$$

as shown in Figure 4.4.14. This results in the cube C', thus showing this set of transformations is equivalent to the inversion shown in Figure 4.4.12.

We should note that performing an inversion on a cube does not change the structure of the graph state within C, but simply provides a 'mirror' of it. Since faces of C and C' are opposite by construction, when building a tessellation and thus concatenating states, one may join C and C' in any direction. For example, in C, F_4 is on the 'right' face whereas in C', F_4 is on the 'left' face (as indicated in Figure 4.4.12). Thus these can be joined, concatenating qubits Q_4 in C and Q'_4 in C'.

We could do this with each face of cube C. This central cube would thus be joined to six cubes at its faces such that each of these adjacent cubes are the inversions of C, given by C'. However, one could also provide a construction so each cube C' may be attached to six cubes such that all of the adjacent cubes are given by C. Since applying the inversion operator twice results in the identity $I^2 = e$, and hence $I(C') = I^2(C) = C$, these two constructions are the same and can be consistently built.

Thus one can tessellate the entirety of R^3 with cubes C and C' such that qubits Q_i are only ever concatenated with qubits Q'_i and C' is the inversion of C. This construction may be thought of as a 3-dimensional checkerboard where one draws all cubes C to be white cubes and all cubes C' to be grey cubes, in turn filling H^3, as depicted in Figure 4.4.15. Clearly, this construction has no preferred direction and while not maximising symmetry on a single polytope (which is achieved by the construction in Figure 4.4.1), there is a clear structure with remarkably high symmetry, when considering the full three-dimensional space.

Now let us return to the cubic tessellation of H^3. In H^3 five cubes meet at each edge and accordingly the construction described above does not work and one cannot consistently concatenate the AME codes associated with each cube in hyperbolic space. It is possible that a similar construction may exist however it is extremely non-trivial, thus one presents the simpler case of the $\{5, 3, 4\}$ honeycomb in the following section.

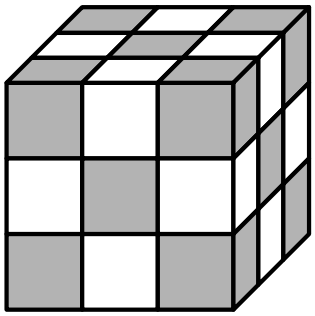

Figure 4.4.15: Tessellation of cubes C and C' forming a checkerboard cubic honeycomb in $\mathbb{R}^3$.

4.4.2 AdS_4: Other regular tessellations

Turning to the other regular tessellations of H^3 (the icosahedral honeycomb $\{3, 5, 3\}$, the order-4 dodecahedral honeycomb $\{5, 3, 4\}$ and the order-5 dodecahedral honeycomb $\{5, 3, 5\}$), the main conclusions are unchanged: one cannot realise AME states with qubits. The polytope tessellated in the icosahedral honeycomb is the icosahedron $\{3, 5\}$ and both other cases are constructed from the dodecahedron $\{5, 3\}$. Just as for the cubic case one can construct two types of graph states corresponding to each polytope.

Interestingly, in this construction, the graph state is a graph corresponding to the connectivity of the faces of the polytope. However, when representing Platonic solids as graphs, one usually considers the graph corresponding to the connectivity of the vertices and this is how many graphs have been stated in the literature. Hence, when sketching a graph state for a polytope p, one can effectively think of drawing the graph G for the dual polytope $\tilde{p}$, corresponding to the connectivity of the vertices.

For example, drawing the graph state for the icosahedron, gives rise to the graph that is often named the 'dodecahedral' graph. Similarly, the graph state for the dodecahedron corresponds to what is commonly referred to as the 'icosahedral' graph. Note that for the cube this issue was not discussed since the cube's dual is simply the cube itself. The two graph states corresponding to tessellations of H^3 consisting of dodecahedrons and icosahedrons which preserve maximal discrete symmetry are depicted in Figure 4.4.16 and Figure 4.4.17 respectively.

As for the previous discussion for the order-5 cubic honeycomb using a cubic tessellation, since one cannot have graph states with $n \geq 7$ qudits that is both AME and preserves maximal discrete symmetry, we must choose to relax one or both of these assumptions. In this section, we present both a construction using non-AME graph states that preserves maximal discrete symmetry and a construction using AME states that eases the restriction on maximal discrete symmetry.

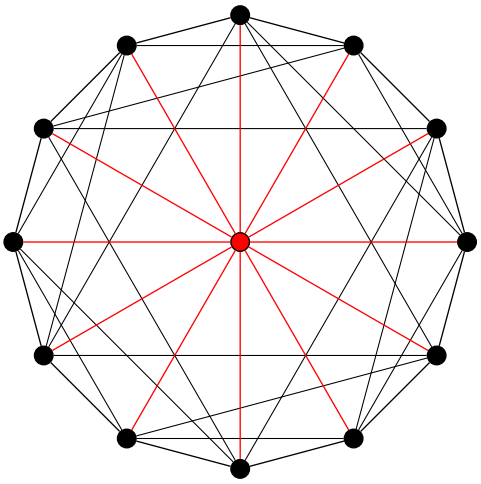

Figure 4.4.16: Graph state preserving maximal discrete symmetry for regular, uniform tessellations of H^3 consisting of dodecahedrons, commonly referred to as an 'icosahedral graph' in the mathematics literature.

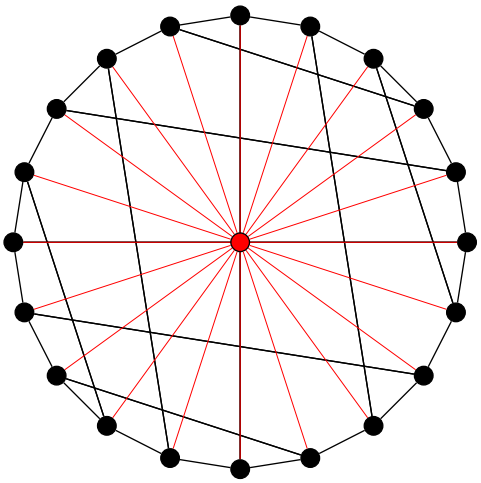

Figure 4.4.17: Graph state preserving maximal discrete symmetry for regular, uniform tessellations of H^3 consisting of icosahedrons, commonly referred to as a 'dodecahedral graph' in the mathematics literature.

4.4.2.1 Order-4 dodecahedral honeycomb non-AME state

Similarly to the order-5 cubic honeycomb, we first try to build a maximally symmetric model for the order-4 dodecahedral honeycomb. We begin by embedding the graph state (Figure 4.4.16) into a single dodecahedron. Here, each of the qudits is placed such that one lives on each face of the dodecahedron with a singular logical qudit represented in the centre of the dodecahedron. Thus, edges connecting qudits in the graph state correspond to two faces being adjacent.

Since we already know this graph state cannot be AME, we do not need to explicitly check this. However, it is required to check that this graph does in fact represent a quantum error correcting code. Here we choose the local dimension to be $D = 2$ for simplicity to demonstrate that the graph is a code.

The resulting stabiliser matrix for the graph state in Figure 4.4.16 can therefore be expressed as:

$$\mathcal{S}_{13} = \begin{pmatrix} X & Z & Z & Z & Z & Z & Z & Z & Z & Z & Z & Z & Z \\ Z & X & Z & I & Z & Z & I & I & I & Z & I & I & Z \\ Z & Z & X & Z & Z & I & I & I & I & I & I & Z & Z \\ Z & I & Z & X & Z & I & Z & Z & I & I & I & Z & I \\ Z & Z & Z & Z & X & Z & Z & I & I & I & I & I & I \\ Z & Z & I & I & Z & X & Z & I & Z & Z & I & I & I \\ Z & I & I & Z & Z & Z & X & Z & Z & I & I & I & I \\ Z & I & I & Z & I & I & Z & X & Z & I & Z & Z & I \\ Z & I & I & I & I & Z & Z & Z & X & Z & Z & I & I \\ Z & Z & I & I & I & Z & I & I & Z & X & Z & I & Z \\ Z & I & I & I & I & I & I & Z & Z & Z & X & Z & Z \\ Z & I & Z & Z & I & I & I & Z & I & I & Z & X & Z \\ Z & Z & Z & I & I & I & I & I & I & Z & Z & Z & X \end{pmatrix}. \tag{4.4.22}$$

We can then repeat the analysis used for the maximally symmetric graph state for a cube (Figure 4.4.2) however this time using the dodecahedron graph state (Figure 4.4.16). We note that it is easier to use the restated version of the SW-theorem presented in [225]:

Restated SW-theorem: *Consider a set of input vertices X and a set of output vertices Y. Then, given a finite abelian group G and the weighted graph with adjacency (coincidence) matrix Ξ, a quantum error correcting code v_Ξ is able to detect an error configuration $\mathcal{E} \subset Y$ iff given*

$$d^X = 0, \quad \textit{and} \quad \Xi^X_{\mathcal{E}} d^{\mathcal{E}} = 0 \tag{4.4.23}$$

then

$$\Xi^{I}_{X\cup\mathcal{E}} d^{X\cup\mathcal{E}} = 0 \Rightarrow d^{X\cup\mathcal{E}} = 0 \tag{4.4.24}$$

with $I = Y\backslash\mathcal{E}$.

We need to apply this theorem to the $\binom{12}{2} = 66$ possible two-error configurations. Here we omit the full details of this lengthy calculation but after performing this analysis it turns out that the graph state shown in Figure 4.4.16 is indeed a valid quantum error correcting code. While further analysis detailing some of the properties of this code would be very interesting, we do not deeply investigate them here as it is sufficient for our construction to show that one is indeed working with a quantum error correcting code.

We now construct the tessellation of the spatial slices of AdS_4 in the form of the order-4 dodecahedral honeycomb by using a consistent method to tessellate the dodecahedrons together, associating labels to each face and gluing them together. For simplicity, we present the arguments for the two-dimensional analogue of the order-4 dodecahedral tessellation, which corresponds to the familiar pentagonal tiling of H^2, with Schläfi symbol $\{5, 4\}$. We may then simply use the method presented in section 4.4.1.1, where one associates a distinct set of labels e_i to each pentagon (where now $i \in \{1, \ldots, 5\}$) at level L and glues pentagons by edges accordingly to level L'. The relevant diagram showing the $\{5, 4\}$ tessellation and subsequent levels beginning from some central pentagon at level $L = 1$ is shown in Figure 4.4.18.

Similarly to the $\{7, 4\}$ tessellation of H^2, we must divide levels into sub-levels from level $L = 3$ onwards for the $\{5, 4\}$ tessellation. However, as explained in section 4.4.1.1, since we are now working with a case in which $q = 4$, there are only two sub-levels for all levels $L > 3$. Hence, one can continuously build this consistent tessellation for any number of discrete levels approaching the spatial boundary of the spacetime.

The construction works in the exact same manner for the full three-dimensional order-4 dodecahedral honeycomb although it is more difficult to visualise. Here, polytopes are matched face-wise rather than edge-wise but otherwise the construction trivially generalises. The important feature is that one now has Schäfi symbol $\{5, 3, 4\}$ and thus there are four dodecahedra around each edge (since $r = 4$), analogous to the four pentagons around each edge in the $\{5, 4\}$ tessellation. Therefore, one will similarly have only two sub-levels for all levels $L > 3$.

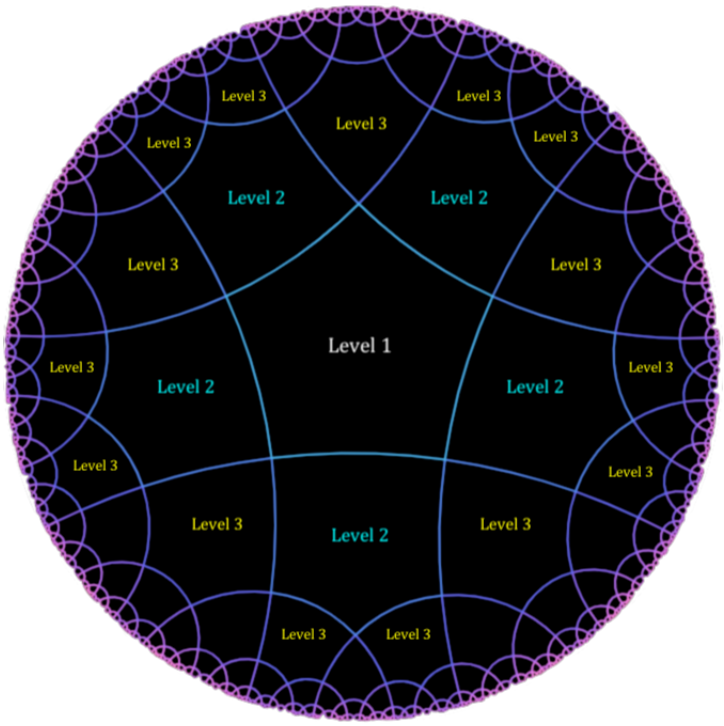

Figure 4.4.18: $\{5, 4\}$ tessellation of hyperbolic plane H^2. We show subsequent levels beginning from some central polytope defined to be at level $L = 1$ and adding a level for each polytope adjacent to a polytope at the previous level.

4.4.2.2 Order-4 dodecahedral honeycomb AME state

When discussing the order-5 cubic honeycomb in section 4.4.1.2, we began by considering the graph state corresponding to the 7 qutrit AME state denoted AME(7,3). If we wish to begin with an analogous construction for the order-4 dodecahedral honeycomb, we require a 13 qudit AME state since a dodecahedron possesses 12 faces, on each of which one of these qudits lives, with one qudit associated with the dodecahedron itself.

Clearly the AME(13,2) state does not exist [210] due to the theorems we have previously mentioned. It turns out that in local dimension $D = 3$, no AME state containing 13 parties exists [226] (i.e. AME(13,3) does not exist) due to constraints imposed by the so-called shadow inequalities. In fact, there is very little literature about the existence of any AME(13,D) state. The AME(13,7) and AME(13,8) states are thought to exist due to arguments presented in [227] (e.g. the existence of the $[[14, 0, 8]]_7$ QMDS code), though little is known about their properties.

Since not much is known about AME(13,D) states, to our knowledge no corresponding graph states have been produced in the literature. However, one would expect that some states do exist provided the AME state is a stabiliser state. In what follows, we assume that for a certain local dimension D there does exist a stabiliser state AME(13,D) and

that one can draw a corresponding graph state.

The advantage of tessellating H^3 using the order-4 dodecahedral honeycomb over the order-5 cubic honeycomb is that when considering their Schläfi symbols $\{p, q, r\}$, the order-4 dodecahedral honeycomb has r even, while the order-5 cubic honeycomb has r odd. Further, since $r = 4$, one can draw many parallels with the order-4 cubic honeycomb that tessellates $\mathbb{R}^3$. Recall the procedure we used for this Euclidean tessellation. We began by attempting to maximise the symmetry of the embedded graph state within the polytope (cube). Then we explicitly defined an inversion mapping I as a product of a rotation $R_{z\pi}$ and a reflection γ_z, such that it possessed the property $I^2 = e$, where e is the identity. We then had two possible cubes, C and its inversion C'. When tessellating $\mathbb{R}^3$, each face of C associated with a qutrit Q_i would be glued to a face of C' associated with a qutrit Q'_i and vice versa (see Figure 4.4.15).

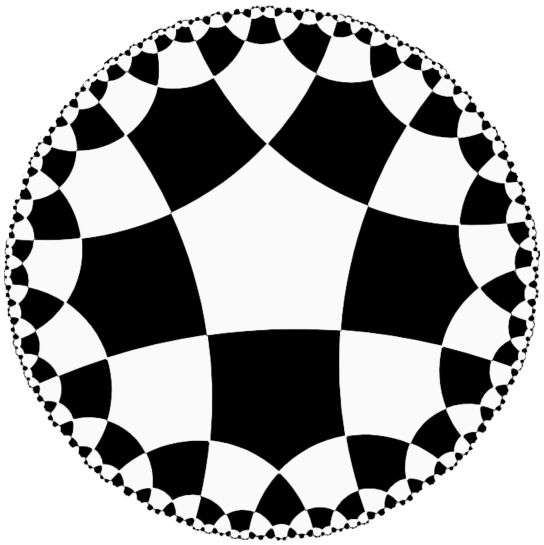

Figure 4.4.19: Checkerboard of the $\{5, 4\}$ tessellation of H^2, analogous to the checkerboard construction of the order-4 dodecahedral honeycomb in H^3.

In order to produce a similar construction for the order-5 dodecahedral honeycomb, we would begin as for the order-4 cubic honeycomb in $\mathbb{R}^3$ case by attempting to maximise the symmetry of the embedded graph state within the polytope. Since dodecahedrons have a more complex structure than cubes, it is likely this would be less straightforward. One would then define an inversion for the dodecahedron analagous to that of the cube consisting of rotations and reflections, so that after the inversion, all faces and vertices are 'opposite' to those in the original dodecahedron. One would once again then have two types of polytope, the original and it's inversion. One can think of this tessellation therefore to be alternating between black dodecahedra and white dodecahedra. Since visualising this tessellation in hyperbolic geometry is challenging, we present its analogous counterpart in Figure 4.4.19, alternating between black and white pentagons forming a checkerboard in H^2.

4.4.3 AdS_5 and higher dimensions

One may wonder whether the obstructions encountered in applying the HaPPY construction to AdS_4 apply generically in higher dimensions. It is straightforward to show that they indeed do, exemplifying the discussion with AdS_5. Spatial slices of AdS_5 correspond to the hyperbolic 4-space H^4 and its possible regular uniform tessellations are given by the Schläfi symbols given in (4.2.13). Since four dimensional objects are hard to visualise, it is useful to introduce the *configuration matrix* C, an object that stores all of the relevant information about a polytope within a single matrix.

Definition: For any regular n-dimensional polytope consisting of N_i i-faces with $0 \leq i < n$, one can write its configuration matrix such that for each i-face element N_i, the number of j-faces incident is denoted N_{ij}, where $i \neq j$. Trivially,

$$N_i N_{ij} = N_j N_{ji}. \tag{4.4.25}$$

One can construct a matrix from these configurational numbers with $N_i = N_{ii}$ as the diagonal elements and N_{ij} as the non-diagonal elements;

$$\begin{bmatrix} N_{0,0} & N_{0,1} & N_{0,2} & \dots & N_{0,n-1} \\ N_{1,0} & N_{1,1} & N_{1,2} & \dots & N_{1,n-1} \\ \vdots & \vdots & \vdots & \ddots & \vdots \\ N_{n-1,0} & N_{n-1,1} & N_{n-1,2} & \dots & N_{n-1,n-1} \end{bmatrix}. \tag{4.4.26}$$

From (4.2.13), we note that the first possible hyperbolic tessellation of H^4 is the order-5 5-cell honeycomb with Schläfi symbol $\{3,3,3,5\}$. The convex, regular 4-dimensional polytope associated with this tessellation is the 5-cell (also referred to as the 4-simplex), with Schläfi symbol $\{3,3,3\}$ and it is bounded by five regular tetrahedra. Hence, provided one follows the HaPPY approach, for each 5-cell there will be five physical qudits (one for each tetrahedra) and one logical qudit associated with the 5-cell, represented by being placed in it's centre.

In order to draw the maximal discrete symmetry-preserving graph state, we need to know which tetrahedra are connected via faces to one another. In this instance we can show each tetrahedron is connected to four other tetrahedra - one for each of its faces. The configuration matrix is rather useful to summarise all of this information

$$C_5 = \begin{bmatrix} 5 & 4 & 6 & 4 \\ 2 & 10 & 3 & 3 \\ 3 & 3 & 10 & 2 \\ 4 & 6 & 4 & 5 \end{bmatrix}. \tag{4.4.27}$$

The diagonal shows that the 5-cell has a total of 5 vertices, 10 edges, 10 faces and 5 cells. Importantly, the element in the fourth row and third column indicates that each cell has 4 faces showing these are comprised of tetrahedra. Since each physical qudit lives on its own tetrahedron, each physical qudit must therefore be connected to 4 other physical qudits in the graph state. However, since there are only 5 physical qudits in the system, the graph state must be maximally connected, as shown in Figure 4.4.20, also imposing the central logical qudit is connected to each physical qudit.

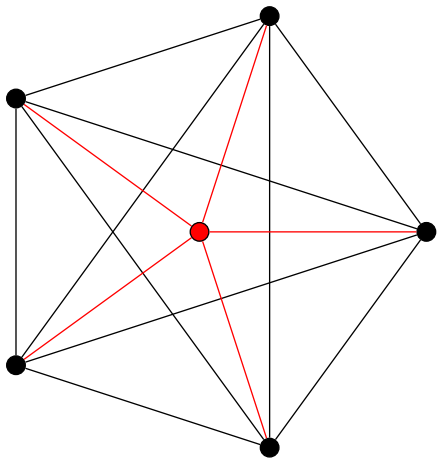

Figure 4.4.20: Graph state preserving maximal discrete symmetry for regular, uniform tessellations of H^4 consisting of 5-cells, a 4-dimensional polytope bounded by five tetrahedra.

Trivially, since this graph is maximally connected, then for any bipartition, one cannot obtain linearly independent vectors when performing the standard check and so this state is not AME. This result can similarly be obtained using the fact that Figure 4.4.20 is not locally Clifford equivalent to the AME(6,2) state. Hence as before one must either ease the maximal discrete symmetry assumption allowing one to work with an AME state (where, in this case one could use the AME(6,2) state) or alternatively, one can work with states that are not AME but preserve maximal discrete symmetry.

Other possible regular compact tessellations of H^4 are given in (4.2.13), but these can be reduced to considering the tessellations of the 120-cell (120-cell honeycomb $\{5,3,3,3\}$, order-4 120-cell honeycomb $\{5,3,3,4\}$ and order-5 120-cell honeycomb $\{5,3,3,5\}$) and that of the tesseract/four-dimensional hypercube (order-5 tesseractic honeycomb $\{4,3,3,5\}$). The 120-cell has Schläfi symbol $\{5,3,3\}$ and configuration matrix C_{120} while the tesseract has Schläfi symbol $\{4,3,3\}$ and configuration matrix C_8 where

$$C_{120} = \begin{bmatrix} 600 & 4 & 6 & 4 \\ 2 & 1200 & 3 & 3 \\ 5 & 5 & 720 & 2 \\ 20 & 30 & 12 & 120 \end{bmatrix}, \qquad C_8 = \begin{bmatrix} 16 & 4 & 6 & 4 \\ 2 & 32 & 3 & 3 \\ 4 & 4 & 24 & 2 \\ 8 & 12 & 6 & 8 \end{bmatrix}. \tag{4.4.28}$$

Following the previous arguments, since both of these polytopes would provide $n > 7$ physical qudits (120 for the 120-cell and 8 for the tesseract), neither polytope can be used to create an AME graph state that also preserves maximal discrete symmetry. For completeness, Figure 4.4.21 is the corresponding maximally symmetric graph state for the tesseract. We do not show the graph state for the 120-cell since it is very complex and does not add anything new to the discussion.

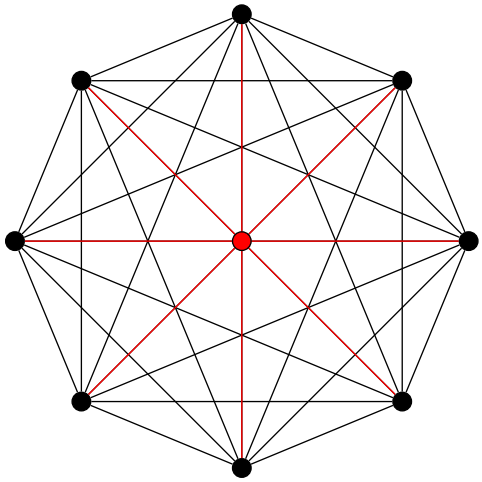

Figure 4.4.21: Graph state preserving maximal discrete symmetry for regular, uniform tessellations of H^4 consisting of tesseracts, a 4-dimensional polytope bounded by eight cubes.

Since there are no compact, regular tessellations of H^5 or higher dimensional space, these constructions cannot be explored using the construction that has been presented. Hence, if one wanted to consider AdS_6 or higher dimensions using a HaPPY type approach, then spatial slices would need to be discretised in a different manner. One could consider paracompact, regular tilings for H^5 but none of these exist for hyperbolic spaces of dimension 6 or higher. In order to be able to extend to general $(d+1)$-dimensional spacetime AdS_{d+1}, it seems that one would need to consider non-compact regular tessellations of the spatial slices H^d or use a qualitatively different approach based on irregular tessellations. We will return to this point in the following subsection as well as in section 4.6.

4.4.4 Summary

In this section we have shown that the HaPPY construction can be generalised to uniform regular tessellations of hyperbolic space in higher dimensions, but with important differences relative to two dimensions. Firstly, one either needs to relax the assumption of maximal discrete symmetry of the graph within the cell to get an AME code, or one needs to work with non AME states, with corresponding subtleties in

concatenating cells. Secondly, only a sparse number of such codes can exist in $d > 2$, due to the limited number of uniform regular tessellations.

In previous literature it has been noted that the perfect tensor/absolutely maximally entangled properties are constraining and various alternatives have been proposed in the context of two spatial dimensions. One class of approaches is based around relaxing the perfect tensor condition, for example to block perfect tensors as in [38, 228]. A block perfect tensor is one which is isometric for partitions into adjacent sets of indices and with this approach one can associate codes to 2d hyperbolic tilings that are not compatible with perfect tensors. There are many other approaches that are similarly related to generalisation to different types of tensors [36, 37]. These constructions are very much analogous in spirit to the non-AME constructions above.

In two dimensions, more complicated generalizations of HaPPY have been considered. For example, one can consider hyperbolic tilings that are not regular but alternate different polygons [202,203]; these can represent Bacon-Shor type codes which include gauge degrees of freedom. Generalizing this approach to higher dimensions would be interesting and would rely on classifications of hyperbolic tessellations involving more than one type of polytope. For example, one could envisage using rectified honeycombs, which alternate different polytopes, as well as runcinated honeycombs which alternate polytopes and have irregular vertex figures. In higher dimensions where no compact regular tessellations exist one would need to use semi-regular honeycombs as a basis for constructing codes.

Other generalizations of HaPPY include adding degrees of freedom on a tensor network connected to copies of HaPPY by an isometry, to give models for bulk gauge fields and gravitons [229]. Clearly for this construction to be lifted to higher dimensions one would need to first develop an AME code before connecting this code to an auxiliary tensor network.

4.5 CSS stabilizer codes and tessellations

In this section we will consider a qualitatively different class of quantum error correcting codes that can be associated with hyperbolic tessellations. This class of codes has the advantage that the generalisation from two to higher dimensions is straightforward as the structure of the code follows directly from the properties of the tessellation. We will compare and contrast this construction to the AME/perfect tensor approach used in the previous section.

The codes discussed in this section are CSS codes, a specific class of stabilizer codes, the best known example of which is perhaps the Steane seven qubit code that is reviewed in section 2.3.2. As in earlier sections, the basic principle of stabilizer codes is to encode k logical qubits in n physical qubits[1] using a code space that is the eigenspace of a set of commuting stabilizers [78]. To make the link with tessellations and cellulations the relevant feature of a CSS code is that the parity check matrix, which characterises the error upon corruption of the message, can be expressed in terms of $\frac{1}{2}(n-k)$ generators that consist of (only) X operations on qubits and $\frac{1}{2}(n-k)$ generators that consist of (only) Z operations on qubits. For example, we can express one of the three X (only) generators on the Steane seven qubit code as $X_1X_5X_6X_7$ where the subscripts denote the physical qubits on which the operators act. The remaining five independent generators are given in (2.3.19).

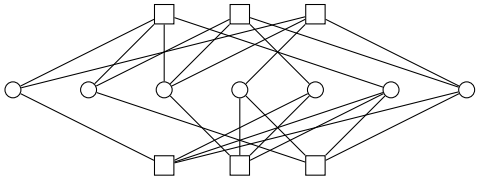

Figure 4.5.1: Tanner graph for the [[7,1,3]] Steane code. This graph is tripartite with the middle row of nodes representing the physical qubits and the top and bottom rows representing Z stabiliser checks and X stabiliser checks respectively.

The Tanner graph for a CSS code provides a visualisation for the parity check matrix. The middle row of a Tanner graph shows the physical qubits as nodes. Stabilizer checks are shown as boxes in the top (Z) and bottom (X) row, with there being an edge between the stabilizer and a qubit if the operator acts on that qubit. Tanner graphs are tripartite, with the partitions being the qubits, the X-checks and the Z-checks. From the check matrix for the Steane code given in (2.3.19) we can draw the associated Tanner graph, shown in Figure 4.5.1.

The main fact that we will use in this section is that any three layer Hasse diagram for a cellulation may be reinterpreted in terms of a Tanner graph for a CSS code. In the case of the tetrahedron shown in Figure 4.2.5, the top row of faces represents the Z checks; the middle row of edges represents the physical qubits and the bottom row of vertices represents the X checks. However, one needs to take into account that not all of the checks are linearly independent. For example, the four Z checks are:

$$Z_1Z_2Z_3 \qquad Z_1Z_4Z_5 \qquad Z_2Z_5Z_6 \qquad Z_3Z_4Z_6, \tag{4.5.1}$$

where as above we use subscripts to denote the qubit on which the check acts. Clearly the product first three gives the fourth, and therefore only three of the Z checks are linearly

[1] From here onwards we restrict to qubits, although the constructions can straightforwardly be extended to qudits.

independent. Similarly, only three out of four of the X checks are linearly independent. Accordingly this code is trivial, as the number of checks is equal to the number of physical qubits, and therefore no logical information can be encoded.

However, even though the code associated with the individual cell encodes no logical qubits, a cellulation constructed from tetrahedrons may encode logical qubits, as explained below. In other words, this approach to constructing codes thus relies inherently on the global properties of the tessellation, rather than on the properties of the individual cells, as the codes in the previous section did.

To exemplify cellulations associated with non-trivial codes, let us consider the case of $\{r, s\}$ regular tessellations of the hyperbolic plane. We can identify $\{r, s\}$ tessellations with CSS codes as follows, see [230]. Each stabilizer X check corresponds to a vertex of the tessellation, acting on all edges incident to the vertex, so has weight s. Each stabilizer Z check corresponds to a face of the tessellation, acting on all associated edges, so has weight r. Starting from a single r-gon, one can reflect in its edges to generate further r-gons, and then keep repeating the process. The polygons of each iteration are labelled by their level, starting from the original polygon (level 1) and continuing to level k. This process clearly generates a tessellation with a boundary.

However, the code associated with such a tessellation encodes no qubits. Associated with each vertex is an X check, but there is one linear dependency between these checks, so the total number is $V-1$, with V the number of vertices. Associated with each face is a Z check and these are linearly independent, so the total number is F, with F the number of faces. The graph is planar and therefore the standard relationship between edges E, F and V holds:

$$E = V - 1 + F. \tag{4.5.2}$$

The number of edges is identified with the number of physical qubits, and therefore the total number of physical qubits is equal to the total number of stabilizers, so the code is trivial. More generally, the properties of a code are determined by homology, see Appendix A.1.3. The number of encoded qubits is zero since the first homology class is trivial.

To obtain non-trivial codes one clearly needs constructions with non-trivial first homology class. There are several distinct approaches to obtaining non-trivial codes in two dimensions and there is considerable literature on the subject. One approach to consider codes associated with closed two-dimensional surfaces; the homology of a closed surface is generically non-trivial, and can be understood in terms of the identifications made to close the surface. A second approach was initiated in [230], which gave a systematic procedure for removing certain X and Z checks at the boundary of an open surface so that the code encodes $(k-1)$ qubits; we will discuss this further below. Adding holes and defects in the interior also gives non-trivial homological codes [231].

One of the main topics of exploration is how to maximise the distance of the code, for a given ratio of logical to physical qubits (k/n), see for example [232–234]. While much of the focus has been on planar and toric codes, recent literature has also explored codes associated with hyperbolic surfaces, see for example [235] which in particular studies codes associated with closed hyperbolic surfaces i.e. quotients H^2/Γ. Here it is assumed that the symmetry group Γ has no fixed points although it could be interesting to generalise these constructions to quotients associated with the spatial sections of wormholes [236, 237].

Much of the literature has focused on codes associated with tessellations of two-dimensional manifolds. However, the procedure for associating a code with a cellulation works in any dimension. For physical applications, one clearly needs to be able to implement the code in a system with three spatial dimensions but various properties of higher dimensional codes have nevertheless been explored in the literature, see [235, 238–245]. For example, codes associated with tori have been constructed not just for three dimensional tori, but also four dimensional tori [238]. To make contact with holography, we will again focus on codes associated with hyperbolic space and these have been studied in a number of recent works [235, 243–245].

In a three-dimensional cellulation one identifies qubits with faces (2-cells), and stabilizer checks with edges (1-cells) and 3-cells. The interpretation of the vertices is that their connections with the edges define linear codes acting on the X-checks. By contrast there is no such linear code acting on the Z checks, and Z checks are linearly independent.

A toy example of a 3d code is illustrated in Figure 4.5.2. The top row shows the Z stabilizers, the second row shows the qubits and the third row shows the X stabilizers. The bottom row is associated with the vertices, and shows the action of the linear code on the X checks. Note that this is a toy example, as in realistic 3d cellulations there would be many more nodes, and many more connections between nodes: the graph captures all cells within the cellulation and the code properties relate to the global structure of the cellulation.

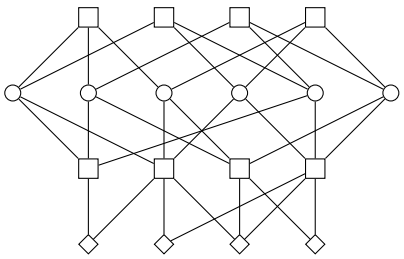

Figure 4.5.2: Tanner graph for toy example of a 3d code.

For four dimensional cellulations, codes have been constructed by again identifying qubits with faces, and stabilizers with edges and 3-cells. In four dimensions there are linear codes acting on both the X checks and the Z checks, associated with the vertices

and 4-cells, respectively. The Tanner graph in this case would have one additional row relative to Figure 4.5.2, above the Z checks, capturing the action of the linear code on these stabilizers. While in principle the construction of codes could be extended to arbitrary dimensions, there does not appear to be previous literature discussing codes in dimensions higher than four.

Most of the four-dimensional hyperbolic codes discussed in the literature are associated with closed manifolds. Properties of codes associated with tessellations of closed 4d hyperbolic manifolds were explored in [241]. Geometric arguments were used to show that such codes would have constant rate (k/n constant) while the distance scales as n^ϵ with $0 < \epsilon < 0.3$. Explicit examples of codes associated with closed 4d hyperbolic cellulations have been constructed recently in [235, 243–245]. These are based on the local regular H^4 cellulations (4.2.13), identifying 3-cells to give a closed manifold. A well-known example of such a closed 4d hyperbolic manifold is the Davis manifold, obtained by identifying boundary dodecahedra in the $\{5, 3, 3, 5\}$ (120-cell) tessellation. The properties of the associated code can be determined from homology, see appendix A.1.3, and the homology of the David manifold was derived in [246]. The examples of closed 4d hyperbolic codes given in [235, 243–245] are based on analogous constructions.

4.5.1 CSS codes for the hyperbolic plane

In this section we will describe the explicit construction of non-trivial CSS codes associated with hyperbolic planes with boundary. From the discussions above, the code associated with a hyperbolic tessellation generated by iterative reflections of a cell is trivial, due to the trivial homology. For holographic applications the most natural way to generate a non-trivial code is following a construction analogous to that of [230], i.e. modifying the qubits and checks at the boundary. We first review the two-dimensional construction of [230] and then explain how this approach can be generalised to higher dimensions. We will illustrate the two-dimensional construction with hyperbolic tessellations following the discussions in [235].

For an $\{r, s\}$ tessellation our starting graph is obtained by iterative reflection of polygons, beginning from a single r-gon. The starting graph encodes no qubits and all of the boundaries are smooth boundaries: the edges of the polygons, at which a string of X-errors can start and end. The reason why X-errors can start and end on smooth boundaries is because the X stabilisers act on all qubits on edges adjacent to vertices; the weights of the X checks at the boundary are two or s (for even s) or $(s-1)$ (for odd s) while in the interior the X checks have weight s.

Suppose the starting graph is generated by k reflections of the original cell. The boundary then consists of the edges that the level k polygons would be reflected in to

generate the graph of $(k+1)$ reflections. The idea is to divide this boundary into $2k$ equally sized regions. Half of these are smooth boundaries while the other half are so-called rough boundaries at which Z-errors can start or end. The process for creating a rough boundary used in [230, 235] is:

- Remove all boundary X-checks of weight two that have two edges within the boundary region considered.
- Remove all qubits on which only a single Z-check acts.
- Add certain weight two ZZ checks to the stabilizer (which ensures that Z-errors can only run between rough regions).

With such a construction the code can encode $(k-1)$ logical qubits [230]. Note that one can interpret the smooth and rough boundaries in terms of the lattice and its dual, see discussions in [230, 235]. Here the logical $\bar{Z}_i$ operators run from the ith to the $(i+1)$th rough boundary with $i = 1, \cdots, (k-1)$. Similarly the logical $\bar{X}_i$ operators run from the ith to the $(i+1)$th smooth boundary. (The definition of logical operators for stabiliser codes is reviewed in section 2.3.) An example with eight boundary segments is illustrated in Figure 4.5.3.

While the details of the construction can be adjusted e.g. to remove boundary X-checks of higher weight within the rough regions, the number of logical qubits was argued in [230] to be optimised at around k for a tessellation based on k symmetry operations acting on an initial cell. Conceptually this limit follows from demanding that the distance between rough regions is minimised by going through the bulk, rather than along the boundary.

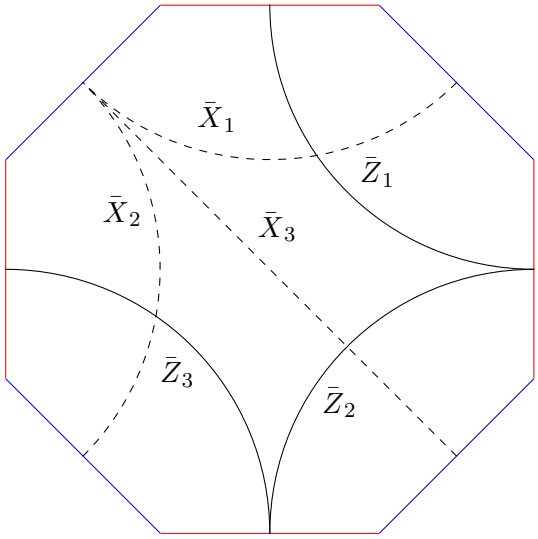

Figure 4.5.3: Example with eight boundary segments. Logical string operators running between rough and smooth boundaries, respectively, are shown.

If the rough regions can be connected via a shorter distance along the boundary, there are no logical qubits encoded, and this leads to the optimal division of the boundary into around $2k$ (equal sized) regions.

4.5.2 CSS codes for hyperbolic manifolds in $d > 2$

Here we outline the construction of CSS codes for higher dimensional hyperbolic manifolds, emphasising the differences relative to two dimensions. In two dimensions the boundary of the starting graph generated by k reflections of the original cell is topologically a circle, and the boundary is tessellated by segments. The construction above is based on alternating rough and smooth segments.

Now let us consider three dimensional hyperbolic space as the simplest prototype for higher dimensions. Our starting configuration is obtained by iteratively reflecting polyhedra beginning from a single cell. This starting configuration as above encodes no qubits: the boundary is topologically a sphere and using the homology as described in Appendix A.1.3 one can show that no logical qubits are encoded.

While the CSS code approach does not inherently rely on uniformity or regularity, let us first consider the case of uniform regular tessellations of hyperbolic space. The two dimensional boundary of the starting configuration will by construction be a regular monogonal tessellation i.e. all of the cells of the tessellation are one type of regular polygons. However, the boundary tessellation will not be vertex transitive (isogonal).

One can see the latter immediately from considering cubic tessellations for which the boundary sphere is tessellated by squares. The only uniform regular isogonal tessellation of a sphere by squares is by six squares, with three edges meeting at each vertex; this tessellation is of course associated with the cube itself. Now consider a tessellation of Euclidean space by cubes, as shown in Figure 4.4.15. Clearly the boundary is topologically a sphere, tessellated by squares, but there are two types of vertices, of order four and three respectively, and it is not isogonal. The boundary of the hyperbolic cubic honeycomb is also not isogonal, but has vertices of order four, three and six. As one reduces the symmetry of the bulk tessellation, the symmetry of the boundary correspondingly decreases, with the number of different vertices and the size of the fundamental region increasing.

Figure 4.5.4: Rough and smooth segments of one-dimensional boundary.

For a one-dimensional boundary one can subdivide the boundary in a binary way into rough and smooth segments, with rough regions separated from each other as shown in

Figure 4.5.4. For a higher dimensional boundary the vertices in the boundary tessellation are of order greater than two and such a binary division is not possible.

Let us consider a uniform square tessellation, illustrated in Figure 4.5.5, as a simple prototype. The simplest generalization of the lower-dimensional construction is to define distinct operations on each of the four cells in the fundamental region, and repeat these throughout the tessellation. Just as above, we can define roughing of boundary area elements through removing qubits and X checks. However, we will need to define two distinct types of roughing R_1 and R_2 for diagonally opposite cells, shown in blue and cyan. The corresponding adjoining smooth regions are also of two distinct types, reflecting the removal of different X checks on adjoining edges etc. These smooth regions S_1 and S_2 are shown in red and magenta. For a square tessellation with $4k^2$ cells, one would accordingly obtain $\approx k^2$ qubits encoded, associated with logical string operators extending in the bulk between neighbouring regions.

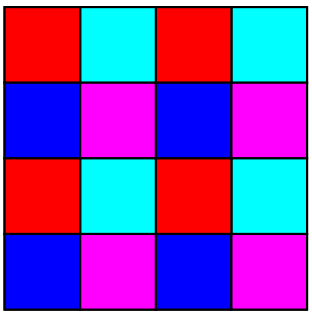

Figure 4.5.5: Square Euclidean tessellation. Rough area elements are shown in blue and cyan while smooth elements are shown in red and magenta.

Now let us consider how such an encoding would work over the entire spherical boundary, illustrating with the case of a cubic tessellation of Euclidean space, as shown in Figure 4.5.6. One can use the construction outlined above to encode logical qubits associated with vertices of order four. However, there are also vertices of order three (the corners of the cube projected onto the sphere) and one would need to adjust the roughing and smoothing at these vertices. As discussed above, cubic tessellations of hyperbolic space are associated with boundary tessellations in which the vertices are of order three, four and six. Accordingly one would need to define alternating roughing and smoothing over the entire fundamental region of the tessellation to construct a consistent code. We leave the detailed construction for future work, but based on the arguments above one would expect to be able to encode around k^2 qubits starting from a level k tessellation. Note that constructions of Euclidean surface codes in three dimensions can be found in works such as [247, 248].

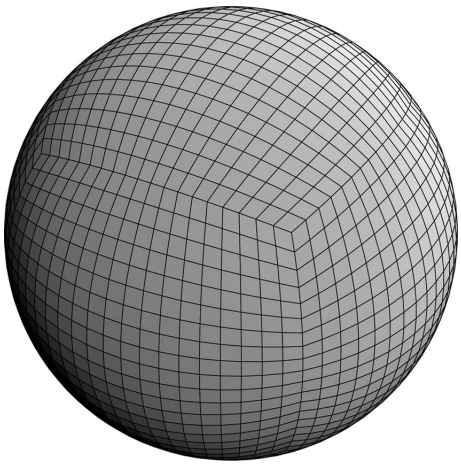

Figure 4.5.6: Cubic tessellation and bounding sphere.

4.5.3 Summary and holographic interpretation

In this section we have discussed CSS codes associated with hyperbolic tessellations. While logical information is encoded in every cell of a HaPPY type construction, the logical information in these CSS code constructions is inherently associated with the boundary of the tessellation. As in the HaPPY approach, we again encounter subtleties in extending from the two dimensional constructions in the literature to higher dimensional constructions. In two dimensions one can divide the boundary into rough and smooth segments, associated with logical $\bar{Z}$ and $\bar{X}$ operators respectively. Since the vertices in the boundary tessellation are of order higher than two in higher dimensions, one will need to use more types of area elements associating them with distinct logical operators. The boundary tessellation is not isogonal and the rough/smooth construction will need to be defined over the fundamental region of the tessellation.

These code constructions are interesting in their own right for quantum information theory. From the perspective of holography, one could envisage two distinct applications of these constructions. The first is to take the limit of large k so that the code is associated with the entire bulk holographic space. The logical string operators running through the bulk should then have an interpretation in terms of the dual gauge theory, perhaps in terms of correlations between operators inserted at the boundary locations.

The second application could be in the context of local holography. A level k code would encode around k^2 qubits. One could envisage gluing together different finite k constructions to cover the full holographic space i.e. using each CSS building block code as an analogue of the unit cell in the HaPPY construction. Consistent concatenation of these CSS codes to cover the bulk would require approaches of the type discussed in the previous section. This approach could be viewed as local holography, in that the boundary of each block is associated with the encoding of logical information within the

block. Using local building blocks to cover the full space is a natural first step towards dynamics: one could envisage that dynamical evolution could change the CSS codes in each block, reflecting the local changes in curvature through dynamics.

4.6 Conclusions and outlook

The main goal of this section has been to generalise quantum error correction codes to new classes of holographic geometries. Much of our discussion focuses on hyperbolic manifolds of dimensions greater than two. We noted at the beginning of the paper that general classes of Einstein/dilaton theories can be understood in terms of toric reductions of negative curvature Einstein spaces so our constructions provide the starting point for analysing these holographic dualities also.

To associate a code with (the spatial section of) a holographic geometry, we discretise the geometry; associate a graph state to each cell; analyse the properties of the code corresponding to the graph state and then explore the concatenation between cells. We begin by exploring the generalisation of the HaPPY construction to dimensions greater than two, i.e. working with uniform regular tessellations and associated perfect tensors/AME states. While it is well-known that HaPPY does not give rise to the required behaviour of entanglement and correlation functions for a 2d CFT [36], many code constructions are based on adaptations of HaPPY e.g. modifications of the tensors to be nearly perfect [33, 34]. In two dimensions quasiperiodic boundaries of regular hyperbolic tilings can on average give correlation function decays in line with those of CFTs, see [204, 249, 250]. Beginning with HaPPY type constructions therefore seems like a natural starting point for higher dimensional codes.

We have shown that non-trivial codes based on uniform regular hyperbolic tessellations can be constructed. However, there are key differences relative to the two-dimensional construction. Firstly, there are only a finite number of uniform regular tessellations in H^3 and H^4, with no uniform regular compact tessellations at all for H^d with $d > 5$. Accordingly the number of codes is much more sparse than in two dimensions.

Secondly, we are forced to break the maximal discrete symmetry associated with the polytope of the tessellation. If we work with AME codes/perfect tensors, the breaking of the symmetry automatically arises in the mapping between the AME state and the cell, and follows immediately from the properties of AME states. In the codes constructed from non-AME states, the graph state apparently respects the discrete symmetry of the polytope cell, but in concatenating cells one does not preserve transitivity i.e. different faces/edges are not equivalent. Our constructions very much mirror the constructions of

2d codes based on block perfect tensors [38], for which there is also no vertex and edge transitivity.

It would be interesting to establish in future work the performance properties of these codes, together with the behaviour for entanglement and correlation functions in the dual theory which they capture. The relative sparsity of AME codes in dimensions higher than two may be linked with the fact that AME codes do not capture CFT behaviour. It would be intriguing to explore whether AME behaviour in dimensions higher than two is parametrically more distant from CFT behaviour than it is in two dimensions i.e. one may not be able to obtain CFT behaviour from small corrections to perfect tensors as in [33].

In section 4.2 we noted that general classes of non-conformal holographic dualities can be obtained from reducing hyperbolic spaces on tori and we illustrated this discussion in section 4.2.1.2 with the example of the reduction of the hyperbolic plane on a circle, which is relevant in the context of AdS_3 and JT gravity. We noted that there are two distinct ways of dealing with tessellations of toroidally reduced spaces: one can either choose the tessellation to respect the toroidal symmetry (at the price of imposing by hand equal area of cells) or one can exploit the discrete symmetry of the hyperbolic tessellation to make identifications in the toroidal directions. Either way one has, as expected, a regulated boundary excising the conical deficit in the interior of the space. It would be interesting to extend the circle reduction discussed in section 4.2.1.2 to more general toroidal reductions of higher dimensional hyperbolic tessellations, and to explore the properties of the codes obtained by discrete identifications.

In section 4.5 we have discussed an alternative approach to associating codes to hyperbolic tessellations, based on the relation between Hasse diagrams of cellulations and Tanner graphs of CSS codes. In this approach the logical qubits are encoded through global properties, rather than being associated with each cell. There are several distinct ways to obtain non-trivial encoding, from including defects in the bulk lattice to topologically non-trivial identifications.

For codes associated with manifolds with boundary, it is natural to use the approach of adjusting the boundary tessellation, adding and removing checks and qubits. Here we discussed the encoding of logical qubits through dividing the boundary into different sections, with logical operators running between disconnected sections of the boundary. In two-dimensional cellulations the boundary is one-dimensional and can be divided in a binary way between rough and smooth regions. In higher dimensions one would need more complicated constructions, with the number of different types of regions increasing with the order of the vertices in the boundary tessellation. Leaving aside applications to holography, our hyperbolic CSS codes would be interesting in their own right and their properties will be explored further in future work.

From a holographic perspective, one could envisage two distinct applications of the hyperbolic CSS codes. In the case that one takes the number of levels of the tessellation k to be very large, the tessellation could be viewed as being associated with the entire regulated hyperbolic spatial slice. The logical operators would then be viewed as logical strings running through the bulk between disconnected regions on the boundary. This seems somewhat analogous to capturing the correlation between local operators in the boundary by geodesics running through the bulk. It would be interesting to explore potential interpretations of the logical strings from the perspective of discrete versions of the AdS/CFT correspondence [251, 252], as well as connections to the codes in lattice CFTs explored in [253].

One could also consider gluing together finite k hyperbolic CSS codes, to obtain a discretisation of hyperbolic space in which each CSS block captures a certain amount of logical information. This could provide a way to think about local holography with each extended block capturing logical information, cf each individual cell within the HaPPY type codes. The concatenation of the blocks would determine the entanglement and correlation functions structure in the dual field theory.

Throughout this paper we have focused on the spatial slice of (static) holographic geometries and the code construction uses explicitly the constant negative curvature. AdS gravity in three dimensions is not dynamical and all gravitational solutions have constant negative curvature. For AdS gravity in higher dimensions gravity is dynamical and Einstein solutions generically have non-trivial Riemann curvature. Accordingly, even without including matter fields, one would expect that the lattice should be such that dynamics can change it in spatial dimensions higher than two i.e. dynamics should be able to change from exactly hyperbolic lattice to a lattice with local curvature variations. This issue would seem to link with the long running attempts to discretise dynamical gravity in dimensions higher than two, and all the associated challenges that are encountered. It could also potentially relate to dynamical hyperbolic networks described by simplicial complexes, see for example [254].

Finally, we note that graphs associated with the hyperbolic plane are used in certain deep learning algorithms [255–257]. Networks associated with hyperbolic geometry have various advantages, including reduction in model parameters and over-fitting of data. The constructions of graphs associated with hyperbolic geometry in this work could be used to generalise these deep learning algorithms with potential applications in natural language processing and image classification [257].

Part II

Gravitational Lensing

CHAPTER 5

Introduction to gravitational lensing

5.1 Gravitational lensing: the general concepts

The phenomenon described by the deflection of light rays due to the presence of a gravitational body, is commonly referred to as gravitational lensing. Predicted by Einstein [39, 45], it is an effective method of testing general relativity using astrophysical observations. The governing theory was pioneered by [49, 51], providing the necessary properties of the point mass lens.

The first observation of gravitational lensing was in [54], where the source 0957+561 produced twin images A and B, that were quasi-stellar objects (QSOs) with the same redshift $z = 1.405$, separated by 5.7 arcseconds. Following this discovery publications in both observational and theoretical work erupted and a number of other gravitational lens systems were observed, most prominently galaxies behind clusters [56, 57] and the first observation of the Einstein ring [58]. Continuous work from both the theoretical physics and astrophysics community has helped lensing develop into a very active research area.

In the following section, we describe all of the general concepts that arise in gravitational lensing, all based in the Schwarzschild regime. For a more detailed discussion of the broad topic of gravitational lensing, we refer the reader to the monographs [83, 258–261], in particular for microlensing see [84].

5.1.1 Light deflection in gravitational fields

For arbitrary curved spacetimes, describing the propagation of light is perceived to be rather difficult computationally. As with most observations in cosmology, we assume an accurate depiction of the universe is one where it is both homogeneous and isotropic, and as such, its geometry can be well approximated by the Friedmann-Lemaître-Robertson-Walker (FLRW) metric [262–266]. In this cosmological model, gravitational lensing phenomena arises due to matter inhomogeneities which are accounted for as local perturbations. We can think about this in the following way: light propagates through the unperturbed (locally flat, Minkowski) spacetime when approaching the lens from a particular source before passing the lens and heading back out to spatial infinity. In the region when this light ray is satisfactorily near the gravitational lens, this spacetime is weakly perturbed by a gravitational potential Φ of mass distribution comprised from the lens. Thus, assigning the metric $\eta_{\mu\nu} = \text{diag}(1, -1, -1, -1)$ to the unperturbed spacetime, the weakly perturbed metric can be given the line element

$$ds^2 = g_{\mu\nu}dx^\mu dx^\nu = \left(1 + \frac{2\Phi}{c^2}\right) c^2dt^2 - \left(1 - \frac{2\Phi}{c^2}\right)(d\vec{x})^2. \tag{5.1.1}$$

We have used the notion of 'weakly' perturbing the spacetime here. When using this phrase, one means we have adopted the assumption that the gravitational potential is significantly smaller than c^2, i.e. $|\Phi|/c^2 \ll 1$, and that the velocity of the lens mass distribution with respect to the cosmological rest frame is also small, i.e. the peculiar velocity v satisfies $v/c \ll 1$. From the perspective of astrophysics, this condition is satisfied by virtually every case we are interested in. For example, the potential in a typical galaxy cluster satisfies $|\Phi|/c^2 \lesssim 10^{-5}$, while peculiar velocities are around $v \lesssim 600kms^{-1}$.

Utilising the condition specified by the propagation of light, $ds = 0$, we can resolve the line element (5.1.1) to find the effective speed of a ray of light in a gravitational field. Then we obtain the expression

$$c' = \left|\frac{d\vec{x}}{dt}\right| = c\sqrt{\frac{1 + \frac{2\Phi}{c^2}}{1 - \frac{2\Phi}{c^2}}} \approx c\left(1 + \frac{2\Phi}{c^2}\right), \tag{5.1.2}$$

where, in the final approximation, we have performed a first-order Taylor expansion. Following geometrical optics, we can characterise the phenomena describing a change in velocity of a light ray propagating through space by introducing an effective index of refraction n. Defining it in the most conventional manner, $n = c/c'$, the effective index of

refraction for a weak gravitational field is

$$n = \left(1 + \frac{2\Phi}{c^2}\right)^{-1} \approx 1 - \frac{2\Phi}{c^2}. \tag{5.1.3}$$

Of course by construction, the Newtonian gravitational potential is taken to be negative in order to normalise it such that it vanishes at infinity, $\Phi \leq 0$, and so the effective index of refraction exceeds unity, $n > 1$, thus requiring that the effective light speed c' is smaller than the vacuum speed of light c.

One may now directly solve for an equation describing the behaviour of paths of light by using *Fermat's principle* [267,268]. The principle states that any path, $\vec{x}(l)$, connecting a fixed starting point A and a fixed end point B, will only be a light path if the following variation vanishes;

$$\delta\tau = \delta \int_A^B n[\vec{x}(l)]dl = 0, \tag{5.1.4}$$

where τ is the optical path of an observer. Notice we are presented with a standard variational problem so achieving our goal amounts to solving for the Euler-Lagrange equations of (5.1.4). Parametrising the path using an appropriate affine parameter λ and expressing the integral in terms of the Lagrangian $L(\vec{\dot{x}}, \vec{x}, \lambda)$, the Euler-Lagrange equations reduce to

$$\frac{d}{d\lambda}(n\,\vec{e}) - \vec{\nabla} n = 0 \quad \Rightarrow \quad n\,\vec{\dot{e}} = \vec{\nabla} n - \vec{e}(\vec{\nabla} n \cdot \vec{e}) = \vec{\nabla}_\perp n, \tag{5.1.5}$$

where we have used the standard vector notation $\vec{e} \equiv \vec{\dot{x}}$ to describe the tangent vector $\vec{\dot{x}} \equiv d\vec{x}/d\lambda$. The second equality arises by realising the entire middle expression corresponds to the gradient of n perpendicular to the path of light, $\vec{\nabla}_\perp n$. Constraining ourselves according to $|\Phi|/c^2 \ll 1$,

$$\vec{\dot{e}} \approx -\frac{2}{c^2}\vec{\nabla}_\perp \Phi. \tag{5.1.6}$$

The change in the tangent vector $\vec{e}$ from the incident ray to the outgoing ray must then characterise the angle of deflection. Hence, we can more formally define the deflection angle $\hat{\vec{\alpha}}$ to be the integral

$$\hat{\vec{\alpha}} = -\int_{\lambda_A}^{\lambda_B} \vec{\dot{e}}\, d\lambda = \frac{2}{c^2}\int_{\lambda_A}^{\lambda_B} \vec{\nabla}_\perp \Phi\, d\lambda. \tag{5.1.7}$$

Of course, explicitly computing this integral is highly non-trivial since one is required to integrate along the entire light path. However, the deflection angle is typically very small for cases of astrophysical interest, as may be expected from the approximation $|\Phi|/c^2 \ll 1$. Hence as an approximation, it is suitably justifiable to integrate over the unperturbed light ray (thus integrating over a straight line), akin to the *Born approximation* [269] used in scattering theory within the realm of quantum mechanics. This is most clearly illustrated using an example.

Consider a light ray propagating with alignment parallel to the z-axis (i.e. light rays beginning at $+\vec{e}_z$ passing through a gravitational lens at $z = 0$) before encountering some gravitational lens with impact parameter ξ. The total deflection angle of the light ray can be found to be

$$\vec{\hat{\alpha}}(\xi) = \frac{2}{c^2}\int_{-\infty}^{+\infty} \vec{\nabla}_\perp \Phi \, dz. \tag{5.1.8}$$

Furthermore, suppose this lens is a point mass, and so the Newtonian gravitational potential can be expressed as

$$\Phi(\xi, z) = -\frac{GM}{(\xi^2 + z^2)^{1/2}}, \tag{5.1.9}$$

where the impact parameter is given by $\xi = \sqrt{x^2 + y^2}$. Then, the unperturbed light path along the z direction is

$$\vec{\nabla}_\perp \Phi(\xi, z) = \begin{pmatrix} \partial_x \Phi \\ \partial_y \Phi \end{pmatrix} = \frac{GM}{(\xi^2 + z^2)^{3/2}} \begin{pmatrix} x \\ y \end{pmatrix} = \frac{GM\vec{\xi}}{(\xi^2 + z^2)^{3/2}}. \tag{5.1.10}$$

Then (5.1.8) takes the form,

$$\vec{\hat{\alpha}}(\xi) = \frac{2GM\vec{\xi}}{c^2}\int_{-\infty}^{+\infty} \frac{dz}{(\xi^2 + z^2)^{3/2}}, \tag{5.1.11}$$

which can be directly solved to give

$$\vec{\hat{\alpha}}(\vec{\xi}) = \frac{4GM\vec{\xi}}{c^2\xi^2}. \tag{5.1.12}$$

Thus taking the norm of (5.1.12) and recalling that the Schwarzschild radius of a point mass lens is given by $R_s = 2GM/c^2$,

$$|\vec{\hat{\alpha}}(\xi)| = \frac{4GM}{c^2\xi} = \frac{2R_s}{\xi}. \tag{5.1.13}$$

For example, as a light ray passes by the surface of the sun, the angle of deflection is,

$$\hat{\alpha}_\odot = \frac{4GM_\odot}{c^2\xi_\odot} \simeq \frac{4 \times 6.674 \times 10^{-11}\mathrm{m^3kg^{-1}s^{-2}} \times 1.989 \times 10^{30}\mathrm{kg}}{(2.998 \times 10^8\mathrm{ms^{-1}})^2 \times 6.957 \times 10^8\mathrm{m}} \simeq 8.492 \times 10^{-6}\mathrm{rad}. \tag{5.1.14}$$

We close this section by briefly discussing the *Shapiro delay* [270]. As we have already mentioned, under the influence of a gravitational field, the speed at which light propagates is reduced, $c' = c/n$. Thus, there must be a delay in the arrival time of a light ray in the gravitational field relative to light rays propagating freely in the vacuum. This delay can explicitly be quantified to be

$$\Delta t = \int \frac{dl}{c'} - \int \frac{dl}{c} = \frac{1}{c}\int (n-1)\, dl = -\frac{2}{c^3}\int \Phi \, dl, \tag{5.1.15}$$

performing the integration over the light path between the observer and the source.

5.1.2 The general lens and thin-screen approximation

Since the distance between the observer and and the lens as well as the distance between the source and the lens are both significantly larger than the distance scale at which the light deflection occurs, we deem the gravitational lens itself as a *geometrically-thin lens*, consisting of a particularly small segment of the light path. With such lenses, one has substantial evidence to use the *thin-screen approximation*: one can project the mass distribution of the lens along the line of sight onto the so-called *lens plane*. The lens plane is a plane orthogonal to the line of sight intercepting the 'centre' of the lens, characterised by the surface mass density distribution $\Sigma(\vec{\xi})$ as

$$\Sigma(\vec{\xi}) = \int \rho(\vec{\xi}, z)\, dz, \tag{5.1.16}$$

where $\vec{\xi}$ is a two-dimensional vector in the lens plane. Now as the deflection angle $\vec{\hat{\alpha}}(\xi)$ as given in (5.1.13) has linear dependence on the mass M, deflection angles of an array of point masses can linearly be superposed. Thus suppose one has N point masses, sparsely distributed on a plane, the deflection angle $\vec{\hat{\alpha}}$ at position $\vec{\xi}$ may be given by

$$\vec{\hat{\alpha}}(\vec{\xi}) = \sum_{i=1}^{N} \vec{\hat{\alpha}}_i(\vec{\xi} - \vec{\xi}_i) = \sum_{i=1}^{N} \frac{4GM_i}{c^2} \frac{\vec{\xi} - \vec{\xi}_i}{|\vec{\xi} - \vec{\xi}_i|^2}, \tag{5.1.17}$$

where $\vec{\xi}_i$ describes the position in the lens plane and M_i the masses of the N point masses, while $\vec{\xi}$ is the position where the light ray intersects the lens plane.

Now, should the thin-screen approximation hold, we may sum the contribution of all the mass elements in the lens plane, defining $dM = \Sigma(\vec{\xi})d^2\xi$, replacing the sum in (5.1.17) with an integral, or in other words, taking the continuum limit in (5.1.17):

$$\vec{\hat{\alpha}}(\vec{\xi}) = \frac{4G}{c^2} \int_{\mathbb{R}^2} d^2\xi'\, \Sigma(\vec{\xi}') \frac{\vec{\xi} - \vec{\xi}_i}{|\vec{\xi} - \vec{\xi}_i|^2}. \tag{5.1.18}$$

Before moving on, we reiterate that this result is only valid when we consider lensing in the presence of weak gravitational fields and so deflections must be small. While these conditions are almost always satisfied for most astrophysical phenomena, certain situations cannot be described by this analysis. For example, the propagation of light in close vicinity to regions of extremely strong gravity, such as black holes, cannot be modelled using these expressions.

5.1.3 Lens geometry and lens equations

The typical gravitational lensing geometry is illustrated in Figure 5.1.1. The optical axis is defined such that it passes through the observer and is perpendicular to both the lens and source planes. The source S at redshift z_s emits a null ray that is deflected by an angle $\vec{\hat{\alpha}}$ by the gravitational lens L at redshift z_l, before reaching the observer at O. The distance between the passing light ray and the lens L is given by the impact parameter $\vec{\xi}$. We assume the deflector has mass distribution M and is separated from the observer with angular distance D_d. Similarly, we denote the distance between the lens and the source as D_{ds}. The true angular separation between the lens and the source is given by $\vec{\beta}$ and the distance between them is D_s, with the distance between the source and the optical axis quantified by $\vec{\eta} = \vec{\beta} D_s$. Finally, the angle between the optical axis and the image position I is denoted $\vec{\theta}$.

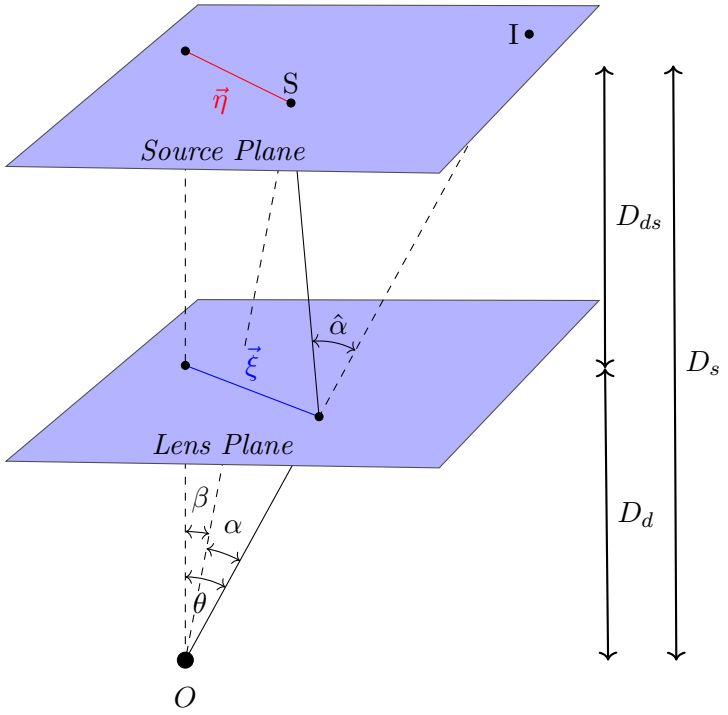

Figure 5.1.1: The gravitational lensing geometry for a spherically-symmetric spacetime (e.g. Schwarzschild). A point mass lens is situated a distance D_d from observer O. The null ray emitted at the source S travels along the solid black line, passing a lens with impact parameter ξ and is subject to deflection $\hat{\alpha}$. The source is positioned at distance D_s from O, with angular separation β from the optical axis. The image seen by the observer is positioned at angular separation θ from the optical axis with $\theta = \xi / D_d$.

Due to the deflection of the null ray, the observer receives the light as if the image located at angle $\vec{\theta}$ emitted it. Provided that $\vec{\beta}$, $\vec{\theta}$ and $\vec{\hat{\alpha}}$ are all suitably small, one can form a relation solely constructed from the geometry (as shown in Figure 5.1.1 for a

spherically-symmetric lens),

$$D_s\vec{\beta} + D_{ds}\vec{\hat{\alpha}} = D_s\vec{\theta}, \tag{5.1.19}$$

noting that $\vec{\theta} = \vec{\xi}/D_d$. It is often convenient to also define the reduced deflection angle,

$$\vec{\alpha} = \frac{D_{ds}}{D_s}\vec{\hat{\alpha}}. \tag{5.1.20}$$

Thus, these two expression can easily be combined to provide a rather simple yet extremely interesting relation between the source and image positions:

$$\vec{\beta} = \vec{\theta} - \vec{\alpha}(\vec{\xi}). \tag{5.1.21}$$

This equation is commonly referred to as the lens (ray-tracing) equation. While this equation may look exceptionally straightforward, it does indeed contain some subtleties. In order for (5.1.21) to hold for general curved spacetimes, one must consider angular-diameter distances. When using a Euclidean background metric, it is of course trivial for the distances to satisfy $D_s = D_d + D_{ds}$. However, since one is considering angular-diameter distances, there is no requirement that distances here are additive. Thus in the most general sense, $D_s \neq D_d + D_{ds}$.

Since the impact parameter satisfies $\vec{\xi} = D_d\vec{\theta}$ by definition, one can substitute (5.1.13) into (5.1.21), giving the expression

$$\vec{\beta} = \vec{\theta} - 2R_s\frac{D_{ds}}{D_dD_s}\frac{\vec{\theta}}{|\vec{\theta}|^2}. \tag{5.1.22}$$

This is another common form of the lens (ray-tracing) equation for a Schwarzschild lens. Due to the spherical symmetry that emerges from the Schwarzschild geometry, we can always switch the coordinate origin to be at the centre of this symmetry and as such, reduce the deflection of light to be modelled in one-dimension. Consequently, we will now drop the vector notation, reducing objects to their one-dimensional scalar counterparts.

Further interesting symmetries arise in (5.1.22) in the special case $\beta = 0$. This corresponds to the particular situation where the observer, the source and the lens are co-linear (when the source lies directly behind the lens) and the entire configuration is rotationally symmetric about the optical axis. The result is a ring-like image whose angular radius is named the Einstein radius.

For the Schwarzschild lens, setting $\beta = 0$ in (5.1.22), one therefore defines the Einstein radius as

$$\theta_E = \left[2R_s\frac{D_{ds}}{D_dD_s}\right]^{1/2}. \tag{5.1.23}$$

The Einstein radius may be naturally thought of as an angular scale for gravitational lensing. Returning to (5.1.22), one can see that it can be reformulated conveniently in terms of the Einstein radius:

$$\beta = \theta - \frac{\theta_E^2}{\theta}, \tag{5.1.24}$$

where we have adopted the notation $\beta = |\vec{\beta}|$ and $\theta = |\vec{\theta}|$. Performing a simple re-scaling of both the angular separation between the lens and the source, β, and the angular position of the image, θ, with respect to θ_E,

$$\tilde{\beta} = \frac{\beta}{\theta_E}, \quad \tilde{\theta} = \frac{\theta}{\theta_E}. \tag{5.1.25}$$

This leads to the simplest and most attractive form of the lens equation,

$$\tilde{\beta} = \tilde{\theta} - \frac{1}{\tilde{\theta}}. \tag{5.1.26}$$

Solving this equation for the image positions, θ, leads us to the conclusion that one will always obtain two images for any isolated background source. We can characterise the positions of these two images from the two possible solutions

$$\tilde{\theta}_{\pm} = \frac{1}{2}\left(\tilde{\beta} \pm \sqrt{\tilde{\beta}^2 + 4}\right). \tag{5.1.27}$$

The images lie either side of the source with the first, $\tilde{\theta}_-$, lying in the interior of the Einstein radius while the other, θ_+, lies in the exterior of the Einstein radius ($|\tilde{\theta}_-| < 1$ and $\tilde{\theta}_+ > 1$). As the angular distance to the source β increases, the outer image, θ_+, will approach the true position of the source, growing in magnification towards unity. On the contrary, during this process, the inner image, θ_-, will become increasingly faint, approaching the lens.

5.1.4 Magnification

During the gravitational lensing process, image distortion occurs due to bundles of the null rays being differentially deflected. Here surface brightness is preserved and so the surface brightness I of a gravitationally lensed image exactly matches the surface brightness of the unlensed source. Consequently, the total flux received from this image is only altered according to the solid angle subtended by the image in the sky (since it is the product of the solid angle and the surface brightness). Then, defining the magnification μ as the ratio between the image flux and the flux of an unlensed source,

$$\mu = \frac{\Delta w}{(\Delta w)_s}, \tag{5.1.28}$$

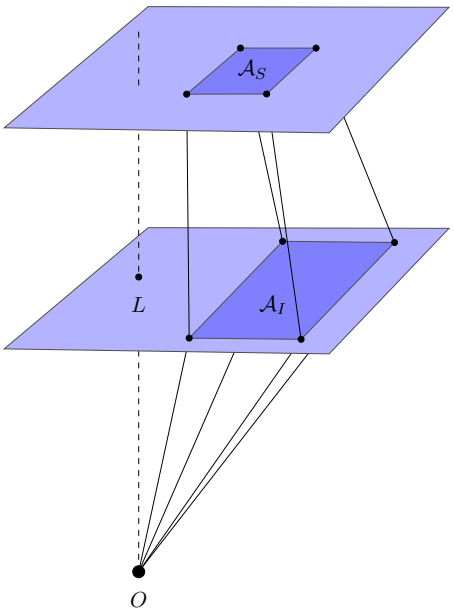

Figure 5.1.2: Solid angle distortion due to gravitational lensing. At the observer O, the solid angle $(\Delta w)_s$ is subtended by the area spanned by the source $\mathcal{A}_S$ in the absence of lensing. Hence, $(\Delta w)_s = \mathcal{A}_S/D_s^2$. Introducing the gravitational lens, the solid angle of the image differs from $(\Delta w)_s$ and is described by $\Delta w = \mathcal{A}_I/D_d^2$. As the surface brightness I is conserved during the light deflection process, the magnification of the total flux is proportional to Δw.

where Δw and $(\Delta w)_s$ are the solid angles of the image and source respectively. This situation is described diagrammatically in figure 5.1.2. In fact, this distortion of the images can be expressed as the determinant of the Jacobian matrix of the form

$$\frac{(\Delta w)_s}{\Delta w} = \frac{\mathcal{A}_S}{\mathcal{A}_I}\left(\frac{D_d}{D_s}\right)^2 = |\det\mathcal{M}|, \qquad \mathcal{M} \equiv \frac{\partial\vec{\beta}}{\partial\vec{\theta}}. \tag{5.1.29}$$

such that $\vec{\beta}$ and $\vec{\theta}$ are the corresponding source and image positions. Therefore one can quantify the magnification factor μ as the inverse of the determinant of the Jacobian matrix $\mathcal{M}$

$$\mu = \frac{1}{\det\mathcal{M}}. \tag{5.1.30}$$

Returning our focus to the Schwarzschild lens, one can explicitly calculate μ. For any axially symmetric lens, the determinant of the Jacobian $\mathcal{A}$ can always be described as

$$\det\mathcal{M} = \frac{\tilde{\beta}}{\tilde{\theta}}\frac{\partial\tilde{\beta}}{\partial\tilde{\theta}} = \left(1-\frac{1}{\tilde{\theta}^2}\right)\left(1+\frac{1}{\tilde{\theta}^2}\right) = 1-\left(\frac{1}{\tilde{\theta}}\right)^4. \tag{5.1.31}$$

Hence the magnification factor of the two images given in (5.1.27) is given by

$$\mu_{\pm} = \left[1 - \left(\frac{1}{\tilde{\theta}_{\pm}}\right)^4\right]^{-1} = \frac{\tilde{\beta}^2 + 2}{2\tilde{\beta}\sqrt{\tilde{\beta}^2 + 4}} \pm \frac{1}{2}. \tag{5.1.32}$$

The magnification of the inner image can be shown to always be negative, $\mu_- < 0$, since $\theta_- < \theta_E$. In this instance we say this image has negative parity with respect to the source, i.e. an observer will see a mirror-inverted image of the original source. A complication arises in the limit of $\beta \to 0$, resulting in a divergence in the magnification. Fortunately, this 'infinite magnification problem' can be resolved when considering extended sources, which always return finite magnifications, thus in reality the source is not actually infinitely bright.

The total magnification of flux measurable for the point mass lens μ_p is the sum of the absolute values of the inner and outer image magnifications,

$$\mu_p = |\mu_+| + |\mu_-| = \frac{\tilde{\beta}^2 + 2}{\tilde{\beta}\sqrt{\tilde{\beta}^2 + 4}}. \tag{5.1.33}$$

5.1.5 Microlensing and occultation

A simple model used to describe a specific class of gravitational lensing phenomena where the relative size of the lens is much smaller than that of the scale of the lensing system is known as *microlensing*. This arises when the multiple images of the source are in too close of a proximity to one another in the sky to be resolved by the observer. The lensing can still be detected however, since these 'micro-images' still appear as a single celestial object undergoing an an apparent increase in brightness. Thus one can classify a *microlensing event* as the apparent increase in magnification of a source object that peaks at some maximum before symmetrically returning back to normal over a given time period, that consists of sufficiently small lens masses and sufficiently large separations between source, lens and observer. Usually Einstein radii considered here are smaller than a milli-arcsecond and masses lie in the range $10^{-6} \leq M/M_{\odot} \leq 10^6$.

The most prominent application of microlensing was first proposed by Paczynski [55], suggesting observing background stars in the Large Magellanic Cloud (LMC), a satellite galaxy to the Milky Way, as a means to search for dark matter. The idea was that one could detect compact objects distributed in the Galactic halo and thus the presence of dark matter (evidenced to exist due rotating curves of spiral galaxies [271–273] etc.), through microlensing - since this instance of gravitational lensing is only dependent up the mass of the lens. These dark baryonic objects of approximately solar mass are appropriately named

MACHOS (Massive Astrophysical Compact Halo Objects) and are traditionally very faint or invisible objects. Typical MACHO candidates include brown dwarfs ($< 0.1M_\odot$), old white dwarfs ($\sim 0.5M_\odot$), neutron stars ($\sim 1.5M_\odot$) and black holes ($> 2M_\odot$). Many different groups such as MACHO, EROS and OGLE continued to search the LMC, Small Magellanic Cloud (SMC) and the Galactic bulge and have produced numerous papers recording their findings [274–278].

Though it is now widely believed that MACHOs are not true dark matter candidates due to observations of cosmic microwave background radiation and nucleosynthesis [279, 280] and further theoretical arguments [281, 282], microlensing has developed into an impressive tool with a diverse range of astrophysical applications [283–286]. The field has indeed progressed immensely since the first discoveries of microlensing events in the seminal works [274, 278]. As a matter of fact, according to [277, 287], it is suggested approximately 2,000 microlensing events are discovered on an annual basis.

Closely related to the concept of microlensing is the idea of occultation; an event where the source is hidden by the lens as it passes between the source and the observer. In fact, microlensing and occultation are just two different limits of the same phenomena when one body passes in front of another [288]. While occultation of the inner image does indeed occur fairly often in galactical microlensing, $R_L \ll R_E$, these effects are usually remarkably faint. However, inclusion of both microlensing and occultation has shown to be of grave importance when considering the case where the order of magnitude of the Einstein radius is similar to that of the radius of the lensing body, $R_E \sim R_L$. These effects are often present when considering lensing by giant stars or when studying eclipsing binaries consisting of compact objects [289, 290]. More specifically, defining the size of the lens star scaled to that of the Einstein radius as $r_L = R_L/R_E$, where $R_E = \theta_E D_d$ is the Einstein radius, we find there are two possible cases for occultation to occur.

Firstly, suppose the Einstein radius is greater than the radius of the lens star, $r_L < 1$. Should the inner image satisfy the inequality, $|\theta_-| < r_L$, then it will be occulted. As a consequence of (5.1.26), rewriting in terms of the source this inequality is $\beta > r_L^{-1} - r_L$, so the inner image is occulted when the distance between the source and the lens is large but unoccults as the source approaches the lens. Secondly, consider the case where the radius of the lens star exceeds the Einstein radius, $r_L > 1$. Now, the outer image will be occulted for $\theta_+ < r_L$ and the inner image will always be occulted. This is the case for a source close to the lens star, and correspondingly $\beta < r_L - r_L^{-1}$. We display this behaviour graphically in figure 5.1.3.

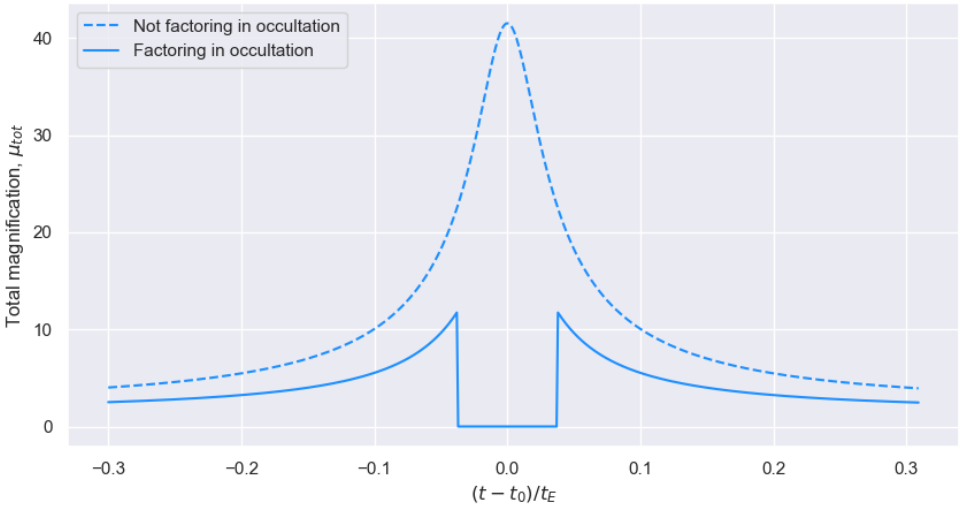

(a) Occultation plot for $M = 2.4 \times 10^6 M_\odot$ and binary separation $r_s = 0.023$ AU.

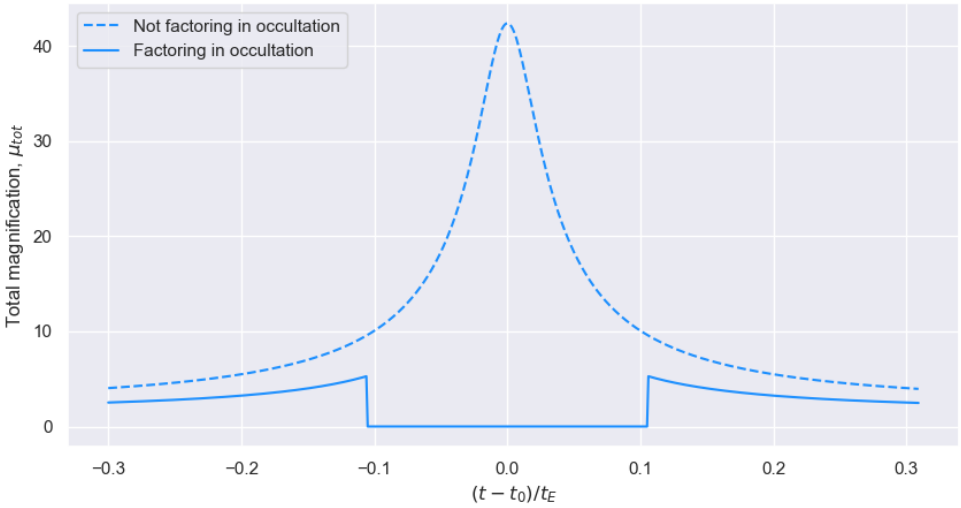

(b) Occultation plot for $M = 2.5 \times 10^6 M_\odot$ and binary separation $r_s = 0.023$ AU.

Figure 5.1.3: Microlensing and occultation plots for the Schwarzschild lens with fixed binary separation (astrophysical separation between the source and the lens) $r_s = 0.023$ AU for various different masses, where μ_{tot} is defined as in (5.1.34). For occultation to occur for separations of this order, the lens mass must be of order $10^6 M_\odot$; i.e. approximately the mass of Sagittarius A*, the supermassive black hole situated at the Galactic Centre of the Milky Way.

In order to include the features displayed by occultation, we adjust the definition of magnification to represent this phenomena. Then, the total magnification for a point source microlensing event, including occultation effects is

$$\mu_{\text{tot}} = \mu_+ \Theta(r_L\beta - r_L^2 + 1) + \mu_- \Theta(1 - r_L^2 - r_L\beta), \tag{5.1.34}$$

where we have introduced the Heaviside step function

$$\Theta(x) = \begin{cases} 1, & x > 0, \\ 0, & x \leq 0, \end{cases} \tag{5.1.35}$$

and $\mu_\pm$ are defined as in (5.1.32). Note that in the plots presented in figure 5.1.3, we have associated the quantity $(t - t_0)/t_E$ with the x-axis, as is often the case in astrophysics literature. Thus we are illustrating the magnification at different instances in time t as the microlensing event unfolds. We define the instance t_0 to be the time at which perfect alignment occurs, noting that in the Schwarzschild regime, this is equivalent to the instant at which magnification is maximised. The quantity t_E, often referred to as the Einstein crossing time, corresponds to the time the lens requires to cross the Einstein radius R_E (i.e. $t_E \equiv R_E/v_t$ where v_t is the velocity of the lens), thus it provides a natural time scale for the duration of the microlensing event.

5.2 General framework in the Kerr geometry

All the discussion presented so far in this section assumes the gravitational lens is approximated by Schwarzschild. While this may be an appropriate model for some celestial bodies, there are many bodies possessing larger spin parameters, such as neutron stars and black holes, where a full extension to a Kerr background may be needed for accurate predictions. It was Carter, [85], who first shed light on the behaviour of null geodesics in Kerr spacetime, by illustrating the separability of the Hamilton-Jacobi equation and showing the existence of another constant of motion, the *Carter constant*. The parameter space was initially explored in [86] and numerous studies followed, as summarised in the detailed monograph [87].

The null geodesic equations of motion were first resolved in the weak deflection limit in [88] up to and including second order corrections in M/ξ and a/ξ where M and a are the mass and the spin of the lens respectively and ξ is the impact parameter. Light rays passing outside a spinning star were considered in [291] using the framework of the Lense-Thirring metric. The paper that inspires much of what follows, [2], succeeded in resolving the null geodesic equations up to third order corrections, following the same procedure as in [88].

While weak gravitational lensing has produced many key results of general relativity, much effort has also been exerted trying to understand the strong gravitational lensing regime. In order to solve for relativistic images [292], this regime is necessary, hence one cannot make approximations and must use the full Kerr null geodesic equations [85, 86]. Strong lensing was first studied analytically in a spherically symmetric and static spacetime

in [293, 294]. Extending to the case of Kerr, the deflection angle of light rays in the equatorial plane were found explicitly in [295], and there have been a number of papers [296–298] considering quasi-equatorial rays, though the approximations used break down when observers move far away from the equatorial plane.

The phenomenology of strong field gravitational lensing by a Kerr black hole and a calculation for the positions and magnification of all images, given an observer and source located far away from the black hole, with arbitrary inclinations, is a harder problem. Accordingly, several numerical investigations attempted to model this phenomena [89, 299–301], most notably [89], where a general procedure to compute image positions and their corresponding magnifications was developed for a distant source and observer, at arbitrary inclinations.

In recent years, significant attention has been given to gravitational lensing in the context of Kerr black holes due to the incredible advancement of observational facilities [90–92, 302, 303], further elevated by a substantial increase in interest due to the famous Event Horizon Telescope (EHT) observations [7]. The full set of solutions for the angular path integrals was expressed in [90] while the complete, fully analytic solutions of all path integrals in the Kerr exterior were consequently found in [91] before being nicely placed within the context of gravitational lensing in [92].

In this section, we aim to perform an overview of gravitational lensing for rotating celestial bodies in the most general possible sense, following [91, 92]. We focus our discussion on the geodesic equations (which form an analogue of the standard lens equations), the geometrical construction describing this phenomena and the deeper meaning behind the Carter constant. For an even deeper review, we highly recommend the comprehensive monograph [87].

5.2.1 Geodesic equations

As we have already stated, gravitational lensing in the Kerr background is significantly more complicated (than in Schwarzschild background), since the addition of the celestial body's rotation breaks much of the symmetry utilised for the Schwarzschild case. Before discussing the geometrical implications that arise when extending to Kerr lensing, we will begin our discussion by analysing the null geodesic equations in Kerr spacetime.

The metric of Kerr spacetime can be expressed in Boyer-Lindquist coordinates (t, r, θ, ϕ), with line element

$$ds^2 = -\frac{\Delta}{\Sigma}(dt - a\sin^2\theta d\phi)^2 + \frac{\Sigma}{\Delta}dr^2 + \Sigma d\theta^2 + \frac{\sin^2\theta}{\Sigma}\big[(r^2+a^2)d\phi - a dt\big]^2, \qquad (5.2.1)$$

where we have used natural units, $G = c = 1$, for simplicity. For the sake of brevity, we have also introduced the length scales

$$\Sigma(r,\theta) = r^2 + a^2\cos\theta, \quad \Delta(r) = r^2 - 2Mr + a^2. \qquad (5.2.2)$$

This metric describes the geometry of a spacetime surrounding a celestial object of mass M that rotates with angular momentum $J = Ma$, such that one restricts $0 < a < M$ (in order to avoid the case of the naked singularity at $a = 0$ and ensure the object does not spin faster than the speed of light). In the case of a black hole, the inner/outer horizons arise from the roots of $\Delta(r)$,

$$r_\pm = M \pm \sqrt{M^2 - a^2}. \qquad (5.2.3)$$

Geodesic motion in the Kerr geometry is entirely characterised by three conserved quantities. The first two of these quantities, interpreted as the total energy of the free particle at infinity and the angular momentum of the free particle parallel to the axis of symmetry are associated with the existence of two Killing vectors ∂_t and ∂_ϕ. These Killing vectors, admitted by the metric, generate time-translational symmetry and axisymmetry isometries respectively. Thus,

$$E = p_\mu \partial_t^\mu = -p_t, \qquad L_z = p_\mu \partial_\phi^\mu = p_\phi, \qquad (5.2.4)$$

where p^μ denotes the four-momentum of a free particle. Particularly, in our case of interest when studying null geodesics, this free particle is of course a photon, hence

$$g^{\mu\nu} p_\mu p_\nu = 0. \qquad (5.2.5)$$

The third constant of motion is more elusive and its physical interpretation is much less well understood. This is further discussed in section 5.2.4. Its existence arises due to there being a third isometry generated by the Kerr metric; an irreducible symmetric Killing tensor

$$K_{\mu\nu} = -J^\gamma_\mu J_{\gamma\mu}, \quad J = a\cos\theta\, dr\wedge(dt - a\sin^2\theta\, d\phi) + r\sin\theta\, d\theta\wedge[(r^2+a^2)\, d\phi - a\, dt]. \qquad (5.2.6)$$

The third conserved quantity, known as the *Carter constant*, is therefore given by

$$k = K^{\mu\nu} p_\mu p_\nu = p_\theta^2 + \left(\frac{p_\phi}{\sin\theta} + a\, p_t \sin\theta\right)^2, \qquad (5.2.7)$$

which can clearly be seen to be manifestly positive. This final conserved quantity was initially shown to exist in [85], as a consequence of the separability of the Hamilton-Jacobi equation. For our purposes, it is useful to work with a slightly different separation constant, sometimes referred to in the literature as the Carter integral:

$$\mathcal{Q} = k - (L_z - aE)^2 = p_\theta^2 - a^2 p_t^2 \cos^2\theta + p_\phi^2 \cot^2\theta. \tag{5.2.8}$$

In fact, in order to minimise the number of parameters, it is convenient to rescale the null ray's angular momentum, L_z, about the spin axis and the Carter integral, $\mathcal{Q}$, by the energy at infinity E in the following manner:

$$\lambda = \frac{L_z}{E}, \quad \eta = \frac{\mathcal{Q}}{E^2}. \tag{5.2.9}$$

These new parameters λ and η play an important role when looking specifically at the geometrical construction of gravitational lensing in Kerr spacetime. As a matter of fact, they replace the single impact parameter ξ that appears in the Schwarzschild case, but we will save this discussion for section 5.2.3.

One can now invert the above equations for the constants of motion $\{E, L_z, k\}$ and explicitly form an expression describing a the instantaneous four-momentum $p = p_\mu dx^\mu$ of particle following a null geodesic in the Kerr geometry. Then, by the appropriate choice of affine parameter for null geodesics, the four-momentum p^μ describing the trajectory of the null geodesics in the Kerr spacetime can be constructed to give the Carter equations [85]

$$\frac{\Sigma}{E} p^r = \pm_r \sqrt{\mathcal{R}(r)}, \tag{5.2.10}$$

$$\frac{\Sigma}{E} p^\theta = \pm_\theta \sqrt{\Theta(\theta)}, \tag{5.2.11}$$

$$\frac{\Sigma}{E} p^\phi = \frac{a}{\Delta(r)}(r^2 + a^2 - a\lambda) + \frac{\lambda}{\sin^2\theta} - a, \tag{5.2.12}$$

$$\frac{\Sigma}{E} p^t = \frac{r^2 + a^2}{\Delta(r)}(r^2 + a^2 - a\lambda) + a(\lambda - a\sin^2\theta), \tag{5.2.13}$$

where the signs $\pm_r$ and $\pm_\theta$ indicate the signs of the four momenta p^r and p^θ respectively. Here we have introduced the radial and angular potentials

$$\mathcal{R}(r) = (r^2 + a^2 - a\lambda)^2 - \Delta(r)\left[\eta + (\lambda - a)^2\right], \tag{5.2.14}$$

$$\Theta(\theta) = \eta + a^2\cos^2\theta - \lambda^2\cot^2\theta, \tag{5.2.15}$$

quantities that are defined such that their zeros correspond to the turning points of the motion in the r and θ directions.

These geodesic equations can be recast as integrals of motion, where one integrates along the trajectory connecting two spacetime events, $x_s^\mu = (t_s, r_s, \theta_s, \phi_s)$ and $x_o^\mu = (t_o, r_o, \theta_o, \phi_o)$, such that the subscripts s and i indicate the event relates to the source or observer respectively. In integral form, the geodesic equations are

$$I_r = G_\theta, \tag{5.2.16}$$

$$\Delta\phi := \phi_o - \phi_s = I_\phi + \lambda G_\phi, \tag{5.2.17}$$

$$\Delta t := t_o - t_s = I_t + a^2 G_t, \tag{5.2.18}$$

where

$$I_r = \fint_{r_s}^{r_o} \frac{dr}{\pm_r \sqrt{\mathcal{R}(r)}}, \tag{5.2.19}$$

$$G_\theta = \fint_{\theta_s}^{\theta_o} \frac{d\theta}{\pm_\theta \sqrt{\Theta(\theta)}}, \tag{5.2.20}$$

$$I_\phi = \fint_{r_s}^{r_o} \frac{a(2Mr - a\lambda)}{\pm_r \Delta(r)\sqrt{\mathcal{R}(r)}}\, dr, \tag{5.2.21}$$

$$G_\phi = \fint_{\theta_s}^{\theta_o} \frac{\csc^2\theta}{\pm_\theta \sqrt{\Theta(\theta)}}\, d\theta, \tag{5.2.22}$$

$$I_t = \fint_{r_s}^{r_o} \frac{r^2\Delta(r) + 2Mr(r^2 + a^2 - a\lambda)}{\pm_r \sqrt{\mathcal{R}(r)}}\, dr, \tag{5.2.23}$$

$$G_t = \fint_{\theta_s}^{\theta_o} \frac{\cos^2\theta}{\pm_\theta \sqrt{\Theta(\theta)}}\, d\theta. \tag{5.2.24}$$

The symbol $\fint$ is used to specify that these integrals should be understood as path integrals along the trajectory of the photon. While only a single angular turning point will be encountered in the weak deflection limit, the photon may encounter several angular inversion points in the strong deflection limit, giving rise to numerous relativistic images [292, 293, 296].

Much work [90, 91] has gone into finding and classifying the roots of the radial and angular potentials, $\mathcal{R}(r)$ and $\Theta(\theta)$, especially finding what the allowed regions for the null geodesics are in the (r, θ)-plane. Gravitational lensing is just one of the possible scenarios that arise when analysing the null geodesic equations and as such, is constrained to specific regions in the (λ, η) parameter space.

Once an allowed region has been established, one can find a real, smooth antiderivative for each integral G_i or I_i over this range in r or θ. The nice property of these antiderivatives is that they all reduce to manifestly real Legendre elliptic form or, in other words, they can be described using incomplete elliptic integrals $F(\varphi \mid k^2)$, $E(\varphi \mid k^2)$ and $\Pi(n; \varphi \mid k^2)$. These elliptic integrals become complete in the case $\varphi = \pi/2$, and these are denoted by

$K(k^2) = F(\pi/2 \,|\, k^2)$, $E(k^2) = E(\pi/2 \,|\, k^2)$ and $\Pi(n; k^2) = \Pi(n; \pi/2 \,|\, k^2)$. Further details on elliptic integrals, including their formal definitions, can be found in Appendix B.1.1. To stay consistent, we will use calligraphic symbols to indicate antiderivatives, choosing the positive sign in the integrand.

5.2.1.1 Angular integrals

When analysing the potential, $\Theta(\theta)$, for turning points in the θ-plane and the angular integrals, it is essential to specify which region of conserved quantity space one is working in, since the behaviour of the angular integrals differs in each region. Assuming one has $0 < \theta < \pi$, thus avoiding spherical coordinate system singularities, and setting $u = \cos^2\theta$, the roots $u_\pm$ for null geodesics can be found from setting $\Theta(\theta) = 0$, giving

$$u_\pm = \Delta_\theta \pm \sqrt{\Delta_\theta^2 + \frac{\eta}{a^2}}, \qquad \Delta_\theta = \frac{1}{2}\left(1 - \frac{\eta + \lambda^2}{a^2}\right). \tag{5.2.25}$$

Hence in terms of θ, the four roots of $\Theta(\theta)$ are given by $\arccos(\pm\sqrt{u_\pm})$,

$$\theta_1 = \arccos(\sqrt{u_+}), \tag{5.2.26}$$
$$\theta_2 = \arccos(\sqrt{u_-}), \tag{5.2.27}$$
$$\theta_3 = \arccos(-\sqrt{u_-}), \tag{5.2.28}$$
$$\theta_4 = \arccos(-\sqrt{u_+}), \tag{5.2.29}$$

coinciding only when $u_+ = u_-$ or if one of the sets of roots is null (i.e $u_+ = 0$ or $u_- = 0$). We can use these conditions to divide the (λ, η)-plane into various regions giving a clear structure to the parameter space. Within each region, the number of real roots of the angular potential and the sign of the potential on each side of them is fixed.

The resulting structure reveals a large portion of parameter space is forbidden, and motion is only allowed when $u_+ > 0$ and $u_- < 1$ giving a lower bound for η:

$$\eta \geq \begin{cases} 0 & \text{for } |\lambda| \geq a, \\ -(|\lambda| - a)^2 & \text{for } |\lambda| \leq a. \end{cases} \tag{5.2.30}$$

There are now two qualitatively different regions within the allowed parameter space describing the oscillatory motion:

A. Ordinary geodesics ($\eta > 0$): Oscillatory motion between two real turning points, $\theta_- = \theta_1 \in (0, \pi/2)$ and $\theta_+ = \theta_4 \in (\pi/2, \pi)$, crossing the equatorial plane each libration.

B. Vortical geodesics ($\eta < 0$): Vortical motion between two real turning points that never crosses the equatorial plane, $0 < \theta_- < \theta_+ < \pi/2$ or $\pi/2 < \theta_+ < \theta_- < \pi$, defining two distinct types of motion. Either $(\theta_-, \theta_+) = (\theta_1, \theta_2)$ and the geodesics are confined to a cone lying entirely in the northern hemisphere. Alternatively, $(\theta_+, \theta_-) = (\theta_3, \theta_4)$ and the geodesics are similarly confined in the southern hemisphere.

Here we quickly discuss the interpretation of the limiting case $\eta = 0$. If there are no turning points, this simply represents equatorial orbits corresponding to a limit of type A motion. If however, one allows non-equatorial turning points, a limit of type B motion is achieved, corresponding to the cone of oscillation reaching the equatorial plane (i.e. $\theta_2 \to \pi/2$ or similarly $\theta_3 \to \pi/2$), developing a nonintegrable singularity for the integrals, thus the motion can only have a single libration[1].

Note, that for the purposes of gravitational lensing, one restricts to ordinary geodesics ($\eta > 0$). While the case for $\eta < 0$, corresponding to vortical motion, can also be analysed [91], it can be shown that excluding these geodesics only removes a small part of the gravitational lensing region, in a region that is usually dark (the region in the centre of the observer's screen) [92].

The turning points $\theta_\pm$ for null geodesics satisfying $\eta > 0$ are found from setting $\Theta(\theta) = 0$, giving

$$\theta_\pm = \arccos(\mp\sqrt{u_+}) \tag{5.2.31}$$

where u_+ is defined as in (5.2.25). As $\eta > 0$ corresponds to type A motion, these turning points satisfy $\theta_- = \theta_1 \in (0, \pi/2)$ and $\theta_+ = \theta_4 \in (\pi/2, \pi)$. Furthermore, the equator acts as a line of symmetry so $\theta_+ = \pi - \theta_-$. Thus one is interested in solving the angular integrals (5.2.20, 5.2.22), in the allowed region satisfying $u_- < 0 \leq \cos^2\theta \leq u_+ < 1$.

Now, as u_+/u_- is negative, one can find the antiderivatives of the integrals of motion by unpacking the path integral as described in [91] by

$$G_i = m\hat{G}_i \pm_o \mathcal{G}_i^o \mp_s \mathcal{G}_i^s. \tag{5.2.32}$$

Here $\hat{G}_i$ indicates value of the corresponding integral G_i over one half-libration,

$$\hat{G}_\theta = \int_{\theta_-}^{\theta_+} \frac{d\theta}{\sqrt{\Theta(\theta)}} = \frac{2}{\sqrt{-u_- a^2}} K\left(\frac{u_+}{u_-}\right), \tag{5.2.33}$$

$$\hat{G}_\phi = \int_{\theta_-}^{\theta_+} \frac{\operatorname{cosec}^2\theta}{\sqrt{\Theta(\theta)}}\, d\theta = \frac{2}{\sqrt{-u_- a^2}} \Pi\left(u_+ \middle| \frac{u_+}{u_-}\right), \tag{5.2.34}$$

[1] We use the term libration throughout this work to refer to an oscillation between two turning points $\theta_\pm$.

$$\hat{G}_t = \int_{\theta_-}^{\theta_+} \frac{\cos^2\theta}{\sqrt{\Theta(\theta)}}\, d\theta = -\frac{4u_+}{\sqrt{-u_- a^2}} E'\left(\frac{u_+}{u_-}\right), \tag{5.2.35}$$

and m represents the number of angular turning points encountered along the trajectory. The antiderivatives $\mathcal{G}_i$ are given by

$$\mathcal{G}_\theta = -\frac{1}{2a}\int_0^{u_j} \frac{du}{\sqrt{u(u_+-u)(u-u_-)}} = -\frac{1}{a\sqrt{-u_-}}\, F\left(\arcsin\left(\frac{\cos\theta}{\sqrt{u_+}}\right)\middle|\frac{u_+}{u_-}\right), \tag{5.2.36}$$

$$\mathcal{G}_\phi = -\frac{1}{2a}\int_0^{u_j} \frac{du}{(1-u)\sqrt{u(u_+-u)(u-u_-)}} = -\frac{1}{a\sqrt{-u_-}}\, \Pi\left(u_+; \arcsin\left(\frac{\cos\theta}{\sqrt{u_+}}\right)\middle|\frac{u_+}{u_-}\right), \tag{5.2.37}$$

$$\mathcal{G}_t = -\frac{1}{2a}\int_0^{u_j} \frac{u\, du}{\sqrt{u(u_+-u)(u-u_-)}} = \frac{2u_+}{a\sqrt{-u_-}}\, E'\left(\arcsin\left(\frac{\cos\theta}{\sqrt{u_+}}\right)\middle|\frac{u_+}{u_-}\right), \tag{5.2.38}$$

where

$$E'(\varphi|k^2) := \partial_{k^2} E(\varphi|k^2) = \frac{E(\varphi|k^2) - F(\varphi|k^2)}{2k^2} \tag{5.2.39}$$

and we have used the substitution $u = u_+ t^2$ to ensure positivity and realness of each integral. The signs $\pm_i$ denote the signs of four momenta p_i^θ at either the source or observer point ($i = s$ and $i = o$ respectively). One should note that since $\mathrm{sign}(p^\theta)$ alters after every turning point, these signs can be related by the constraint

$$\pm_s = \pm_o (-1)^m. \tag{5.2.40}$$

So, the full set of angular path integrals for $\eta > 0$ can be expressed in terms of elliptic integrals [90, 91]:

$$G_\theta = \frac{1}{a\sqrt{-u_-}}\left[2mK\left(\frac{u_+}{u_-}\right) \pm_s F\left(\Psi_s^+\middle|\frac{u_+}{u_-}\right) \mp_o F\left(\Psi_o^+\middle|\frac{u_+}{u_-}\right)\right], \tag{5.2.41}$$

$$G_\phi = \frac{1}{a\sqrt{-u_-}}\left[2m\Pi\left(u_+\middle|\frac{u_+}{u_-}\right) \pm_s \Pi\left(u_+; \Psi_s^+\middle|\frac{u_+}{u_-}\right) \mp_o \Pi\left(u_+; \Psi_o^+\middle|\frac{u_+}{u_-}\right)\right], \tag{5.2.42}$$

$$G_t = -\frac{2u_+}{a\sqrt{-u_-}}\left[2mE'\left(\frac{u_+}{u_-}\right) \pm_s E'\left(\Psi_s^+\middle|\frac{u_+}{u_-}\right) \mp_o E'\left(\Psi_o^+\middle|\frac{u_+}{u_-}\right)\right], \tag{5.2.43}$$

where

$$\Psi_j^+ = \arcsin\left(\frac{\cos\theta_j}{\sqrt{u_+}}\right) \tag{5.2.44}$$

and we have used the notation $E'(k^2) = E'(\pi/2|k^2)$ as in the other elliptic integrals.

If one considers the particular case of Schwarzschild lensing, $a = 0$, there is a singular turning point at

$$u_m = \frac{\eta}{\lambda^2 + \eta}. \tag{5.2.45}$$

One is required then to have $\eta > 0$ and the oscillation is described by type A motion. Further, the allowed region one considers is $0 \leq \cos^2\theta \leq u_m < 1$ and the angular integrals

reduce to

$$\tilde{G}_\theta = \sqrt{\frac{u_m}{\eta}}\Big[\pi m \pm_s \arcsin\sqrt{\frac{u_s}{u_m}} \mp_o \arcsin\sqrt{\frac{u_o}{u_m}}\Big], \tag{5.2.46}$$

$$\tilde{G}_\phi = \frac{1}{\sqrt{\eta}}\sqrt{\frac{u_m}{1-u_m}}\Big[\pi m \pm_s \arcsin\sqrt{\frac{u_s}{u_m}\Big(\frac{1-u_m}{1-u_s}\Big)} \mp_o \arcsin\sqrt{\frac{u_o}{u_m}\Big(\frac{1-u_m}{1-u_o}\Big)}\Big], \tag{5.2.47}$$

$$\tilde{G}_t = \frac{1}{2}\Big[u_m\tilde{G}_\theta - \sqrt{\frac{u_m}{\eta}}\big(\pm_s \sqrt{u_s(u_m-u_s)} \mp_o \sqrt{u_o(u_m-u_o)}\big)\Big]. \tag{5.2.48}$$

It is also worth noting that inverting the G_θ integral for either the observer angle θ_o or the source angle θ_s, allows us to express θ_o or θ_s as a function of G_θ [90,91,304]. Denoting the Jacobi elliptic sine function by $\mathrm{sn}(\varphi|k^2)$, explicitly performing this inversion gives

$$\frac{\cos\theta_s}{\sqrt{u_+}} = \mathrm{sn}\left(F\left(\arcsin\Big(\frac{\cos\theta_o}{\sqrt{u_+}}\Big)\Big|\frac{u_+}{u_-}\right) \pm_o \mathrm{sign}(\eta)a\sqrt{-u_-}G_\theta\Big|\frac{u_+}{u_-}\right). \tag{5.2.49}$$

5.2.1.2 Radial integrals

One can perform a similar analysis of the radial potential, $\mathcal{R}(r)$, in order to gain an insight into the radial behaviour. In order to find the roots at $\mathcal{R}(r) = 0$, it is convenient to rewrite our expression in the form

$$\mathcal{R}(r) = r^4 + (a^2 - \eta - \lambda^2)r^2 + 2M\zeta r - a^2\eta = 0, \tag{5.2.50}$$

where

$$\zeta = \eta + (\lambda - a)^2 \geq 0, \tag{5.2.51}$$

and its positivity is necessary in order for the motion to be in the region allowed by $\eta \geq 0$. (Note: this inequality is necessary for the stronger case when considering both ordinary and vortical motion.) It is important to notice that the following analysis does not include trajectories at $\zeta = 0$ since these correspond to principal null congruences [87]. In that specific instance, the conserved quantities λ and η satisfy

$$(\lambda, \eta) = (a\sin^2\theta_o, -a^2\cos^4\theta_o), \tag{5.2.52}$$

therefore the roots of the radial potential in this case are trivially

$$r = \pm ia\cos\theta_0. \tag{5.2.53}$$

As shown in [91], it is possible to calculate the roots by combining numerous techniques, where one now excludes principal null congruences $\zeta = 0$. One can implement Ferrari's method in order to find a general solution to the quartic equation, together with Cardano's

method to solve the resolvent cubic. Here we simply state the solution, but to see these methods performed in depth to solve $\mathcal{R}(r) = 0$, one refers the reader to [91]. The roots can then be found to be

$$r_1 = -z - \sqrt{-\frac{a^2 - \eta - \lambda^2}{2} - z^2 + \frac{2M\zeta}{4z}}, \tag{5.2.54}$$

$$r_2 = -z + \sqrt{-\frac{a^2 - \eta - \lambda^2}{2} - z^2 + \frac{2M\zeta}{4z}}, \tag{5.2.55}$$

$$r_3 = z - \sqrt{-\frac{a^2 - \eta - \lambda^2}{2} - z^2 - \frac{2M\zeta}{4z}}, \tag{5.2.56}$$

$$r_4 = z + \sqrt{-\frac{a^2 - \eta - \lambda^2}{2} - z^2 - \frac{2M\zeta}{4z}}, \tag{5.2.57}$$

where

$$z = \sqrt{\frac{\xi_0}{2}} > 0 \tag{5.2.58}$$

and ξ_0 is any root of the resolvent cubic. In our case, it is given by

$$\xi_0 = \omega_+ + \omega_- - \frac{a^2 - \eta - \lambda^2}{3}, \tag{5.2.59}$$

where

$$\omega_\pm = \sqrt[3]{-\frac{\mathcal{Q}}{2} \pm \sqrt{\left(\frac{\mathcal{P}}{3}\right)^3 + \left(\frac{\mathcal{Q}}{2}\right)^2}} \tag{5.2.60}$$

such that

$$\mathcal{P} = -\frac{(a^2 - \eta - \lambda^2)^2}{12} + a^2\eta, \tag{5.2.61}$$

$$\mathcal{Q} = -\frac{a^2 - \eta - \lambda^2}{3}\left[\left(\frac{a^2 - \eta - \lambda^2}{6}\right)^2 + a^2\eta\right] - \frac{M^2\zeta^2}{2}. \tag{5.2.62}$$

Due to lack of an r^3 term in the expression for the radial potential (5.2.50), the sum of the roots vanish,

$$r_1 + r_2 + r_3 + r_4 = 0, \tag{5.2.63}$$

which is to be expected since this is a general law for depressed quartic equations.

An in depth analysis of all the different classifications of roots is performed in [91], using a similar type of analysis to that for the angular integrals. The basic idea is to determine where the radial roots $\{r_1(\lambda,\eta), r_2(\lambda,\eta), r_3(\lambda,\eta), r_4(\lambda,\eta)\}$ coincide as these critical cases provide the boundaries of the various regions in the (λ,η)-plane. One further applies the angular restrictions on the parameter space (5.2.30) in order to find where all possible radii where any of the radial roots coincide.

For each of these double, triple or quadruple roots $\tilde{r}$, one may find corresponding equations for $\tilde{\lambda}(\tilde{r})$ and $\tilde{\eta}(\tilde{r})$. This results in the construction of two critical curves $\mathcal{C}_{\pm}$ in the (λ, η)-plane. Similarly to the analysis of the angular integrals, these critical curves $\mathcal{C}_{\pm}$ divide the allowed parameter space, the (λ, η)-plane, into four further subregions.

For each subregion, we know the exact number of real roots which we detail shortly and due to the smoothness of the roots $\{r_1, r_2, r_3, r_4\}$, any real roots with ordering, retain this ordering. Here, the roots have purposefully been labelled such that $r_1 < r_2 < r_3 < r_4$ in the case that they are all real. Similarly, at the inner and outer horizons one obtains a double root, thus this ordering remains when moving through the horizons within each region.

Thus to determine the general properties for each region of the (λ, η)-plane that a solution of radial roots may lie in, it is sufficient to evaluate one set of radial roots $\{r_1, r_2, r_3, r_4\}$ via (5.2.54, 5.2.55, 5.2.56, 5.2.57) at a single point in that region of the parameter space. This results in the general classification:

I. Four real roots such that two lie outside the horizon: $r_1 < r_2 < r_- < r_+ < r_3 < r_4$.

II. Four real roots that all lie within the horizon: $r_1 < r_2 < r_3 < r_4 < r_- < r_+$.

III. Two real roots that both lie within the horizon: $r_1 < r_2 < r_- < r_+$ and $r_3 = \bar{r}_4$.

IV. No real roots: $r_1 = \bar{r}_2$ and $r_3 = \bar{r}_4$.

Further, we may then find the allowed ranges of r when considering each of these subregions. This can be achieved by determining the sign of the radial potential $\mathcal{R}(r)$ for a particular choice of conserved quantities λ and η. Should the radial potential be positive, the range is considered to be allowed, ensuring real solutions to the integrals (5.2.19, 5.2.21). Exploring this avenue, and restricting oneself to consider only motion outside the horizon, the relevant ranges are as follows:

Now we have discussed the allowed parameter space for the radial integrals, we begin to focus on our case of interest. When considering gravitational lensing, it is important to note that in this paper we are assuming a distant observer i.e. $r_o \to \infty$.

In order to find whether the light ray encounters a turning point, it is sufficient to calculate $r_4(\lambda, \eta)$ and determine its position. If r_4 lies outside the horizon and is real, the ray has a turning point at r_4, otherwise it does not encounter any turning points. Trivially, a ray reaching an observer at infinity originates from either the event horizon (in the case of a white hole) or from infinity.

Ia. White hole to black hole: $r_+ < r < r_3$ - the null ray is emitted from the white hole before reaching a turning point $r = r_3$ and subsequently falling into the black hole.

Ib. Scattering: $r_4 < r < \infty$ - the null ray originates from infinity prior to reaching a turning point at $r = r_4$, before returning to infinity (the case of interest corresponding to gravitational lensing).

II, III, IV. Flying in or out: $r_+ < r < \infty$ - the null ray either originates from infinity and falls into a black hole horizon or is emitted from a white hole horizon and ends at infinity.

Therefore one can express the total of the radial integral I_r for a null ray reaching infinity as

$$I_r^{\text{total}} = \begin{cases} 2\int_{r_4}^{\infty} \frac{dr}{\sqrt{\mathcal{R}(r)}}, & r_+ < r_4 \in \mathbb{R}, \\ \int_{r_+}^{\infty} \frac{dr}{\sqrt{\mathcal{R}(r)}}, & \text{otherwise}, \end{cases} \tag{5.2.64}$$

and similarly for the other radial integrals I_θ and I_ϕ. Here we summarise the basic ideology for I_r, noting that similar calculations can be performed for I_θ and I_ϕ, which can be viewed in full in [91]. For the purposes of our work, we are only interested in the case where r_4 is greater than the horizon r_+, since for astrophysical purposes we wish to focus on null rays originating at infinity, corresponding to case (2) in Appendix B of [91]. So, the relative antiderivative is given by

$$\mathcal{I}_r^{(2)}(r) = \frac{2}{\sqrt{r_{31}r_{42}}} F\left(\arcsin\sqrt{\frac{r-r_4}{r-r_3}\frac{r_{31}}{r_{41}}}\middle|\frac{r_{32}r_{41}}{r_{31}r_{42}}\right), \tag{5.2.65}$$

where we have introduced the notation $r_{ij} = r_i - r_j$. Thus, the complete radial integral (5.2.64) is then expressed as

$$I_r^{\text{total}} = \frac{4}{\sqrt{r_{31}r_{42}}} F\left(\arcsin\sqrt{\frac{r_{31}}{r_{41}}}\middle|\frac{r_{32}r_{41}}{r_{31}r_{42}}\right). \tag{5.2.66}$$

For simplicity, we define the following quantities:

$$\Psi = \arcsin\sqrt{\frac{r_{31}}{r_{41}}}, \qquad k^2 = \frac{r_{32}r_{41}}{r_{31}r_{42}} \tag{5.2.67}$$

and so

$$I_r^{\text{total}} = \frac{4}{\sqrt{r_{31}r_{42}}} F(\Psi \mid k^2). \tag{5.2.68}$$

The same analysis can be performed for the second radial integral I_ϕ. Thus, the second radial integral takes the form,

$$I_\phi^{\text{total}} = 2\int_{r_4}^{\infty} \frac{a(2Mr - a\lambda)}{\Delta(r)\sqrt{\mathcal{R}(r)}} dr = g\sum_{i=1}^{2} \Gamma_i[(1-\beta_i^2)\Pi(\alpha_i^2; \Psi \mid k^2) + \beta_i^2 F(\Psi \mid k^2)], \quad (5.2.69)$$

where

$$g = \frac{4a}{\sqrt{r_{31}r_{42}}}, \qquad \Gamma_i = \frac{K_i}{r_4 - r_i}, \quad (5.2.70)$$

$$r_i = M + (-1)^{i+1}\sqrt{M^2 - a^2}, \qquad K_i = M + (-1)^{i+1}\frac{M^2 - a\lambda/2}{\sqrt{M^2 - a^2}}, \quad (5.2.71)$$

$$\alpha_i^2 = \frac{(r_i - r_3)r_{41}}{(r_i - r_4)r_{31}}, \qquad \beta_i^2 = \frac{r_i - r_4}{r_i - r_3}, \quad (5.2.72)$$

provided $a \neq M$.

To close this section, one makes some short comments discussing the special case where one considers an extremal Kerr geometry, $a = M$. For maximally spinning celestial objects, the roots of the radial potential $\mathcal{R}(r)$ takes a particularly nice form

$$r = \pm_1 \Delta_r \pm_2 \sqrt{(\Delta_r \mp_1 M)^2 + M(\lambda - 2M)}, \quad (5.2.73)$$

where

$$\Delta_r = \frac{1}{2}\sqrt{\eta + (\lambda - M)^2} \quad (5.2.74)$$

and there are four possible independent configurations based on the choice of signs. We note that in the particular situation where there is a double root of the radial potential (i.e. $\mathcal{R}(r) = \mathcal{R}'(r) = 0$), the double root $\tilde{r}$ must satisfy

$$(\tilde{r}^2 + a^2 - a\lambda)^2 - (\eta + (\lambda - a)^2)\Delta(\tilde{r}) = 0 \quad (5.2.75)$$

and

$$4\tilde{r}(\tilde{r}^2 + a^2 - a\lambda) - 2(\eta + (\lambda - a)^2)(\tilde{r} - M) = 0. \quad (5.2.76)$$

Then if $\tilde{r} = M$, as a consequence, the only possible solutions are where $a = M$ and $\lambda = 2M$: a special case of (5.2.73). Interestingly, this corresponds to the superradiant bound of an extremal black hole. As in the finite a case, the form of the first integral for the extremal case, I_r, is (5.2.68). The second radial integral, however, takes a more complicated form when $a = M$. Using partial fractions, I_ϕ can be expressed as

$$I_\phi = 2M^2 \int_{r_a}^{\infty} \left[\frac{2M - \lambda}{(r - M)^2} + \frac{2}{r - M}\right] \frac{dr}{\sqrt{\mathcal{R}(r)}}. \quad (5.2.77)$$

Now using the standard integrals and integration techniques in [305]:

$$I_\phi = \frac{gM}{r_4 - M}\Big\{\beta^2\Big[2+\frac{\beta^2(2M-\lambda)}{r_4-M}\Big]u+2(1-\beta^2)\Big[1+\frac{\beta^2(2M-\lambda)}{r_4-M}\Big]p+\frac{(1-\beta^2)^2(2M-\lambda)}{r_4-M}V\Big\}, \tag{5.2.78}$$

where

$$V = \frac{1}{2(\alpha^2-1)(k^2-\alpha^2)}\Big[\alpha^2 E(u)+(k^2-\alpha^2)\mathcal{F}+(2\alpha^2(k^2+1)-\alpha^4-3k^2)\mathcal{P}-\frac{\alpha^4 \mathrm{sn}u\ \mathrm{cn}u\ \mathrm{dn}u}{1-\alpha^2\mathrm{sn}^2 u}\Big]. \tag{5.2.79}$$

Here, g is as defined in (5.2.70), of course with $a \to M$. Similarly,

$$\alpha^2 = \frac{(M-r_3)r_{41}}{(M-r_4)r_{31}}, \qquad \beta^2 = \frac{M-r_4}{M-r_3}. \tag{5.2.80}$$

and one also uses the following shorthand to denote elliptic integrals,

$$\mathcal{F} = F(\Psi \mid k^2), \qquad \mathcal{P} = \Pi(\alpha^2; \Psi \mid k^2). \tag{5.2.81}$$

5.2.2 Critical rays

As previously illustrated, the radial potential has four distinct roots for generic values of the conserved quantities λ and η. If however, these variables take specific values $\tilde{\lambda}$ and $\tilde{\eta}$, then at a certain radius $\tilde{r}$, the radial potential emits a double root,

$$\mathcal{R}(r) = \mathcal{R}'(r) = 0. \tag{5.2.82}$$

We use the tilde notation to denote these 'critical values'. The critical radius $\tilde{r}$ only exists for $\tilde{r} > r_+$ if and only if [86, 91]

$$\tilde{\lambda} = a + \frac{\tilde{r}}{a}\Big[\tilde{r} - \frac{2\tilde{\Delta}}{\tilde{r}-M}\Big], \tag{5.2.83}$$

$$\tilde{\eta} = \frac{\tilde{r}^3}{a^2}\Big[\frac{4M\tilde{\Delta}}{(\tilde{r}-M)^2} - \tilde{r}\Big], \tag{5.2.84}$$

such that $\tilde{r}$ lies in the range $\tilde{r} \in [\tilde{r}_-, \tilde{r}_+]$ where

$$\tilde{r}\pm = 2M\Big[1+\cos\Big(\frac{2}{3}\arccos\Big(\pm\frac{a}{M}\Big)\Big)\Big]. \tag{5.2.85}$$

The existence of this double root indicates there are orbits that have a fixed Boyer-Lindquist radius $\tilde{r}$, which one associates with *bound photon orbits*. These are circular, equatorial orbits located at the boundaries $\tilde{r}_\pm$, as given in (5.2.85), where $\tilde{r}_+$ indicates retrograde motion and $\tilde{r}_-$ corresponds to prograde motion. Intermediate radii librate between turning points $\theta_\pm$ and so the region where bound photon orbits span the

Kerr spacetime, form a spherical shell, the 'photon shell', thats maximum thickness occurs at its equator, varying to its minimum at the pole. Some interesting limits worth noting are the non-rotating case ($a \to 0$) and the extremal limit ($a \to M$):

$$\lim_{a\to 0} \tilde{r}_{\pm} = 3M, \qquad \lim_{a\to M} \tilde{r}_{+} = 4M, \qquad \lim_{a\to M} \tilde{r}_{-} = M. \tag{5.2.86}$$

The non-rotating case results in the usual 'photon sphere' as the shell becomes vanishingly thin everywhere, while in the extremal limit, one is left with the largest thickness shell.

5.2.3 Kerr gravitational lensing geometry

Now we have analysed the geodesic equations in a Kerr spacetime, it is important to understand the geometry of our system. Since we are interested in non-planar orbits, one cannot apply many of the symmetries used in the Schwarzschild case. We will now explicitly derive a set of Cartesian coordinates, often called the 'screen coordinates' or alternatively the 'celestial coordinates', consisting of the orthogonal impact parameter (α, β), following [86, 306].

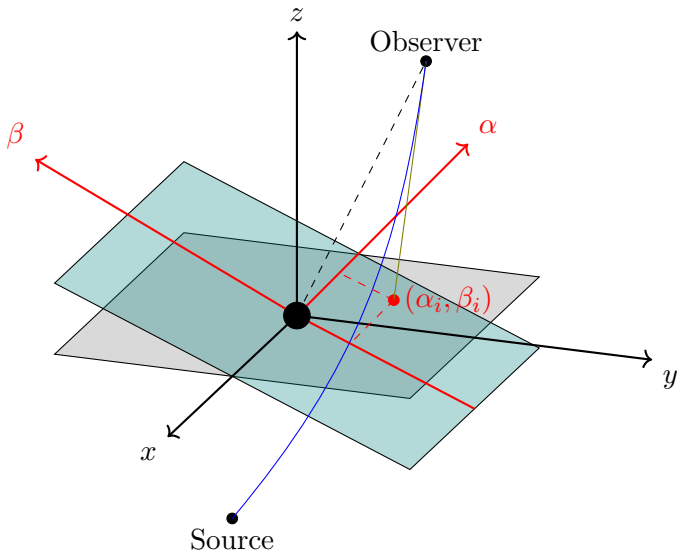

Figure 5.2.1: The geometric construction of a gravitational lens associated with the Kerr metric. A distant observer ($r_o \to \infty$) can establish a reference Cartesian coordinate system $\{x, y, z\}$ with the lens lying at its origin such that from infinity the lens is chosen to rotate about the z-axis. The observer and source positions are given by (r_o, θ_o, ϕ_o) and (r_s, θ_s, ϕ_s) respectively and the straight line from the observer that intersects the origin is normal to the celestial plane. The tangent vector of a null geodesic emitted by the source then intersects the celestial plane at some point (α_i, β_i).

To begin, we consider a geometry where the gravitational lens is placed at the origin and the observer and source positions are given by (r_s, θ_s, ϕ_s) and (r_o, θ_o, ϕ_o). For large r_o curvature becomes negligible and thus the Boyer-Lindquist coordinates may be expressed as a reference Cartesian coordinate system $\{x, y, z\}$, which is chosen such that the lens object rotates around the z axis (where $a > 0$ assumes the counterclockwise direction). One can choose θ_o such that the observer lies in the upper hemisphere (i.e. $\theta_o \in [0, \pi/2)$) using a reflection symmetry. Now without loss of generality, we may use axisymmetry to set the observer azimuthal angle to be zero, $\phi_o = 0$. With this set up, an incoming null ray can be described in the observers reference frame using a parametric curve

$$\vec{r}_\gamma = (x(r), y(r), z(r)), \tag{5.2.87}$$

such that $r^2 = x^2 + y^2 + z^2$ and r is the radial coordinate in Boyer-Lindquist coordinates.

One now introduces a plane intersecting with the origin describing the image as seen by the observer. We refer to this plane as the either the 'observer's sky', the 'celestial plane' or simply the (α, β)-plane. Similarly, α and β are known as 'celestial' or 'screen coordinates'. The unit vectors in the celestial plane are related to the Cartesian coordinate system by

$$\hat{\alpha} = -\sin\phi_o \hat{x} + \cos\phi_o \hat{y}, \tag{5.2.88}$$

$$\hat{\beta} = \mp\cos\theta_o(\cos\phi_o \hat{x} + \sin\phi_o \hat{y}) \pm \sin\theta_o \hat{z}. \tag{5.2.89}$$

Here, the upper (lower) sign corresponds to an image situated in the northern (southern) hemisphere of the observer's sky. The apparent position of the source on the screen, (α_i, β_i), can then be expressed as

$$(\alpha_i, \beta_i) = \alpha_i\hat{\alpha} + \beta_i\hat{\beta} = -(\alpha_i \sin\phi_o \pm \beta_i \cos\theta_o \cos\phi_o)\hat{x} + (\alpha_i \cos\phi_o \mp \beta_i \cos\theta_o \sin\phi_o)\hat{y} \pm \beta_i \sin\theta_o \hat{z}. \tag{5.2.90}$$

An alternative way to obtain the apparent position of the source is to extend the unit tangent vector $\vec{v}_\gamma$ of the null ray by a distance r_o. Expressing the unit tangent vector in terms of the four-momentum of the null ray at the observer p_o^μ,

$$v_o^i = \frac{p_o^i}{p_o^t}, \qquad i \in \{1, 2, 3\} \tag{5.2.91}$$

and noting the unit vectors appropriate for spherical coordinates are

$$\hat{r} = \sin\theta\cos\phi\hat{x} + \sin\theta\sin\phi\hat{y} + \cos\theta\hat{z}, \tag{5.2.92}$$

$$\hat{\theta} = \cos\theta\cos\phi\hat{x} + \cos\theta\sin\phi\hat{y} - \sin\theta\hat{z}, \tag{5.2.93}$$

$$\hat{\phi} = -\sin\phi\hat{x} + \cos\phi\hat{y}, \tag{5.2.94}$$

one can find

$$(\alpha_i, \beta_i) = -r_o^2 \left[\left(\cos\theta_o \cos\phi_o \frac{p_o^\theta}{p_o^t} - \sin\theta_o \sin\phi_o \frac{p_o^\phi}{p_o^t} \right) \hat{x} - \left(\cos\theta_o \sin\phi_o \frac{p_o^\theta}{p_o^t} + \sin\theta_o \cos\phi_o \frac{p_o^\phi}{p_o^t} \right) \hat{y} + \sin\theta_o \frac{p_o^\theta}{p_o^t} \hat{z} \right]. \quad (5.2.95)$$

Now we are left with two expressions (5.2.90), (5.2.95) which can trivially be equated so

$$\alpha_i = -r_o^2 \sin\theta_o \frac{p_o^\phi}{p_o^t}, \qquad \beta_i = \pm r_o^2 \frac{p_o^\theta}{p_o^t}. \quad (5.2.96)$$

These celestial coordinates can now be evaluated by substituting in the known expressions for the four momenta (5.2.11), (5.2.12) and (5.2.13) and taking the assumption that our observer is distant $r_o \to \infty$. So our equations reduce to

$$\alpha_i \approx -\frac{\lambda}{\sin\theta_o}, \qquad \beta_i \approx \pm\sqrt{\Theta(\theta_o)}. \quad (5.2.97)$$

There are two possibilities when considering the origin of the ray from the observer's perspective; either it came from the white hole[2] or from the celestial plane. This origin can be traced backwards to see whether it started at $r = r_+$ or $r \to \infty$. Consequently, there exists a boundary between the two possibilities in which, tracing back, the null ray will indefinitely orbit the lens approaching some bound orbit located at radius $\tilde{r}$. This bound orbit is the critical curve $\mathcal{C}$ and the conserved quantities of rays trapped here correspond to $\tilde{\lambda}(\tilde{r})$ and $\tilde{\eta}(\tilde{r})$, as given in (5.2.83) and (5.2.84) respectively. One can then use these critical conserved quantities to parametrise the critical curve in the celestial plane using (5.2.83), (5.2.84) and (5.2.97), constraining the (α, β) parameter space in gravitational lensing to only lie outside of $\mathcal{C}$. This can be shown more explicitly in figure 5.2.2.

Now, (5.2.97) can be put into another useful form,

$$\lambda \approx -\alpha_i \sin\theta_o, \quad (5.2.98)$$

$$\eta \approx (\alpha_i^2 - a^2)\cos^2\theta_o + \beta_i^2, \quad (5.2.99)$$

where the conserved quantities λ, η are now the subjects of the equations.

In order to test if screen point (α_i, β_i) is inside or outside the horizon, one substitutes (5.2.98), (5.2.99) into (5.2.57). If we find $r_4(\alpha_i, \beta_i)$ is real and outside the horizon then (α_i, β_i) is outside $\mathcal{C}$. Otherwise, $r_4(\alpha_i, \beta_i)$ lies inside the critical curve $\mathcal{C}$.

[2]We note that while white holes are fascinating mathematical constructs, from an astrophysical standpoint, white holes are not expected to truly exist as they would violate the second law of thermodynamics.

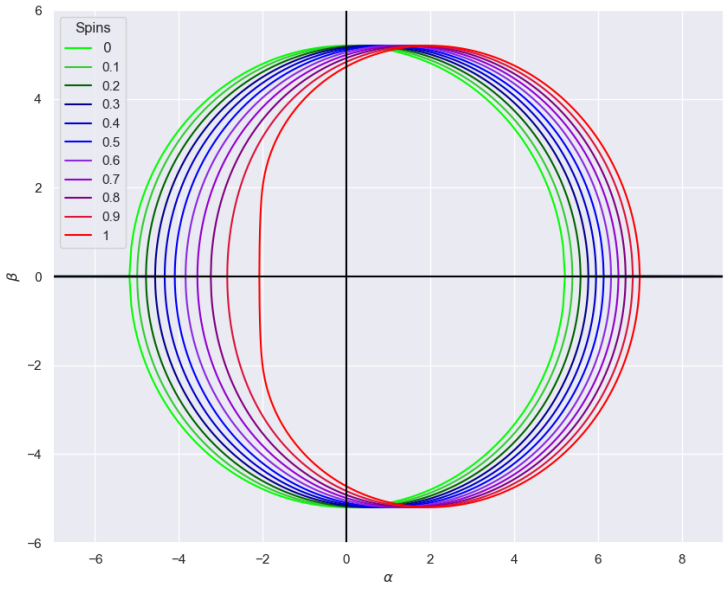

Figure 5.2.2: Critical curves for Kerr gravitational lenses at various spins in the observer's sky, restricting to $\eta > 0$ and assuming we are in the equatorial plane. Only null geodesics outside of the critical curves in the (α, β)-plane are subject to a single turning point r_4 and thus represent the desired scattering required for gravitational lensing. Consequently, from the perspective of a distant observer, a gravitationally lensed Kerr black hole would appear to have the shape of its critical curve $\mathcal{C}$, should the magnified source have a larger angular size than that of the black hole. This dark region in the observer's sky is often referred to as the shadow of the black hole.

Another useful expression to formulate is the angular position of the source in the absence of a lens $\{B_1, B_2\}$, in terms of the sources angular Boyer-Lindquist coordinates $\{\theta_s, \phi_s\}$. Rigorously studying the geometry of the Kerr gravitational lens (as depicted in figure 5.2.1) provides the general expressions

$$\tan B_1 = \frac{r_s \sin\theta_s \sin\phi_s}{r_o - r_s(\sin\theta_o \sin\theta_s \cos\phi_s + \cos\theta_o \cos\theta_s)}, \tag{5.2.100}$$

$$\tan B_2 = \frac{r_s(\sin\theta_o \cos\theta_s - \cos\theta_o \sin\theta_s \cos\phi_s)}{r_o - r_s(\sin\theta_o \sin\theta_s \cos\phi_s + \cos\theta_o \cos\theta_s)}. \tag{5.2.101}$$

Expressing these equations such that they have consistent notation with the usual Schwarzschild gravitational lensing variables, we are able to define the following distances:

$$D_d = r_o, \tag{5.2.102}$$

$$D_{ds} = -r_s(\sin\theta_o \sin\theta_s \cos\phi_s + \cos\theta_o \cos\theta_s), \tag{5.2.103}$$

$$D_s = D_d + D_{ds}. \tag{5.2.104}$$

As in the previous chapter, D_s represents the distance along the optical axis from the observer to the source plane, D_{ds} the distance along the optical axis between the lens and source planes, while D_d is the distance between the observer and the lens. Thus, equations (5.2.100) and (5.2.101) reduce to

$$D_s \tan B_1 = r_s \sin\theta_s \sin\phi_s, \tag{5.2.105}$$

$$D_s \tan B_2 = r_s(\sin\theta_o \cos\theta_s - \cos\theta_o \sin\theta_s \cos\phi_s). \tag{5.2.106}$$

These equations will play an essential role in what follows, specifically when we try to solve the Kerr lens equations (5.2.16), (5.2.17) in the weak deflection limit. More details on this will follow in chapter 6.2.1.

We now take a slight detour away from the specifics of Kerr gravitational lensing in order to try and understand the physical meaning behind the mysterious, third constant of motion that arises, the Carter constant.

5.2.4 The Carter constant

The interpretation of two of the constants of motion, E and L_z, generated by the Killing vectors ∂_t and ∂_ϕ respectively, are relatively straightforward and are well-known. The first, E, represents the total energy of the free particle at infinity (as seen by a distant observer), while L_z is the axial component of the particle's angular momentum. Of course when considering general free particles, we also have a third constant of motion in the form of that particle's rest mass m. Since in this discussion we are only concerned with modelling null rays, we only need to consider massless particles.

As previously mentioned, [85] discovered there was an additional constant of motion arising from separability of the Hamilton-Jacobi equation for a free particle in a Kerr geometry. This separation constant is generated from the symmetries of the Kerr metric (5.2.1), specifically the existence of the irreducible symmetric Killing tensor $K_{\mu\nu}$ given in (5.2.6).

While we have a clear description of the Carter constant mathematically, its physical meaning is somewhat more ambiguous. When considering the case of the Schwarzschild limit, $a \to 0$, the expression for the Carter constant k (5.2.7) can be drastically simplified

$$k = p_\theta^2 + \left(\frac{L_z}{\sin\theta}\right)^2, \tag{5.2.107}$$

recalling that $p_\phi = L_z$. Since we have the freedom to rotate coordinates in the Schwarzschild limit, one may trivially place this orbit in the equatorial plane $\theta = \pi/2$,

so $p_\theta = 0$ and

$$k = L_z^2. \tag{5.2.108}$$

Thus, in the Schwarzschild limit, the Carter constant has the physical interpretation of the square modulus of the total angular momentum of the particle (projected in the equatorial plane) as measured by a distant observer. However, the meaning behind the Carter constant in Kerr spacetime is not so straightforward. While one may intuitively think that it should have similar meaning to the $a \to 0$ case, and it does seem to (from $a \neq 0$ corrections), it is clear that the meaning certainly is not strictly the same.

Recalling the equation for the Carter constant k (5.2.7) and explicitly implementing the constants of motion where relevant,

$$k = p_\theta^2 + \left(\frac{L_z}{\sin\theta} - aE\sin\theta\right)^2. \tag{5.2.109}$$

Following the analysis of [307], it is useful to define a new separation constant K where $K = k + 2aEL_z$ such that

$$K = p_\theta^2 + L_z^2 \mathrm{cosec}^2\theta + a^2E^2\sin^2\theta. \tag{5.2.110}$$

Since they are the exact same expressions that appear when studying the Schwarzschild case, the first two terms in (5.2.110) are trivially identifiable, corresponding to the declination and azimuthal components of angular motion with reference to the origin O of the coordinate frame. The only term that provides uncertainty is the final one, arising in the Kerr case as one introduces the spin, a, into the framework. Clearly, since we are considering photons and the Kerr metric is asymptotically flat, E^2 corresponds to the square modulus of the photon's linear momentum at infinity. One may of course check this by considering the Kerr metric $g^{\mu\nu}$ as $r \to \infty$. Then, under this new metric $g_\infty^{\mu\nu}$, we can express the square modulus of the photon's linear momentum as

$$p^2 = |p_r|^2 + |p_\theta|^2 + |p_\phi|^2 = g_\infty^{rr}p_r^2 + g_\infty^{\theta\theta}p_\theta^2 + g_\infty^{\phi\phi}p_\phi^2. \tag{5.2.111}$$

Clearly, evaluating these expressions as $r \to \infty$, the only non-trivial solution is

$$g_\infty^{rr}p_r^2 \xrightarrow{r\to\infty} E^2 = p^2 \tag{5.2.112}$$

as expected. Thus for a photon at asymptotic infinity, the total four-momenta of the photon p^2 comes solely from the radial term $|p_r|^2$. Hence, one can rewrite (5.2.110) as

$$K = p_\theta^2 + L_z^2 \mathrm{cosec}^2\theta + |p_r|^2 a^2\sin^2\theta. \tag{5.2.113}$$

In fact, as shown in [307], a similar result with equivalent interpretation holds for the case of massive particles and though we do not discuss that here the physical meaning of the Carter constant is much the same as for massless particles.

So, the separation constant K does not have the physical meaning of the 'square modulus of the 'usual' angular momentum of the photon' (i.e. the angular momentum derived by considering θ and ϕ motion only), as is the naive interpretation in the Schwarzschild case. Instead it is the algebraic sum of the squared angular momenta, taking into account all three contributions from angular motion θ, ϕ and radial motion r.

One should note that similarly to when interpreting the physical meaning of E as the total energy at infinity and L_z as the axial angular momentum at infinity, discussion of the interpretation of the Carter constant presented in this section assumes one is considering the weak-field region of the Kerr metric. Further, obviously the identifications of these constants of motion discussed here are as seen by a distant observer. For additional material involving the interpretation of the Carter constant, see [307, 308]

5.3 Uncovering fundamental physics

There are several motivations to explore the lensing properties of near-extremal black holes from a fundamental theory perspective. In this thesis, it is our intention to try and provide incentive to utilise gravitational lensing to study two specific notions in fundamental theory. We dedicate this section to providing a very brief description of these concepts, the first being the fuzzball proposal, originally posed in [93, 94]. The topic is most broadly reviewed in the following works [95, 96]. Secondly we turn our attention to the Kerr/CFT correspondence [97, 98], an extension to the more well-recognised AdS/CFT correspondence [25] which was heavily discussed in Part I.

5.3.1 The fuzzball proposal

Motivated by the information loss problem [104], there have been many proposals within the literature for black hole geometries having small deviations from Einstein solutions close to the black hole horizon. These small deviations typically capture the nature of the specific black hole microstate. One of the best studied proposals is the fuzzball (or black hole microstate) hypothesis. The fuzzball proposal [93–96] states that individual black hole microstates are captured by geometries that resemble the black hole up to near horizon scales, but the microstate geometries differ very close to the horizon and do not have sharp horizons.

When studied in full generality, microstate geometries must be understood as full solutions of quantum gravity i.e. string and quantum effects are required to describe the microstate in detail. These configurations are especially complicated, quantum stringy objects which cannot (yet) be described using current tools, however subsets of fuzzballs may be constructed using supergravity solutions. Furthermore, the region outside the black hole can be understood in terms of gravitational solutions, in which there are additional fields as well as the metric and typically there is no exact rotational or time translation symmetry.

Fuzzball geometries are best understood in the context of near extremal (low temperature) black holes, as they have been extensively explored within string theory in this regime [309–328]. While it becomes increasingly difficult to find microstate geometries which are non-supersymmetric, various have been constructed [329–339], though most consider *overspinning* compact objects (similar to the case of $a > M$ when considering a Kerr black hole). With regards to the asymptotics of near-horizon extremal Kerr (NHEK), microstate geometries have rather recently been uncovered [340]. The construction of microstates for Schwarzschild black holes is considerably less well-understood and these are believed to be captured less well by gravity with additional fields.

5.3.2 The Kerr/CFT correspondence

A second important motivation for exploring lensing of near extremal black holes is the Kerr/CFT correspondence. The Kerr/CFT correspondence [97, 98] proposes that near extremal Kerr black holes can be described holographically by a conformal field theory[3]. The terminology of 'conformal field theory' is imprecise: the proposed dual field theory is actually not a relativistic conformal field theory, but rather a non-relativistic warped theory with scale invariance.

Moreover, the Kerr/CFT correspondence is not understood to the level of detail as AdS/CFT. In Kerr/CFT the relations between bulk fields and dual operators of specific scaling dimension are understood, but relatively few features of the dynamics have been explored. Nevertheless, the Kerr/CFT correspondence has proven to be useful in understanding the structure of certain infalling (plunge) orbits in near extremal Kerr geometries. More specifically, the Kerr/CFT correspondence made manifest underlying symmetries of the plunge orbit equations related to the scale invariance (see for example [341–343]), and these could be exploited to understand better the structure of these orbits.

[3]For more details on holography and the AdS/CFT correspondence, see Part I.

CHAPTER 6

Gravitational microlensing in Kerr spacetime

6.1 Introduction

Judging from the Galaxy's current stellar population, there appears to be an abundance of black holes contained within the Milky Way. In fact, current predictions quantify the total number of black holes present in our Galaxy to be of order $\simeq 10^8$ [344–346], under the assumption that stars greater than $\sim 20M_\odot$ end their lives as black holes [347–351]. The most prominent success with regards to the discovery of black holes stems from astrophysical observations of binary systems in which a compact object (neutron star or black hole) accretes matter from its companion star resulting in the emission of X-rays [352]. Significant study of these X-ray binary systems and the development of numerous modelling techniques (for reviews see [352, 353]) has led to detection and mass determination of various black holes (e.g. [354–356]).

While various dynamical methods may be implemented to determine the mass of compact objects (e.g. [353]), explicitly obtaining the mass using gravitational lensing has historically been difficult, often relying on methods involving the microlensing parallax [357, 358]. Despite this, great persistence has led to many intriguing results [285, 286]. One of the most staggering properties of the observed mass distribution for these compact objects is the apparent existence of a 'mass gap' between low-mass black holes and high-mass neutron stars (e.g. binary radio pulsars [359, 360]);

i.e. there had been no observations of compact remnants for which masses lie within the range $2M_\odot - 5M_\odot$. While observations of accreting binary systems consisting of black holes and their companion stars (via their X-ray emission spectra) has provided a glimpse into the nature of astrophysical black holes, there is sufficient evidence suggesting these systems only make up a significantly small proportion of binaries within our Galaxy [361, 362].

When considering binary systems in this paper, we mainly study (the self-lensing effects of) non-accreting systems that may be considered pristine; i.e. the compact objects within have never accreted any material since they were formed so maintain much of their innate structure. In most recent times, examples of non-accreting or weakly accreting compact objects with masses contained within the mass gap have been found in a number of binary systems [363–365]. Further, an enormous population of binary systems consisting of different combinations of black holes and neutron stars (binary black holes, black hole - neutron star pairs and neutron star binaries) has recently been unveiled by the Laser Interferometry Gravitational Wave Observatory (LIGO) and Virgo Collaboration [6], a direct consequence from the first detection of gravitational waves. In the subsequent work [366, 367], the corresponding black hole masses present in the pre-merger systems was inferred to be in the range $6M_\odot - 95M_\odot$, albeit with two distinct outliers present in the secondary masses. These low-mass compact objects were projected to have masses of $2.6M_\odot$ and $2.8M_\odot$, lying in the mass gap thus with the potential to be characterised as either black holes or neutron stars.

It has become extremely evident that understanding this mass gap is crucial to gain insight into black hole/neutron star formation and the supernova process [368, 369]. Since pristine compact objects have not accreted any mass since their initial formation, there is considerable reason to suggest that their mass distributions will unravel a more detailed description of the supernova explosion mechanism than possible from studying X-ray binaries. Binaries that do not exhibit accretion can be detected most notably using signatures obtained from self-lensing [370] (a form of microlensing) though other methods exist (such as those presented in [371, 372]).

Gravitational microlensing [45] is an observed astrophysical phenomenon consisting of isolated or binary lenses (stars, compact objects and even exo-planets) that pass between a background source and an observer. With the continuous evolution of modern instruments [373, 374] microlensing has indeed become a very effective tool for the discovery and characterisation of faint objects that may be invisible to other conventional methods. One of its most vital applications is its ability to constrain the available parameter space for the mass in massive compact halo objects (MACHOs) [375].

A specific type of microlensing may occur when studying binary systems consisting of a compact object and its optically bright companion star. As the two celestial objects come into alignment from the perspective of an observer, the compact object acts as a gravitational lens for its companion star [370]. This phenomenon is referred to as self-lensing. At the time of writing, a total of five binaries have been observed to exhibit self-lensing, each accommodating at least one white dwarf [376–378]. Studies of self-lensing populations in optical surveys [362] have shown the vast majority ($\gtrsim 99\%$) of neutron star and black hole gravitational lenses present in self-lensing are indeed pristine compact objects. Thus, these systems become a natural object to study, from the perspective of self-lensing, to explore both the black hole formation mechanism (via core collapse supernova) and the binary evolution process.

In this section, we focus our attention to the modelling of self-lensing binaries as well as the even more elusive microlensing of isolated compact objects. For both phenomena, we consider the particular instance where the minimum distance between the light ray and the compact object (lens) always lies far outside of the gravitational radius of the lens (i.e in the weak deflection limit) and the system is subject to large astrophysical separations. Similar to binaries of pristine compact objects, isolated compact objects are unlikely to have been drastically altered by external effects since their formation and so probing them offers a potentially unique outlet to understanding the supernova process. Recent advancements were made with the initial detection and subsequent mass measurement of isolated stellar-mass black holes (or neutron stars) [285, 286].

Although many fascinating phenomena have been detected using current astrophysical models, there is an obvious limitation. Since all of these models assume a regime in which the lens can be described using a Schwarzschild background metric, the effect of the spin of the compact object has been negated. While this may provide a sufficient characterisation for low-spinning compact objects and one expects gravitational lenses that possess higher spins to have similar behaviour, in order to appropriately model these highly spinning compact objects, it is essential to adopt a Kerr background metric.

Enlightenment on the behaviour of null geodesics in Kerr spacetime was first provided by Carter [85] and has been extensively studied since [2, 86–92, 295–302, 306, 379]. On one hand, significant focus has been dedicated to understanding the effects of strong field gravitational lensing [89–92, 296, 300–302, 306] for Kerr black holes and finding the positions of the resultant relativistic images [292]. Most recently, the publication of the interferometric observations of the Galactic black hole M87 by the Event Horizon Telescope (EHT) collaboration [7–12] has inspired various works concerning black hole shadows and photon rings (e.g. [302, 303]).

On the other hand, the weak deflection limit has received much less attention when considering gravitational lensing in a Kerr background [2, 88]. Utilising the expansions of [2], we aim to show the importance of the inclusion of the spin of the compact object. While the magnification of the source in the Schwarzschild case is dependent upon the astrophysical (or binary) separation, the mass and the radius of the compact object, we will see that the spin plays an equally important role.

Although the utilisation of microlensing to model these astrophysical phenomena may be the most obvious application of the analysis contained within these works, one may wish to purse alternative avenues, particularly those concerning fundamental theory. Accordingly, we can place this work under the context of both the fuzzball (black hole microstate) proposal [93–96] and that of the Kerr/CFT correspondence [97, 98] through the use of extremal (or near-extremal) black holes. Extremal black holes have provided an abundant supply of novel concepts and techniques within the realms of quantum gravity and quantum field theory [25, 97, 103, 212, 213].

Our best understanding of fuzzball geometries stems from the study of near-extremal (low temperature) black holes, with significant work dedicated to exploring this regime [309–328]. Further, microstate geometries for non-extremal and non-supersymmetric black holes remain elusive and so there are many difficulties that arise when attempting to compare observations of astrophysical black holes to observational results expected from microstate geometries. For example, Schwarzschild black holes microstate structure is poorly understood and is believed to be captured less well by gravity with additional fields.

In recent literature [380–382] there have been a number of suggestions of ways to characterise near extremal black hole microstates astrophysically. Effects described from the analysis of lensing and occultation may provide a new way to physically distinguish between black holes and microstate geometries.

Similarly, extremal black holes play an essential role in the Kerr/CFT correspondence. This conjecture states that these near-extremal Kerr black holes are dual to a non-relativistic warped theory with scale invariance[1], according to the holographic principle. Analytic solutions of the gravitational lens equations in Kerr spacetime [2, 89–92] could indeed help uncover a fresh understanding of underlying symmetries of the dynamics and give us new insights from the perspective of the dual field theory.

In section 6.2, we review the analytic formulation of gravitational lensing by a rotating, compact object in the weak deflection limit [2, 88]. Then, in section 6.3, we

[1]While the terminology refers to the dual field theory as a CFT, it is not actually a relativistic CFT.

discuss the deep implications of the spin asymmetry that arises in Kerr lensing. More explicitly, we illustrate these effects by considering the point source magnification curves for various different spin and inclination configurations, comparing them to the analogous magnification curves that would arise in the Schwarzschild case. We then extend this analysis by considering extended sources and limb darkening effects in section 6.4, before concluding and exploring future directions for research in section 6.5, providing insight to applications in both astrophysics and fundamental theory.

6.2 Kerr gravitational lensing: the weak deflection limit

As we have touched upon, gravitational lensing is extremely well understood in the Schwarzschild regime, but considerably less studied using a Kerr background. While the full geodesic equations, (5.2.16) and (5.2.17), are required when considering the case of strong gravitational fields [89, 293, 294] and thus studying relativistic images [292], in the weak deflection limit, the situation dramatically simplifies. Following the analysis in [2, 88], in this section we describe Kerr lensing in the weak deflection limit, from a purely analytical perspective.

The weak deflection limit is founded upon the assumption that the point of closest approach is situated far beyond the Schwarzschild radius of the gravitational lens. Since there is only a single turning point r_4 present in the weak deflection limit [88] and the impact parameter can be well approximated (exactly equal to in the spherically symmetric case) by

$$\xi = \sqrt{\alpha^2 + \beta^2} \simeq \sqrt{\lambda^2 + \eta}, \tag{6.2.1}$$

then we are in the weak deflection limit if $r_{\rm sch} \ll \sqrt{\lambda^2 + \eta}$. Consequently, one introduces the two new independent quantities, $\hat{M}$ and $\hat{a}$, defined as functions of the constants of motion λ and η,

$$\hat{M} = \frac{M}{\sqrt{\eta + \lambda^2}}, \qquad \hat{a} = \frac{a}{\sqrt{\eta + \lambda^2}}. \tag{6.2.2}$$

By definition, both $\hat{M}$ and $\hat{a}$ must be suitably small and can therefore be used as expansion parameters. When performing any expansions using these parameters, we do so up to order $\mathcal{O}(\epsilon^3)$ where we adopt the notation that terms of order $\mathcal{O}(\epsilon^n)$ consist of terms of order $\mathcal{O}(\hat{M}^i \hat{a}^j)$ with $n = i + j$.

Note it is very clear that two terms of the same formal order such as $\mathcal{O}(\hat{M}^2\hat{a})$ and $\mathcal{O}(\hat{M}^3)$ (both order $\mathcal{O}(\epsilon^3)$) do not necessarily have the same physical order. The only expansions in which this would indeed be true is for the particular case of an extremal (or near-extremal) Kerr black hole, since in this instance, $|a| \sim M$. In appendix B.1.2.2, the

minimum radial distance r_4 between a light ray and the gravitational lens is shown to be

$$r_4 \approx (\lambda^2+\eta)^{1/2}\Big\{1-\frac{r_{\rm sch}}{2\sqrt{\lambda^2+\eta}}-\frac{a^2\lambda^2}{2(\lambda^2+\eta)^2}+\frac{ar_{\rm sch}\lambda}{(\lambda^2+\eta)^{3/2}}-\frac{3r_{\rm sch}^2}{8(\lambda^2+\eta)}-\frac{r_{\rm sch}^3}{2(\lambda^2+\eta)^{3/2}}$$
$$+\frac{3a\lambda r_{\rm sch}^2}{2(\lambda^2+\eta)^2}-\frac{\lambda^2a^2r_{\rm sch}}{(\lambda^2+\eta)^{5/2}}-\frac{\lambda^2(\lambda^2-4\eta)a^4}{8(\lambda^2+\eta)^4}+\frac{\lambda(\lambda^2-\eta)r_{\rm sch}a^3}{(\lambda^2+\eta)^{7/2}}+\frac{(8\eta-51\lambda^2)r_{\rm sch}^2a^2}{16(\lambda^2+\eta)^3}$$
$$+\frac{3\lambda r_{\rm sch}^3a}{(\lambda^2+\eta)^{5/2}}-\frac{105r_{\rm sch}^4}{128(\lambda^2+\eta)^2}+\mathcal{O}(\epsilon^5)\Big\}. \quad (6.2.3)$$

This series expansion was first performed in [88] up to order $\mathcal{O}(\epsilon^3)$ before being extended to $\mathcal{O}(\epsilon^4)$ in [2].

6.2.1 Lens equations in the weak deflection limit

One may view the lens equations (5.2.16, 5.2.17) as a map between the angular source position $\{\mu_s,\phi_s\}$ and the image position $\{\theta_1,\theta_2\}$, where we define $\mu_s=\cos\theta_s$. The starting point is to represent the lens equations as a function of the conserved quantities $\{\lambda,\eta\}$, through a series expansion using the small parameters $\hat{M}$ and $\hat{a}$. In doing so, one must resolve the entire set of angular and radial integrals present in (5.2.16) and (5.2.17), to which we provide the supplement materials in appendices B.1.2.1 and B.1.2.2 to detail this analysis. Subsequently, the first lens equation (5.2.16) may then be expressed rather concisely as

$$\mu_s=-\mu_o\cos\delta+(-1)^k\sin\delta\left(\frac{\eta}{\lambda^2+\eta}-\mu_o^2\right)^{1/2}, \quad (6.2.4)$$

with

$$\delta=\frac{2r_{\rm sch}}{\sqrt{\lambda^2+\eta}}+\frac{15\pi r_{\rm sch}^2}{16(\lambda^2+\eta)}-\frac{4\lambda r_{\rm sch}a}{(\lambda^2+\eta)^{3/2}}+\frac{16r_{\rm sch}^3}{3(\lambda^2+\eta)^{3/2}}-\frac{15\pi\lambda ar_{\rm sch}^2}{4(\lambda^2+\eta)^2}$$
$$+\left(\mu_o^2+\frac{5\lambda^2-3\eta}{\lambda^2+\eta}+\frac{\eta}{\frac{\lambda^2\mu_o^2}{\mu_o^2-1}+\eta}\right)\frac{r_{\rm sch}a^2}{(\lambda^2+\eta)^{3/2}}-(\lambda^2+\eta)^{1/2}\frac{r_o+r_s}{r_or_s}-\frac{(\lambda^2+\eta)^{3/2}}{6}\frac{r_o^3+r_s^3}{r_o^3r_s^3}$$
$$+\frac{a^2\mu_o^2(1-\mu_o^2)\sqrt{\lambda^2+\eta}}{2(\lambda^2\mu_o^2-\eta(1-\mu_o^2))}\frac{r_o+r_s}{r_or_s}+\mathcal{O}(\epsilon^4), \quad (6.2.5)$$

where we have used the expansions (B.1.36) and (B.1.54). The second geodesic equation that describes the azimuthal motion, (5.2.17), can be expressed as

$$-\phi_s=\frac{\lambda}{|\lambda|}\pi+\frac{\lambda\delta}{\sqrt{\lambda^2+\eta}}\frac{1}{1-\mu_o^2}\left[1-(-1)^k\delta\frac{\mu_o}{\sqrt{1-\mu_o^2}}\sqrt{\frac{\eta}{\lambda^2+\eta}-\mu_o^2}\right]+\frac{2ar_{\rm sch}}{\lambda^2+\eta}+\delta\phi_s, \quad (6.2.6)$$

where one has used the expansions (B.1.47) and (B.1.56). Here, $\delta\phi_s$ is a small contribution of order $\sim\epsilon^3$ given by

$$\delta\phi_s = \frac{5\pi r_{\rm sch}^2 a}{4(\lambda^2+\eta)^{3/2}} - \frac{8\lambda r_{\rm sch}^3(2(\lambda^2+\eta)\mu_o^4+(2\lambda^2-\eta)\mu_o^2-\eta)}{3(\lambda^2+\eta)^3(1-\mu_o^2)^3} - \left(\frac{\eta}{\eta-(\lambda^2+\eta)\mu_o^2}+3\right)\frac{\lambda r_{\rm sch}a^2}{(\lambda^2+\eta)^2}$$
$$- \frac{a^2\lambda\mu_o^2}{2(\lambda^2\mu_o^2-\eta(1-\mu_o^2))}\frac{r_o+r_s}{r_o r_s} + \frac{\lambda(2\lambda^2\mu_o^2(\mu_o^2+1)-\eta(-2\mu_o^4+\mu_o^2+1))}{(\lambda^2+\eta)(1-\mu_o^2)^3}$$
$$\times\left[\frac{1}{3}(\lambda^2+\eta)\frac{(r_o+r_s)^2}{r_o^2 r_s^2} - \frac{2(r_o+r_s)r_{\rm sch}}{r_o r_s} + \frac{4r_{\rm sch}^2}{\lambda^2+\eta}\right]\frac{r_o+r_s}{r_o r_s}. \quad (6.2.7)$$

These two, fairly compact forms of the lens equations were first derived in [88] up to order $\mathcal{O}(\epsilon^2)$, prior to further extensions to $\mathcal{O}(\epsilon^4)$ in [2].

Now, it is desirable to express the lens equations in the Kerr background to have a form that aligns with the one that appears in the Schwarzschild description. Hence, one is required to introduce the angular image positions $\{\theta_1, \theta_2\}$, representing the angular position of the image situated on the observer's sky. We use the geometric description introduced in (5.2.3), writing the apparent position of the source (α_i, β_i) previously defined in (5.2.97), in terms of the traditional angular image positions:

$$r_o\frac{\tan\theta_1}{\sqrt{1+\tan^2\theta}} = -\frac{\lambda}{\sin\theta_o}, \quad (6.2.8)$$

$$r_o\frac{\tan\theta_2}{\sqrt{1+\tan^2\theta}} = \pm\sqrt{\Theta(\theta_o)}. \quad (6.2.9)$$

Here, θ is the separation of the image from the lens and $\tan^2\theta = \tan^2\theta_1 + \tan^2\theta_2$. Clearly, prograde photons (i.e. photons that traverse the equatorial plane in the same direction as the axis of rotation of the lens), specified by $\lambda > 0$, $\eta = 0$, produce images positioned to the left of the optical axis ($\theta_1 < 0$) and correspondingly retrograde photons (i.e. photons that traverse the equatorial plane in the opposite direction as the axis of rotation of the lens), specified by $\lambda < 0$, $\eta = 0$, produce images positioned to the right of the optical axis ($\theta_1 > 0$). Now, recall the equations for the angular positions of the source given in (5.2.105) and (5.2.106), with distances (5.2.102), (5.2.103) and (5.2.104). Combining these equations with (6.2.8) and (6.2.9), one can establish an expression that resembles the original form of the lens equations

$$B_1 = B_1(\theta_1, \theta_2), \quad (6.2.10)$$

$$B_2 = B_2(\theta_1, \theta_2). \quad (6.2.11)$$

In order to reduce these to a similar form, as we did for Schwarzschild, one introduces a series expansion parameter related to the angular Einstein ring. This small parameter has the form

$$\epsilon = \frac{\theta_E}{4D}, \quad (6.2.12)$$

where

$$\theta_E = \left[2\, r_{\rm sch} \frac{r_s}{r_o(r_o + r_s)}\right]^{1/2} \tag{6.2.13}$$

and $D \equiv r_s/(r_o + r_s)$. It should be noted that this definition of the Einstein radius uses radial distances, however in usual analysis within the weak deflection limit, distances measured along the optical axis are used (as in (5.1.23)). After applying this rescaling, we assume that the angular image positions can be expressed as series expansions in ϵ,

$$\theta_1 = \theta_E \left(\theta_{1(0)} + \epsilon\, \theta_{1(1)} + \epsilon^2 \theta_{1(2)} + \mathcal{O}(\epsilon^3)\right), \tag{6.2.14}$$

$$\theta_2 = \theta_E \left(\theta_{2(0)} + \epsilon\, \theta_{2(1)} + \epsilon^2 \theta_{2(2)} + \mathcal{O}(\epsilon^3)\right), \tag{6.2.15}$$

the details of which we will delve into in the next section. The full angular separation of the image from the lens is

$$\theta = \theta_E \left(\theta_{(0)} + \epsilon\, \theta_{(1)} + \epsilon^2 \theta_{(2)} + \mathcal{O}(\epsilon^3)\right). \tag{6.2.16}$$

Now, one is able to rescale the source position by $\beta_i \equiv \tan B_i/\theta_E$. Further, assuming the thin lens approximation (i.e. all angles are small), we may reduce the lens equations to a familiar, simple form:

$$B_1 = \theta_1 - D\hat{\alpha}_1(\theta_1, \theta_2), \tag{6.2.17}$$

$$B_2 = \theta_2 - D\hat{\alpha}_1(\theta_1, \theta_2), \tag{6.2.18}$$

where $\hat{\alpha}$ represents the angle of deflection of the null ray as defined previously and we have included terms up to $\sim \epsilon^2$ [2].

6.2.2 Image Positions

Consider the perturbative solutions to the lens equations, (6.2.17) and (6.2.18). These can be solved term by term, assuming the series expansions (6.2.14), (6.2.15) and (6.2.16), to find the image positions $\{\theta_1, \theta_2\}$. To lowest order in ϵ, the Kerr lens equations reduce to the familiar Schwarzschild lens equations,

$$\beta_1 = \theta_{1(0)}\left(1 - \frac{1}{\theta^2_{(0)}}\right), \tag{6.2.19}$$

$$\beta_2 = \theta_{2(0)}\left(1 - \frac{1}{\theta^2_{(0)}}\right), \tag{6.2.20}$$

such that $\theta^2_{(0)} = \sqrt{\theta^2_{1(0)} + \theta^2_{2(0)}}$. Then consequently the corresponding image positions are given by

$$\theta^{\pm}_{1(0)} = \frac{1}{2}\Big(1 \pm \sqrt{1 + \frac{4}{\beta^2}}\Big)\beta_1, \tag{6.2.21}$$

$$\theta^{\pm}_{2(0)} = \frac{1}{2}\Big(1 \pm \sqrt{1 + \frac{4}{\beta^2}}\Big)\beta_2, \tag{6.2.22}$$

with $\beta^2 = \beta_1^2 + \beta_2^2$. In [2], terms are computed up to $\mathcal{O}(\epsilon^2)$, with the lens spin parameter a appearing for the first time at order $\mathcal{O}(\epsilon)$. Below, we state the second order terms in order to show how the expansion varies when a is first introduced:

$$\theta_{1(1)} = \theta^{\rm Sch}_{(1)}\frac{\theta_{1(0)}}{\theta_{(0)}} + \frac{(1 - \theta^2_{1(0)} + \theta^2_{2(0)})\sqrt{1-\mu_o^2}}{1 - \theta^4_{(0)}}\frac{a}{M}, \tag{6.2.23}$$

$$\theta_{2(1)} = \theta^{\rm Sch}_{(1)}\frac{\theta_{2(0)}}{\theta_{(0)}} - \frac{2\theta_{1(0)}\theta_{2(0)}\sqrt{1-\mu_o^2}}{1 - \theta^4_{(0)}}\frac{a}{M}, \tag{6.2.24}$$

where

$$\theta^{\rm Sch}_{(1)} = \frac{15\pi}{16(1 + \theta^2_{(0)})}. \tag{6.2.25}$$

When studying these second order contributions, one notices interesting behaviour: a degeneracy arises between lenses in the Kerr background and 'shifted' lenses in the Schwarzschild background. This degeneracy becomes manifest such that these shifted Schwarzschild lenses have undergone a displacement from the optical axis along the equatorial plane at $\{\theta_1, \theta_2\} \simeq \theta_E\{a\sqrt{1-\mu_o^2}\epsilon, 0\}$. From the perspective of the observer, the two weak field images produced would appear to have undergone an anti-clockwise rotation about the optical axis, with respect to line intercepting the unperturbed image in the Schwarzschild regime [383].

The third order contributions take the form

$$\begin{aligned}\theta_{1(2)} = \theta^{\rm Sch}_{(2)}\frac{\theta_{1(0)}}{\theta_{(0)}} + \frac{16r_s^2}{3(r_o + r_s)^2}\theta_{1(0)}\theta^2_{2(0)} + \frac{a}{M}\Big[- \frac{4\theta_{2(0)}\mu_o}{\theta^2_{(0)}} + \frac{5\sqrt{1-\mu_o^2}\pi}{16\theta^3_{(0)}(1-\theta^2_{(0)})(1+\theta^2_{(0)})^3} \\ \times [\theta^2_{(0)}(1+\theta^2_{(0)})^2(1+4\theta^2_{(0)}) - (12\theta^6_{(0)} + 5\theta^4_{(0)} + 4\theta^2_{(0)} - 1)\theta^2_{1(0)}]\Big] \\ + \frac{a^2}{M^2}\Big[- \theta_{1(0)}(1-\mu_o^2)\Big\{\frac{4(\theta^4_{(0)} + \theta^2_{(0)} + 1)\theta^2_{2(0)}}{(1-\theta^2_{(0)})^2(\theta^2_{(0)}+1)^3} - \frac{\theta^2_{(0)}}{(\theta^2_{(0)}+1)^3}\Big\}\Big],\end{aligned} \tag{6.2.26}$$

$$\theta_{2(2)} = \theta^{\text{Sch}}_{(2)}\frac{\theta_{2(0)}}{\theta_{(0)}} + \frac{16r_s^2}{3(r_o+r_s)^2}\theta^2_{1(0)}\theta_{2(0)} + \frac{a}{M}\left[\frac{4\theta_{1(0)}\mu_o}{\theta^2_{(0)}} + \frac{5(-12\theta^6_{(0)} - 5\theta^4_{(0)} - 4\theta^2_{(0)} + 1)\theta_{1(0)}\theta_{2(0)}\sqrt{1-\mu_o^2}\pi}{16\theta^3_{(0)}(1-\theta^2_{(0)})(\theta^2_{(0)}+1)^3}\right] + \frac{a^2}{M^2}\left[\frac{\theta_{2(0)}(\theta^2_{(0)}(3\theta^4_{(0)} + 2\theta^2_{(0)} + 3) - 4(\theta^4_{(0)} + \theta^2_{(0)} + 1)\theta^2_{(0)})(1-\mu_o^2)}{(1-\theta^2_{(0)})^2(\theta^2_{(0)}+1)^3}\right], \quad (6.2.27)$$

where

$$\theta^{\text{Sch}}_{(2)} = \frac{225\pi^2(2\theta^2_{(0)}+1)}{256\theta_{(0)}(\theta^2_{(0)}+1)^3} - \frac{8[3(\theta^4_{(0)} - \theta^2_{(0)} - 1)r_o^2 - 3r_s(\theta^4_{(0)} - \theta^2_{(0)} + 3)r_o + r_s^2(2\theta^6_{(0)} - 7\theta^4_{(0)} + 6\theta^2_{(0)} - 6)]}{3(r_o+r_s)^2\theta_{(0)}(1+\theta^2_{(0)})}. \quad (6.2.28)$$

Taking into account these non-linear couplings between the physical parameters a and M (i.e considering expansions of order $\mathcal{O}(\epsilon^2)$) results in the degeneracy between Kerr lenses and the shifted Schwarzschild lenses being broken [383].

The total angular separation of an image with respect to the lens has the coefficients

$$\theta_{(1)} = \theta^{\text{Sch}}_{(1)} + \frac{a}{M}\frac{\theta_{1(0)}\sqrt{1-\mu_o^2}}{\theta_{(0)}(\theta^2_{(0)}+1)}, \quad (6.2.29)$$

$$\theta_{(2)} = \theta^{\text{Sch}}_{(2)} + \frac{a}{M}\frac{5(4\theta^4_{(0)} + 2\theta^2_{(0)} + 1)\theta_{1(0)}\sqrt{1-\mu_o^2}\pi}{8\theta^2_{(0)}(\theta^2_{(0)}+1)^3} + \frac{a^2}{M^2}\frac{2(1-\theta^2_{(0)})\theta^6_{(0)} + (4\theta^6_{(0)} + 3\theta^4_{(0)} + 4\theta^2_{(0)} + 1)\theta^2_{2(0)}}{2\theta_{(0)}(1-\theta^2_{(0)})(\theta^2_{(0)}+1)^3}(1-\mu_o^2). \quad (6.2.30)$$

6.2.3 Magnification

Recall from section 5.1.4 that the luminous amplification of an image or its magnification is given by the inverse of the Jacobian determinant of the lens mapping (5.1.29). In this instance, we are interested in the angular areas of the image in the observer's sky, $d\theta_1 d\theta_2$, and correspondingly, the source in the absence of lensing, $dB_1 dB_2$. Thus (5.1.29) reduces to

$$\mu = \left[\frac{\partial B_1}{\partial \theta_1}\frac{\partial B_2}{\partial \theta_2}\right]^{-1} \quad (6.2.31)$$

recalling $\mu = (\det\mathcal{M})^{-1}$. Should a source be emitting null rays isotropically, it is known that the unlensed source seen by the observer is smaller than as seen by an observer at

the lens position, more specifically by a factor of $(r_s/r_{os})^2$ [384]. Hence,

$$\det\mathcal{M} = \left(\frac{r_s}{r_{os}}\right)^2 \left[\frac{\partial\mu_s}{\partial\theta_1}\frac{\partial\phi_s}{\partial\theta_2}\right], \tag{6.2.32}$$

where r_{os} is the linear path from the source to the observer along the optical axis. Therefore, one can express the Jacobian determinant, $\det\mathcal{M}$, as a Taylor expansion in the expansion parameter ϵ

$$\begin{aligned}\det\mathcal{M} = 1 - \frac{1}{\theta_{(0)}^4} + \epsilon\left[\frac{15(1-\theta_{(0)}^2)\pi}{16\theta_{(0)}^5(1+\theta_{(0)}^2)} - \frac{4\theta_{1(0)}a\sqrt{1-\mu_o^2}}{M\theta_{(0)}^4(1+\theta_{(0)}^2)}\right] - \epsilon^2\Bigg\{\frac{8(1-\theta_{(0)}^2)}{(r_o+r_s)^2\theta_{(0)}^6(1+\theta_{(0)}^2)} \\ \times\left[(\theta_{(0)}^8+2\theta_{(0)}^6+2\theta_{(0)}^4+1)r_o^2 - r_s^2(\theta_{(0)}^8+2\theta_{(0)}^6+4\theta_{(0)}^4-8\theta_{(0)}^2+3) - 2r_sr_o\theta_{(0)}^2(\theta_{(0)}^4+2\theta_{(0)}^2-4)\right] \\ + \frac{225\pi^2}{256}\frac{(1-\theta_{(0)}^2)(1-5\theta_{(0)}^4-2\theta_{(0)}^2)}{\theta_{(0)}^6(1+\theta_{(0)}^2)^3} - \frac{5a(-12\theta_{(0)}^8+27\theta_{(0)}^6+7\theta_{(0)}^4-7\theta_{(0)}^2+1)\theta_{1(0)}\sqrt{1-\mu_o^2}\pi}{16M\theta_{(0)}^7(\theta_{(0)}^2+1)^3} \\ - \frac{2a^2(\theta_{(0)}^2(\theta_{(0)}^2+1)^2+2(1-3\theta_{(0)}^4)\theta_{1(0)}^2)(1-\mu_o^2)}{M^2\theta_{(0)}^4(1-\theta_{(0)}^2)(\theta_{(0)}^2+1)^3}\Bigg\} + \mathcal{O}(\epsilon^3).\end{aligned} \tag{6.2.33}$$

Then, we can trivially invert this series to obtain the corresponding magnification

$$\begin{aligned}\mu = \frac{\theta_{(0)}^4}{\theta_{(0)}^4-1} - \epsilon\left[\frac{15\theta_{(0)}^3\pi}{16(1+\theta_{(0)}^2)^3} + \frac{4a\theta_{(0)}^4\theta_{1(0)}\sqrt{1-\mu_o^2}}{M(1-\theta_{(0)}^2)^2(1+\theta_{(0)}^2)^3}\right] - \epsilon^2\Bigg\{\frac{\theta_{(0)}^2}{(1-\theta_{(0)}^2)(1+\theta_{(0)}^2)^5} \\ \times\Bigg[\frac{675\theta_{(0)}^4\pi^2}{128} - \frac{8(1+\theta_{(0)}^2)^2}{(r_o+r_s)^2}[(\theta_{(0)}^8+2\theta_{(0)}^6+2\theta_{(0)}^4+1)r_o^2 - 2r_sr_o\theta_{(0)}^2(\theta_{(0)}^4+2\theta_{(0)}^2-4) \\ - r_s^2(\theta_{(0)}^8+2\theta_{(0)}^6+4\theta_{(0)}^4-8\theta_{(0)}^2+3)]\Bigg] + \frac{5\theta_{(0)}(1-12\theta_{(0)}^8+27\theta_{(0)}^6-17\theta_{(0)}^4+17\theta_{(0)}^2)\theta_{1(0)}\pi}{16(1-\theta_{(0)}^2)^2(\theta_{(0)}^2+1)^5} \\ \times\frac{a}{M}\sqrt{1-\mu_o^2} + \left[\theta_{(0)}^2 - \frac{6(1+\theta_{(0)}^4)\theta_{1(0)}^2}{(1+\theta_{(0)}^2)^2}\right]\frac{2\theta_{(0)}^4}{(1-\theta_{(0)}^2)^3(1+\theta_{(0)}^2)^3}\left(\frac{a}{M}\right)^2(1-\mu_o^2)\Bigg\} + \mathcal{O}(\epsilon^3).\end{aligned} \tag{6.2.34}$$

Thus the magnification factor for Kerr gravitational lensing in the weak deflection limit only has dependence on the lens spin parameter a by means of terms proportional to $a\sqrt{1-\mu_o^2}$. This formula for magnification can alternatively be presented as the two separate magnifications for positive and negative parity images, originally presented in [385], expressed in terms of the source position β. Then,

$$\mu^+ = \frac{(\beta+\sqrt{\beta^2+4})^4}{(\beta+\sqrt{\beta^2+4})^4-16} - \frac{1}{(4+\beta^2)^{3/2}}\left(\frac{15\pi}{16} - \frac{4\beta_1}{\beta^3}\frac{a\sqrt{1-\mu_o^2}}{M}\right)\epsilon + \mathcal{O}(\epsilon^2), \tag{6.2.35}$$

$$\mu^- = \frac{(\beta-\sqrt{\beta^2+4})^4}{(\beta-\sqrt{\beta^2+4})^4-16} - \frac{1}{(4+\beta^2)^{3/2}}\left(\frac{15\pi}{16} + \frac{4\beta_1}{\beta^3}\frac{a\sqrt{1-\mu_o^2}}{M}\right)\epsilon + \mathcal{O}(\epsilon^2). \tag{6.2.36}$$

We obtained these expressions by implementing (6.2.21), (6.2.22), (6.2.23) and (6.2.24) into (6.2.34). We do not explicitly include terms of order ϵ^2 here since they will not enter our discussion but one could trivially do so following the same procedure. Further, we note that the sum of the signed magnifications is

$$\mu^+ + \mu^- = 1 - \frac{15\pi}{8(4+\beta^2)^{3/2}}\epsilon + \mathcal{O}(\epsilon^2). \tag{6.2.37}$$

One may notice that this sum is devoid of any terms involving the spin parameter a and therefore exactly matches the analogous expression for the Schwarzschild lens at this order. In reality, the resolution of the two weak field images is rather difficult and the only microlensing observable is the total absolute magnification. Considering the absolute magnifications for each of the images, $|\mu^+| = \mu^+$ and $|\mu^-| = -\mu^-$, the total absolute magnification for Kerr spacetime is

$$\mu_{\rm tot} = |\mu^+| + |\mu^-| = \frac{\beta^2+2}{\beta\sqrt{\beta^2+4}} + \frac{8\beta_1}{\beta^3(\beta^2+4)^{3/2}}\frac{a\sqrt{1-\mu_o^2}}{M}\epsilon + \mathcal{O}(\epsilon^2). \tag{6.2.38}$$

As expected [386], when reducing the configuration such that we have a circularly symmetric lens, either by considering $a = 0$ or placing the observer on the gravitational lens's axis of rotation (i.e. $\theta_o = 0$), the $\mathcal{O}(\epsilon)$ term vanishes.

6.3 Implications for fundamental physics and astrophysics

Understanding the properties of gravitational lensing using a Kerr background has fascinating implications not only in astrophysics, but also in fundamental physics. In order to gain a clear insight of these effects, we must consider the essential ingredient in any microlensing analysis, the distribution of magnification. Consequently, when studying a particular lensing system (in the weak deflection limit), we focus our attention on the simulation of magnification curves utilising the series expansions in [2].

6.3.1 Regularisation for point sources

Since the consideration of a point source, in the instance of perfect alignment (the observer, lens and source all lying on the optical axis, i.e. $\beta = 0$) naturally gives rise to an infinite magnification, one must find a mechanism to subjugate the influence this has on the magnification curve. In order to do so, we first consider the significantly more understood Schwarzschild lens, where astrophysical observations clearly provide a quantifiable, finite peak to the magnification curve should $\beta = 0$. Thus, should we wish to suitably model the astrophysical system exhibiting gravitational lensing phenomena, we desire to supplant the purely mathematical infinity at the peak of the curve (and equally values so close

to perfect alignment that they supersede the true, measured magnifications), with finite values that match astrophysical observations.

We achieve this goal by introducing an appropriate regularisation term $\delta \ll 1$. Rather than considering a system that lies exactly in the equatorial plane $\theta_o = \theta_s = \pi/2$, we instead approximate this planar alignment such that the source angle remains fixed in the equatorial plane, $\theta_s = \pi/2$, while the observer angle is shifted by the infinitesimally small angle δ,

$$\theta_o = \pi/2 + \delta. \tag{6.3.1}$$

Thus during the microlensing event, as the background source passes behind the lens and then subsequently re-emerges (i.e as the azimuthal angle to the source ϕ_s evolves in time), the magnification curve reaches a smooth, finite peak and the value for the magnification at each source position, (θ_s, ϕ_s) is extremely well-approximated. Equivalently, one may think of this regularisation term as effectively removing the source from the optical axis (i.e. hence $\beta_2 \neq 0$) thus removing the divergence to infinity.

It is certainly worth mentioning that when considering true astrophysical configurations, sources are not point-like but instead finite, and as such, possess a fixed radius R_s. Allowing for the inclusion of these extended sources provides a similar means to avoid divergent magnifications at perfect alignment, thus the appearance of the Einstein ring has finite brightness. Whilst we save the full discussion of extended sources until section 6.4, we note that for a fixed system, restricting the radius of the source object to have a finite size (at perfect alignment) is degenerate to introducing a lower bound to β_2 when considering point sources.

Of course to obtain an appropriate value for δ we must ensure the peak of the curve, $\mu^{\delta}_{\text{peak}}$, matches astrophysical observations. We consider various gravitational lensing systems, for which we know the true magnification at the peak of the curve, μ_{peak}[2]. Then, since at the peak of the Schwarzschild magnification curve, we know $\beta_1 = 0$ yet choose $\beta_2 \neq 0$ to regularise, then

$$\mu_{\text{peak}} = \frac{\beta_2^2 + 2}{\beta_2\sqrt{\beta_2^2 + 4}}, \tag{6.3.2}$$

from (5.1.33). Implementing the known value for the peak magnification, one simply inverts this equation to find the value of β_2. For example, implementing the peak magnification obtained from the central panel of figure 8 from [3], returns us the source position $\beta_2 \sim 0.15$, aligning our results with theirs. Once we have β_2 and appropriately

[2]We know the true magnification at the peak either by simulating with an extended source model, using real astrophysical data or in the particular case where we consider a supermassive black hole (figure 6.3.1c), utilising the peaks in [3] so that our results directly align with theirs.

scale with the Einstein radius θ_E (i.e. using $\beta_2 \equiv \tan B_2/\theta_E$) to obtain B_2 we can similarly invert (5.2.101) to find an appropriate approximation for δ. More explicitly, since $\theta_s = \pi/2$, (5.2.101) reduces to

$$\tan B_2 = \frac{-r_s \cos\theta_o \cos\phi_s}{r_o - r_s \sin\theta_o \cos\phi_s}. \tag{6.3.3}$$

Then, since θ_o is now defined as in (6.3.1) and $\phi_s = \pi$ in this instance,

$$\tan B_2 = \frac{r_s \cos(\frac{\pi}{2} + \delta)}{r_o + r_s \sin(\frac{\pi}{2} + \delta)}. \tag{6.3.4}$$

Using well-known trigonometric identities and noting that δ should satisfy small angle approximations,

$$\cos\left(\frac{\pi}{2} + \delta\right) = \cos\frac{\pi}{2}\cos\delta - \sin\delta\sin\frac{\pi}{2} = \sin\delta \sim -\delta, \tag{6.3.5}$$

$$\sin\left(\frac{\pi}{2} + \delta\right) = \sin\frac{\pi}{2}\cos\delta + \sin\delta\cos\frac{\pi}{2} = \cos\delta \sim 1, \tag{6.3.6}$$

hence

$$\tan B_2 = -\frac{r_s\delta}{r_o + r_s} = -D\delta, \tag{6.3.7}$$

recalling that $D \equiv r_s/(r_o + r_s)$. Therefore we define our small shift to the observer angle, θ_o, to take the form

$$\delta = -\frac{(r_o + r_s)\tan B_2}{r_s} = -\frac{\tan B_2}{D} \ll 1, \tag{6.3.8}$$

where B_2 is computed by inverting (6.3.2) and scaling appropriately, where we know the value of μ_{peak}.

Magnification curves produced in this way, for various different Schwarzschild lensing systems, are shown in figure 6.3.1. Figures 6.3.1a and 6.3.1b depict the total absolute magnification for two astrophysical systems, with the former in the self-lensing regime (smaller separations) and the latter in the microlensing regime (larger separations), where μ_{peak} is evaluated using an extended source model (see section 6.4.1). We note that in figure 6.3.1b, we consider a high magnification event. Magnifications of this scale are realised astrophysically, exemplified by the recent detection of the high magnification MOA-11-191/OGLE-11-462 microlensing event, describing an astrophysical system containing an isolated stellar-mass black hole [285]. For a different approach, in figure 6.3.1c, we have exploited the magnification curve presented in the central panel of figure 8 from [3], such that $\beta_2 \sim 0.15$ and our results align with those studied in this work. In what follows, we will analyse each of these cases by modelling the deflection of light rays due to gravitational lensing utilising a lens imbued with the Kerr metric such that we are in the weak deflection limit.

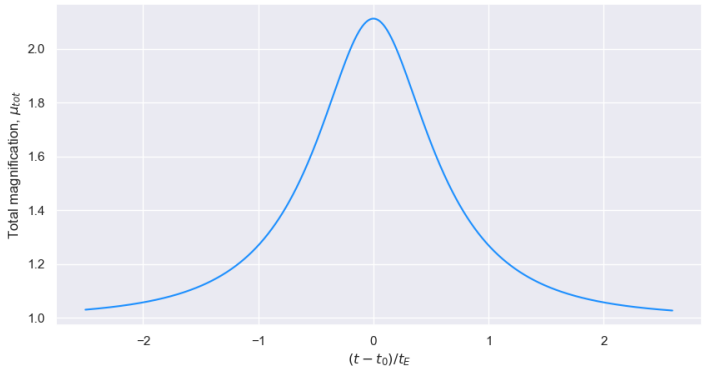

(a) Magnification curve for a Schwarzschild lens of mass $M = 10M_\odot$ with binary separation $r_s = 47$ AU and Einstein radius $R_E = 0.92R_\odot$.

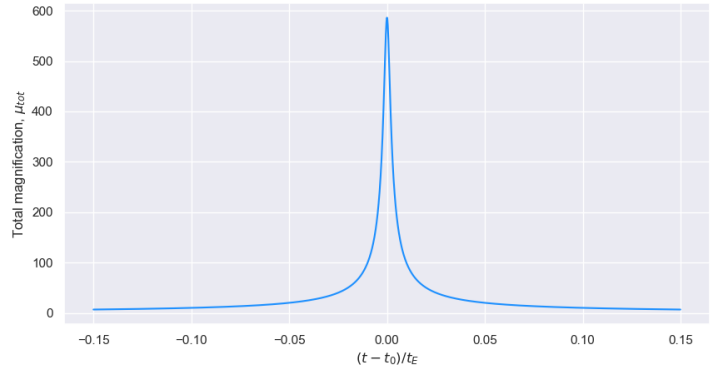

(b) Magnification curve for a Schwarzschild lens of mass $M = 10M_\odot$ such that the separation between the source and the lens is $r_s = 4.7 \times 10^6$ AU and the Einstein radius is $R_E = 291.83R_\odot$.

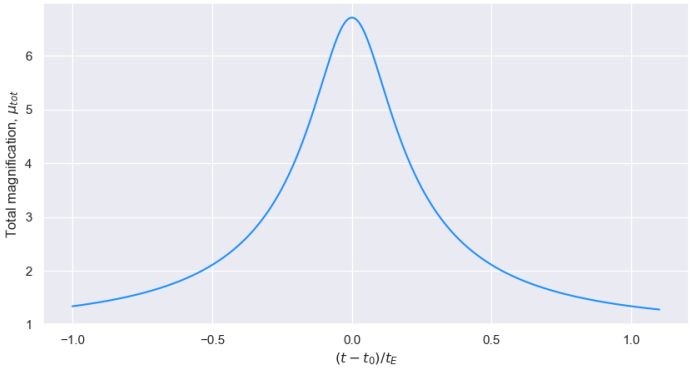

(c) Magnification curve for a Schwarzschild lens of mass $M = 3.61 \times 10^6 M_\odot$ [387], constituting the supermassive black hole Sagittarius A*. In agreement with [3], distances are chosen such that $r_o = 7.62$ kpc and $r_s = 4.85 \times 10^{-5}$ pc.

Figure 6.3.1: Magnification curves for three distinct gravitational lensing systems of interest; a self-lensing binary system and a microlensing system for solar-mass black holes as well as a particular case involving the supermassive black hole Sagittarius A*.

Before studying the direct consequences associated with the inclusion of spin, we note that should we wish to extend this regularisation process to consider Kerr gravitational lenses, we can use a similar methodology. Should the system similarly lie in the equatorial plane ($\beta_2 = 0$), infinitely bright critical curves appear as the source approaches a point-like caustic $(\beta_1^{\text{cau}}, 0) = (a/(\theta_E r_o) + \mathcal{O}(\epsilon^3), 0)$. In this case, our arguments can remain unchanged and we can choose δ in the same manner.

However, should we wish to consider different inclinations, we must slightly adjust our definitions. Since the effects of microlensing will only ever be visible when we are in the small angle approximation, we may restrict ourselves to the situation $\theta_o + \theta_s \simeq \pi$ where equality corresponds to perfect alignment[3]. Consequently, the regularisation term δ may more generally be defined by

$$\theta_o = \pi - \theta_s + \delta, \tag{6.3.9}$$

where $\delta \ll 1$.

6.3.2 Magnification curves for Kerr microlensing

There are various different parameter combinations of the Kerr gravitational lensing system that can alter the luminous amplification of incident light rays, that are either not present or do not have an impact in the Schwarzschild regime. As we have continuously alluded to throughout this work, the quintessential property that drives this change in magnification, is the lens spin parameter a. In figure 6.3.2, we illustrate the magnification curve for a system with identical parameters to those presented in figure 6.3.1c, however in this instance considering a gravitational lens in the Kerr background. Note, that the plots in figure 6.3.2 are such that both the observer and source lie in the equatorial plane $\theta_o = \theta_s = \pi/2$.

Since the corrections due to spin are only present in terms ϵ or higher, there is no reason to expect a significant difference in the behaviour of the magnification curves as we dial up the spin. Studying a single curve at spin $a = 0$ alone, we see that as the background source and the compact object constituting the gravitational lens approach perfect alignment from the perspective of the observer (i.e. when $\beta_1 < 0$), we observe a gradual increase in steepness to the total absolute magnification from $\mu_{\text{tot}} = 1$. Post-alignment (i.e. when $\beta_1 > 0$), we see the opposing effect.

[3]In fact, if we consider instances of gravitational lensing where observable magnification is possible but $\theta_o + \theta_s \not\simeq \pi$ (i.e. strong lensing), then by definition, since we do not have near-perfect alignment, there is no 'infinite magnification problem' and one does not need to mitigate for it.

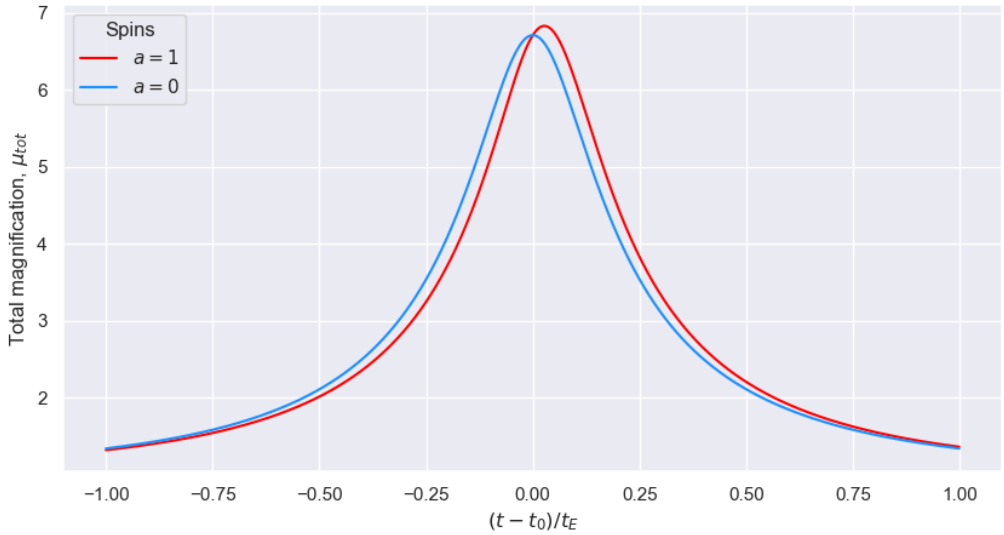

(a) Magnification curves for the supermassive black hole system with the parameters defined below for both non-spinning ($a = 0$) and extremal ($a = 1$) black holes.

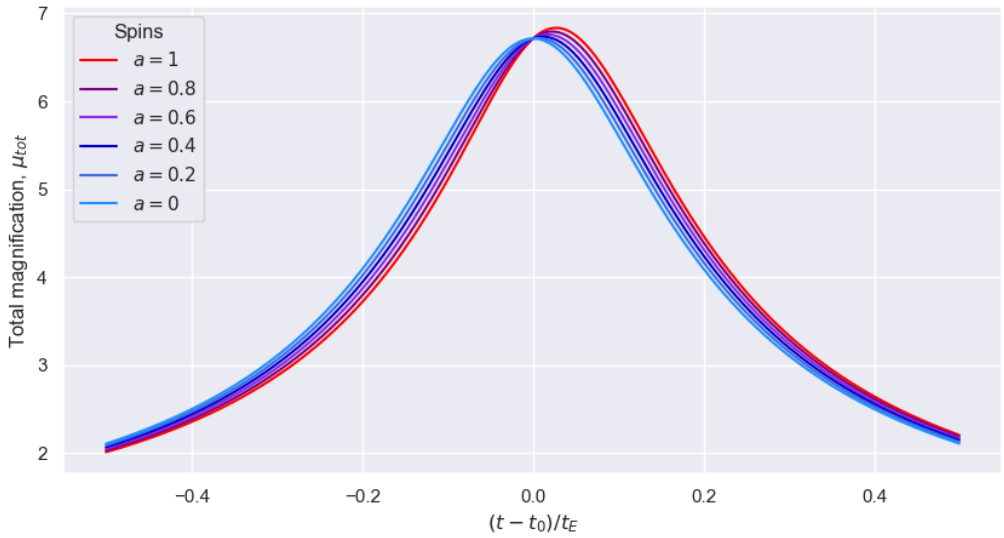

(b) Magnification curves for the supermassive black hole system with the parameters defined below for Kerr black holes at incrementally increasing spins a.

Figure 6.3.2: Magnification curves for a gravitational lensing system involving the supermassive black hole Sagittarius A* for a source and observer situated in the equatorial plane, in analogy to figure 6.3.1c. Specifically, each plot consists of a Kerr lens of mass $M = 3.61 \times 10^6 M_\odot$ with astrophysical separations, $r_o = 7.62$ kpc and $r_s = 4.85 \times 10^{-5}$ pc, where each curve represents different values for the spin parameter a. Furthermore, we note that the plots are fitted by choosing an appropriate δ, such that $\beta_2 \sim 0.15$ in alignment with [3].

Now, plotting distinct, finite values for the spin a, as in figure 6.3.2, one can characterise a number of captivating features from the behaviour of the magnification curves that differ from the $a = 0$ distribution. Firstly, there is a clear rightward shift in the magnification curve, peaking at a larger azimuthal angle ϕ_s or in other words, at a later instance in time relative to the motion of the source. As may be expected, should we reverse the spin axis of rotation to be clockwise as opposed to anti-clockwise, the shift in the magnification curve would be reversed such that we have a leftward displacement.

During astrophysical observations, this shift in the magnification signature will not be visible within the measured dataset since the variation of the azimuthal angle to the source ϕ_s is generally unknown at given time increments and the Einstein crossing time is used as the dependent variable instead. Thus, simple symmetry arguments imply astrophysical measurements will always be encoded such that the peak of the curve is centralised.

The most noteworthy property of the magnification curves in figure 6.3.2 is the definitive growth in the total magnitude for increasing spins a, with the peaks reaching higher maximum values. The astrophysical implications of this relationship between a and the total magnification of the incident light rays are vast. Since compact objects described in a Kerr background with linearly increasing spins ($0 < a < 1$) lead to proportionally larger magnifications than their non-spinning counterparts ($a = 0$), we find that higher populations of supermassive black holes are detectable than one would predict should we exclude spin effects.

From an astrophysical perspective one expects this asymmetric behaviour for rotating, compact lenses due to the introduction of spin. More explicitly, this asymmetry arises between photons that co-rotate with the deflector (*prograde* photons) and those that counter-rotate opposing the lens (*retrograde* photons). It is well-known that the deflection angle for prograde and retrograde photons differ; for example in the case of equatorial motion ($\theta_o = \theta_s = \pi/2$), the bending angle reduces to

$$\hat{\alpha} = 2\frac{r_{\rm sch}}{\xi}\frac{\xi_1}{\xi} + \frac{15\pi}{16}\Big(\frac{r_{\rm sch}}{\xi}\Big)^2\frac{\xi_1}{\xi} + 2\frac{ar_{\rm sch}}{\xi^2} + \frac{16\pi}{3}\Big(\frac{r_{\rm sch}}{b}\Big)^3\frac{\xi_1}{\xi} + \frac{a^2 r_{\rm sch}}{\xi^3}\frac{\xi_1}{\xi} + \frac{5\pi}{2}\frac{ar_{\rm sch}^2}{\xi^3} + \mathcal{O}(\epsilon^4), \tag{6.3.10}$$

where $\xi = \sqrt{\xi_1^2 + \xi_2^2} = \sqrt{\lambda^2 + \eta}$ is the impact parameter and $\xi_1 = -\lambda$. Consequently, for retrograde photons the bending angle becomes enhanced, while for prograde photons it is reduced. This topic has been vastly studied in the literature [297, 388, 389]. For our purposes, prograde photons ($\lambda > 0$, $\eta = 0$) are seen by observers as the source approaches perfect alignment (i.e. when $\theta_1 < 0$) and retrograde photons ($\lambda < 0$, $\eta = 0$) are seen by observers after perfect alignment has occurred (i.e. when $\theta_1 > 0$) and the source heads back to infinity.

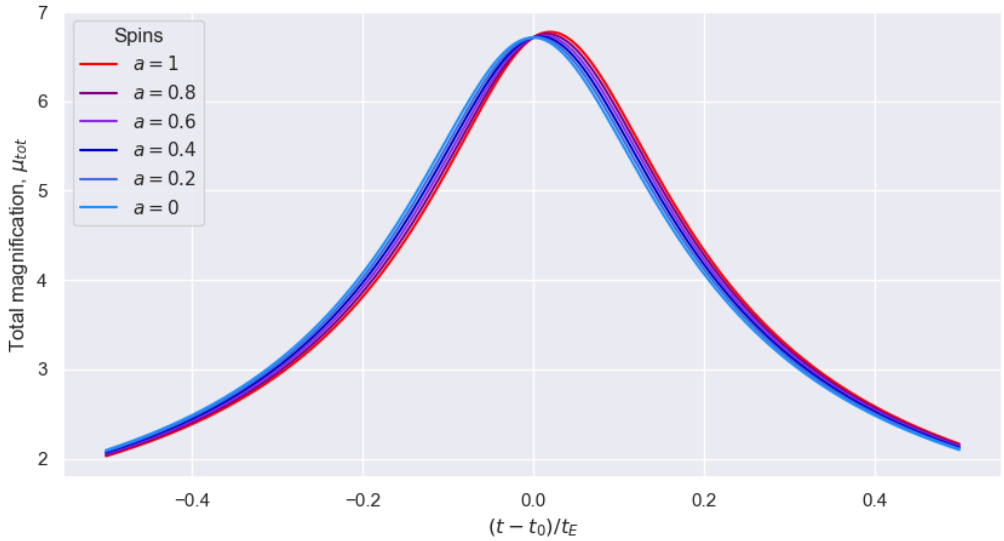

(a) Magnification curves for the supermassive black hole system with the parameters defined below for Kerr black holes at incrementally increasing spins a. Here we consider the source at $\theta_s = 3\pi/4$ and the observer at $\theta_o = \pi/4$.

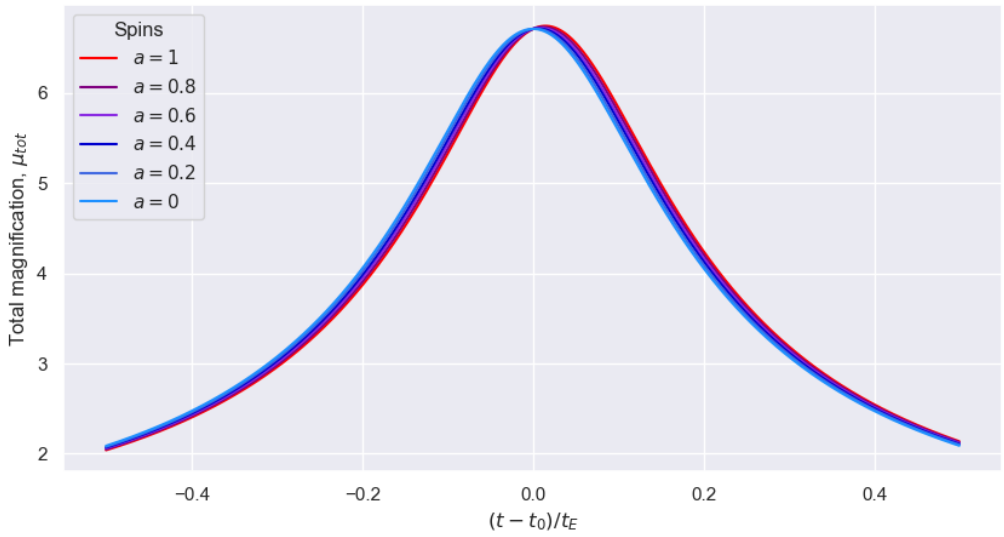

(b) Magnification curves for the supermassive black hole system with the parameters defined below for Kerr black holes at incrementally increasing spins a. Here we consider the source at $\theta_s = 5\pi/6$ and the observer at $\theta_o = \pi/6$.

Figure 6.3.3: Magnification curves for a gravitational lensing system involving the supermassive black hole Sagittarius A* for sources and observers situated at different inclinations. Specifically, each plot consists of a Kerr lens of mass $M = 3.61 \times 10^6 M_\odot$ with astrophysical separations, $r_o = 7.62$ kpc and $r_s = 4.85 \times 10^{-5}$ pc, where each curve represents different values for the spin parameter a. Furthermore, we note that the plots are fitted by choosing an appropriate δ, such that $\beta_2 \sim 0.15$ in alignment with [3].

The final interesting feature arising in figure 6.3.2 is the existence of an apparent intersection point between all magnification curves and the peak of the magnification curve at $a = 0$. Mathematically, this simply arises since this point of intersection corresponds to $\beta_1 = 0$ and so the correction to the magnification at order $\mathcal{O}(\epsilon)$ simply vanishes. When considering higher order corrections, however, we do see that this behaviour no longer persists.

When modelling astrophysical objects, the exact geometric configuration is often unknown and it is highly unlikely we will be in the situation where both the source and observer lie in the equatorial plane (though this is the case for self-lensing binaries which are very close to edge-on ($\theta_s = \theta_o = \pi/2$)). For isolated lenses however, the geometric construction must be considered in the most general sense, thus it is essential we analyse the effect that different inclinations have on the image magnifications.

In figure 6.3.3, we plot the magnification curves for numerous spins a at different source and observer inclinations, once again focusing our attention on gravitational lensing by Sagittarius A*, in analogy with figure 6.3.2. The immediate connection we establish is that the further the inclinations deviate from the equatorial plane, the lesser effect the spin has on the resultant magnification. This behaviour is to be expected since the spin only ever appears in the expansion through the coupling $a\sqrt{1-\mu_o^2}$.

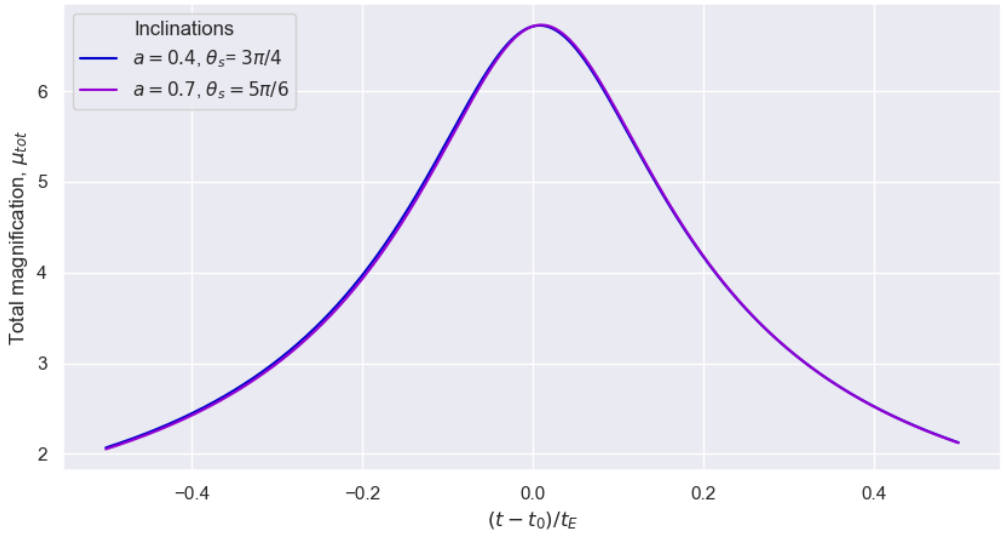

Figure 6.3.4: Magnification curves for a gravitational lensing system involving the supermassive black hole Sagittarius A* using different combinations of parameters. Specifically, both curves model a Kerr lens of mass $M = 3.61 \times 10^6 M_\odot$ with astrophysical separations, $r_o = 7.62$ kpc and $r_s = 4.85 \times 10^{-5}$ pc. However, for each curve we implement different combinations of spin a and inclination θ_s (and accordingly θ_o).

The most challenging aspect that we must still overcome to perform astrophysical simulations arises from the similarities that are exhibited between two entirely different gravitational lensing systems. It can become incredibly difficult to distinguish between the two systems despite the fact that they have different physical parameters and may even consist of different astrophysical objects.

We demonstrate this issue by illustrating a number of qualitatively different magnification curves that look remarkably similar in figure 6.3.4. While both systems consist of a Kerr lens with mass $M = 3.61 \times 10^6 M_\odot$ and have the same astrophysical separations, $r_s = 4.85 \times 10^{-5}$pc, $r_o = 7.62$kpc, they possess different combinations of alignment and spin. Our hope is that by having full spin-mass distributions, as opposed to just mass-distributions for the relevant lensing systems we study, one will be able to somewhat mitigate this problem.

6.3.3 Self-lensing and microlensing

The formalism we have presented in this section considering the phenomena of gravitational lensing in the weak deflection limit, describing light rays deflected by a gravitational lens associated with the Kerr metric, admits exciting astrophysical extensions. The qualitative differences observed in the magnification curves for the supermassive black hole Sagittarius A*, combined with ongoing spectroscopic and photometric studies, could indeed provide a mechanism to measure the spin parameter, a, of Sagittarius A* and test the cosmic censorship conjecture, as suggested in [385].

While gravitational lensing studies of Sagittarius A* in the weak deflection limit certainly warrants further research, we focus our attention on astrophysical systems in which the compact object constituting the lens is a stellar-mass black hole (i.e. a black hole with mass $5M_\odot < M < 50M_\odot$). In particular, we are interested in pristine binary systems exhibiting self-lensing behaviour as well as isolated compact lenses in systems with large separations (so that we are in the microlensing regime) and we will begin our discussion with the former.

Indeed, should one successfully find pristine self-lensing binary systems and probe them accordingly, the determination of their mass distributions can directly provide us with insights into the supernova mechanism (e.g. [390]). Should we also be able to determine their joint spin-mass distributions, one may be able to understand this process in even further depth. Similarly, should we apply this analysis to neutron stars, one may be able to test their internal structure. We will discuss these potential applications further in section 6.5.

Now, once again consider the self-lensing binary system we studied in the case of Schwarzschild (associated with the magnification curve in figure 6.3.1a). In figure 6.3.5 we plot the change in the total magnification μ_{tot} that arises solely as a consequence of contribution terms involving the spin parameter a, denoting this change in magnification as $\delta\mu_{\text{tot}}$. As should already be obvious by now, for astrophysical spins in the range $0 \leq a \leq 1$, the larger the value of a, the more prominent its influence of the total magnification.

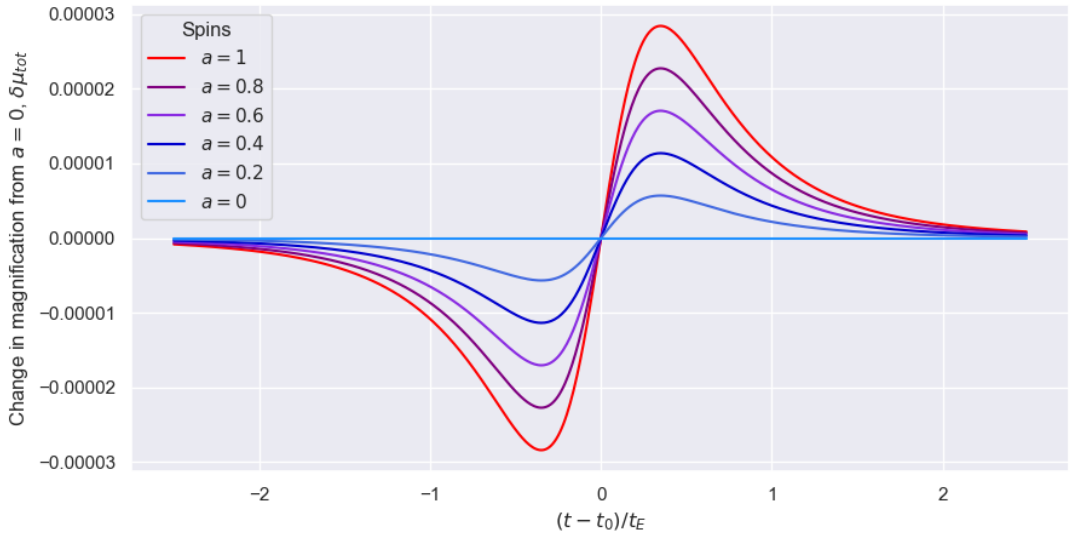

Figure 6.3.5: The change in the total magnification μ_{tot}, denoted $\delta\mu_{\text{tot}}$, solely due to to contributions involving the spin parameter a for a self-lensing binary system, plotted for a discrete range of spins $0 \leq a \leq 1$. The self-lensing binary system involves a Kerr lens of mass $M = 10M_{\odot}$ with astrophysical binary separation $r_s = 47$ AU and Einstein radius $R_E = 0.92R_{\odot}$, for a source and observer situated extremely close to the equatorial plane (incrementally shifted off-equatorial by δ).

As may be expected, at early and late times, terms involving the spin do not play a significant role. Similarly, at perfect alignment ($\beta_1 = 0$), all spin profiles intercept such that $\delta\mu_{\text{tot}} = 0$ and the total magnification reduces to Schwarzschild. We have already explained the origin of this interception point in section 6.3.2, and in order to avoid repetition, we will not discuss it further here. The most crucial segments of the profiles for our interests are those where the absolute value of $\delta\mu_{\text{tot}}$ is maximised, i.e. the turning points in figure 6.3.5. Since the spin, a, modifies the total magnification μ_{tot} by the most significant amount here, this is the most likely portion of the profile that we will be able to observe astrophysically. Further, the values we obtain for $\delta\mu_{\text{tot}}$ (of order $\sim 10^{-5}$) in regions near these turning points are within the detection capabilities of existing observational instruments [391].

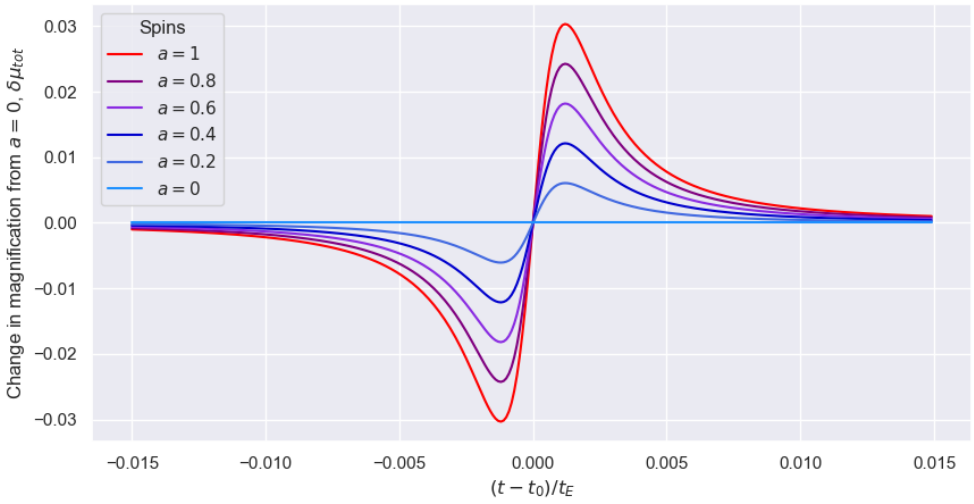

(a) The change in the total magnification $\mu_{\rm tot}$, solely due to to contributions involving the spin parameter a for a microlensing system, plotted for a discrete range of spins $0 \leq a \leq 1$. Here, the source and observer situated extremely close to the equatorial plane (incrementally shifted off-equatorial by δ).

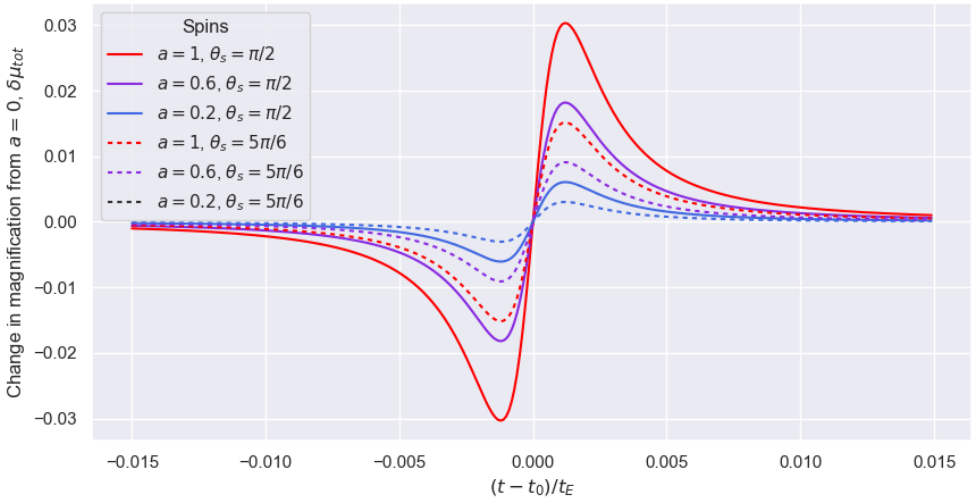

(b) The change in the total magnification $\mu_{\rm tot}$, solely due to to contributions involving the spin parameter a for a microlensing system, emphasising the importance of the inclination (i.e. different combinations of the observer and source angles, θ_o and θ_s). Solid lines indicate that the system is equatorial whereas dashed lines correspond to inclinations where $\theta_s = 5\pi/6$ (and $\theta_o = \pi/6 - \delta$ accordingly).

Figure 6.3.6: Two plots illustrating the change in the total magnification $\mu_{\rm tot}$, denoted $\delta\mu_{\rm tot}$, solely due to to contributions involving the spin parameter a for a microlensing system for different combinations of parameters. Specifically, the microlensing system consists of a Kerr lens of mass $M = 10M_\odot$ such that the astrophysical separation between the lens and the source is $r_s = 4.7 \times 10^6$ AU and the corresponding Einstein radius is $R_E = 291.83R_\odot$.

One comment which we should disclose is that the rightward shift in the magnification curve that our plots demonstrate may be harder to distinguish astrophysically. This is due to the fact that observationally, magnification curves will always be centralised in time by their peak. Consequently, should this problem be unavoidable by means of current modelling techniques, the observable effects due to spin will therefore be smaller. We note that even in this case, the minimum observable effect will be the total change in magnification (due to spin) at the peak of the magnification curves post-alignment[4], $\delta\mu^A_{\rm peak}$. Our current predictions estimate that for this self-lensing system, $\delta\mu^A_{\rm peak} \sim 1.6\times10^{-9}$ when $a = 1$ and finding a value for the total observable effect (should we be forced to align the curves) is subject to ongoing work. While this initial value may be beyond the capabilities of current observational instruments, as we enter a high-precision era of astronomy, one indeed expects these effects to become detectable in the near future.

We note here that current optical survey predictions of self-lensing binary populations have only considered Schwarzschild backgrounds [362]. While one may anticipate that these are underestimates of true detectable population sizes, since the spin parameter a has a direct influence on the total magnification $\mu_{\rm tot}$, because the detectable changes are so small, we expect that this effect on population predictions is negligible. Thus, the total number of observable self-lensing events that can be detected with current instruments will remain unchanged when accounting for the compact object's spin.

We now move on to our second, equally exciting potential application: testing astrophysical scenarios that exhibit microlensing, such as those recently detected in [285, 286], in which the gravitational lens is an isolated, compact object. Understanding and testing microlensing for isolated compact objects is essential as there is strong evidence to suggest a substantial portion of stellar-mass black holes are indeed single and do not belong to binaries (e.g. because around 30% of massive stars are born single and the compact object is its remnant [392, 393]). Testing the spins for these objects could provide the additional information required to classify the specific remnant encountered. More discussion on this front will follow in section 6.5.

Now, although the analysis in this section has so far only considered observers and sources that lie equatorially (since binaries are always edge-on), it is essential we consider different inclinations when constructing models for isolated, compact lenses. As illustrated in section 6.3.2, since the spin parameter always appears in the magnification coupled with an inclination term (i.e. as $a\sqrt{1-\mu_o^2}$), spin effects are maximised in the equatorial plane $\theta_o = \theta_s = \pi/2$. As we consider inclinations that become increasingly further from equatorial, the effect of spin becomes increasingly smaller, before vanishing at the poles $\theta_o = \theta_s = 0$.

[4]Post-alignment here refers to the situation after we have aligned the magnification curves such that their peaks are aligned at $(t - t_0)/t_E = 0$.

We now return to the microlensing system we studied for Schwarzschild lensing (associated with the magnification curve in figure 6.3.1b). As for the self-lensing case, we plot the change in the total magnification $\delta\mu_{\text{tot}}$ that arises solely as a consequence of contribution terms involving the spin parameter a for the microlensing case, as depicted in 6.3.6a. We also demonstrate how different inclinations can influence these shifts in figure 6.3.6b. In this instance, the curves exhibit the same behaviour as described in the self-lensing case, though we note that the scale of the effect due to spin here is much larger (e.g. for the extremal case $a = 1$, we see peaks in $\delta\mu_{\text{tot}}$ at approximately 0.03). Similarly, should we be forced to accept that the magnification curves, for each spin a, must be aligned at their peaks (if no mechanism exists to maintain the rightward shift in time) when considering true astrophysical observations, our initial findings predict the total change in magnification at the peak is approximately $\delta\mu^{A}_{\text{peak}} \sim 5 \times 10^{-7}$ in the case where $a = 1$. Either way, spin contributions can have a significantly larger magnitude when considering microlensing systems, as opposed to self-lensing binaries, thus there is an increased likelihood that the behaviour displayed will be detectable within this regime.

6.3.4 Extremal Kerr black holes

A particular class of compact objects, namely extremal black holes ($a = 1$), are of particular interest to us. When considering objects that are well described by the Kerr metric, the relevant angular momentum of the compact object is restricted by the cosmic-censorship hypothesis and so the spin is bounded such that $0 < a < 1$. Further, according to the third law of black hole thermodynamics [17], no process exists that will evolve a non-extremal black hole into an extremal one.

It certainly is surprising then that astrophysical black holes that come close to being extremal, such as GRS 1905+105 [394–396] and Cygnus X-1 [397, 398], have indeed been claimed to exist. Near-extremal black holes exhibit some of general relativity's most exhilarating features and so studying them can provide us further insight into both the core theory and astrophysical observations.

Further, extremal black holes lie at the epicentre of various other intriguing concepts and techniques, most prominently in the realm of quantum gravity and field theory. These fundamental ideas have been developed into extremely valuable mathematical theories but require validation from experimental observations. In this thesis, we believe the most interesting avenues to explore within fundamental theory are those relating to the fuzzball proposal [93–96] and the Kerr/CFT correspondence [97, 98]. Our ideas to utilise gravitational lensing to shed light on these theories is provided in section 6.5.

When considering strong gravitational lensing, the full lens equations (5.2.16, (5.2.17)) must be solved. In this instance, when considering the extremal case, one obtains a unique solution for the second radial integral I_ϕ, as given in (5.2.78). However in the weak deflection limit, the expansion holds true for $a = 1$ and the case need not any special consideration.

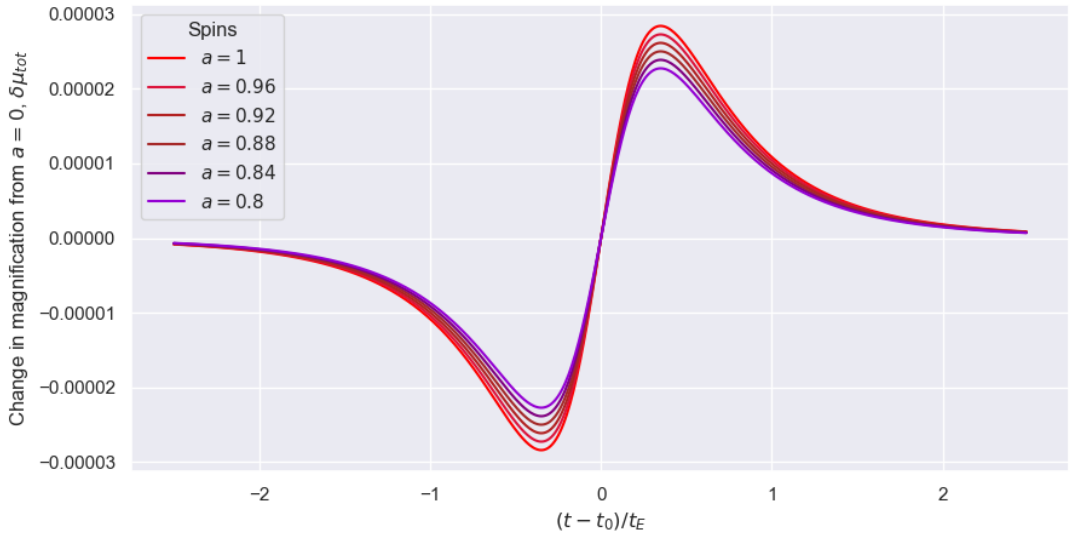

Figure 6.3.7: The change in the total magnification μ_{tot} solely due to the spin for a self-lensing binary system considering numerous different near-extremal spins a in the region $0.8 < a \leq 1$. Specifically, this system consists of a Kerr lens of mass $M = 10M_\odot$ with astrophysical binary separation $r_s = 47$ AU and Einstein radius $R_E = 0.92R_\odot$, for a source and observer situated in the equatorial plane.

As can be seen from all the previous figures in this section, magnifications curves in the extremal limit $a \to 1$ exhibit the same pattern of behaviour as those with spins $0 < a < 1$. To demonstrate this behaviour explicitly and show the extremal case is simply an analytic extension of the non-extremal case for rotating, compact objects in the weak deflection limit, we plot the spin-only contributions to the magnification for spins approaching $a \to 1$ in figure 6.3.7. In other words, we plot the change in total magnification due to spin, $\delta\mu_{\text{tot}}$, considering the spin parameter in the region $0.8 < a \leq 1$ in the same self-lensing regime that we have already previously explored in figures 6.3.1a and 6.3.5.

6.4 Extended sources

As we have already discussed, modelling the phenomena of gravitational lensing can indeed be well described utilising point sources, though these arguments break down as one approaches perfect alignment $\beta = (\beta_1, \beta_2) = (0, 0)$. This is since the image

magnifications diverge resulting in the appearance of an infinitely bright Einstein ring. In true astrophysical scenarios however, the object constituting the source must have a finite radius that smooths the peak of the magnification curve to be finite. In this section, we focus on describing the image configuration, and more crucially, the arising magnification, due to the gravitational lensing of an extended source by a point mass lens.

6.4.1 Extended uniform sources in Schwarzschild spacetime

We begin our discussion by summarising the methodology used to describe extended sources in Schwarzschild spacetime, pioneered by the seminal work [399]. For these purposes, we consider circular sources with finite radius R_s and emit light rays such that the surface brightness is uniform. Since this extended source is now a two-dimensional object, one introduces complex notation to define a lens equation of the same dimensionality [399],

$$\zeta = z - \frac{1}{\bar{z}}. \tag{6.4.1}$$

In this language, ζ is the complex coordinate associated with the source plane, $z = x+iy$ is the complex coordinate associated with the lens plane and $\bar{z}$ denotes the complex conjugate of z. Further, these quantities are normalised to possess units of $R_E D_s/D_d$ and R_E respectively by normalising the radius of the extended source as

$$\mathcal{R}_s = \frac{R_s D_d}{R_E D_s}. \tag{6.4.2}$$

In analogy with the point source lens equation (5.1.26), we notice that $|\vec{\beta}| = |\zeta|$ and $|\vec{\theta}| = |z|$.[5] One may trivially solve (6.4.1) to obtain the two image positions

$$z_\pm = \frac{\zeta}{2}\left(1 \pm \sqrt{1 + \frac{4}{\zeta\bar{\zeta}}}\right), \tag{6.4.3}$$

which similarly represents the complex analogue of (5.1.27). We make the assumption that the source has uniform brightness in the circular region described by $\zeta(r,\phi) = \zeta_0 + re^{i\phi}$. Here we choose ζ_0 to be real and positive and constrain our parameters to the ranges $0 \leq r \leq \mathcal{R}_s$ and $0 \leq \phi \leq 2\pi$. One can accordingly express the image positions to be parametrised by r and ϕ so that

$$z_\pm = \frac{\zeta_0 + re^{i\phi}}{2}\left(1 \pm \sqrt{1 + \frac{4}{\zeta_0^2 + 2r\zeta_0\cos\phi + r^2}}\right). \tag{6.4.4}$$

[5] We note here that β and θ here refer to the source and image positions normalised by θ_E.

Now, for an extended source with surface brightness profile $I(\vec{\beta})$, the general formula for the magnification due to gravitational lensing is [83],

$$\mu_e = \frac{\int d^2\vec{\beta}\; I(\vec{\beta})\; \mu_p(\vec{\beta})}{\int d^2\vec{\beta}\; I(\vec{\beta})}, \tag{6.4.5}$$

where $\vec{\beta} = (\beta_1, \beta_2)$ is the position of source and $\mu_p(\vec{\beta})$ denotes the point source magnification for a source at position $\vec{\beta}$ (which has been normalised to have units in R_E) given in (5.1.33). The brightness profile $I(\vec{\beta})$ can always be chosen to be normalised so that the denominator of (6.4.5) simply becomes the area of the source. Thus, for a circular source with radius $\mathcal{R}_s$, the denominator of (6.4.5) may always be reduced to give

$$\int d^2\vec{\beta}\; I(\vec{\beta}) = \int d\beta_1 d\beta_2\; I(\vec{\beta}) = \pi\mathcal{R}_s^2, \tag{6.4.6}$$

hence

$$\mu_e = \frac{1}{\pi\mathcal{R}_s^2}\int d^2\vec{\beta}\; I(\vec{\beta})\; \mu_p(\vec{\beta}). \tag{6.4.7}$$

With regards to the numerator of (6.4.5), for our current purposes we are interested in the discussion of sources that are uniformly bright, therefore one has the luxury that the brightness profile is satisfied by $I(\vec{\beta}) = 1$. Thus, one must simply evaluate the simplified equation

$$\mu_e = \frac{1}{\pi\mathcal{R}_s^2}\int d^2\vec{\beta}\; \mu_p(\vec{\beta}). \tag{6.4.8}$$

In order to understand how we intend to evaluate this integral, it is useful to visualise the situation from the perspective of an astrophysical observer, as shown in figure 6.4.1. Recalling $|\vec{\beta}| = |\zeta|$, one can explicitly write

$$|\vec{\beta}(\zeta)| = \zeta\bar{\zeta} = \sqrt{\zeta_0^2 + 2\zeta_0 r\cos\phi + r^2}. \tag{6.4.9}$$

Thus, each point on the extended source is separated from the optical axis by an angular distance $|\vec{\beta}(\zeta)|$. In the particular case in which we consider the centre of the extended source, we would have $R_s = 0$ and so the angular distance would become $|\vec{\beta}(\zeta = \zeta_0)|$.

So, when we are evaluating the integral in (6.4.8), we must evaluate the point source magnification such that $\mu_p(\vec{\beta}) = \mu_p(\vec{\beta}(\zeta))$. Since we wish to integrate over a circular boundary, the integration is most easily computed by utilising polar coordinates. Therefore our final equation for the magnification of an extended source with uniform surface brightness is

$$\mu_e = \frac{1}{\pi\mathcal{R}_s^2}\int_0^{2\pi}\int_0^{\mathcal{R}_s} \mu_p(\vec{\beta}(\zeta))\; r\; dr d\phi. \tag{6.4.10}$$

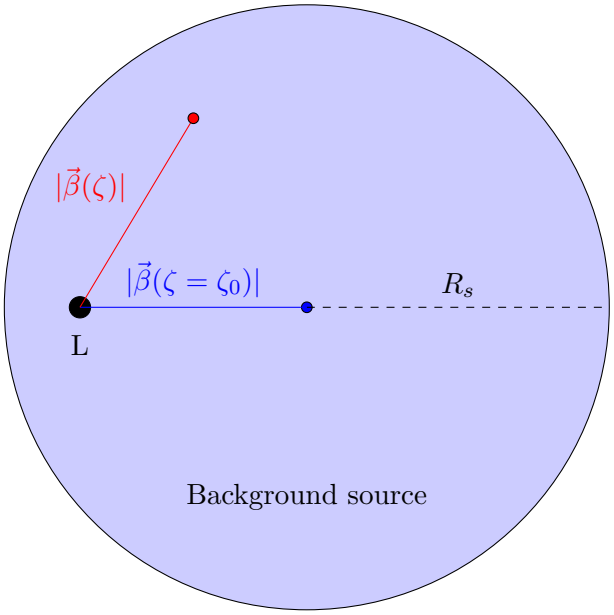

Figure 6.4.1: The perspective of the observer of the gravitational lensing event, where a background source with radius R_s passes behind a compact object L that distorts incident rays. The angular distance between the optical axis and the centre of the extended source is given by $|\vec{\beta}(\zeta = \zeta_0)|$ while the angular distance between the optical axis and an arbitrary point on the extended source is given by $|\vec{\beta}(\zeta)|$.

We close this section by demonstrating the qualitative similarities and differences one observes when considering an extended source with uniform surface brightness as opposed to a point source. Most notably, the magnification curve for extended sources becomes much broader (more rounded) when considering an extended source with a significantly less sharp peak. In figure 6.4.2, we plot the magnification curves associated with the self-lensing and microlensing cases we previously illustrated in the top and middle panels in figure 6.3.1, though this time we consider sources possessing a fixed, finite radius. In particular, the curves presented in figure 6.4.2 consider extended sources with radius $R_s = 1R_\odot$ that are situated in the equatorial plane $\theta_o = \theta_s = \pi/2$.

Firstly, we notice that the curves match at peak magnifications with their analogous curves in figure 6.3.1. We recall that this is of course by construction and due to our choice of δ. However since the geometric construction is indeed different for our point source model and extended source model (as the extended source is situated equatorially as opposed to being shifted by δ), we note that these are distinct from one another. In fact, point sources can indeed have slightly larger or smaller peak magnifications than extended sources (with a fixed radius) for the exact same geometric configurations. For brevity we do not discuss this in more depth here, but the intricate details connecting point source magnifications and extended source magnifications are explicitly illustrated in [399].

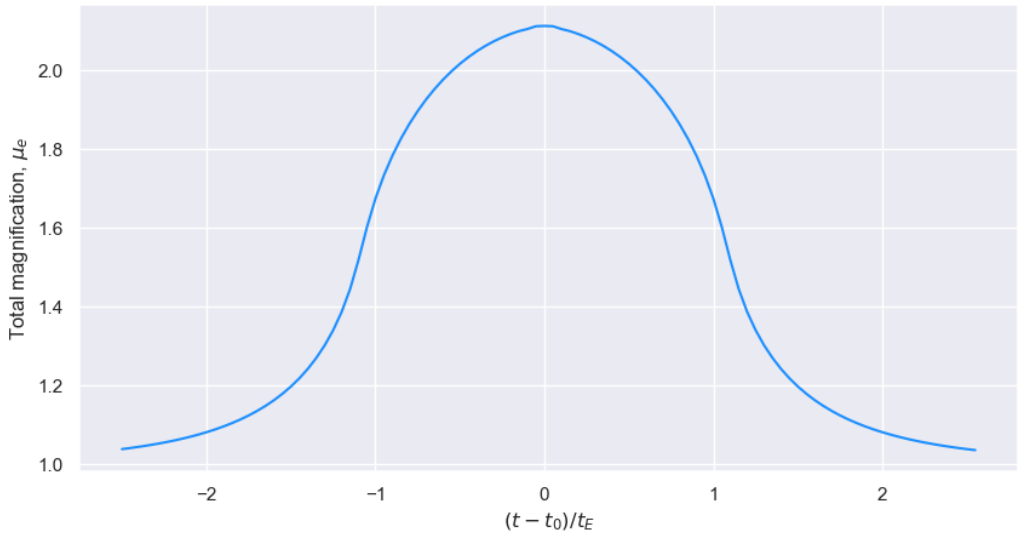

(a) Magnification curve for a Schwarzschild lens of mass $M = 10M_\odot$ with binary separation $r_s = 47$ AU and Einstein radius $R_E = 0.92R_\odot$. Here we consider an extended source with fixed radius $R_s = 1R_\odot$ and uniform surface brightness.

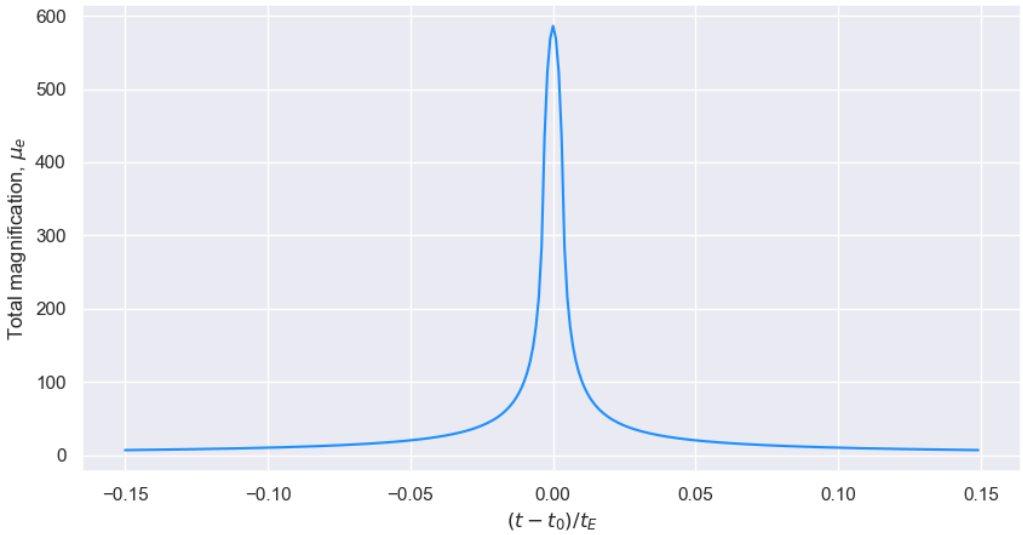

(b) Magnification curve for a Schwarzschild lens of mass $M = 10M_\odot$ such that the separation between the source and the lens is $r_s = 4.7 \times 10^6$ AU and the Einstein radius is $R_E = 291.83R_\odot$. Here we consider an extended source with fixed radius $R_s = 1R_\odot$ and uniform surface brightness.

Figure 6.4.2: Magnification curves for two distinct gravitational lensing systems of interest; a self-lensing binary system and a microlensing system analogous to those presented in figure 6.3.1. In both astrophysical scenarios we consider an extended source with fixed radius $R_s = 1R_\odot$ and uniform surface brightness.

6.4.2 Extended uniform sources in Kerr spacetime

Now we have discussed the mechanism in which we describe extended uniform sources for systems containing Schwarzschild lenses, we now illustrate how one would broaden our approach to include Kerr lensing systems in the weak deflection limit. While gravitational lensing extensions from Schwarzschild to Kerr for point sources tend to require one to add an additional dimension to the problem (since one breaks the azimuthal symmetry so that the observer's sky becomes two-dimensional as opposed to one-dimensional), we note that we are not required to here. This is since extended sources similarly require that the problem is no longer one-dimensional.

In fact, the first step in the generalisation to Kerr can be performed by simply breaking the previous assumption invoked that ζ_0 be real and positive. In the Schwarzschild regime, by making this assumption, one is effectively fixing the centre of the extended source to lie in the equatorial plane. In other words, when considering extended sources, we have projected a circle of radius R_s around the source position of a point source. For example, we take a point source with source position $\vec{\beta} = (\beta_1, \beta_2) = (\zeta_0, 0)$ and project a circular region around it providing the position of the extended source:

$$\beta_1 = \zeta_0 + r\cos\phi, \qquad \beta_2 = r\sin\phi. \tag{6.4.11}$$

Hence the total angular distance between each point within our finite source and the optical axis is given by the function

$$|\vec{\beta}(\zeta)| = \sqrt{\beta_1^2 + \beta_2^2} = \sqrt{\zeta_0^2 + 2\zeta_0 r\cos\phi + r^2}, \tag{6.4.12}$$

as we already discussed in section 6.4.1. Thus, since we restrict ζ_0 to be real, the centre of the extended source always lies on the equatorial plane. As we have extensively explained, the angles of inclination θ_o and θ_s play an essential role in describing geodesics in Kerr lensing and so one must consider cases away from the equatorial plane. Then, we simply allow ζ_0 to have both real and complex components;

$$\zeta_0 = \zeta_0^R + i\zeta_0^I. \tag{6.4.13}$$

Thus, we centre our extended sources around a singular point with position $\vec{\beta} = (\beta_1, \beta_2) = (\zeta_0^R, \zeta_0^I)$ so that the source positions of our extended sources can be parametrised by

$$\beta_1 = \zeta_0^R + r\cos\phi, \qquad \beta_2 = \zeta_0^I + r\sin\phi. \tag{6.4.14}$$

Now, although we are still able to express the region encompassing the uniformly bright source using $\zeta(r,\phi) = \zeta_0 + re^{i\phi}$, we clearly cannot use the lens equation (6.4.1). Since we are considering Kerr lensing in the weak deflection limit however, we can invoke the

lens equations (6.2.4) and (6.2.6) in order to evaluate the image positions. Fortunately, using this formalism involves implementing the source positions in component form (i.e. as β_1 and β_2), so one can repeat the previous method explored in section 6.2, however now evaluating by using the source positions in (6.4.14). That is to say, the image positions are still given by the series expansions

$$\theta_1 = \theta_E \left(\theta_{1(0)} + \epsilon\, \theta_{1(1)} + \epsilon^2 \theta_{1(2)} + \mathcal{O}(\epsilon^3)\right), \tag{6.4.15}$$

$$\theta_2 = \theta_E \left(\theta_{2(0)} + \epsilon\, \theta_{2(1)} + \epsilon^2 \theta_{2(2)} + \mathcal{O}(\epsilon^3)\right), \tag{6.4.16}$$

with the full angular separation of the image from the lens being

$$\theta = \theta_E \left(\theta_{(0)} + \epsilon\, \theta_{(1)} + \epsilon^2 \theta_{(2)} + \mathcal{O}(\epsilon^3)\right), \tag{6.4.17}$$

where the expressions for each of the terms remain unchanged but are now evaluated such that β_1 and β_2 are defined as in (6.4.14).

The formula for the total absolute magnification for a uniform extended source when considering Kerr gravitational lensing remains unchanged from the Schwarzschild case,

$$\mu_e = \frac{\int d^2\vec{\beta}\; I(\vec{\beta})\; \mu_p(\vec{\beta})}{\int d^2\vec{\beta}\; I(\vec{\beta})}, \tag{6.4.18}$$

though upon evaluation we note that β_1 and β_2 are defined as in (6.4.14) and $\mu_p(\vec{\beta})$ now denotes the point source magnification at source position $\vec{\beta} = (\beta_1, \beta_2)$, given by equation (6.2.38). We can make the same simplifications as in the Schwarzschild case to reduce (6.4.18) to be

$$\mu_e = \frac{1}{\pi \mathcal{R}_s^2} \int d^2\vec{\beta}\; \mu_p(\vec{\beta}). \tag{6.4.19}$$

We once again illustrate a visual interpretation of the astrophysical configuration from the perspective of the observer, as shown in figure 6.4.3. The discussion from the previous section remains true, however since ζ_0 is now complex, there is no constraint restricting the centre of the source to lie equatorially. Thus, in this case,

$$|\vec{\beta}(\zeta)| = \sqrt{\beta_1^2 + \beta_2^2} = \sqrt{|\zeta_0|^2 + 2\zeta_0^R r\cos\phi + 2\zeta_0^I r \sin\phi + r^2}. \tag{6.4.20}$$

As before, the integration must be performed in (6.4.19) over a circular boundary therefore it is convenient to express it using polar coordinates. So, the total absolute magnification for an extended source of uniform brightness when considering Kerr lensing in the weak deflection limit is

$$\mu_e = \frac{1}{\pi \mathcal{R}_s^2} \int_0^{2\pi} \int_0^{\mathcal{R}_s} \mu_p(\vec{\beta}(\zeta))\; r\; dr d\phi, \tag{6.4.21}$$

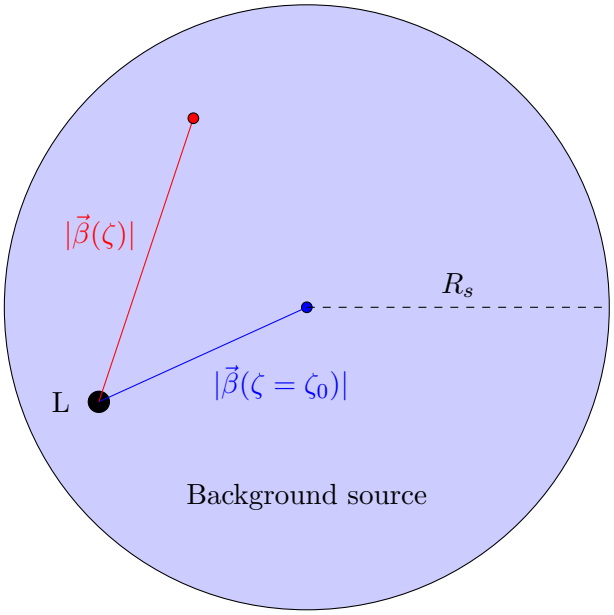

Figure 6.4.3: The observer's perspective of the Kerr gravitational lensing event, constituting the passing of a background source with radius R_s behind a compact object L. The angular distance between the optical axis and the centre of the extended source is given by $|\vec{\beta}(\zeta = \zeta_0)|$ while the angular distance between the optical axis and an arbitrary point on the extended source is given by $|\vec{\beta}(\zeta)|$. In the case of Kerr lensing, the centre of the source is no longer fixed to lie on the equatorial plane.

where $\mu_p(\vec{\beta}(\zeta))$ is the point source magnification described in (6.2.38) and β_1 and β_2 are given by (6.4.14).

Concluding this section on extended uniforms sources in Kerr spacetime, we consider the total change in magnification, $\delta\mu_e$, due to the influence of spin. In figure 6.4.4, we explicitly illustrate these effects for the same astrophysical system considered in figure 6.4.2a, with higher spins demonstrating larger values of $\delta\mu_e$, as may be expected from our previous analysis utilising point sources.

We note here that in order to reduce the total runtime of our model significantly, we have plotted our results for positive times only, i.e. $(t - t_0)/t_E > 0$. We have chosen to do so since numerical instabilities arise as one approaches $(t - t_0)/t_E = 0$ and in order to reduce them and smooth the curve, one must perform the integration in (6.4.21) over an increasing number of loops (requiring larger runtimes). Secondly, should we consider the region $(t - t_0)/t_E < 0$, one will simply see the same plot reflected in the $y = -x$ axis (e.g. reminiscent of the point source behaviour in figure 6.3.5) and this additional symmetry adds no interesting behaviour of note.

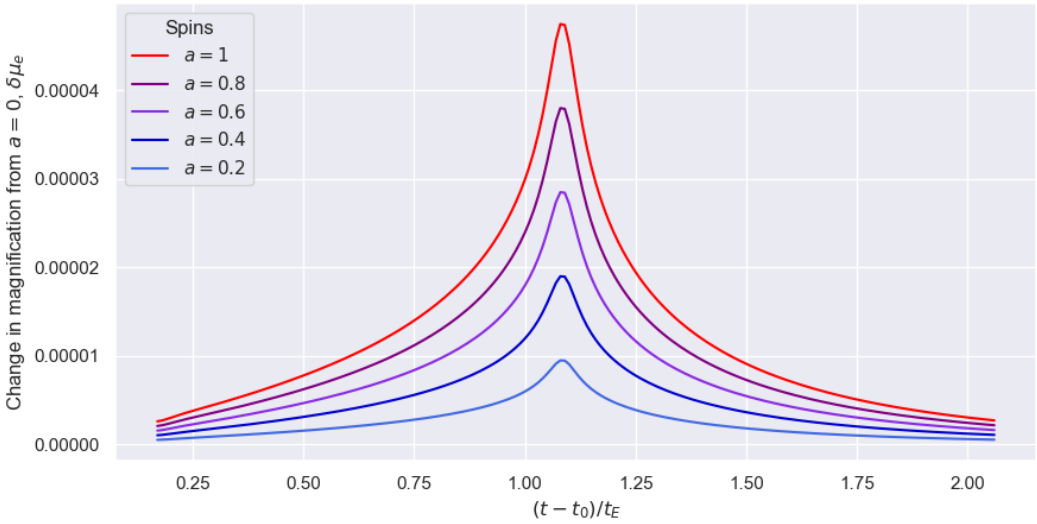

Figure 6.4.4: The change in the total magnification $\delta\mu_e$, solely due to to contributions involving the spin parameter a for a self-lensing binary system, plotted for a discrete range of spins $0 \leq a \leq 1$. The self-lensing binary system involves a Kerr lens of mass $M = 10M_\odot$ with astrophysical binary separation $r_s = 47$ AU and Einstein radius $R_E = 0.92R_\odot$, for an extended, uniform source (with radius $R_s = 1R_\odot$) and an observer situated in the equatorial plane.

6.4.3 Limb darkening

So far we have considered extended sources that have a constant surface brightness. In reality, the surface brightness of the source object is not uniform and instead varies according to its position within the source. Further, one expects the source to have the highest surface brightness at its centre, and lowest surface brightness at its edge. This occurs since photons transported from the centre of the stellar disk originate from deeper regions in the stellar atmosphere than at the edge of the source. Consequently, these photons are excited by higher temperatures and as a result will have a higher luminosity at the associated wavelength. This phenomenon is colloquially known as the limb darkening of the source. Thus, when simulating magnification curves, the inclusion of this effect is vital as the total magnification becomes larger and thus the impact of the spin a differs from the case of the extended, uniform source. The addition of limb darkening into the formula for the total magnification for an extended source (6.4.18) arises through the brightness profile, which we now formally define to be [83],

$$I(\vec{\beta}(\zeta)) = I_0 \, f\left(\frac{|\vec{\beta}(\zeta)|}{\mathcal{R}_s}\right) \tag{6.4.22}$$

as opposed to simply being reduced to $I(\vec{\beta}(\zeta)) = 1$ in the case of a uniform source. I_0 here refers to the surface brightness present at the centre of the source (i.e. at $\vec{\beta}(\zeta = \zeta_0)$) which

imposes an upper limit on the exact brightness profile, $I_0 \geq I(\vec{\beta}(\zeta))$. The function f is the function that encodes the relevant limb darkening law, which we will shortly discuss.

Explicitly including the dependence on ζ, (i.e. substituting $\vec{\beta} = \vec{\beta}(\zeta)$), the integral we desire to evaluate has the form

$$\mu_e = \frac{\int d^2\vec{\beta}\; I(\vec{\beta}(\zeta))\; \mu_p(\vec{\beta}(\zeta))}{\int d^2\vec{\beta}\; I(\vec{\beta}(\zeta))}, \tag{6.4.23}$$

and subsequently we once again find it is most conveniently expressed using polar coordinates,

$$\mu_e = \frac{\int_0^{2\pi}\int_0^{\mathcal{R}_s} I(\vec{\beta}(\zeta))\; \mu_p(\vec{\beta}(\zeta))\; r\; dr d\phi}{\int_0^{2\pi}\int_0^{\mathcal{R}_s} I(\vec{\beta}(\zeta))\; r\; dr d\phi}, \tag{6.4.24}$$

where the brightness profile is described by (6.4.22). Then the only remaining term left to discuss is the function f which imposes our choice of limb darkening law. The only constraints one has is that the function should reduce the surface brightness as we deviate away from the centre of the source and we are restricted by the upper bound $I_0 \geq I(\vec{\beta}(\zeta))$ which implies that $f(|\vec{\beta}(\zeta)|/\mathcal{R}_s) \leq 1$. We of course note that the bound is saturated when we are at the centre of the source $\zeta = \zeta_0$. Since this function will be heavily dependent upon ζ_0, it makes sense to write it in a slightly different manner;

$$f\Big(\frac{|\vec{\beta}(\zeta)|}{\mathcal{R}_s}\Big) = g\Big(\frac{|\vec{\beta}(\zeta-\zeta_0)|}{\mathcal{R}_s}\Big). \tag{6.4.25}$$

This can be interpreted in an even easier manner. Since $\zeta - \zeta_0 = re^{i\phi}$, then

$$|\vec{\beta}(\zeta-\zeta_0)| = \sqrt{(\beta_1(\zeta-\zeta_0))^2 + (\beta_2(\zeta-\zeta_0))^2} = r. \tag{6.4.26}$$

Hence, our function really takes the form

$$f\Big(\frac{|\vec{\beta}(\zeta)|}{\mathcal{R}_s}\Big) = g\Big(\frac{r}{\mathcal{R}_s}\Big). \tag{6.4.27}$$

Then, we must simply define a function with dependence on $r/\mathcal{R}_s$ and since we know that g should become smaller as we deviate further from the centre of the source (now at $r = 0$ in polar coordinates), this becomes rather trivial. For our purposes we choose a function, g, that encodes a quadratic limb darkening law (as in [400]). In particular,

$$g\Big(\frac{r}{\mathcal{R}_s}\Big) = \frac{I(\vec{\beta}(\zeta))}{I_0} = 1 - \gamma_1(1-\sigma) - \gamma_2(1-\sigma)^2, \tag{6.4.28}$$

where

$$\sigma = \sqrt{1 - \Big(\frac{r}{\mathcal{R}_s}\Big)^2} \tag{6.4.29}$$

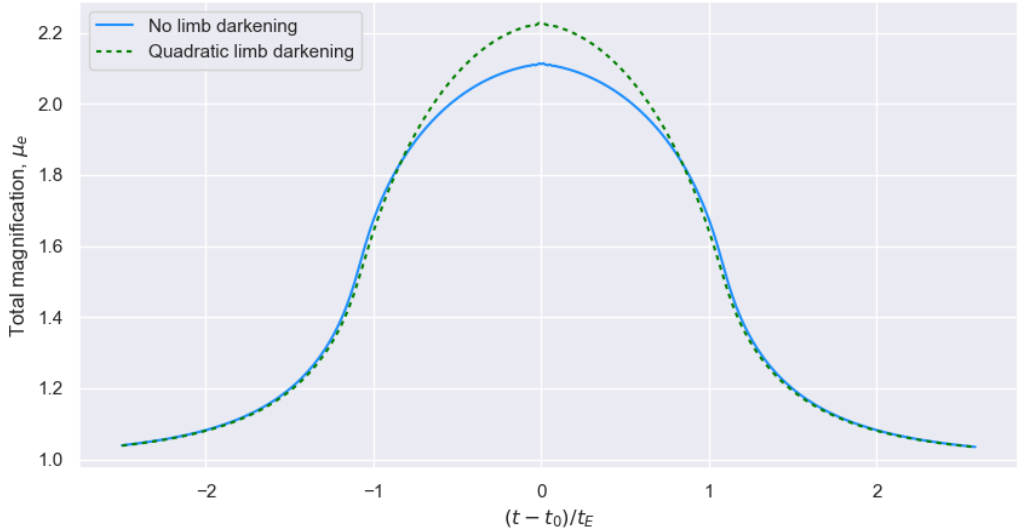

(a) Magnification curves considering a Schwarzschild lens of mass $M = 10M_\odot$ with binary separation $r_s = 47$ AU and Einstein radius $R_E = 0.92R_\odot$. Here we consider both an extended source with uniform surface brightness and one obeying a quadratic limb darkening law.

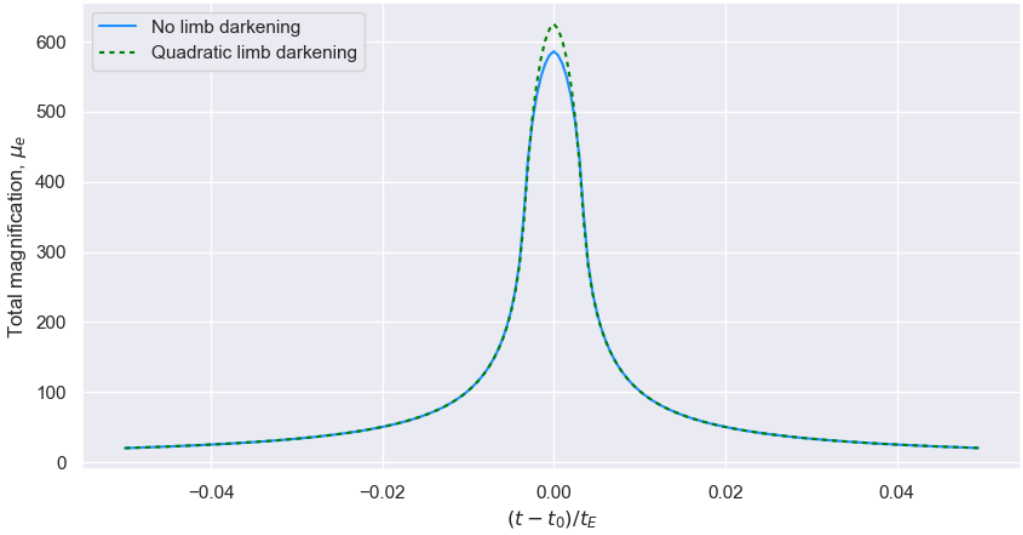

(b) Magnification curves considering a Schwarzschild lens of mass $M = 10M_\odot$ such that the separation between the source and the lens is $r_s = 4.7 \times 10^6$ AU and the Einstein radius is $R_E = 291.83R_\odot$.

Figure 6.4.5: Magnification curves for two distinct gravitational lensing systems of interest; a self-lensing binary system and a microlensing system analogous to those presented in figures 6.3.1 and 6.4.2. In particular, in both astrophysical scenarios we consider an extended source with uniform surface brightness and one obeying a quadratic limb darkening law. Specifically, we choose the source to have a fixed radius $R_s = 1R_\odot$ and $\gamma_1 = \gamma_2 = 0.3$ where we consider limb darkening.

and γ_1 and γ_2 are free parameters satisfying the relation $\gamma_1 + \gamma_2 < 1$. We note that there are various choices of limb darkening laws that have been studied in the literature (e.g. [401–405]), though for our purposes the quadratic law will suffice. Further, we can check that at the centre of the source $r = 0$, our function reduces to $g(0) = 1$ as desired.

Thus, to summarise, our models compute the total absolute magnification of a limb-darkened extended source by numerically evaluating the integral

$$\mu_e = \frac{\int_0^{2\pi} \int_0^{\mathcal{R}_s} g(\frac{r}{\mathcal{R}_s})\, \mu_p(\vec{\beta}(\zeta))\, r\, dr d\phi}{\int_0^{2\pi} \int_0^{\mathcal{R}_s} g(\frac{r}{\mathcal{R}_s})\, r\, dr d\phi}, \tag{6.4.30}$$

where $g(r/\mathcal{R}_s)$ is defined by the quadratic limb darkening law (6.4.28) and $\mu_p(\vec{\beta}(\zeta))$ is the point source magnification (6.2.38) for a source at position $\vec{\beta}$.

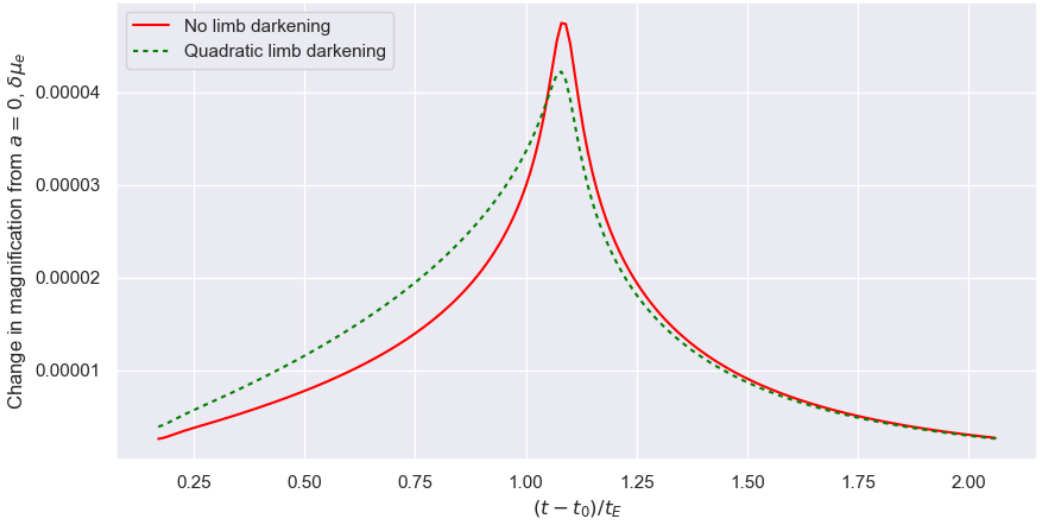

Figure 6.4.6: The change in the total magnification, $\delta\mu_e$, solely due to spin contributions considering a self-lensing binary system for both an extended source with uniform surface brightness and one obeying a quadratic limb darkening law, such that $a = 1$ and $\gamma_1 = \gamma_2 = 0.3$. In particular, the source is chosen to have a fixed radius $R_s = 1R_\odot$ and our astrophysical system consists of a Kerr lens of mass $M = 10M_\odot$ with binary separation $r_s = 47$ AU and Einstein radius $R_E = 0.92R_\odot$.

In figure 6.4.5, we once again plot the Schwarzschild extended uniform source magnification curves (as in figure 6.4.2) for the self-lensing and microlensing scenarios we have continuously used throughout this chapter. This time however, we plot a second curve, where we have assumed the surface brightness satisfies a quadratic limb darkening law (i.e is described by (6.4.28)) such that we have taken $\gamma_1 = \gamma_2 = 0.3$. As we have already mentioned, by adding limb darkening to the model, we can explicitly see that the profile not only has a sharper peak, but the total peak magnification takes a larger value than in the case of a uniform extended source. While we have already justified this

behaviour from the perspective of astrophysics, mathematically one could interpret this as 'effectively reducing β_2'.

Finally, the addition of limb darkening not only increases the peak magnification but it has consequences for the change in magnification due to spin contributions, $\delta\mu_e$, as can be seen in figure 6.4.6. In particular, we have plotted $\delta\mu_e$ (for the same self-lensing system) for an extended uniform source and a limb-darkened source with $\gamma_1 = \gamma_2 = 0.3$ and such that $a = 1$[6]. It would certainly be interesting to understand conceptually why the limb darkening broadens and shifts the profile and we plan to investigate this in more depth in upcoming work.

6.5 Discussion

In this thesis chapter we have attempted to address the necessity for the use of the Kerr metric when considering astrophysical gravitational lensing problems. Qualitative differences immediately emerge in the magnification curves subject to the asymmetry associated with introduction of spin. In order to achieve this, we considered the case of the weak deflection limit, utilising the geodesic equations of null rays and perturbatively solving for the appropriate lensing quantities following [2]. Thus, we include corrections up to order $\mathcal{O}(a^2 r_{\rm sch})$ and $\mathcal{O}(a r_{\rm sch}^2)$ noting that quantities that are purely spin terms (e.g. terms $\propto a^2$, a^3) do not contribute to any observables.

Indeed, it would be especially useful to draw insight from the strong deflection limit to see how our results generalise to cases that the weak deflection do not describe (e.g. considering relativistic images and photon rings of Kerr black holes). Doing so would provide enlightenment on astrophysical phenomena where the separations in the system are significantly smaller than in the weak deflection limit and the prime candidate to study would likely be X-ray binaries [352]. However, the fundamental difficulty residing in this extension is that should we wish to consider systems that are not edge-on (such as isolated, compact objects), one must consider a significantly larger parameter space, particularly for the choice of source and observer angles. Both analytic [90–92, 296, 302, 303, 384, 406] and numerical [89, 299–301] studies have been undertaken to try to best model the lens equations in these scenarios.

The mass and spin measured in the vast majority of black hole X-ray binaries is unlikely to be natal, as the accretion process which allows them to be located, results in large amounts of mass and angular momentum being transferred to the compact object [407]. Consequently, one cannot study the object's initial mass and we are unable to deduce

[6] We note that we have once again chosen to only plot for $(t-t_0)/t_E > 0$ to reduce runtime (as explained in section 6.4.2).

whether the natal spin is low (as expected where the helium core is spinning slowly prior to collapse, e.g. [390]).

As we have already alluded to, the majority of the self-lensing systems we expect to detect in upcoming surveys [362] will be pristine, i.e. unchanged in mass and angular momentum since their formation. By modelling the self-lensing events, we can obtain an estimate for the compact object masses via dynamics (i.e. with a period, magnification and mass estimate for the secondary star) and, utilising the full Kerr metric, the spin. Thus, we have provided the initial steps to build a model that will allow us to obtain the natal properties and make direct comparisons to predictions from core collapse supernova models.

It is commonly believed that one can immediately identify any gravitational lens with a sufficiently large mass, M, or a spin, $a > 0.3$, as a black hole (e.g. since the fastest spinning pulsar has $a \sim 0.3$ [408]). In regions where neutron stars are unambiguously located (i.e. with masses $1-2M_{\odot}$), limits on the spin together with pulse periods detected in the radio would allow the moment-of-inertia to be explored, constraining the equation-of-state.

Alternatively, the lensing profiles are sensitive to the object's radius (i.e. a large radius leads to additional occultation), and we hypothesise that these may allow a direct measurement of the compactness, again constraining the equation-of-state should data quality be sufficiently high. Since we assume large distances in our models (as we are in the weak deflection limit), occultation effects are unlikely to occur and so we are unable to explicitly test this. However, should we extend this work to include strong lensing effects, magnification curves will indeed be prone to occultation effects and one can investigate this avenue in more detail.

Further, recent results from LIGO imply that the population of merging black holes have low spins when compared to X-ray binaries [409]. This could point towards different evolutionary tracks; certainly accretion given long enough can change the black hole spin [407]. Since our model provides the tantalising opportunity to constrain the spin/inclination distribution of isolated black holes detected by microlensing surveys (e.g. [285, 286]) and test whether the non-accreting black holes, ejected from the natal supernova could eventually be the seeds for mergers.

But, as we have alluded to, astrophysical applications are not our only source of interest in this work. Gravitational microlensing has the potential to be an effective tool to understanding key concepts in fundamental theory. Furthermore, it may lay the groundwork to further investigate two particularly fascinating ideas: the fuzzball proposal [93–96] and the Kerr/CFT correspondence [97, 98].

The lensing and occultation effects explored in this thesis may provide a new way to physically distinguish between black holes and microstate geometries. For example, the lack of rotational symmetry of black hole microstates may change qualitatively the shapes of the occultation curves. These curves can be measured over extended timescales, hence allowing detailed analysis of the curve shape. It is important to note that deviations between black hole microstates and the Einstein black hole solutions are expected to be very small even close to the black hole horizon, so these effects may be too small to see with current observational capabilities. However, establishing a qualitative feature that distinguishes between microstates and black holes is conceptually important even if beyond the limits of current detectability.

Similarly, it would be interesting to explore whether the structure of lensing and occultation of near extremal rotating black holes can similarly be understood in Kerr/CFT. There has been progress recently in finding analytic solutions for lensing equations in Kerr [91, 92]. Analysis of the equations and the occultation curves in the limit of $a \to 1$ could give rise to new understanding of underlying symmetries of the dynamics. It would also be interesting to explore whether one could describe the occultation curves in the language of the dual field theory.

Finally, the study of Einstein gravity coupled to axions is well motivated, as axions are often invoked as a key component of dark matter. Moreover, axions often arise in top down constructions of beyond the standard model physics e.g. in string theory compactifications. Phenomenological implications of axions have been studied extensively in recent years [410], with a particular focus on gravitational wave observations. The study of microlensing and occultation in axionic models would allow new regimes to be tested, imposing additional constraints on the parameter space of such models.

Conclusions and outlook

Conclusions and outlook

The primary purpose of this thesis was to explore the nature of spacetime by investigating two distinct areas of theoretical physics, namely holographic quantum error correcting codes and gravitational lensing in Kerr backgrounds. We dedicated Part I to the former branch of research and investigated the latter discipline in Part II. We end our journey by providing a summary of the contained work, together with the subsequent conclusions we have drawn. We also provide a brief outlook on our future objectives arising as a result of these studies and how these extensions could more broadly influence their respective fields. For the sake of brevity and in order to avoid repetition, we point the reader to the more detailed conclusion sections present at the end of their respective chapters (i.e. sections 4.6 and 6.5).

The opening chapters of this thesis were dedicated to reviewing previous literature relevant for our studies in chapter 4. A prominent focus was given to introducing the holographic principle and its most explicit realisation, the AdS/CFT correspondence, in chapter 1. In chapter 2 we shifted our attention to the extensive subject of quantum information theory, summarising particular aspects such as the phenomenon of quantum entanglement, tensor networks and most notably, the notion of quantum error correcting codes. The key properties of these codes was discussed, prior to introducing a particular class of codes known as stabiliser codes [78]. Chapter 3 established the confluence of these two major fields of study, providing insight into the fascinating connections between them. In particular, we devoted ourselves to exploring how quantum information concepts present in the CFT can be translated into geometrical features in the dual gravitational theory in AdS. We thus illustrated the ideas behind holographic entanglement entropy [30, 31], the Ryu-Takayanagi conjecture [26, 27] and holographic codes [1, 32, 79].

In chapter 4, we detail the work of [80]. This consists of a systematic study of holographic codes associated with holographic geometries in higher dimensions, in which we construct analogues of the HaPPY code [1] for three-dimensional hyperbolic space (AdS_4), utilising both absolutely maximally entangled (AME) and non-AME codes. Our codes are based on uniform regular tessellations of hyperbolic space and our investigations lead us to the revelation that no AME codes exist that preserve the discrete symmetry of the polytope of the tessellation above two dimensions. We then take a different approach to the study of holographic codes, constructing stabiliser codes for hyperbolic spaces in which the logical information is associated with the boundary, before discussing their potential interpretation. We explain how our codes may be applied to interesting classes of holographic dualities based on gravity-scalar theories through toroidal reductions of hyperbolic spaces.

Chapter 5 consists of a comprehensive literature review for the second part of this thesis, concerning gravitational lensing. We provide a general overview of Schwarzschild lensing, introducing the lens equations, deriving the deflection angle and providing a concise summary of microlensing. Accounting for the addition of spin, we then explain how one may generalise this theory by understanding the behaviour of null geodesics in Kerr spacetime. This chapter is concluded by reviewing two particularly fascinating concepts with regards to the fundamentals of spacetime, namely the fuzzball proposal and the Kerr/CFT correspondence.

In chapter 6 we discuss our ongoing work exploring the importance of the spin asymmetry that arises in Kerr lensing in the weak deflection limit (i.e. for large astrophysical separations), utilising the expansions in [2]. We analyse these effects by studying the point source magnification curves for various geometrical configurations constituting different combinations of inclinations and spins. We extend this work through the consideration of more realistic astrophysical models encompassing spherical (finite) sources of uniform brightness as well as cases involving limb darkening effects.

There are numerous directions in which our studies can be taken further for both holographic quantum error correcting codes and gravitational lensing in Kerr spacetime, so we split our concluding remarks accordingly beginning with discussion of the former research branch.

Firstly, it would be interesting to investigate the performance properties of the codes we constructed by breaking the maximal discrete symmetry associated with the polytope of the tessellation. Further, it would be worthwhile to dedicate future works to studying the behaviour of specific quantities in the dual theory, most notably the entanglement entropy and correlation functions. One may uncover a potential connection between the relative sparsity of AME codes in dimensions higher than two and the dual theory, with

the possibility that CFT behaviour will no longer be captured by AME codes. In other words, by providing small correction to perfect tensors, one may not be able to reproduce CFT behaviour in the dual theory.

In section 4.2, we discussed toroidal compactifications of hyperbolic spaces and exemplified these concepts by considering the reduction of the hyperbolic plane on a circle. We would be intrigued to understand the properties of the codes that arise by discretising these unique geometries as well as those of more general toroidal reductions of higher dimensional hyperbolic tessellations.

We discussed an alternative approach with regards to the association of quantum codes to hyperbolic tessellations in section 4.5. We would find it stimulating to study the hyperbolic CSS codes we developed in this section in enhanced depth, both exploring their interpretation from a holographic standpoint as well as investigating their capabilities and potential applications.

Another possible avenue to investigate concerns the qualitative differences we observe between hyperbolic codes with dimensions $d = 2$ and those with $d > 2$. More specifically, we notice that considering geometries with $d > 2$ leads to an increasing sparsity in the number of tessellations that exist, constraining possible code constructions. Since the case where $d = 2$ corresponds to studying AdS gravity in $(2 + 1)$-dimensions (which is non-dynamical[7]), it would be interesting to explore whether this sparseness has a relation to the arising dynamics present in higher-dimensional AdS gravity.

One of the most exciting directions for further work involves the underlying association between graphs in the hyperbolic plane and deep learning algorithms [255–257]. Moreover, hyperbolic space has advantageous geometrical characteristics that may provide significant improvements in model performance, especially when considering data possessing a hierarchical structure. Our constructions of graphs/codes associated with high-dimensional hyperbolic geometries may provide a means to generalise these deep learning algorithms, with notable applications including natural language processing and image classification [257].

We now discuss future avenues in which our studies of gravitational lensing can be explored. Upcoming surveys [362] predict that the vast majority of self-lensing systems we expect to detect will be pristine. In other words, their mass and angular momentum remain unaltered (by effects such as subsequent mass accretion) since their formation. Combining our model with existing resources allows us the unique opportunity to estimate both the mass and the spin of a compact object, which may provide the stepping stones that

[7]This is since the Riemann curvature trivially reduces to be the Ricci curvature so all gravitational solutions possess constant negative curvature.

allow us to directly draw comparisons with current predictions describing the explosion mechanisms of core collapse supernova.

Of course, while our model is capable of describing gravitational lensing scenarios where astrophysical separations are large, it would be extremely useful to generalise this to situations where separations are smaller. Doing so would require us to consider strong lensing effects and could provide enlightenment on astrophysical phenomena such as X-ray binaries and the photon rings of Kerr black holes. Similarly, by studying the occultation effects in strong lensing systems, one may be able to perform a direct measurement of the compactness of neutron stars. Thus by considering mass ranges where neutron stars are unambiguously located (i.e. with masses $1 - 2M_{\odot}$), one could constrain the equation-of-state should the quality of data be sufficiently high.

Another intriguing potential direction stems from the emergence of new populations of binary systems that arose in conjunction with the first detection of gravitational waves [6]. Further analysis of these systems revealed that the black holes contained within these systems have much lower spins than those present in X-ray binaries [409]. Since our models explicitly consider spin effects, they could provide new insight into the nature of isolated black holes, thus we intend to draw comparisons with data collected from recent microlensing surveys (such as those detected in [285, 286]) in the near future.

Our work may also provide a foundation to furthering our understanding of key concepts in fundamental theory that would be rather interesting to investigate. We focus on three particularly fascinating ideas; the fuzzball proposal, the Kerr/CFT correspondence and axion black holes. Firstly, extending our studies to include microstate geometries may allow us to perceive deviations from the Kerr black hole case, providing a potential method to differentiate between the two phenomena, though we emphasise that these effects are likely too small to see with current observational capabilities. We could also explore whether one can fathom the gravitational lensing structure of near extremal rotating black holes from the perspective of the Kerr/CFT correspondence. Analysis of the lens equations and the magnification curves in the extremal limit could provide a fresh perspective of underlying symmetries of the dynamics while having a fascinating interpretation in the language of the dual field theory.

Finally, top down constructions of beyond the standard model physics often give rise to the appearance of axions, hypothetical elementary particles and dark matter candidates that resolve strong CP problem present in quantum chromodynamics. Studying microlensing effects in scenarios where Einstein gravity is coupled to axions is duly justified and may allow us to further constrain the parameter space for axionic models which are currently under investigation utilising gravitational wave observations [410].

Appendices

APPENDIX A

Appendix for part I: Holographic codes

A.1 Appendix for part I

Contained within these sections are any supplementary materials to the main text in Chapter 1, which revolves around the material relating to holographic codes. For expediency, we try to summarise the details of each section in the most concise fashion possible but should the reader be interested in further details, many longer texts exist covering each of these topics.

A.1.1 Conformal compactifications and the conformal boundary

Throughout this thesis, one often refers to the conformal boundary of AdS spacetime. Similarly, we have defined asymptotically locally AdS spacetime as Einstein metrics with a negative cosmological constant that can be conformally compactified to have the same conformal structure as AdS. In the following section, we define these concepts more formally.

In order to begin, we consider the notion of *conformal compactification* [411]. Consider some non-compact manifold $\mathcal{M}$ possessing the metric $g_{\mu\nu}$. Introducing a *defining function*

Ω, one can rescale the metric under the conformal transformation

$$\bar{g}_{\mu\nu} = \Omega^2 g_{\mu\nu}, \tag{A.1.1}$$

such that Ω is a smooth function. This metric is *conformally compact* if a smooth manifold $\bar{\mathcal{M}} = \mathcal{M} \cup \partial\mathcal{M}$ exists with boundary $\partial\mathcal{M}$, adjoining $\partial\mathcal{M}$ to $\mathcal{M}$, provided the defining function satisfies

$$\Omega(\partial\mathcal{M}) = 0, \qquad d\Omega(\partial\mathcal{M}) \neq 0, \qquad \Omega(\mathcal{M}) > 0. \tag{A.1.2}$$

The definition can be understood as trying to bring the diverging distances to within a finite distance. Thus Ω must continuously decrease, reaching zero on the boundary itself. Now consider an embedding $\Phi : \mathcal{M} \to \tilde{\mathcal{M}}$ where $\tilde{\mathcal{M}}$ is another manifold forming the spacetime $(\tilde{\mathcal{M}}, \tilde{g})$. This manifests as the 'push-forward' of $\tilde{g}$,

$$\Phi^*(\tilde{g}) = \Omega^2 g, \tag{A.1.3}$$

with respect to Φ, embedding the manifold $\mathcal{M}$ with boundary $\partial\mathcal{M}$ in $\tilde{\mathcal{M}}$. The process of performing this embedding is known as the *conformal compactification* of the spacetime $(\mathcal{M}, g)$ and one defines the *conformal boundary* to be

$$\partial\mathcal{M} \equiv \partial(\Phi(\mathcal{M})) \subset \tilde{\mathcal{M}}. \tag{A.1.4}$$

A.1.2 Details on the smearing function and the AdS-Rindler reconstruction

In section 3.2.1, we introduced the concept of the smearing function, defined in (3.2.3). The smearing function therefore provides a well-motivated prescription to represent a field in the bulk as a non-local operator in the CFT. This intuition follows by considering the canonical quantisation of a free scalar field in AdS_{d+1}. In particular, we consider the specific background to be given by the AdS-Rindler wedge with metric (3.2.4) which we restate slightly differently here for the convenience of the reader;

$$ds^2 = -(\rho^2 - 1)d\tau^2 + \frac{d\rho^2}{\rho^2 - 1} + \rho^2 dH^2_{d-1}, \tag{A.1.5}$$

with the final term being rewritten such that dH^2_{d-1} is the usual metric on the hyperbolic ball in $d-1$ dimensions, H^2_{d-1}. The corresponding solution in the Heisenberg picture for a free real scalar field is then

$$\mathcal{O}_{\mathrm{Bulk}}(\rho, \tau, \alpha) = \int_0^\infty \frac{d\omega}{2\pi} \sum_\lambda \left(f_{\omega\lambda}(\rho, \tau, \alpha) a_{\omega\lambda} + f^*_{\omega\lambda}(\rho, \tau, \alpha) a^\dagger_{\omega\lambda} \right), \tag{A.1.6}$$

where one chooses $f_{\omega\lambda}(\rho,\tau,\alpha)$ to be a basis of solutions to the Klein-Gordon equation, explicitly taking the form

$$f_{\omega\lambda}(\rho,\tau,\alpha) = e^{-i\omega\tau}Y_\lambda(\alpha)\psi_{\omega\lambda}(\rho). \tag{A.1.7}$$

Here, the spherical harmonic $Y_\lambda(\alpha)$ is an eigenfunction of the Laplacian on the hyperbolic ball, with corresponding eigenvalue λ. Using standard differential equation solving techniques, the final element $\psi_{\omega\lambda}(\rho)$ in the AdS-Rindler background can be shown to be

$$\begin{aligned}\psi_{\omega\lambda}(\rho) = \mathcal{N}_{\omega\lambda}\,\rho^{-\Delta}\Big(1-\frac{1}{\rho^2}\Big)^{-\frac{i\omega}{2}}\mathcal{F}\,\Big(&-\frac{(d-2)}{4}+\frac{\Delta}{2}-\frac{i\omega}{2}+\frac{1}{2}\sqrt{\frac{(d-2)^2}{4}-\lambda},\\ &-\frac{(d-2)}{4}+\frac{\Delta}{2}-\frac{i\omega}{2}-\frac{1}{2}\sqrt{\frac{(d-2)^2}{4}-\lambda},\Delta-\frac{d-2}{2},\frac{1}{\rho^2}\Big)\end{aligned} \tag{A.1.8}$$

where $\mathcal{F}$ is a hypergeometric function that reduces to unity as $\rho\to\infty$, the constant

$$\mathcal{N}_{\omega\lambda} = \frac{1}{\sqrt{2|\omega|}}\frac{\Gamma\Big(-\frac{(d-2)}{4}+\frac{\Delta}{2}+\frac{i\omega}{2r_s}+\frac{1}{2}\sqrt{\frac{(d-2)^2}{4}-\frac{\lambda}{r_s^2}}\Big)\Gamma\Big(-\frac{(d-2)}{4}+\frac{\Delta}{2}+\frac{i\omega}{2r_s}-\frac{1}{2}\sqrt{\frac{(d-2)^2}{4}-\frac{\lambda}{r_s^2}}\Big)}{\Gamma\Big(\Delta-\frac{d-2}{2}\Big)\Gamma\Big(\frac{i\omega}{r_s}\Big)} \tag{A.1.9}$$

ensures the modes $\psi_{\omega\lambda}(\rho)$ are appropriately normalised[1] to one and the conformal dimension is given by

$$\Delta = \frac{d}{2}+\frac{1}{2}\sqrt{d^2+4m^2}. \tag{A.1.10}$$

Furthermore, we note that the normalisation has been chose so that the creation and annihilation operators, $a^\dagger_{\omega\lambda}$ and $a_{\omega\lambda}$, satisfy the usual algebra. Substituting (A.1.6) and (A.1.8) into the so-called extrapolate dictionary,

$$\lim_{r\to\infty} r^\Delta \mathcal{O}_{\text{Bulk}}(\rho,\tau,\alpha) = \mathcal{O}(\tau,\alpha), \tag{A.1.11}$$

where $\mathcal{O}(\tau,\alpha)$ represents the local CFT operators at the boundary, we obtain

$$\mathcal{O}(\tau,\alpha) = \sum_\lambda \mathcal{N}_{\omega\lambda}e^{-i\omega\tau}Y_\lambda(\alpha)a_{\omega\lambda}. \tag{A.1.12}$$

Thus taking the Fourier transform gives

$$a_{\omega\lambda} = \frac{1}{\mathcal{N}_{\omega\lambda}}\int d\tau d\alpha e^{i\omega\tau}Y^*_\lambda(\alpha)\mathcal{O}(\tau,\alpha), \tag{A.1.13}$$

[1]This is achieved utilising the Klein-Gordon inner product $< g,f >\equiv i\int_\Sigma d^dx\sqrt{\gamma}n^\mu(g^*\partial_\mu f-\partial g^* f)$. The surface one integrates over, denoted Σ is a Cauchy slice, n_μ the unit normal to Σ and γ the induced metric on Σ.

and subsequent substitution back into (A.1.6) gives us the desired form of our equations,

$$\mathcal{O}_{\text{Bulk}}(\rho,\tau,\alpha) = \int d\tau' d\alpha' \mathcal{K}(\rho,\tau,\alpha;\tau'\alpha')\mathcal{O}(\tau',\alpha'), \tag{A.1.14}$$

where one has formally exchanged the $\tau\alpha$ integral with the $\omega\lambda$ sum/integral. Then one can read off the smearing function to explicitly be

$$\mathcal{K}(\rho,\tau,\alpha;\tau'\alpha') = \int_{-\infty}^{\infty} \frac{d\omega}{2\pi} \sum_{\lambda} \frac{1}{\mathcal{N}_{\omega\lambda}} f_{\omega\lambda}(\rho,\tau,\alpha) e^{i\omega\tau'} Y_{\lambda}^{*}(\alpha') \tag{A.1.15}$$

Thus it has the interpretation as a kernel for which one constructs a bulk solution of the Klein-Gordon equation in the AdS-Rindler wedge under provided arbitrary boundary conditions at spatial infinity.

A.1.3 Relation between CSS codes and homology of cellulations

Any cellulation of a manifold can be associated with a CSS code and the properties of the code are associated with homological properties of the cellulation. Let the i cells (the number of which is denoted $\dim(C_i)$) be associated with qubits i.e. $n = \dim(C_i)$. The boundaries of the $(i+1)$ cells are used to define Z checks and the coboundaries of $(i-1)$ cells define X checks. The number of each is denoted $\dim(B_i)$ and $\dim(B^i)$ respectively. The number of encoded qubits k is calculated by subtracting the number of stabilisers from the number of physical qubits:

$$k = \dim(C_i) - \dim(B_i) - \dim(B^i) = \dim(H_i), \tag{A.1.16}$$

where H_i is the ith homology group.

The generating sets of stabilisers are not in general independent. For the Z checks, the number can be expressed in terms of the number of cells with dimension greater than i and the dimensions of the homology groups of dimension greater than i:

$$\dim(B_i) = \sum_{j=1}^{D-i} (-1)^{j+1} \left(\dim(C_{i+j}) - \dim(H_{i+j})\right), \tag{A.1.17}$$

where we have used recursively the relationship

$$\dim(B_i) = \dim(C_{i+1}) - \dim(H_{i+1}) + \dim(B_{i+1}). \tag{A.1.18}$$

Similarly for the X checks the relation is

$$\dim(B^i) = \sum_{j=1}^{i} (-1)^{j+1} \left(\dim(C_{i-j}) - \dim(H^{i-j})\right). \tag{A.1.19}$$

In the case of a $D = 2$ cellulation that is topologically a disk, only $H^0 = 1$ is non-trivial: the number of Z checks is equal to the number of faces, while the number of X edges is equal to the number of vertices minus one.

The distance of the code is the same as the minimum length of an essential i cycle in the cell complex, or its dual.

A.1.4 Codes and Hilbert spaces

Quantum error correcting codes are those in which all the information within the code subspace of the Hilbert space is accessible from a subset of the physical degrees of freedom. Accordingly, the full Hilbert space $\mathcal{H}$ can be expressed as a direct product

$$\mathcal{H} = \mathcal{H}_{\mathcal{R}} \otimes \mathcal{H}_{\bar{\mathcal{R}}} \tag{A.1.20}$$

where

- All logical operators may be represented on $\mathcal{R}$.
- There is no correlation between $\bar{\mathcal{R}}$ and the encoded information.

Suppose that the Hilbert space $\mathcal{H}_{\mathcal{R}}$ factorises as

$$\mathcal{H}_{\mathcal{R}} = \mathcal{H}_{\mathcal{R}_1} \otimes \mathcal{H}_{\mathcal{R}_2}, \tag{A.1.21}$$

where the dimension of $\mathcal{H}_{\mathcal{R}_1}$ is the same as the logical dimension; $\mathcal{H}_{\mathcal{R}_1}$ is the logical subspace. The other factor is associated with the redundancy that protects from errors. In this context we can represent a state in the code subspace as

$$|\tilde{\psi}\rangle = \mathcal{U}_{\mathcal{R}} \left(|\psi\rangle_{\mathcal{R}_1} |\chi\rangle_{\mathcal{R}_2 \bar{\mathcal{R}}} \right), \tag{A.1.22}$$

where $|\psi\rangle_{\mathcal{R}_1}$ is the logical state; $|\chi\rangle_{\mathcal{R}_2 \bar{\mathcal{R}}}$ is an entangled state and $\mathcal{U}_{\mathcal{R}}$ is a unitary operator on $\mathcal{H}_{\mathcal{R}}$. In the context of holography, $\mathcal{R}$ is associated with a subset of the conformal boundary where $\bar{\mathcal{R}}$ is its complement.

Suppose that we want to encode k logical qudits into n physical qudits i.e. the dimension of the code subspace is d^k and that of the full Hilbert space is d^n. The quantum Singleton bound says that the information encoded in the logical qudits can be recovered from m qudits where

$$m \geq \frac{1}{2} (n + k) . \tag{A.1.23}$$

For holographic encodings associated with two dimensional geometries, the encoding map

is related to a tensor structure i.e.

$$T_{i_1\cdots i_n;j_1\cdots j_k} \propto \langle i_1\cdots i_n|\tilde{j}_1\cdots\tilde{j}_k\rangle, \tag{A.1.24}$$

where the physical qudits are denoted by $i_i\cdots i_n$ and the logical qudits are denoted by $\tilde{j}_1\cdots\tilde{j}_k$.

A.1.5 Generalised Pauli Operators

The generalised Pauli operators [412–414] for the D-dimensional qudits can be defined as

$$Z\,|k\rangle := \omega^k\,|k\rangle\,, \tag{A.1.25}$$

$$X\,|k\rangle := |k+1\rangle\,, \tag{A.1.26}$$

where $\omega = e^{2\pi i/D}$ and $k \in \mathbb{Z}_D$. One can similarly generalise controlled gates to qudits, for example the controlled-Z operator between two qudits, i and j can be implemented as

$$CZ_{ij} := \sum_{k=0}^{D-1} |k\rangle\langle k|_i \otimes Z_j^k = \sum_{k,l=0}^{D-1} \omega^{kl}\,|k\rangle\langle k|_i \otimes |l\rangle\langle l|_j\,. \tag{A.1.27}$$

Trivially, one can check the commutation relation is

$$ZX = \omega XZ \tag{A.1.28}$$

and each generalised operator has the property that when applied to a state D times, one is simply left with the identity operator; i.e. $Z^D = X^D = CZ^D = \mathbb{1}$. Another useful operator is the Fourier gate

$$F = \frac{1}{\sqrt{D}} \sum_{k=0}^{D-1} \omega^{kl}\,|k\rangle\langle l|\,, \tag{A.1.29}$$

which allows one to transform between the Z-eigenbasis and the X-eigenbasis;

$$|\bar{k}\rangle = F^\dagger\,|k\rangle = \frac{1}{\sqrt{D}} \sum_{l=0}^{D-1} \omega^{-kl}\,|l\rangle\,. \tag{A.1.30}$$

Hence, this is simply the generalisation of the Hadamard gate.

Stabiliser states can also be written in terms of generalised operators when extending from qubits to qudits [415, 416]. The generalised Pauli group acting on n qudits can be defined as

$$\mathcal{P}_n := \{\omega^a \otimes_{j=1}^n P_j\}, \tag{A.1.31}$$

where $\omega = e^{2\pi i/D}$ and $a \in \mathbb{Z}_D$.

APPENDIX B

Appendix for part II: Gravitational lensing

B.1 Appendix for part II

Contained within these sections are any supplementary materials to the main text in part II. Here we first discuss the conventions used with regards to the Legendre elliptic integrals. Then, much of the following content within this section consists of the explicit calculations of specific instances of these integrals that we omitted from the main text in order to preserve a clear focus on the predominant subject matter.

For further details regarding elliptic integrals, the reader is recommended to study [417] and for the original papers discussing the weak deflection limit expansion of the elliptic integrals in the Kerr geodesic equations (5.2.16, 5.2.17), see [2, 88].

B.1.1 Elliptic integrals

Throughout part II of this thesis, we frequently make use of Legendre's elliptic integrals. This section of the appendix is dedicated to define the conventions we adopt for these elliptic integrals, which we choose in order to align with *Mathematica 12's* built-in implementation.

B.1.1.1 Incomplete elliptic integrals

In trigonometric form, one defines the incomplete elliptical integral of the first kind F to be

$$F(\varphi \mid k^2) = \int_0^{\varphi} \frac{d\theta}{\sqrt{1 - k^2 \sin^2 \theta}}. \tag{B.1.1}$$

Equally, performing the substitution $t = \sin\theta$ results in the Legendre normal form:

$$F(\varphi \mid k^2) = \int_0^{\sin\varphi} \frac{dt}{\sqrt{(1-t^2)(1-k^2t^2)}}. \tag{B.1.2}$$

The incomplete elliptical integral of the second kind E in trigonometric form is defined as

$$E(\varphi \mid k^2) = \int_0^{\varphi} \sqrt{1 - k^2 \sin^2 \theta}\, d\theta. \tag{B.1.3}$$

Similarly to the incomplete elliptic integral of the first kind, performing the substitution $t = \sin\theta$ results in the Legendre normal form:

$$E(\varphi \mid k^2) = \int_0^{\sin\varphi} \frac{\sqrt{1-k^2t^2}}{\sqrt{1-t^2}}\, dt. \tag{B.1.4}$$

We will also make use of the derivative of $E(\varphi \mid k^2)$ with respect to k^2 , which we denote as

$$E'(\varphi \mid k^2) \equiv \frac{\partial}{\partial k^2} E(\varphi \mid k^2) = -\frac{1}{2} \int_0^{\sin\varphi} \frac{t^2}{\sqrt{(1-t^2)(1-k^2t^2)}} dt. \tag{B.1.5}$$

The incomplete elliptical integral of the third kind Π in trigonometric form is defined as

$$\Pi(n; \varphi \mid k^2) = \int_0^{\varphi} \frac{1}{(1 - n\sin^2\theta)} \frac{d\theta}{\sqrt{1 - k^2 \sin^2 \theta}}. \tag{B.1.6}$$

Similarly to the previous integrals, performing the substitution $t = \sin\theta$ results in the Legendre normal form:

$$\Pi(n; \varphi \mid k^2) = \int_0^{\sin\varphi} \frac{1}{(1 - nt^2)} \frac{dt}{\sqrt{(1-t^2)(1-k^2t^2)}}. \tag{B.1.7}$$

It is worth noting that the notation in much of the literature for the Legendre elliptic integrals is rather inconsistent. As a result, while we have adopted a particular notation here, should the reader be interested in many of the sourcebooks for these integrals (such as [417]), they will notice multiple different conventions are used.

B.1.1.2 Complete elliptic integrals

Should any of the previous incomplete elliptic integrals have amplitude satisfying $\varphi = \pi/2$, then the result is a 'complete' elliptic integral. For example, the complete elliptical integral of the first kind K may be defined as

$$K(k^2) = F\left(\frac{\pi}{2} \,\middle|\, k^2\right) = \int_0^{\frac{\pi}{2}} \frac{d\theta}{\sqrt{1 - k^2 \sin^2\theta}}. \tag{B.1.8}$$

We can also define this complete elliptic integral as in terms of the ordinary hypergeometric function ${}_2F_1$ as

$$K(k^2) = \frac{\pi}{2}\, {}_2F_1\Big(\frac{1}{2}, \frac{1}{2}; 1; k^2\Big). \tag{B.1.9}$$

Similarly, the complete elliptical integral of the second kind E may be defined as

$$E(k^2) = E\left(\frac{\pi}{2} \,\middle|\, k^2\right) = \int_0^{\frac{\pi}{2}} \sqrt{1 - k^2 \sin^2\theta}\, d\theta. \tag{B.1.10}$$

Again, we can define this complete elliptic integral as in terms of the ordinary hypergeometric function as

$$E(k^2) = \frac{\pi}{2}\, {}_2F_1\Big(\frac{1}{2}, -\frac{1}{2}; 1; k^2\Big). \tag{B.1.11}$$

The complete elliptical integral of the third kind Π may be defined as

$$\Pi(n, k^2) = \Pi\left(n; \frac{\pi}{2} \mid k^2\right) = \int_0^{\frac{\pi}{2}} \frac{1}{(1 - n\sin^2\theta)} \frac{d\theta}{\sqrt{1 - k^2 \sin^2\theta}}. \tag{B.1.12}$$

This integral can most neatly be expressed as

$$\Pi(n, k^2) = \frac{\pi}{2}\, F_1\Big(\frac{1}{2}; \frac{1}{2}, 1; 1; k^2, n\Big), \tag{B.1.13}$$

where F_1 is the hypergeometric Appell function.

B.1.2 Computation of elliptic integrals in the weak deflection limit

In order to form the Kerr lensing equations in the weak deflection limit, (6.2.4, 6.2.6), we recast the initial geodesic equations, (5.2.16), (5.2.17), by implementing the expansion parameters, (6.2.2). In order to do so, there are various elliptic integrals that must be resolved, namely the two angular integrals, (5.2.20, 5.2.22), and the two radial integrals, (5.2.19, 5.2.21). While we solved the integrals here independently, they were initially resolved up to order ϵ^2 in [88] and were further explored to order ϵ^3 in [2].

B.1.2.1 Angular integrals

One begins by considering the angular integrals, initially starting with G_θ. Expressing the angular potential $\Theta(\theta)$ defined in (5.2.15) as a function of a new variable $u = \cos^2\theta$,

$$\Theta(\theta) = \frac{\eta u + u^2(-\eta - \lambda^2 + a^2) - a^2 u^3}{u(1-u)}. \tag{B.1.14}$$

Thus the integral (5.2.20) may also be expressed in terms of u:

$$G_\theta = \int_{u_o}^{u_s} \frac{du}{2\sqrt{\eta u + u^2(-\eta - \lambda^2 + a^2) - a^2 u^3}}. \tag{B.1.15}$$

Since we wish to manipulate this integral according to the weak deflection limit described in section 6.2, the closest point of approach must lie far outside the gravitational radius; $r_{sch} \ll \sqrt{\lambda^2 + \eta}$. Thus, following the logic previously presented, one introduces two new independent quantities, $\hat{m}$ and $\hat{a}$, defined as in 6.2.2. By simple substitution,

$$G_\theta = \frac{1}{2\sqrt{\eta + \lambda^2}} \int_{u_o}^{u_s} \frac{du}{\sqrt{\frac{\eta}{\eta+\lambda^2} u + ((\hat{a}^2 - 1)u^2 - \hat{a}^2 u^3)}}. \tag{B.1.16}$$

Recall, when considering the case of a Schwarzschild lens (i.e. when $a = 0$), the turning points in θ are given by (5.2.45),

$$u_m = \frac{\eta}{\eta + \lambda^2}. \tag{B.1.17}$$

Here one adopts this notation for simplicity and so the form of the integral G_θ takes a relatively convenient form

$$G_\theta = \frac{1}{2}\sqrt{\frac{u_m}{\eta}} \int_{u_o}^{u_s} \frac{du}{\sqrt{u}\sqrt{u_m - \hat{a}^2 u^2 - (1 - \hat{a}^2)u}}. \tag{B.1.18}$$

In order to further develop this integral such that it has the desired form, we require that the quadratic equation in u appearing in the denominator of the integrand be factorised. So introducing new variables $\bar{u}_1$ and $\bar{u}_2$, the integral takes the form

$$G_\theta = \frac{1}{2}\sqrt{\frac{u_m}{\eta}} \int_{u_o}^{u_s} \frac{du}{\sqrt{u}\sqrt{(\bar{u}_1 - u)(\bar{u}_2 + \hat{a}^2 u)}}, \tag{B.1.19}$$

such that $\bar{u}_1$ and $\bar{u}_2$ satisfy the following relations:

$$\begin{cases} \bar{u}_1 \bar{u}_2 = u_m, \\ \bar{u}_1(\hat{a}^2 u) - \bar{u}_2 u = -(1 - \hat{a}^2)u. \end{cases} \tag{B.1.20}$$

One can obtain expressions for $\bar{u}_1$ and $\bar{u}_2$ explicitly by solving the simultaneous equations (B.1.20) perturbatively utilising the scaled spin variable $\hat{a}^2$. Performing this anlysis, we

find that

$$\bar{u}_1 = u_m + u_m(1-u_m)\hat{a}^2 + u_m(1-3u_m+2u_m^2)\hat{a}^4 + O(\hat{a}^6), \tag{B.1.21}$$

$$\bar{u}_2 = 1 - (1-u_m)\hat{a}^2 + u_m(1-u_m)\hat{a}^4 + O(\hat{a}^6). \tag{B.1.22}$$

One should note that performing this change in variables adjusts the turning point of θ to be $\bar{u}_1$, therefore when considering integrals that must be evaluated at the turning point, one should replace u_m with $\bar{u}_1$ at finite a. We can now expand the integral (B.1.19) as a series around the point $\hat{a} = 0$,

$$G_\theta = \frac{1}{2}\sqrt{\frac{u_m}{\eta}}\left[\frac{1}{\sqrt{\bar{u}_2}}\int_{u_o}^{u_s}\frac{du}{\sqrt{u(\bar{u}_1-u)}} - \frac{\hat{a}^2}{2\bar{u}_2^{3/2}}\int_{u_o}^{u_s}\sqrt{\frac{u}{\bar{u}_1-u}}du + \dots\right]. \tag{B.1.23}$$

As previously shown, angular integrals are unpacked as multiple integrals between 0 and u_j or $\bar{u}_1$ where u_j represents a generic upper integration limit $u_j \in \{u_o, u_s\}$. For efficiency purposes, we evaluate the integrals using one of the generic upper limits u_j to begin with before investigating the turning point integral. Expressing G_θ as the sum of each of the integrals present in (B.1.23), we can evaluate G_θ with integration limits $(0, u_j)$ as

$$G_\theta^{u_j} = G_\theta^{u_j'} + G_\theta^{u_j''} + \dots \tag{B.1.24}$$

such that the first integral in (B.1.23), which we denote $G_\theta^{u_j'}$, can be evaluated as

$$G_\theta^{u_j'} = \frac{1}{\sqrt{\bar{u}_2}}\int_0^{u_j}\frac{du}{\sqrt{u(\bar{u}_1-u)}} = \frac{2}{\sqrt{\bar{u}_2}}\arcsin\sqrt{\frac{u_j}{\bar{u}_1}}, \tag{B.1.25}$$

while the second becomes

$$G_\theta^{u_j''} = -\frac{\hat{a}^2}{2\bar{u}_2^{3/2}}\int_0^{u_j}\sqrt{\frac{u}{\bar{u}_1-u}}du = -\frac{\hat{a}^2}{2\bar{u}_2^{3/2}}\left[\sqrt{u_j(\bar{u}_1-u_j)} - \bar{u}_1\arcsin\sqrt{\frac{u_j}{\bar{u}_1}}\right]. \tag{B.1.26}$$

Substituting in $\bar{u}_1$ and $\bar{u}_2$ explicitly according to the relations (B.1.21) and (B.1.22), we can obtain $G_\theta^{j'}$ and $G_\theta^{j''}$ as series expansions at $\hat{a} = 0$,

$$G_\theta^{u_j'} = 2\arcsin\sqrt{\frac{u_j}{u_m}} + \hat{a}^2(u_m-1)\left(\sqrt{\frac{u_j}{u_m-u_j}} - \arcsin\sqrt{\frac{u_j}{u_m}}\right) + \dots, \tag{B.1.27}$$

$$G_\theta^{u_j''} = -\frac{\hat{a}^2}{2}\left[\sqrt{u_j(u_m-u_j)} - u_m\arcsin\sqrt{\frac{u_j}{u_m}}\right] + \dots. \tag{B.1.28}$$

Clearly this calculation can be performed for each integral in the series (B.1.23), hence independently evaluating each of these terms and summing them,

$$G_\theta^{u_j} = 2\arcsin\sqrt{\frac{u_j}{u_m}} - \frac{\hat{a}^2}{2}\left(\sqrt{u_j(u_m-u_j)} - 2(u_m-1)\sqrt{\frac{u_j}{u_m-u_j}} + (2-3u_m)\arcsin\sqrt{\frac{u_j}{u_m}}\right) + \dots . \tag{B.1.29}$$

One can perform similar analysis at the turning point integral (i.e. the series (B.1.23) with upper integration limit $\bar{u}_1$), which for finite a is

$$G_\theta^{\bar{u}_1} = \frac{1}{\sqrt{\bar{u}_2}}\int_0^{\bar{u}_1}\frac{du}{\sqrt{u(\bar{u}_1-u)}} - \frac{\hat{a}^2}{2\bar{u}_2^{3/2}}\int_0^{\bar{u}_1}\sqrt{\frac{u}{\bar{u}_1-u}}du + \dots . \tag{B.1.30}$$

Explicitly computing this integral,

$$G_\theta^{\bar{u}_1} = \frac{2}{\sqrt{\bar{u}_2}}\arcsin\sqrt{\frac{\bar{u}_1}{\bar{u}_1}} - \frac{\hat{a}^2}{2\bar{u}_2^{3/2}}\left[\sqrt{\bar{u}_1(\bar{u}_1-\bar{u}_1)} - \bar{u}_1\arcsin\sqrt{\frac{\bar{u}_1}{\bar{u}_1}}\right] + \dots , \tag{B.1.31}$$

which trivially reduces to

$$G_\theta^{\bar{u}_1} = \frac{\pi}{\sqrt{\bar{u}_2}} - \frac{\hat{a}^2}{2\bar{u}_2^{3/2}}\left[-\frac{\bar{u}_1\pi}{2}\right] + \dots . \tag{B.1.32}$$

Substituting in the series expansions for $\bar{u}_1$ and $\bar{u}_2$ given in (B.1.21) and (B.1.22), we return the expansion in terms of the original variables

$$G_\theta^{\bar{u}_1} = \pi + \frac{\pi(2-3u_m)}{4}\hat{a}^2 + \dots . \tag{B.1.33}$$

Combining these various different unpacked elements of (B.1.23) provided by the multiple possible integration limits returns the full resolved expansion of the angular integral

$$G_\theta = \frac{1}{2}\sqrt{\frac{u_m}{\eta}}(2mG_\theta^{\bar{u}_1} + G_\theta^{u_s} - G_\theta^{u_o}), \tag{B.1.34}$$

which can now be expressed as a series in the small parameter $\hat{a}$:

$$G_\theta = \sqrt{\frac{u_m}{\eta}}\left[\pi m + \arcsin\sqrt{\frac{u_s}{u_m}} - \arcsin\sqrt{\frac{u_o}{u_m}} + \frac{\hat{a}^2}{4}\left\{\frac{u_o(u_o+2-3u_m)}{\sqrt{u_o(u_m-u_o)}} - \frac{u_s(u_s+2-3u_m)}{\sqrt{u_s(u_m-u_s)}} + (2-3u_m)\left(\pi m + \arcsin\sqrt{\frac{u_s}{u_m}} - \arcsin\sqrt{\frac{u_o}{u_m}}\right)\right\} + \dots\right]. \tag{B.1.35}$$

Finally, in order to express u_m and $\hat{a}$ back in terms of the initial parameters (i.e the conserved quantities λ, η and spin parameter a) one re-substitutes these variables back in using (5.2.45) and (6.2.2). Thus we have the final equation for the angular integral G_θ:

$$G_\theta = \frac{1}{\sqrt{\lambda^2+\eta}}\left[\pi m + \arcsin\mu_s - \arcsin\mu_o + \frac{a^2}{4(\lambda^2+\eta)^2}\left\{(2\lambda^2-\eta)\left(\pi m + \arcsin\mu_s - \arcsin\mu_o\right) + \right.\right.$$

$$(2\lambda^2-\eta(1-\mu_o^2))\frac{\mu_o}{\sqrt{1-\mu_o^2}}-(2\lambda^2-\eta(1-\mu_s^2))\frac{\mu_s}{\sqrt{1-\mu_s^2}}+\dots\Big\}\Big] \quad \text{(B.1.36)}$$

where $\mu_j=\sqrt{u_j/u_m}$ as in [2].

We can follow this approach to also gain a series expansion for the second angular integral G_ϕ. Once again, since we are interested in resolving the integrals in the weak deflection limit, we use the small expansion parameters (6.2.2) and similarly introduce the notation for u_m as in (B.1.17). The resulting integral takes the form

$$G_\phi=\frac{1}{2}\sqrt{\frac{u_m}{\eta}}\int_{u_o}^{u_s}\frac{1}{\sqrt{u}\sqrt{u_m-\hat{a}^2u^2-(1-\hat{a}^2)u}}\frac{du}{1-u}. \quad \text{(B.1.37)}$$

Factorising the quadratic equation in the denominator of the integrand as before by introducing $\bar{u}_1$ and $\bar{u}_2$, this becomes

$$G_\phi=\frac{1}{2}\sqrt{\frac{u_m}{\eta}}\int_{u_o}^{u_s}\frac{1}{\sqrt{u}\sqrt{(\bar{u}_1-u)(\bar{u}_2+\hat{a}^2u)}}\frac{du}{1-u}, \quad \text{(B.1.38)}$$

where $\bar{u}_1$, $\bar{u}_2$ again satisfy (B.1.20) and consequently can be solved perturbatively to be (B.1.21) and (B.1.22) respectively. Performing a series expansion about the point $\hat{a}=0$ thus results in

$$G_\phi=\frac{1}{2}\sqrt{\frac{u_m}{\eta}}\Big[\frac{1}{\sqrt{\bar{u}_2}}\int_{u_o}^{u_s}\frac{du}{(1-u)\sqrt{u(\bar{u}_1-u)}}-\frac{\hat{a}^2}{2\bar{u}_2^{3/2}}\int_{u_o}^{u_s}\frac{du}{1-u}\sqrt{\frac{u}{\bar{u}_1-u}}+\dots\Big]. \quad \text{(B.1.39)}$$

Accordingly, we can evaluate each term in (B.1.39) independently for a generic upper integration limit u_j using the notation,

$$G_\phi^{u_j}=G_\phi^{u_j'}+G_\phi^{u_j''}+\dots \quad \text{(B.1.40)}$$

where

$$G_\phi^{u_j'}=\frac{1}{\sqrt{\bar{u}_2}}\int_0^{u_j}\frac{du}{(1-u)\sqrt{u(\bar{u}_1-u)}}=\frac{\pi}{\sqrt{\bar{u}_2}\sqrt{1-\bar{u}_1}}-\frac{2\arctan\sqrt{\frac{\bar{u}_1-u_j}{u_j(1-\bar{u}_1)}}}{\sqrt{\bar{u}_2}\sqrt{1-\bar{u}_1}} \quad \text{(B.1.41)}$$

and

$$G_\phi^{u_j''}=\frac{\hat{a}^2}{2\bar{u}_2^{3/2}}\int_0^{u_j}\frac{du}{1-u}\sqrt{\frac{u}{\bar{u}_1-u}}=\frac{\hat{a}^2}{2\bar{u}_2^{3/2}}\Big[\frac{\pi}{\sqrt{1-\bar{u}_1}}-\frac{2\arctan\sqrt{\frac{\bar{u}_1-u_j}{u_j(1-\bar{u}_1)}}}{\sqrt{1-\bar{u}_1}}-2\arcsin\sqrt{\frac{u_j}{\bar{u}_1}}\Big]. \quad \text{(B.1.42)}$$

Substituting in $\bar{u}_1$ and $\bar{u}_2$ using (B.1.21) and (B.1.22) and combining each of the unpacked integrals as $G_\phi^{u_j}=G_\phi^{u_j'}+G_\phi^{u_j''}+\dots$, one forms the following expression for the series

expansion at $\hat{a} = 0$:

$$G_\phi^{u_j} = \frac{2\arctan\sqrt{\frac{u_j(1-u_m)}{u_m-u_j}}}{\sqrt{1-u_m}} + \hat{a}^2\Big[\arcsin\sqrt{\frac{u_j}{u_m}} - \sqrt{\frac{u_j}{u_m-u_j}}\Big] + \dots, \tag{B.1.43}$$

noting here that we have used the trigonometric identity $\arctan x = \pi/2 - \arctan(1/x)$. A similar expansion can be obtained when evaluating the turning point integral, following the same procedure we previously performed for the first integral. We compute this to be

$$G_\phi^{\bar{u}_1} = \frac{\pi}{\sqrt{1-u_m}} + \frac{\pi}{2}\hat{a}^2 + \dots. \tag{B.1.44}$$

From here, we may multiply through by the prefactor and sum the appropriate terms of the form,

$$G_\phi = \frac{1}{2}\sqrt{\frac{u_m}{\eta}}(2mG_\phi^{\bar{u}_1} + G_\phi^{u_s} - G_\phi^{u_o}), \tag{B.1.45}$$

resulting in a full expression for the integral

$$\begin{aligned} G_\phi = \sqrt{\frac{u_m}{\eta}}\Big[&\frac{\pi m}{\sqrt{1-u_m}} + \frac{\arctan\sqrt{\frac{u_s(1-u_m)}{u_m-u_s}}}{\sqrt{1-u_m}} - \frac{\arctan\sqrt{\frac{u_o(1-u_m)}{u_m-u_o}}}{\sqrt{1-u_m}} \\ &+ \hat{a}^2\Big\{\frac{\pi m}{2} + \frac{1}{2}\arcsin\sqrt{\frac{u_s}{u_m}} - \frac{1}{2}\sqrt{\frac{u_s}{u_m-u_s}} - \frac{1}{2}\arcsin\sqrt{\frac{u_o}{u_m}} + \frac{1}{2}\sqrt{\frac{u_o}{u_m-u_o}}\Big\} + \dots\Big]. \end{aligned} \tag{B.1.46}$$

Finally, writing this equation in terms of λ, η and a, one has

$$\begin{aligned} G_\phi = &\frac{\pi m}{|\lambda|} + \frac{\arctan\big(\frac{\lambda\mu_s}{\sqrt{\lambda^2+\eta\sqrt{1-\mu_s^2}}}\big)}{|\lambda|} - \frac{\arctan\big(\frac{\lambda\mu_o}{\sqrt{\lambda^2+\eta\sqrt{1-\mu_o^2}}}\big)}{|\lambda|} \\ &+ \frac{a^2}{2(\lambda^2+\eta)^{3/2}}\Big[\pi m + \arcsin\mu_s - \arcsin\mu_o - \Big(\frac{\mu_s}{\sqrt{1-\mu_s^2}} - \frac{\mu_o}{\sqrt{1-\mu_o^2}}\Big)\Big] + \dots. \end{aligned} \tag{B.1.47}$$

B.1.2.2 Radial integrals

In order to compute the radial integrals, we manipulate the expression following [88] and then perform an expansion using the suitably small parameters $\hat{M}$ and $\hat{a}$ as defined in (6.2.2). First, we note it is possible to solve the quartic equation $\mathcal{R}(r) = 0$ asymptotically to find the radial roots. For the purposes of this problem, one is only interested in the largest root r_4, which we expect to be of order $(\lambda^2+\eta)^{1/2}$ for small deflections. This is since for $\theta_o = \pi/2$ and large r_o, one has $\alpha_i \approx -\lambda$ and $\beta \approx \pm\sqrt{\eta}$. Thus given the assumption,

$$r_4 \approx (\lambda^2+\eta)^{1/2}\Big[1 + \sum_j c_j x_j\Big], \tag{B.1.48}$$

we asymptotically solve $\mathcal{R}(r) = 0$, where we have used c_j to represent real coefficients, while x_j denotes the expansion terms in $\hat{M}$ and $\hat{a}$. Then, expressed as a power series, we find that

$$r_4 \approx (\lambda^2+\eta)^{1/2}\Big\{1 - \frac{r_{sch}}{2\sqrt{\lambda^2+\eta}} - \frac{a^2\lambda^2}{2(\lambda^2+\eta)^2} + \frac{a r_{sch}\lambda}{(\lambda^2+\eta)^{3/2}} - \frac{3r_{sch}^2}{8(\lambda^2+\eta)} - \frac{r_{sch}^3}{2(\lambda^2+\eta)^{3/2}} + \frac{3a\lambda r_{sch}^2}{2(\lambda^2+\eta)^2} - \frac{\lambda^2 a^2 r_{sch}}{(\lambda^2+\eta)^{5/2}} - \frac{\lambda^2(\lambda^2-4\eta)a^4}{8(\lambda^2+\eta)^4} + \frac{\lambda(\lambda^2-\eta)r_{sch}a^3}{(\lambda^2+\eta)^{7/2}} + \frac{(8\eta-51\lambda^2)r_{sch}^2 a^2}{16(\lambda^2+\eta)^3} + \frac{3\lambda r_{sch}^3 a}{(\lambda^2+\eta)^{5/2}} - \frac{105 r_{sch}^4}{128(\lambda^2+\eta)^2} + \mathcal{O}(\epsilon^5)\Big\}. \quad \text{(B.1.49)}$$

Now we have found an expression for the radial turning point r_4, we can unpack the radial integrals (5.2.19, 5.2.21) in the usual manner and explicitly compute the relevant pieces. Our intention is to firstly solve the radial integral (5.2.19),

$$I_r = \oint_{r_s}^{r_o} \frac{dr}{\pm_r\sqrt{\mathcal{R}(r)}} \approx 2\int_{r_4}^{\infty} \frac{dr}{\sqrt{\mathcal{R}(r)}} - \frac{r_s + r_o}{r_s r_o}. \quad \text{(B.1.50)}$$

Now, as in [88], it is convenient to introduce the new variable $x = r_4/r$ as well as the functions

$$f(x) = \frac{\eta(1+x^2)}{\lambda^2+\eta-a^2}, \qquad g(x) = -2\left[\frac{(\lambda-a)^2+\eta}{\lambda^2+\eta-a^2}\right]\left[\frac{x^2+x+1}{x+1}\right]. \quad \text{(B.1.51)}$$

Then we are able to express the first radial integral I_r in a compact and practical manner

$$I_r \approx 2\int_{r_4}^{\infty} \frac{dr}{\sqrt{\mathcal{R}(r)}} = \frac{2}{(\lambda^2+\eta-a^2)^{1/2}}\int_0^1 dx\,\left[(1-x^2)^{1/2}\left(1 + \frac{a^2}{r_4^2}f(x) + \frac{M}{r_4}g(x)\right)\right]^{-1/2} \quad \text{(B.1.52)}$$

which simplifies to

$$I_r \approx \frac{2}{(\lambda^2+\eta-a^2)^{1/2}}\int_0^1 \frac{dx}{(1-x^2)^{1/2}}\left[1 - \frac{a^2}{2r_4^2}f(x) - \frac{m}{2r_4}g(x) + \frac{3M^2}{8r_4^2}g^2(x)\right]. \quad \text{(B.1.53)}$$

Performing the full series expansion of (B.1.53) using small expansion parameters (6.2.2) together with the series expansion for r_4 (B.1.49), one therefore obtains

$$I_r \approx \frac{\pi}{\sqrt{\lambda^2+\eta}} + \frac{2r_{sch}}{\lambda^2+\eta} + \frac{15\pi r_{sch}^2}{16(\lambda^2+\eta)^{3/2}} - \frac{4\lambda a r_{sch}}{(\lambda^2+\eta)^2} + \frac{a^2\pi(2\lambda^2-\eta)}{4(\lambda^2+\eta)^{5/2}} + \frac{a^4(6\lambda^2-2\eta)r_{sch}}{(\lambda^2+\eta)^3} - \frac{\lambda^2+\eta}{6r_o^3} - \frac{\lambda^2+\eta}{6r_s^3} - \frac{1}{r_o} - \frac{1}{r_s} + \ldots \quad \text{(B.1.54)}$$

We can perform the exact same method to obtain the second radial integral (5.2.21),

$$I_\phi \approx \frac{2}{(\lambda^2+\eta-a^2)^{1/2}}\int_0^1 \frac{a(\frac{2Mr_4}{x} - a\lambda)}{\Delta(\frac{r_4}{x})\,(1-x^2)^{1/2}}\left[1 - \frac{a^2}{2r_4^2}f(x) - \frac{m}{2r_4}g(x) + \frac{3M^2}{8r_4^2}g^2(x)\right]dx, \quad \text{(B.1.55)}$$

using the same transformations (B.1.51) where $x = r_4/r$. Then, using (6.2.2) and (B.1.49),

$$I_\phi \approx \frac{2r_{sch}a}{\lambda^2+\eta} - \frac{\pi a^2\lambda}{2(\lambda^2+\eta)^{3/2}} - \frac{4\lambda r_{sch}a^2}{(\lambda^2+\eta)^2} + \frac{5\pi r_{sch}^2 a}{4(\lambda^2+\eta)^{3/2}} + \dots . \tag{B.1.56}$$

Bibliography

[1] F. Pastawski, B. Yoshida, D. Harlow and J. Preskill, *Holographic quantum error-correcting codes: Toy models for the bulk/boundary correspondence*, *JHEP* **06** (3, 2015) 149, [1503.06237].

[2] M. Sereno and F. De Luca, *Analytical Kerr black hole lensing in the weak deflection limit*, *Phys. Rev. D* **74** (Dec, 2006) 123009, [0609435].

[3] G. N. Gyulchev and S. S. Yazadjiev, *Analytical Kerr-Sen dilaton-axion black hole lensing in the weak deflection limit*, *Phys. Rev. D* **81** (Jan, 2010) 023005, [0909.3014].

[4] G. Aad, T. Abajyan, B. Abbott, J. Abdallah, S. Abdel Khalek, A. Abdelalim et al., *Observation of a new particle in the search for the Standard Model Higgs boson with the ATLAS detector at the LHC*, *Physics Letters B* **716** (2012) 1–29, [1207.7214].

[5] S. Chatrchyan, V. Khachatryan, A. Sirunyan, A. Tumasyan, W. Adam, E. Aguilo et al., *Observation of a new boson at a mass of 125 GeV with the CMS experiment at the LHC*, *Physics Letters B* **716** (2012) 30–61, [1207.7235].

[6] LIGO Scientific Collaboration and Virgo Collaboration, B. P. Abbott, R. Abbott, T. D. Abbott, M. R. Abernathy, F. Acernese et al., *Observation of Gravitational Waves from a Binary Black Hole Merger*, *Phys. Rev. Lett.* **116** (Feb, 2016) 061102, [1602.03837].

[7] Event Horizon Telescope Collaboration, K. Akiyama, A. Alberdi, W. Alef, K. Asada, R. Azulay et al., *First M87 Event Horizon Telescope Results. I. The Shadow of the Supermassive Black Hole*, *Astrophysical Journal Letters* **875** (Apr., 2019) L1, [1906.11238].

[8] Event Horizon Telescope Collaboration, K. Akiyama, A. Alberdi, W. Alef, K. Asada, R. Azulay et al., *First M87 Event Horizon Telescope Results. II. Array and Instrumentation*, *Astrophysical Journal Letters* **875** (Apr., 2019) L2, [1906.11239].

[9] Event Horizon Telescope Collaboration, K. Akiyama, A. Alberdi, W. Alef, K. Asada, R. Azulay et al., *First M87 Event Horizon Telescope Results. III. Data Processing and Calibration*, *Astrophysical Journal Letters* **875** (Apr., 2019) L3, [1906.11240].

[10] Event Horizon Telescope Collaboration, K. Akiyama, A. Alberdi, W. Alef, K. Asada, R. Azulay et al., *First M87 Event Horizon Telescope Results. IV. Imaging the Central Supermassive Black Hole*, *Astrophysical Journal Letters* **875** (Apr., 2019) L4, [1906.11241].

[11] Event Horizon Telescope Collaboration, K. Akiyama, A. Alberdi, W. Alef, K. Asada, R. Azulay et al., *First M87 Event Horizon Telescope Results. V. Physical Origin of the Asymmetric Ring*, *Astrophysical Journal Letters* **875** (Apr., 2019) L5, [1906.11242].

[12] Event Horizon Telescope Collaboration, K. Akiyama, A. Alberdi, W. Alef, K. Asada, R. Azulay et al., *First M87 Event Horizon Telescope Results. VI. The Shadow and Mass of the Central Black Hole*, *Astrophysical Journal Letters* **875** (Apr., 2019) L6, [1906.11243].

[13] J. Polchinski, *String theory. Vol. 1: An introduction to the bosonic string.* Cambridge Monographs on Mathematical Physics. Cambridge University Press, 12, 2007, 10.1017/CBO9780511816079.

[14] J. Polchinski, *String theory. Vol. 2: Superstring theory and beyond.* Cambridge Monographs on Mathematical Physics. Cambridge University Press, 12, 2007, 10.1017/CBO9780511618123.

[15] M. B. Green, J. H. Schwarz and E. Witten, *Superstring theory. Vol. 1: Introduction.* Cambridge Monographs on Mathematical Physics. Cambridge University Press, 7, 1988, 10.1017/CBO9781139248563.

[16] S. W. Hawking, *Gravitational Radiation from Colliding Black Holes*, *Phys. Rev. Lett.* **26** (May, 1971) 1344–1346.

[17] J. M. Bardeen, B. Carter and S. W. Hawking, *The Four laws of black hole mechanics*, *Commun. Math. Phys.* **31** (1973) 161–170.

[18] J. D. Bekenstein, *Black holes and the second law*, *Lettere al Nuovo Cimento (1971-1985)* **4** (1972) 737–740.

[19] J. D. Bekenstein, *Black Holes and Entropy*, *Phys. Rev. D* **7** (Apr, 1973) 2333–2346.

[20] J. D. Bekenstein, *Generalized second law of thermodynamics in black-hole physics*, *Phys. Rev. D* **9** (Jun, 1974) 3292–3300.

[21] S. W. HAWKING, *Black hole explosions?*, *Nature* **248** (1974) 30–31.

[22] S. W. Hawking, *Particle Creation by Black Holes*, *Commun. Math. Phys.* **43** (1975) 199–220.

[23] G. 't Hooft, *Dimensional reduction in quantum gravity*, *Conf. Proc. C* **930308** (1993) 284–296, [gr-qc/9310026].

[24] L. Susskind, *The world as a hologram*, *Journal of Mathematical Physics* **36** (1995) 6377–6396, [hep-th/9409089].

[25] J. M. Maldacena, *The Large N limit of superconformal field theories and supergravity*, *Adv. Theor. Math. Phys.* **2** (1998) 231–252, [hep-th/9711200].

[26] S. Ryu and T. Takayanagi, *Holographic Derivation of Entanglement Entropy from AdS/CFT*, *Physical Review Letters* **96** (2, 2006) , [hep-th/0603001].

[27] V. E. Hubeny, M. Rangamani and T. Takayanagi, *A covariant holographic entanglement entropy proposal*, *Journal of High Energy Physics* **2007** (Jul, 2007) 062–062, [0705.0016].

[28] A. C. Wall, *Maximin surfaces, and the strong subadditivity of the covariant holographic entanglement entropy*, *Classical and Quantum Gravity* **31** (nov, 2014) 225007, [1211.3494].

[29] M. Headrick and T. Takayanagi, *Holographic proof of the strong subadditivity of entanglement entropy*, *Phys. Rev. D* **76** (Nov, 2007) 106013, [0704.3719].

[30] S. Ryu and T. Takayanagi, *Aspects of Holographic Entanglement Entropy*, *JHEP* **08** (5, 2006) 045, [hep-th/0605073].

[31] M. Rangamani and T. Takayanagi, *Holographic Entanglement Entropy*, *Lecture Notes in Physics* **931** (05, 2017) , [1609.01287].

[32] A. Almheiri, X. Dong and D. Harlow, *Bulk Locality and Quantum Error Correction in AdS/CFT*, *Journal of High Energy Physics* **2015** (11, 2014) , [1411.7041].

[33] A. Bhattacharyya, Z.-S. Gao, L.-Y. Hung and S.-N. Liu, *Exploring the Tensor Networks/AdS Correspondence*, *JHEP* **08** (2016) 086, [1606.00621].

[34] A. Bhattacharyya, L.-Y. Hung, P. H. C. Lau and S.-N. Liu, *Inspecting non-perturbative contributions to the Entanglement Entropy via wavefunctions*, *Entropy* **19** (2017) 671, [1608.00145].

[35] Z. Yang, P. Hayden and X.-L. Qi, *Bidirectional holographic codes and sub-AdS locality*, *Journal of High Energy Physics* **2016** (10, 2015) 1–24, [1510.03784].

[36] P. Hayden, S. Nezami, X.-L. Qi, N. Thomas, M. Walter and Z. Yang, *Holographic duality from random tensor networks*, *JHEP* **11** (2016) 009, [1601.01694].

[37] X.-L. Qi and Z. Yang, *Space-time random tensor networks and holographic duality*, *arXiv pre-print* (1, 2018) , [1801.05289].

[38] R. J. Harris, N. A. McMahon, G. K. Brennen and T. M. Stace, *Calderbank-Steane-Shor Holographic Quantum Error Correcting Codes*, *Phys. Rev. A* **98** (6, 2018) , [1806.06472].

[39] A. Einstein, *Über den Einfluß der Schwerkraft auf die Ausbreitung des Lichtes*, *Annalen der Physik* **340** (1911) 898–908.

[40] A. Einstein, *Die Feldgleichungen der Gravitation*, *Sitzungsberichte der Königlich Preußischen Akademie der Wissenschaften* (Jan., 1915) 844–847.

[41] J. Soldner, *Über die Ablenkung eines Lichtstrahls von seiner geradlinigen Bewegung durch die Attraktion eines Weltkörpers, an welchem er nahe vorbeigeht*, *Annalen der Physik* **370** (1921) 593–604.

[42] F. W. Dyson, A. S. Eddington and C. Davidson, *IX. A determination of the deflection of light by the sun's gravitational field, from observations made at the total eclipse of May 29, 1919*, *Philosophical Transactions of the Royal Society of*

London. Series A, Containing Papers of a Mathematical or Physical Character **220** (1920) 291–333.

[43] A. S. Eddington, *Space, Time, and Gravitation: An Outline of the General Relativity Theory.* Cambridge University Press, 1920.

[44] O. Chwolson, *Über eine mögliche Form fiktiver Doppelsterne*, *Astronomische Nachrichten* **221** (June, 1924) 329.

[45] A. Einstein, *Lens-Like Action of a Star by the Deviation of Light in the Gravitational Field*, *Science* **84** (1936) 506–507.

[46] F. Zwicky, *Nebulae as Gravitational Lenses*, *Phys. Rev.* **51** (Feb, 1937) 290–290.

[47] F. Zwicky, *On the Probability of Detecting Nebulae Which Act as Gravitational Lenses*, *Phys. Rev.* **51** (Apr, 1937) 679–679.

[48] Y. G. Klimov, *The deflection of light rays in the gravitational fields of galaxies*, *Sov. Phys. Dokl* **8** (1963) 119–122.

[49] S. Liebes, *Gravitational Lenses*, *Phys. Rev.* **133** (Feb, 1964) B835–B844.

[50] A. W. K. Metzner, *Observable Properties of Large Relativistic Masses*, *Journal of Mathematical Physics* **4** (1963) 1194–1205.

[51] S. Refsdal and H. Bondi, *The Gravitational Lens Effect*, *Monthly Notices of the Royal Astronomical Society* **128** (09, 1964) 295–306.

[52] S. Refsdal, *On the possibility of determining Hubble's parameter and the masses of galaxies from the gravitational lens effect*, *Monthly Notices of the Royal Astronomical Society* **128** (Jan., 1964) 307.

[53] S. Refsdal, *On the possibility of testing cosmological theories from the gravitational lens effect*, *Monthly Notices of the Royal Astronomical Society* **132** (Jan., 1966) 101.

[54] D. Walsh, R. F. Carswell and R. J. Weymann, *0957 + 561 A, B: twin quasistellar objects or gravitational lens?*, *Nature* **279** (1979) 381–384.

[55] B. Paczynski, *Gravitational Microlensing by the Galactic Halo*, *Astrophysical Journal* **304** (May, 1986) 1.

[56] G. Soucail, Y. Mellier, B. Fort, G. Mathez and M. Cailloux, *The giant arc in A 370 : spectroscopic evidence for gravitational lensing from a source at Z=0.724.*, *Astronomy and Astrophysics* **191** (Feb., 1988) L19–L21.

[57] D. Narasimha and S. M. Chitre, *Giant Luminous Arcs in Galaxy Clusters*, *Astrophysical Journal* **332** (Sept., 1988) 75.

[58] J. N. Hewitt, E. L. Turner, D. P. Schneider, B. F. Burke, G. I. Langston and C. R. Lawrence, *Unusual radio source MG1131+0456: a possible Einstein ring*, *Nature* **333** (1988) 537–540.

[59] B. Paczyński, *Gravitational Microlensing in the Local Group*, *Annual Review of Astronomy and Astrophysics* **34** (1996) 419–459, [astro-ph/9604011].

[60] J. P. Beaulieu, D. P. Bennett, P. Fouqué, A. Williams, M. Dominik, U. G. Jørgensen et al., *Discovery of a cool planet of 5.5 Earth masses through gravitational microlensing*, *Nature* **439** (2006) 437–440, [astro-ph/0601563].

[61] C. S. Kochanek, *Quantitative Interpretation of Quasar Microlensing Light Curves*, *Astrophysical Journal* **605** (Apr., 2004) 58–77, [astro-ph/0307422].

[62] T. Treu and L. V. E. Koopmans, *Massive Dark Matter Halos and Evolution of Early-Type Galaxies to z ∼1*, *Astrophysical Journal* **611** (Aug., 2004) 739–760, [astro-ph/0401373].

[63] S. Mao and P. Schneider, *Evidence for substructure in lens galaxies?*, *Monthly Notices of the Royal Astronomical Society* **295** (Apr., 1998) 587–594, [astro-ph/9707187].

[64] N. Dalal and C. S. Kochanek, *Direct Detection of Cold Dark Matter Substructure*, *Astrophysical Journal* **572** (June, 2002) 25–33, [astro-ph/0111456].

[65] G. Soucail, B. Fort, Y. Mellier and J. P. Picat, *A blue ring-like structure in the center of the A 370 cluster of galaxies.*, *Astronomy and Astrophysics* **172** (Jan., 1987) L14–L16.

[66] S. S. Gubser, I. R. Klebanov and A. M. Polyakov, *Gauge theory correlators from noncritical string theory*, *Phys. Lett. B* **428** (1998) 105–114, [hep-th/9802109].

[67] E. Witten, *Anti-de Sitter space and holography*, *Advances in Theoretical and Mathematical Physics* **2** (1998) 253–291, [hep-th/9802150].

[68] M. Henningson and K. Skenderis, *The Holographic Weyl Anomaly*, *Journal of High Energy Physics* **1998** (Jul, 1998) 023–023, [hep-th/9806087].

[69] S. D. Haro, K. Skenderis and S. N. Solodukhin, *Holographic Reconstruction of Spacetime and Renormalization in the AdS/CFT Correspondence*, *Communications in Mathematical Physics* **217** (2000) 595–622, [hep-th/0002230].

[70] K. Skenderis, *Asymptotically Anti-de Sitter spacetimes and their stress energy tensor*, *International Journal of Modern Physics A* **16** (2022/07/11, 2001) 740–749, [hep-th/0010138].

[71] K. Skenderis, *Lecture Notes on Holographic Renormalization*, *Classical and Quantum Gravity* **19** (9, 2002) 5849–5876, [hep-th/0209067].

[72] M. A. Nielsen and I. L. Chuang, *Quantum Computation and Quantum Information*. Cambridge University Press, Cambridge, 12, 2010, 10.1017/cbo9780511976667.

[73] R. Horodecki, P. Horodecki, M. Horodecki and K. Horodecki, *Quantum entanglement*, *Rev. Mod. Phys.* **81** (Jun, 2009) 865–942, [quant-ph/0702225].

[74] J. Biamonte and V. Bergholm, *Tensor Networks in a Nutshell*, *arXiv pre-print* (7, 2017) , [quant-ph/1708.00006].

[75] R. Orús, *A practical introduction to tensor networks: Matrix product states and projected entangled pair states*, *Annals of Physics* **349** (2014) 117–158, [1306.2164].

[76] J. Preskill, *Lecture Notes on Quantum Computation*, *California Institute of Technology* (1997) .

[77] D. Lidar and T. Brun, *Quantum error correction*, *Quantum Error Correction* (01, 2012) 1–666.

[78] D. Gottesman, *Stabilizer Codes and Quantum Error Correction*. PhD thesis, California Institute of Technology, 5, 1997. quant-ph/9705052.

[79] D. Harlow, *TASI Lectures on the Emergence of Bulk Physics in AdS/CFT*, *PoS* **TASI2017** (2018) 002, [1802.01040].

[80] M. Taylor and C. Woodward, *Holography, cellulations and error correcting codes*, *arXiv pre-print* (12, 2021) , [2112.12468].

[81] C. Teitelboim, *Gravitation and hamiltonian structure in two spacetime dimensions*,

Physics Letters B **126** (1983) 41–45.

[82] R. Jackiw, *Lower dimensional gravity*, *Nuclear Physics B* **252** (1985) 343–356.

[83] P. Schneider, J. Ehlers and E. E. Falco, *Gravitational Lenses*. Astronomy and Astrophysics Library. Springer Berlin Heidelberg, Berlin, Heidelberg, 1992, 10.1007/978-3-662-03758-4.

[84] J. Wambsganss, *Gravitational Microlensing*, *arXiv e-prints* (Apr., 2006) , [astro-ph/0604278].

[85] B. Carter, *Global Structure of the Kerr Family of Gravitational Fields*, *Phys. Rev.* **174** (Oct, 1968) 1559–1571.

[86] J. M. Bardeen, *Timelike and null geodesics in the Kerr metric.*, in *Les Houches Summer School of Theoretical Physics: Black Holes*, pp. 215–239, Jan., 1973.

[87] S. Chandrasekhar, *The mathematical theory of black holes*. Oxford University Press, 1983.

[88] I. Bray, *The Kerr Black Hole as a Gravitational Lens*, *Phys. Rev. D* **34** (1986) 367.

[89] S. E. Vázquez and E. P. Esteban, *Strong-field gravitational lensing by a Kerr black hole*, *Nuovo Cimento B Serie* **119** (May, 2004) 489, [gr-qc/0308023].

[90] D. Kapec and A. Lupsasca, *Particle motion near high-spin black holes*, *Classical and Quantum Gravity* **37** (Dec, 2019) 015006, [1905.11406].

[91] S. E. Gralla and A. Lupsasca, *Null geodesics of the Kerr exterior*, *Phys. Rev. D* **101** (Feb, 2020) 044032, [1910.12881].

[92] S. E. Gralla and A. Lupsasca, *Lensing by Kerr black holes*, *Phys. Rev. D* **101** (Feb, 2020) 044031, [1910.12873].

[93] O. Lunin and S. D. Mathur, *AdS/CFT duality and the black hole information paradox*, *Nuclear Physics B* **623** (2002) 342–394, [hep-th/0109154].

[94] O. Lunin and S. D. Mathur, *Statistical Interpretation of the Bekenstein Entropy for Systems with a Stretched Horizon*, *Phys. Rev. Lett.* **88** (May, 2002) 211303, [hep-th/0202072].

[95] K. Skenderis and M. Taylor, *The fuzzball proposal for black holes*, *Phys. Rept.* **467**

(2008) 117–171, [0804.0552].

[96] S. D. Mathur, *The Fuzzball proposal for black holes: An Elementary review*, *Fortsch. Phys.* **53** (2005) 793–827, [hep-th/0502050].

[97] M. Guica, T. Hartman, W. Song and A. Strominger, *The Kerr/CFT correspondence*, *Phys. Rev. D* **80** (Dec, 2009) 124008, [0809.4266].

[98] G. Compère, *The Kerr/CFT Correspondence and its Extensions*, *Living Reviews in Relativity* **15** (2012) 11, [1203.3561].

[99] R. Bousso, *The holographic principle*, *Rev. Mod. Phys.* **74** (Aug, 2002) 825–874, [hep-th/0203101].

[100] R. Bousso, *A covariant entropy conjecture*, *Journal of High Energy Physics* **1999** (Jul, 1999) 004–004, [hep-th/9905177].

[101] J. D. Bekenstein, *Universal upper bound on the entropy-to-energy ratio for bounded systems*, *Phys. Rev. D* **23** (Jan, 1981) 287–298.

[102] R. Bousso, *Bound states and the Bekenstein bound*, *JHEP* **02** (2004) 025, [hep-th/0310148].

[103] A. Strominger and C. Vafa, *Microscopic origin of the Bekenstein-Hawking entropy*, *Phys. Lett. B* **379** (1996) 99–104, [hep-th/9601029].

[104] S. W. Hawking, *Breakdown of predictability in gravitational collapse*, *Phys. Rev. D* **14** (Nov, 1976) 2460–2473.

[105] G. Penington, *Entanglement wedge reconstruction and the information paradox*, *Journal of High Energy Physics* **2020** (2020) 2, [1905.08255].

[106] A. Almheiri, N. Engelhardt, D. Marolf and H. Maxfield, *The entropy of bulk quantum fields and the entanglement wedge of an evaporating black hole*, *Journal of High Energy Physics* **2019** (2019) 63, [1905.08762].

[107] A. Almheiri, R. Mahajan, J. M. Maldacena and Y. Zhao, *The Page curve of Hawking radiation from semiclassical geometry*, *Journal of High Energy Physics* **2020** (2020) 1–24, [1908.10996].

[108] A. Almheiri, T. Hartman, J. Maldacena, E. Shaghoulian and A. Tajdini, *Replica wormholes and the entropy of Hawking radiation*, *Journal of High Energy Physics*

2020 (2020) 13, [1911.12333].

[109] A. Almheiri, T. Hartman, J. Maldacena, E. Shaghoulian and A. Tajdini, *The entropy of Hawking radiation*, *Rev. Mod. Phys.* **93** (Jul, 2021) 035002, [2006.06872].

[110] S. W. Hawking, M. J. Perry and A. Strominger, *Soft Hair on Black Holes*, *Phys. Rev. Lett.* **116** (2016) 231301, [1601.00921].

[111] O. Aharony, O. Bergman, D. L. Jafferis and J. Maldacena, $\mathcal{N} = 6$ *superconformal Chern-Simons-matter theories, M2-branes and their gravity duals*, *Journal of High Energy Physics* **2008** (oct, 2008) 091–091, [0806.1218].

[112] O. Aharony, Y. Oz and Z. Yin, *M theory on AdSp×S11-p and superconformal field theories*, *Physics Letters B* **430** (1998) 87–93, [9803051].

[113] A. Kehagias, *New type IIB vacua and their F-theory interpretation*, *Physics Letters B* **435** (1998) 337–342, [9805131].

[114] J. D. Brown and M. Henneaux, *Central charges in the canonical realization of asymptotic symmetries: An example from three dimensional gravity*, *Communications in Mathematical Physics* **104** (1986) 207–226.

[115] M. Bañados, C. Teitelboim and J. Zanelli, *Black hole in three-dimensional spacetime*, *Phys. Rev. Lett.* **69** (Sep, 1992) 1849–1851, [9204099].

[116] H. J. Boonstra, K. Skenderis and P. K. Townsend, *The domain wall / QFT correspondence*, *JHEP* **01** (1999) 003, [hep-th/9807137].

[117] N. Itzhaki, J. M. Maldacena, J. Sonnenschein and S. Yankielowicz, *Supergravity and the large N limit of theories with sixteen supercharges*, *Phys. Rev. D* **58** (1998) 046004, [hep-th/9802042].

[118] A. Jevicki and T. Yoneya, *Space-time uncertainty principle and conformal symmetry in D-particle dynamics*, *Nuclear Physics* **535** (1998) 335–348, [9805069].

[119] I. Kanitscheider, K. Skenderis and M. Taylor, *Precision holography for non-conformal branes*, *JHEP* **09** (7, 2008) 094, [0807.3324].

[120] M. Taylor, *Non-relativistic holography*, *arXiv e-prints* (12, 2008) , [0812.0530].

[121] E. Witten, *Anti-de Sitter space, thermal phase transition, and confinement in*

gauge theories, *Adv. Theor. Math. Phys.* **2** (1998) 505–532, [hep-th/9803131].

[122] A. Karch and E. Katz, *Adding flavor to AdS / CFT*, *JHEP* **06** (2002) 043, [hep-th/0205236].

[123] T. Sakai and S. Sugimoto, *Low energy hadron physics in holographic QCD*, *Progress of Theoretical Physics* **113** (2005) 843–882, [0412141].

[124] T. Sakai and S. Sugimoto, *More on a holographic dual of QCD*, *Prog. Theor. Phys.* **114** (2005) 1083–1118, [hep-th/0507073].

[125] J. Zaanen, Y. Liu, Y.-W. Sun and K. Schalm, *Holographic Duality in Condensed Matter Physics*. Cambridge University Press, 2015, 10.1017/CBO9781139942492.

[126] S. A. Hartnoll, A. Lucas and S. Sachdev, *Holographic quantum matter*, *arXiv e-prints* (12, 2016) , [1612.07324].

[127] S. A. Hartnoll, *Lectures on holographic methods for condensed matter physics*, *Class. Quant. Grav.* **26** (2009) 224002, [0903.3246].

[128] J. McGreevy, *Holographic duality with a view toward many-body physics*, *Adv. High Energy Phys.* **2010** (2010) 723105, [0909.0518].

[129] S. Bhattacharyya, S. Minwalla, V. E. Hubeny and M. Rangamani, *Nonlinear fluid dynamics from gravity*, *Journal of High Energy Physics* **2008** (Feb, 2008) 045–045, [0712.2456].

[130] M. Rangamani, *Gravity and hydrodynamics: lectures on the fluid-gravity correspondence*, *Classical and Quantum Gravity* **26** (Oct, 2009) 224003, [0905.4352].

[131] D. T. Son and A. O. Starinets, *Viscosity, Black Holes, and Quantum Field Theory*, *Ann. Rev. Nucl. Part. Sci.* **57** (2007) 95–118, [0704.0240].

[132] G. Policastro, D. T. Son and A. O. Starinets, *Shear Viscosity of Strongly Coupled $N = 4$ Supersymmetric Yang-Mills Plasma*, *Phys. Rev. Lett.* **87** (Aug, 2001) 081601, [0104066].

[133] P. K. Kovtun, D. T. Son and A. O. Starinets, *Viscosity in Strongly Interacting Quantum Field Theories from Black Hole Physics*, *Phys. Rev. Lett.* **94** (Mar, 2005) 111601, [hep-th/0405231].

[134] J. de Boer, E. Verlinde and H. Verlinde, *On the Holographic Renormalization Group*, *Journal of High Energy Physics* **2000** (Aug, 2000) 003–003, [hep-th/9912012].

[135] I. Papadimitriou and K. Skenderis, *AdS / CFT correspondence and geometry*, *IRMA Lect. Math. Theor. Phys.* **8** (2005) 73–101, [hep-th/0404176].

[136] C. Fefferman and C. R. Graham, *Conformal invariants*, in *Élie Cartan et les mathématiques d'aujourd'hui - Lyon, 25-29 juin 1984*, no. S131 in Astérisque, pp. 95–116. Société mathématique de France, 1985.

[137] J. W. York, *Role of Conformal Three-Geometry in the Dynamics of Gravitation*, *Phys. Rev. Lett.* **28** (Apr, 1972) 1082–1085.

[138] G. W. Gibbons and S. W. Hawking, *Action integrals and partition functions in quantum gravity*, *Phys. Rev. D* **15** (May, 1977) 2752–2756.

[139] C. H. Bennett, G. Brassard, C. Crépeau, R. Jozsa, A. Peres and W. K. Wootters, *Teleporting an unknown quantum state via dual classical and Einstein-Podolsky-Rosen channels*, *Phys. Rev. Lett.* **70** (Mar, 1993) 1895–1899.

[140] C. H. Bennett and S. J. Wiesner, *Communication via one- and two-particle operators on Einstein-Podolsky-Rosen states*, *Phys. Rev. Lett.* **69** (Nov, 1992) 2881–2884.

[141] C. H. Bennett and G. Brassard, *Quantum cryptography: Public key distribution and coin tossing*, *Theor. Comput. Sci.* **560** (2014) 7–11, [2003.06557].

[142] E. Schmidt, *Zur Theorie der linearen und nichtlinearen Integralgleichungen*, *Mathematische Annalen* **63** (1907) 433–476.

[143] A. Ekert and P. L. Knight, *Entangled quantum systems and the Schmidt decomposition*, *American Journal of Physics* **63** (1995) 415–423.

[144] J. von Neumann, *Mathematische Grundlagen der Quantenmechanik*. "Die" Grundlehren der mathematischen Wissenschaften / "Die" Grundlehren der mathematischen Wissenschaften. Springer Berlin Heidelberg, 2013.

[145] A. Klumper, A. Schadschneider and J. Zittartz, *Equivalence and solution of anisotropic spin-1 models and generalized t-J fermion models in one dimension*, *Journal of Physics A: Mathematical and General* **24** (aug, 1991) L955–L959.

[146] M. Fannes, B. Nachtergaele and R. F. Werner, *Finitely correlated states on quantum spin chains*, *Communications in Mathematical Physics* **144** (1992) 443–490.

[147] F. Verstraete and J. I. Cirac, *Renormalization algorithms for quantum-many body systems in two and higher dimensions*, *arXiv e-prints* (7, 2004) , [cond-mat/0407066].

[148] Y.-Y. Shi, L.-M. Duan and G. Vidal, *Classical simulation of quantum many-body systems with a tree tensor network*, *Phys. Rev. A* **74** (Aug, 2006) 022320, [quant-ph/0511070].

[149] G. Vidal, *Class of Quantum Many-Body States That Can Be Efficiently Simulated*, *Phys. Rev. Lett.* **101** (Sep, 2008) 110501, [quant-ph/0610099].

[150] M. B. Hastings, *Solving gapped Hamiltonians locally*, *Phys. Rev. B* **73** (Feb, 2006) 085115, [cond-mat/0508554].

[151] M. B. Hastings, *An area law for one-dimensional quantum systems*, *Journal of Statistical Mechanics: Theory and Experiment* **2007** (Aug, 2007) P08024–P08024, [0705.2024].

[152] J. Eisert, M. Cramer and M. B. Plenio, *Colloquium: Area laws for the entanglement entropy*, *Rev. Mod. Phys.* **82** (Feb, 2010) 277–306, [0808.3773].

[153] D. Perez-Garcia, F. Verstraete, M. M. Wolf and J. I. Cirac, *Peps as Unique Ground States of Local Hamiltonians*, *Quantum Info. Comput.* **8** (Jul, 2008) 650–663, [0707.2260].

[154] J. L. Cardy and I. Peschel, *Finite-size dependence of the free energy in two-dimensional critical systems*, *Nuclear Physics B* **300** (1988) 377–392.

[155] C. Holzhey, F. Larsen and F. Wilczek, *Geometric and renormalized entropy in conformal field theory*, *Nuclear Physics B* **424** (1994) 443–467, [hep-th/9403108].

[156] P. Calabrese and J. Cardy, *Entanglement Entropy and Quantum Field Theory*, *Journal of Statistical Mechanics: Theory and Experiment* (5, 2004) , [hep-th/0405152].

[157] G. Vidal, *Entanglement Renormalization*, *Phys. Rev. Lett.* **99** (Nov, 2007) 220405, [cond-mat/0512165].

[158] B. Swingle, *Entanglement renormalization and holography*, *Phys. Rev. D* **86** (Sep, 2012) 065007, [0905.1317].

[159] B. Swingle, *Constructing holographic spacetimes using entanglement renormalization*, *Bulletin of the American Physical Society* (2012) , [1209.3304].

[160] S. Singh, *Tensor network state correspondence and holography*, *Phys. Rev. D* **97** (Jan, 2018) 026012, [1701.04778].

[161] C. Bény, *Causal structure of the entanglement renormalization ansatz*, *New Journal of Physics* **15** (feb, 2013) 023020, [1110.4872].

[162] G. Evenbly, *Hyperinvariant Tensor Networks and Holography*, *Phys. Rev. Lett.* **119** (Oct, 2017) 141602, [1704.04229].

[163] R. P. Feynman, *Simulating physics with computers*, *International Journal of Theoretical Physics* **21** (1982) 467–488.

[164] P. W. Shor, *Scheme for reducing decoherence in quantum computer memory*, *Phys. Rev. A* **52** (Oct, 1995) R2493–R2496.

[165] E. Knill and R. Laflamme, *A Theory of Quantum Error-Correcting Codes*, *Phys. Rev. Lett.* **84** (4, 1996) 2525, [quant-ph/9604034].

[166] C. H. Bennett, D. P. DiVincenzo, J. A. Smolin and W. K. Wootters, *Mixed-state entanglement and quantum error correction*, *Phys. Rev. A* **54** (Nov, 1996) 3824–3851, [quant-ph/9604024].

[167] A. Ekert and C. Macchiavello, *Quantum error correction for communication*, *arXiv e-prints* (2, 1996) , [quant-ph/9602022].

[168] E. Rains, *Nonbinary quantum codes*, *IEEE Transactions on Information Theory* **45** (1999) 1827–1832, [quant-ph/9703048].

[169] A. R. Calderbank and P. W. Shor, *Good Quantum Error-Correcting Codes Exist*, *Phys. Rev. A* **54** (12, 1995) 1098–1105, [quant-ph/9512032].

[170] A. Steane, *Multiple Particle Interference and Quantum Error Correction*, *Proceedings of the Royal Society A: Mathematical, Physical and Engineering Sciences* **452** (1, 1996) 2551–2577, [quant-ph/9601029].

[171] D. Gottesman, *Pasting Quantum Codes*, *arXiv e-prints* (1996) ,

[quant-ph/9607027].

[172] A. R. Calderbank, E. M. Rains, P. W. Shor and N. J. A. Sloane, *Quantum error correction via codes over GF(4)*, quant-ph/9608006.

[173] R. Cleve, D. Gottesman and H.-K. Lo, *How to Share a Quantum Secret*, *Phys. Rev. Lett.* **83** (Jul, 1999) 648–651, [quant-ph/9901025].

[174] P. Calabrese and J. Cardy, *Entanglement Entropy and Conformal Field Theory*, *Journal of Physics A: Mathematical and Theoretical* **42** (Dec, 2009) 504005, [0905.4013].

[175] M. Srednicki, *Entropy and area*, *Phys. Rev. Lett.* **71** (Aug, 1993) 666–669, [hep-th/9303048].

[176] L. Bombelli, R. K. Koul, J. Lee and R. D. Sorkin, *Quantum source of entropy for black holes*, *Phys. Rev. D* **34** (Jul, 1986) 373–383.

[177] P. Hayden, M. Headrick and A. Maloney, *Holographic mutual information is monogamous*, *Phys. Rev. D* **87** (Feb, 2013) 046003, [1107.2940].

[178] N. Bao, S. Nezami, H. Ooguri, B. Stoica, J. Sully and M. Walter, *The Holographic Entropy Cone*, *JHEP* **09** (2015) 130, [1505.07839].

[179] V. E. Hubeny, M. Rangamani and M. Rota, *Holographic entropy relations*, *Fortsch. Phys.* **66** (2018) 1800067, [1808.07871].

[180] M. Van Raamsdonk, *Building up spacetime with quantum entanglement*, *General Relativity and Gravitation* **42** (2010) 2323–2329, [1005.3035].

[181] M. Van Raamsdonk, *Comments on quantum gravity and entanglement*, *arXiv e-prints* (7, 2009) , [0907.2939].

[182] J. Maldacena, *Eternal black holes in anti-de Sitter*, *Journal of High Energy Physics* **2003** (apr, 2003) 021–021, [hep-th/0106112].

[183] J. Maldacena and L. Susskind, *Cool horizons for entangled black holes*, *Fortsch. Phys.* **61** (2013) 781–811, [1306.0533].

[184] A. Almheiri, D. Marolf, J. Polchinski and J. Sully, *Black holes: complementarity or firewalls?*, *Journal of High Energy Physics* (2013) 62, [1207.3123].

[185] T. Banks, M. R. Douglas, G. T. Horowitz and E. J. Martinec, *AdS dynamics from conformal field theory*, *arXiv e-prints* (8, 1998) , [hep-th/9808016].

[186] A. Hamilton, D. Kabat, G. Lifschytz and D. A. Lowe, *Holographic representation of local bulk operators*, *Phys. Rev. D* **74** (Sep, 2006) 066009.

[187] R. Bousso, S. Leichenauer and V. Rosenhaus, *Light-sheets and AdS/CFT*, *Phys. Rev. D* **86** (Aug, 2012) 046009, [1203.6619].

[188] B. Czech, J. L. Karczmarek, F. Nogueira and M. V. Raamsdonk, *The gravity dual of a density matrix*, *Classical and Quantum Gravity* **29** (Jul, 2012) 155009, [1204.1330].

[189] R. Bousso, B. Freivogel, S. Leichenauer, V. Rosenhaus and C. Zukowski, *Null geodesics, local CFT operators, and AdS/CFT for subregions*, *Phys. Rev. D* **88** (Sep, 2013) 064057, [1209.4641].

[190] A. Hamilton, D. Kabat, G. Lifschytz and D. A. Lowe, *Holographic representation of local bulk operators*, *Physical Review D - Particles, Fields, Gravitation and Cosmology* **74** (6, 2006) , [hep-th/0606141].

[191] A. Hamilton, D. Kabat, G. Lifschytz and D. A. Lowe, *Local bulk operators in AdS/CFT: a boundary view of horizons and locality*, *Physical Review D - Particles, Fields, Gravitation and Cosmology* **73** (6, 2005) , [hep-th/0506118].

[192] V. E. Hubeny and M. Rangamani, *Causal holographic information*, *Journal of High Energy Physics* **2012** (2012) 114, [1204.1698].

[193] X. Dong, D. Harlow and A. C. Wall, *Reconstruction of Bulk Operators within the Entanglement Wedge in Gauge-Gravity Duality*, *Phys. Rev. Lett.* **117** (Jul, 2016) 021601, [1601.05416].

[194] M. Headrick, V. E. Hubeny, A. Lawrence and M. Rangamani, *Causality & holographic entanglement entropy*, *Journal of High Energy Physics* **2014** (2014) 162, [1408.6300].

[195] D. Harlow, *The Ryu–Takayanagi Formula from Quantum Error Correction*, *Communications in Mathematical Physics* **354** (2017) 865–912, [1607.03901].

[196] F. Pastawski and J. Preskill, *Code Properties from Holographic Geometries*, *Phys. Rev. X* **7** (2017) 021022, [1612.00017].

[197] E. Gesteau and M. J. Kang, *The infinite-dimensional HaPPY code: entanglement wedge reconstruction and dynamics*, *arXiv pre-print* (5, 2020) , [2005.05971].

[198] L. Niermann and T. J. Osborne, *Holographic networks for (1+1)-dimensional de Sitter spacetime*, *arXiv pre-print* (2, 2021) , [2102.09223].

[199] T. Kohler and T. Cubitt, *Toy Models of Holographic Duality between local Hamiltonians*, *JHEP* **08** (10, 2019) 017, [1810.08992].

[200] F. Verstraete and J. I. Cirac, *Continuous Matrix Product States for Quantum Fields*, *Phys. Rev. Lett.* **104** (2010) 190405, [1002.1824].

[201] J. Haegeman, T. J. Osborne, H. Verschelde and F. Verstraete, *Entanglement Renormalization for Quantum Fields in Real Space*, *Phys. Rev. Lett.* **110** (2013) 100402, [1102.5524].

[202] C. Cao and B. Lackey, *Approximate Bacon-Shor Code and Holography*, *JHEP* **05** (2021) 127, [2010.05960].

[203] C. Cao and B. Lackey, *Quantum Lego: Building Quantum Error Correction Codes from Tensor Networks*, *arXiv pre-print* (9, 2021) , [2109.08158].

[204] A. Jahn and J. Eisert, *Holographic tensor network models and quantum error correction: A topical review*, *Quantum Science and Technology* **6** (2, 2021) 033002, [2102.02619].

[205] M. Cvetič and I. Papadimitriou, *AdS_2 holographic dictionary*, *JHEP* **12** (2016) 008, [1608.07018].

[206] M. Taylor, *Generalized conformal structure, dilaton gravity and SYK*, *JHEP* **01** (2018) 010, [1706.07812].

[207] I. Kanitscheider and K. Skenderis, *Universal hydrodynamics of non-conformal branes*, *JHEP* **04** (1, 2009) 062, [0901.1487].

[208] W. Helwig, W. Cui, A. Riera, J. I. Latorre and H.-K. Lo, *Absolute Maximal Entanglement and Quantum Secret Sharing*, *Phys. Rev. A* **86** (4, 2012) , [1204.2289].

[209] W. Helwig, *Absolutely Maximally Entangled Qudit Graph States*, *arXiv pre-print* (6, 2013) , [1306.2879].

[210] F. Huber, O. Gühne and J. Siewert, *Absolutely maximally entangled states of seven qubits do not exist*, *Phys. Rev. Lett.* **118** (8, 2016) 200502, [1608.06228].

[211] D. Goyeneche, D. Alsina, J. I. Latorre, A. Riera and K. Życzkowski, *Absolutely Maximally Entangled states, combinatorial designs and multi-unitary matrices*, *Phys. Rev. A* **92** (6, 2015) 032316, [1506.08857].

[212] J. Maldacena and D. Stanford, *Remarks on the Sachdev-Ye-Kitaev model*, *Phys. Rev. D* **94** (2016) 106002, [1604.07818].

[213] J. Maldacena, D. Stanford and Z. Yang, *Conformal symmetry and its breaking in two dimensional Nearly Anti-de-Sitter space*, *PTEP* (2016) 12C104, [1606.01857].

[214] H. Coxeter, *Regular Polytopes*, vol. 4. Dover Publication Inc., New York, 3rd ed., 1973, 10.1017/S0008439500024413.

[215] N. P. Breuckmann, *Homological Quantum Codes Beyond the Toric Code*, *PhD Thesis* (2, 2018) , [1802.01520].

[216] M. Bahramgiri and S. Beigi, *Graph States Under the Action of Local Clifford Group in Non-Binary Case*, *arXiv pre-print* (10, 2006) , [quant-ph/0610267].

[217] M. Hein, J. Eisert and H. J. Briegel, *Multi-party entanglement in graph states*, *Phys. Rev. A* **69** (7, 2003) 062311, [quant-ph/0307130].

[218] M. V. d. Nest, J. Dehaene and B. De Moor, *Graphical description of the action of local Clifford transformations on graph states*, *Phys. Rev. A* **69** (8, 2003) 022316, [quant-ph/0308151].

[219] W. Helwig and W. Cui, *Absolutely Maximally Entangled States: Existence and Applications*, *arXiv pre-print* (6, 2013) , [1306.2536].

[220] F. Huber and M. Grassl, *Quantum Codes of Maximal Distance and Highly Entangled Subspaces*, *Quantum* **4** (6, 2020) 284, [1907.07733].

[221] E. Rains, *Quantum Weight Enumerators*, *IEEE Transactions on Information Theory* **44** (1998) 1388–1394, [quant-ph/9612015].

[222] P. Mazurek, M. Farkas, A. Grudka, M. Horodecki and M. Studziński, *Quantum error correction codes and absolutely maximally entangled states*, *Phys. Rev. A* **101** (10, 2019) 042305, [1910.07427].

[223] D. Schlingemann and R. F. Werner, *Quantum error-correcting codes associated with graphs*, *Phys. Rev. A* **65** (12, 2000) 012308, [quant-ph/0012111].

[224] D. Schlingemann, *Stabilizer codes can be realized as graph codes*, *Quantum Information and Computation* **2 (4)** (2001) 307–323, [quant-ph/0111080].

[225] C. Cafaro, D. Markham and P. van Loock, *Scheme for constructing graphs associated with stabilizer quantum codes*, *arXiv pre-print* (7, 2014) , [1407.2777].

[226] F. Huber, C. Eltschka, J. Siewert and O. Gühne, *Bounds on absolutely maximally entangled states from shadow inequalities, and the quantum MacWilliams identity*, *Journal of Physics A: Mathematical and Theoretical* **51** (3, 2017) 175301, [1708.06298].

[227] M. Grassl and M. Rotteler, *Quantum MDS codes over small fields*, *2015 IEEE International Symposium on Information Theory (ISIT)* (2015) 1104–1108, [1502.05267].

[228] R. J. Harris, E. Coupe, N. A. McMahon, G. K. Brennen and T. M. Stace, *Decoding Holographic Codes with an Integer Optimisation Decoder*, *Phys. Rev. A* **102** (12, 2020) 062417, [2008.10206].

[229] W. Donnelly, B. Michel, D. Marolf and J. Wien, *Living on the Edge: A Toy Model for Holographic Reconstruction of Algebras with Centers*, *JHEP* **04** (2017) 093, [1611.05841].

[230] S. B. Bravyi and A. Y. Kitaev, *Quantum codes on a lattice with boundary*, *arXiv pre-print* (11, 1998) , [quant-ph/9811052].

[231] M. H. Freedman and D. A. Meyer, *Projective plane and planar quantum codes*, *Foundations of Computational Mathematics* **1** (10, 2001) 325–332, [quant-ph/9810055].

[232] G. Zémor, *On Cayley Graphs, Surface Codes, and the Limits of Homological Coding for Quantum Error Correction*, in *Coding and Cryptology*, pp. 259–273, Springer Berlin Heidelberg, 2009.

[233] S. Bravyi, D. Poulin and B. Terhal, *Tradeoffs for reliable quantum information storage in 2D systems*, *Phys. Rev. Lett.* **104** (9, 2009) 050503, [0909.5200].

[234] N. Delfosse, *Tradeoffs for reliable quantum information storage in surface codes and color codes*, *IEEE International Symposium on Information Theory -*

Proceedings (1, 2013) 917–921, [1301.6588].

[235] N. P. Breuckmann, C. Vuillot, E. Campbell, A. Krishna and B. M. Terhal, *Hyperbolic and Semi-Hyperbolic Surface Codes for Quantum Storage*, *Quantum Science and Technology* **2** (3, 2017) 035007, [1703.00590].

[236] K. Krasnov, *Holography and Riemann surfaces*, *Adv. Theor. Math. Phys.* **4** (2000) 929–979, [hep-th/0005106].

[237] K. Skenderis and B. C. van Rees, *Holography and wormholes in 2+1 dimensions*, *Commun. Math. Phys.* **301** (2011) 583–626, [0912.2090].

[238] E. Dennis, A. Kitaev, A. Landahl and J. Preskill, *Topological quantum memory*, *Journal of Mathematical Physics* **43** (10, 2001) 4452–4505, [quant-ph/0110143].

[239] G. Arakawa, I. Ichinose, T. Matsui and K. Takeda, *Self-Duality and Phase Structure of the 4D Random-Plaquette Z_2 Gauge Model*, *Nuclear Physics B* **709** (9, 2004) 296–306, [hep-th/0409076].

[240] R. Alicki, M. Horodecki, P. Horodecki and R. Horodecki, *On thermal stability of topological qubit in Kitaev's 4D model*, *Open Systems and Information Dynamics* **17** (11, 2008) 1–20, [0811.0033].

[241] L. Guth and A. Lubotzky, *Quantum error-correcting codes and 4-dimensional arithmetic hyperbolic manifolds*, *Journal of Mathematical Physics* **55** (10, 2013) 082202, [1310.5555].

[242] H. Bombin, *Single-shot fault-tolerant quantum error correction*, *Phys. Rev. X* **5** (4, 2014) 031043, [1404.5504].

[243] N. P. Breuckmann, K. Duivenvoorden, D. Michels and B. M. Terhal, *Local Decoders for the 2D and 4D Toric Code*, *Quantum Information and Computation* **17** (9, 2016) 181–208, [1609.00510].

[244] V. Londe and A. Leverrier, *Golden codes: quantum LDPC codes built from regular tessellations of hyperbolic 4-manifolds*, *Quantum Information and Computation* **19** (12, 2003) 361, [1712.08578].

[245] N. P. Breuckmann and V. Londe, *Single-Shot Decoding of Linear Rate LDPC Quantum Codes with High Performance*, *IEEE Transactions on Information Theory* **68** (Jan, 2022) 272–286, [2001.03568].

[246] J. G. Ratcliffe and S. T. Tschantz, *On the Davis hyperbolic 4-manifold*, *Topology and its Applications* **111** (2001) 327.

[247] M. Vasmer and D. E. Browne, *Three-dimensional surface codes: Transversal gates and fault-tolerant architectures*, *Phys. Rev. A* **100** (1, 2018) 012312, [1801.04255].

[248] A. M. Kubica, *The ABCs of the color code: A study of topological quantum codes as toy models for fault-tolerant quantum computation and quantum phases of matter*, *PhD Thesis* (2018) .

[249] A. Jahn, M. Gluza, F. Pastawski and J. Eisert, *Majorana dimers and holographic quantum error-correcting codes*, *Phys. Rev. Research* **1** (11, 2019) 033079, [1905.03268].

[250] A. Jahn, Z. Zimborás and J. Eisert, *Central charges of aperiodic holographic tensor network models*, *Phys. Rev. A* **102** (10, 2019) 042407, [1911.03485].

[251] L. Boyle, M. Dickens and F. Flicker, *Conformal Quasicrystals and Holography*, *Phys. Rev. X* **10** (2020) 011009, [1805.02665].

[252] A. Jahn, Z. Zimborás and J. Eisert, *Tensor network models of AdS/qCFT*, *Quantum* **6** (Feb, 2022) 643, [2004.04173v3].

[253] A. Dymarsky and A. Shapere, *Quantum stabilizer codes, lattices, and CFTs*, *JHEP* **21** (2020) 160, [2009.01244].

[254] G. Bianconi and C. Rahmede, *Emergent Hyperbolic Network Geometry*, *Scientific Reports* **7** (7, 2016) , [1607.05710].

[255] M. Nickel and D. Kiela, *Poincaré Embeddings for Learning Hierarchical Representations*, *NIPS'17: Proceedings of the 31st International Conference on Neural Information Processing Systems* **30** (2017) 6341–6350, [1705.08039].

[256] V. Khrulkov, L. Mirvakhabova, E. Ustinova, I. V. Oseledets and V. S. Lempitsky, *Hyperbolic Image Embeddings*, *2020 IEEE/CVF Conference on Computer Vision and Pattern Recognition (CVPR)* (2020) 6417–6427, [1904.02239].

[257] W. Peng, T. Varanka, A. Mostafa, H. Shi and G. Zhao, *Hyperbolic Deep Neural Networks: A Survey*, *IEEE Transactions on Pattern Analysis and Machine Intelligence* (Dec, 2021) , [2101.04562].

[258] A. O. Petters, H. Levine and J. Wambsganss, *Singularity Theory and Gravitational*

Lensing. Birkhäuser Boston, MA, 2001, 10.1007/978-1-4612-0145-8.

[259] J. Wambsganss, *Gravitational Lensing in Astronomy.*, *Living Rev Relativ* **1** (1998) 12.

[260] R. Narayan and M. Bartelmann, *Lectures on Gravitational Lensing*, *arXiv e-prints* (June, 1996) , [astro-ph/9606001].

[261] M. Meneghetti, *Introduction to Gravitational Lensing: With Python Examples*, vol. 956 of *Lecture Notes in Physics*. Springer International Publishing, Cham, 2021, 10.1007/978-3-030-73582-1.

[262] A. Friedmann, *Über die Krümmung des Raumes*, *Zeitschrift fur Physik* **10** (Jan., 1922) 377–386.

[263] A. Friedmann, *Über die Möglichkeit einer Welt mit konstanter negativer Krümmung des Raumes*, *Zeitschrift fur Physik* **21** (Dec., 1924) 326–332.

[264] G. Lemaître, *Expansion of the universe, A homogeneous universe of constant mass and increasing radius accounting for the radial velocity of extra-galactic nebulae*, *Monthly Notices of the Royal Astronomical Society* **91** (Mar., 1931) 483–490.

[265] G. Lemaître, *L'Univers en expansion*, *Annales de la Société; Scientifique de Bruxelles* **53** (Jan., 1933) 51.

[266] H. P. Robertson, *Kinematics and World-Structure*, *Astrophysical Journal* **82** (Nov., 1935) 284.

[267] P. Schneider, *A new formulation of gravitational lens theory, time-delay, and Fermat's principle*, *Astronomy and Astrophysics* **143** (Feb., 1985) 413–420.

[268] R. Blandford and R. Narayan, *Fermat's Principle, Caustics, and the Classification of Gravitational Lens Images*, *Astrophysical Journal* **310** (Nov., 1986) 568.

[269] M. Born, *Quantenmechanik der Stoßvorgänge*, *Zeitschrift für Physik* **38** (1926) 803–827.

[270] I. I. Shapiro, *Fourth Test of General Relativity*, *Phys. Rev. Lett.* **13** (Dec, 1964) 789–791.

[271] V. C. Rubin and J. Ford, W. Kent, *Rotation of the Andromeda Nebula from a Spectroscopic Survey of Emission Regions*, *Astrophysical Journal* **159** (Feb., 1970)

379.

[272] A. Bosma, *The distribution and kinematics of neutral hydrogen in spiral galaxies of various morphological types*. PhD thesis, University of Groningen, Netherlands, Mar., 1978.

[273] V. C. Rubin, J. Ford, W. K. and N. Thonnard, *Rotational properties of 21 SC galaxies with a large range of luminosities and radii, from NGC 4605 (R=4kpc) to UGC 2885 (R=122kpc).*, *Astrophysical Journal* **238** (June, 1980) 471–487.

[274] C. Alcock, C. W. Akerlof, R. A. Allsman, T. S. Axelrod, D. P. Bennett, S. Chan et al., *Possible gravitational microlensing of a star in the Large Magellanic Cloud*, *Nature* **365** (1993) 621–623, [astro-ph/9309052].

[275] C. Alcock, R. A. Allsman, D. R. Alves, T. S. Axelrod, A. C. Becker, D. P. Bennett et al., *The MACHO Project: Microlensing Results from 5.7 Years of Large Magellanic Cloud Observations*, *The Astrophysical Journal* **542** (Oct, 2000) 281–307, [astro-ph/0001272].

[276] A. Udalski, M. Szymanski, J. Kaluzny, M. Kubiak, W. Krzeminski, M. Mateo et al., *The Optical Gravitational Lensing Experiment. Discovery of the First Candidate Microlensing Event in the Direction of the Galactic Bulge*, *Acta Astronomica* **43** (July, 1993) 289–294.

[277] A. Udalski, M. K. Szymański and G. Szymański, *OGLE-IV: Fourth Phase of the Optical Gravitational Lensing Experiment*, *Acta Astronomica* **65** (Mar., 2015) 1–38, [1504.05966].

[278] E. Aubourg, P. Bareyre, S. Bréhin, M. Gros, M. Lachièze-Rey, B. Laurent et al., *Evidence for gravitational microlensing by dark objects in the Galactic halo*, *Nature* **365** (1993) 623–625.

[279] E. Komatsu, K. M. Smith, J. Dunkley, C. L. Bennett, B. Gold, G. Hinshaw et al., *Seven-year Wilkinson Microwave Anisotropy Probe (WMAP) Observations: Cosmological Interpretation*, *Astrophysical Journal Supplement Series* **192** (Feb., 2011) 18, [1001.4538].

[280] G. Steigman, *Primordial Nucleosynthesis in the Precision Cosmology Era*, *Annual Review of Nuclear and Particle Science* **57** (2022/07/07, 2007) 463–491, [0712.1100].

[281] B. D. Fields, K. Freese and D. S. Graff, *Chemical Abundance Constraints on White*

Dwarfs as Halo Dark Matter, *The Astrophysical Journal* **534** (May, 2000) 265–276, [astro-ph/9904291].

[282] A. M. Green and B. J. Kavanagh, *Primordial black holes as a dark matter candidate*, *Journal of Physics G: Nuclear and Particle Physics* **48** (Feb, 2021) 043001, [2007.10722].

[283] S. Mao, *Astrophysical applications of gravitational microlensing*, *Research in Astronomy and Astrophysics* **12** (Aug, 2012) 947–972, [1207.3720].

[284] P. Mróz, R. Poleski, A. Gould, A. Udalski, T. Sumi, M. K. Szymański et al., *A Terrestrial-mass Rogue Planet Candidate Detected in the Shortest-timescale Microlensing Event*, *The Astrophysical Journal Letters* **903** (Oct, 2020) L11, [2009.12377].

[285] K. C. Sahu, J. Anderson, S. Casertano, H. E. Bond, A. Udalski, M. Dominik et al., *An Isolated Stellar-mass Black Hole Detected through Astrometric Microlensing*, *Astrophysical Journal* **933** (July, 2022) 83, [2201.13296].

[286] C. Y. Lam, J. R. Lu, A. Udalski, I. Bond, D. P. Bennett, J. Skowron et al., *An Isolated Mass-gap Black Hole or Neutron Star Detected with Astrometric Microlensing*, *The Astrophysical Journal Letters* **933** (Jul, 2022) L23, [2202.01903].

[287] S.-L. Kim, C.-U. Lee, B.-G. Park, D.-J. Kim, S.-M. Cha, Y. Lee et al., *KMTNET: A Network of 1.6 M Wide-Field Optical Telescopes installed at three Southern Observatories*, *JKAS* **49** (2016) 2288–890.

[288] E. Agol, *Occultation and Microlensing*, *The Astrophysical Journal* **579** (Nov, 2002) 430–436, [astro-ph/0207228].

[289] A. Maeder, *Light Curves of the Gravitational Lens-like Action for Binaries with Degenerate Stars*, *Astronomy and Astrophysics* **26** (July, 1973) 215.

[290] T. R. Marsh, *Gravitational lensing in eclipsing binary stars*, *Monthly Notices of the Royal Astronomical Society* **324** (06, 2001) 547–552, [astro-ph/0012390].

[291] J. F. Glicenstein, *Gravitational lensing by rotating stars*, *Astronomy and Astrophysics* **343** (Mar., 1999) 1025–1029.

[292] K. S. Virbhadra and G. F. R. Ellis, *Schwarzschild black hole lensing*, *Phys. Rev. D* **62** (Sep, 2000) 084003, [astro-ph/9904193].

[293] V. Bozza, S. Capozziello, G. Iovane and G. Scarpetta, *Strong Field Limit of Black Hole Gravitational Lensing*, *General Relativity and Gravitation* **33** (2001) 1535–1548, [gr-qc/0102068].

[294] V. Bozza, *Gravitational lensing in the strong field limit*, *Phys. Rev. D* **66** (Nov, 2002) 103001, [gr-qc/0208075].

[295] S. V. Iyer and E. C. Hansen, *Light's bending angle in the equatorial plane of a Kerr black hole*, *Phys. Rev. D* **80** (Dec, 2009) 124023, [0907.5352].

[296] V. Bozza, *Quasiequatorial gravitational lensing by spinning black holes in the strong field limit*, *Phys. Rev. D* **67** (May, 2003) 103006, [gr-qc/0210109].

[297] A. B. Aazami, C. R. Keeton and A. O. Petters, *Lensing by Kerr black holes. II: Analytical study of quasi-equatorial lensing observables*, *Journal of Mathematical Physics* **52** (2011) 102501, [1102.4304].

[298] A. B. Aazami, C. R. Keeton and A. O. Petters, *Lensing by Kerr black holes. I. General lens equation and magnification formula*, *Journal of Mathematical Physics* **52** (2011) 092502, [1102.4300].

[299] K. P. Rauch and R. D. Blandford, *Optical Caustics in a Kerr Spacetime and the Origin of Rapid X-Ray Variability in Active Galactic Nuclei*, *Astrophysical Journal* **421** (Jan., 1994) 46.

[300] V. Bozza, *Optical caustics of Kerr spacetime: The full structure*, *Phys. Rev. D* **78** (Sep, 2008) 063014, [0806.4102].

[301] V. Bozza, *Gravitational lensing by black holes*, *General Relativity and Gravitation* **42** (2010) 2269–2300, [0911.2187].

[302] S. E. Gralla, D. E. Holz and R. M. Wald, *Black hole shadows, photon rings, and lensing rings*, *Phys. Rev. D* **100** (Jul, 2019) 024018, [1906.00873].

[303] M. D. Johnson, A. Lupsasca, A. Strominger, G. N. Wong, S. Hadar, D. Kapec et al., *Universal interferometric signatures of a black hole's photon ring*, *Science Advances* **6** (2020) , [1907.04329].

[304] J. Dexter, *A public code for general relativistic, polarised radiative transfer around spinning black holes*, *Monthly Notices of the Royal Astronomical Society* **462** (06, 2016) 115–136, [1602.03184].

[305] Gradshteyn, I. S. and Ryzhik, I. M., *Table of Integrals, Series, and Products Seventh Edition*. Elsevier/Academic Press, Amsterdam, Seventh ed., 2007.

[306] S. E. Gralla, A. Lupsasca and A. Strominger, *Observational Signature of High Spin at the Event Horizon Telescope*, *Mon. Not. Roy. Astron. Soc.* **475** (2018) 3829–3853, [1710.11112].

[307] F. de Felice and G. Preti, *On the meaning of the separation constant in the Kerr metric*, *Classical and Quantum Gravity* **16** (Sept., 1999) 2929–2935.

[308] K. Rosquist, T. Bylund and L. Samuelsson, *Carter's constant revealed*, *Int. J. Mod. Phys. D* **18** (2009) 429–434, [0710.4260].

[309] O. Lunin and S. D. Mathur, *Metric of the multiply wound rotating string*, *Nuclear Physics B* **610** (2001) 49–76, [hep-th/0105136].

[310] O. Lunin, J. M. Maldacena and L. Maoz, *Gravity solutions for the D1-D5 system with angular momentum*, *arXiv e-prints* (12, 2002) , [hep-th/0212210].

[311] M. Taylor, *General 2 charge geometries*, *Journal of High Energy Physics* **2006** (mar, 2006) 009–009, [hep-th/0507223].

[312] I. Kanitscheider, K. Skenderis and M. Taylor, *Fuzzballs with internal excitations*, *Journal of High Energy Physics* **2007** (Jun, 2007) 056–056, [0704.0690].

[313] S. D. Mathur, A. Saxena and Y. Srivastava, *Constructing 'hair' for the three charge hole*, *Nuclear Physics B* **680** (2004) 415–449, [hep-th/0311092].

[314] I. Bena and P. Kraus, *Three charge supertubes and black hole hair*, *Phys. Rev. D* **70** (2004) 046003, [hep-th/0402144].

[315] O. Lunin, *Adding momentum to D1-D5 system*, *Journal of High Energy Physics* **2004** (apr, 2004) 054–054, [hep-th/0404006].

[316] S. Giusto, S. D. Mathur and A. Saxena, *Dual geometries for a set of 3-charge microstates*, *Nuclear Physics B* **701** (2004) 357–379, [hep-th/0405017].

[317] I. Bena and N. P. Warner, *One ring to rule them all and in the darkness bind them?*, *Advances in Theoretical and Mathematical Physics* **9** (2005) 667 – 701, [hep-th/0408106].

[318] S. Giusto, S. D. Mathur and A. Saxena, *3-charge geometries and their CFT duals*,

Nuclear Physics B **710** (2005) 425–463, [hep-th/0406103].

[319] S. Giusto and S. D. Mathur, *Geometry of D1–D5–P bound states*, *Nuclear Physics B* **729** (2005) 203–220, [hep-th/0409067].

[320] I. Bena and N. P. Warner, *Bubbling supertubes and foaming black holes*, *Phys. Rev. D* **74** (Sep, 2006) 066001, [hep-th/0505166].

[321] P. Berglund, E. G. Gimon and T. S. Levi, *Supergravity microstates for BPS black holes and black rings*, *Journal of High Energy Physics* **2006** (Jun, 2006) 007–007, [hep-th/0505167].

[322] I. Bena, C.-W. Wang and N. P. Warner, *Foaming three-charge black holes*, *Phys. Rev. D* **75** (Jun, 2007) 124026, [hep-th/0604110].

[323] I. Bena, C.-W. Wang and N. P. Warner, *Mergers and typical black hole microstates*, *Journal of High Energy Physics* **2006** (Nov, 2006) 042–042, [hep-th/0608217].

[324] I. Bena, C.-W. Wang and N. P. Warner, *Plumbing the abyss: black ring microstates*, *Journal of High Energy Physics* **2008** (Jul, 2008) 019–019, [0706.3786].

[325] A. Saxena, G. Potvin, S. Giusto and A. W. Peet, *Smooth geometries with four charges in four dimensions*, *Journal of High Energy Physics* **2006** (Apr, 2006) 010–010, [hep-th/0509214].

[326] V. Balasubramanian, E. G. Gimon and T. S. Levi, *Four dimensional black hole microstates: from D-branes to spacetime foam*, *Journal of High Energy Physics* **2008** (Jan, 2008) 056–056, [hep-th/0606118].

[327] I. Bena, J. de Boer, M. Shigemori and N. P. Warner, *Double, Double Supertube Bubble*, *JHEP* **10** (2011) 116, [1107.2650].

[328] S. Giusto, R. Russo and D. Turton, *New D1-D5-P geometries from string amplitudes*, *Journal of High Energy Physics* **2011** (2011) 62, [1108.6331].

[329] V. Jejjala, O. Madden, S. F. Ross and G. Titchener, *Nonsupersymmetric smooth geometries and D1-D5-P bound states*, *Phys. Rev. D* **71** (Jun, 2005) 124030, [hep-th/0504181].

[330] S. Giusto, A. Saxena and S. F. Ross, *Non-supersymmetric microstates of the D1-D5-KK system*, *Journal of High Energy Physics* **2007** (Dec, 2007) 065–065,

[0708.3845].

[331] I. Bena, S. Giusto, C. Ruef and N. P. Warner, *Multi-center non-BPS black holes — the solution*, *Journal of High Energy Physics* **2009** (Nov, 2009) 032–032, [0908.2121].

[332] I. Bena, S. Giusto, C. Ruef and N. P. Warner, *A (running) bolt for new reasons*, *Journal of High Energy Physics* **2009** (Nov, 2009) 089–089, [0909.2559].

[333] G. Dall'Agata, S. Giusto and C. Ruef, *U-duality and non-BPS solutions*, *Journal of High Energy Physics* **2011** (2011) 74, [1012.4803].

[334] I. Bena, A. Puhm and B. Vercnocke, *Metastable supertubes and non-extremal black hole microstates*, *Journal of High Energy Physics* **2012** (Apr., 2012) 100, [1109.5180].

[335] I. Bena, A. Puhm and B. Vercnocke, *Non-extremal black hole microstates: fuzzballs of fire or fuzzballs of fuzz?*, *Journal of High Energy Physics* **2012** (2012) 14, [1208.3468].

[336] S. D. Mathur and D. Turton, *Oscillating supertubes and neutral rotating black hole microstates*, *Journal of High Energy Physics* **2014** (2014) 72, [1310.1354].

[337] I. Bena, G. Bossard, S. Katmadas and D. Turton, *Non-BPS multi-bubble microstate geometries*, *Journal of High Energy Physics* **2016** (2016) 73, [1511.03669].

[338] I. Bena, G. Bossard, S. Katmadas and D. Turton, *Bolting multicenter solutions*, *Journal of High Energy Physics* **2017** (2017) 127, [1611.03500].

[339] G. Bossard, S. Katmadas and D. Turton, *Two kissing bolts*, *Journal of High Energy Physics* **2018** (2018) 8, [1711.04784].

[340] P. Heidmann, *Bubbling the NHEK*, *Journal of High Energy Physics* **2019** (Jan., 2019) 108, [1811.08256].

[341] S. Hadar, A. P. Porfyriadis and A. Strominger, *Gravity waves from extreme-mass-ratio plunges into Kerr black holes*, *Phys. Rev. D* **90** (Sep, 2014) 064045, [1403.2797].

[342] S. Hadar, A. P. Porfyriadis and A. Strominger, *Fast plunges into Kerr black holes*, *Journal of High Energy Physics* **2015** (2015) 78, [1504.07650].

[343] S. Hadar and A. P. Porfyriadis, *Whirling orbits around twirling black holes from conformal symmetry*, *JHEP* **03** (2017) 014, [1611.09834].

[344] S. L. Shapiro and S. A. Teukolsky, *Black holes, white dwarfs, and neutron stars : the physics of compact objects*. Wiley, 1983, 10.1002/9783527617661.

[345] G. E. Brown and H. A. Bethe, *A Scenario for a Large Number of Low-Mass Black Holes in the Galaxy*, *Astrophysical Journal* **423** (Mar., 1994) 659.

[346] M. Samland, *Modeling the Evolution of Disk Galaxies. II. Yields of Massive Stars*, *Astrophysical Journal* **496** (Mar., 1998) 155–171.

[347] C. L. Fryer and V. Kalogera, *Theoretical Black Hole Mass Distributions*, *Astrophysical Journal* **554** (June, 2001) 548–560, [astro-ph/9911312].

[348] S. E. Woosley, A. Heger and T. A. Weaver, *The evolution and explosion of massive stars*, *Rev. Mod. Phys.* **74** (Nov, 2002) 1015–1071.

[349] A. Heger, C. L. Fryer, S. E. Woosley, N. Langer and D. H. Hartmann, *How Massive Single Stars End Their Life*, *Astrophysical Journal* **591** (July, 2003) 288–300, [astro-ph/0212469].

[350] M. Spera, M. Mapelli and A. Bressan, *The mass spectrum of compact remnants from the PARSEC stellar evolution tracks*, *Monthly Notices of the Royal Astronomical Society* **451** (Aug., 2015) 4086–4103, [1505.05201].

[351] T. Sukhbold, T. Ertl, S. E. Woosley, J. M. Brown and H. T. Janka, *Core-collapse Supernovae from 9 to 120 Solar Masses Based on Neutrino-powered Explosions*, *Astrophysical Journal* **821** (Apr., 2016) 38, [1510.04643].

[352] R. A. Remillard and J. E. McClintock, *X-Ray Properties of Black-Hole Binaries*, *Annual Review of Astronomy and Astrophysics* **44** (Sept., 2006) 49–92, [astro-ph/0606352].

[353] J. Casares and P. G. Jonker, *Mass Measurements of Stellar and Intermediate-Mass Black Holes*, *Space Science Reviews* **183** (Sept., 2014) 223–252, [1311.5118].

[354] F. Özel, D. Psaltis, R. Narayan and J. E. McClintock, *The Black Hole Mass Distribution in the Galaxy*, *Astrophysical Journal* **725** (Dec., 2010) 1918–1927, [1006.2834].

[355] W. M. Farr, N. Sravan, A. Cantrell, L. Kreidberg, C. D. Bailyn, I. Mandel et al.,

The Mass Distribution of Stellar-mass Black Holes, *Astrophysical Journal* **741** (Nov., 2011) 103, [1011.1459].

[356] L. Kreidberg, C. D. Bailyn, W. M. Farr and V. Kalogera, *Mass Measurements of Black Holes in X-Ray Transients: Is There a Mass Gap?*, *Astrophysical Journal* **757** (Sept., 2012) 36, [1205.1805].

[357] A. Gould, *Extending the MACHO Search to approximately 10 6 M sub sun*, *Astronomical Journal* **392** (June, 1992) 442.

[358] A. Gould, *Measuring the Remnant Mass Function of the Galactic Bulge*, *The Astrophysical Journal* **535** (Jun, 2000) 928–931, [astro-ph/9906472].

[359] M. Linares, T. Shahbaz and J. Casares, *Peering into the Dark Side: Magnesium Lines Establish a Massive Neutron Star in PSR J2215+5135*, *Astrophysical Journal* **859** (May, 2018) 54, [1805.08799].

[360] H. T. Cromartie, E. Fonseca, S. M. Ransom, P. B. Demorest, Z. Arzoumanian, H. Blumer et al., *Relativistic Shapiro delay measurements of an extremely massive millisecond pulsar*, *Nature Astronomy* **4** (Jan., 2020) 72–76, [1904.06759].

[361] G. Wiktorowicz, Y. Lu, Ł. Wyrzykowski, H. Zhang, J. Liu, S. Justham et al., *Noninteracting Black Hole Binaries with Gaia and LAMOST*, *Astrophysical Journal* **905** (Dec., 2020) 134, [2006.08317].

[362] G. Wiktorowicz, M. Middleton, N. Khan, A. Ingram, P. Gandhi and H. Dickinson, *Predicting the self-lensing population in optical surveys*, *Monthly Notices of the Royal Astronomical Society* **507** (Oct., 2021) 374–384, [2104.12666].

[363] T. A. Thompson, C. S. Kochanek, K. Z. Stanek, C. Badenes, R. S. Post, T. Jayasinghe et al., *A noninteracting low-mass black hole-giant star binary system*, *Science* **366** (Nov., 2019) 637–640, [1806.02751].

[364] B. Giesers, S. Kamann, S. Dreizler, T.-O. Husser, A. Askar, F. Göttgens et al., *A stellar census in globular clusters with MUSE: Binaries in NGC 3201*, *Astronomy and Astrophysics* **632** (Dec., 2019) A3, [1909.04050].

[365] T. Jayasinghe, K. Z. Stanek, T. A. Thompson, C. S. Kochanek, D. M. Rowan, P. J. Vallely et al., *A unicorn in monoceros: the 3 $M_\odot$ dark companion to the bright, nearby red giant V723 Mon is a non-interacting, mass-gap black hole candidate*, *Monthly Notices of the Royal Astronomical Society* **504** (05, 2021) 2577–2602, [2101.02212].

[366] The LIGO Scientific Collaboration, the Virgo Collaboration, R. Abbott, T. D. Abbott, S. Abraham, F. Acernese et al., *GWTC-2: Compact Binary Coalescences Observed by LIGO and Virgo during the First Half of the Third Observing Run*, *Phys. Rev. X* **11** (Jun, 2021) 021053, [2010.14527].

[367] The LIGO Scientific Collaboration, the Virgo Collaboration, the KAGRA Collaboration, R. Abbott, T. D. Abbott, F. Acernese et al., *GWTC-3: Compact Binary Coalescences Observed by LIGO and Virgo During the Second Part of the Third Observing Run*, *arXiv e-prints* (Nov., 2021) , [2111.03606].

[368] K. Belczynski, G. Wiktorowicz, C. L. Fryer, D. E. Holz and V. Kalogera, *Missing Black Holes Unveil the Supernova Explosion Mechanism*, *The Astrophysical Journal* **757** (Sep, 2012) 91, [1110.1635].

[369] Ł. Wyrzykowski and I. Mandel, *Constraining the masses of microlensing black holes and the mass gap with Gaia DR2*, *Astronomy and Astrophysics* **636** (03, 2020) , [1904.07789].

[370] A. Gould, *Self-lensing by Binaries*, *Astrophysical Journal* **446** (June, 1995) 541, [astro-ph/9409057].

[371] A. Gould and S. Salim, *Searching for Failed Supernovae with Astrometric Binaries*, *Astrophysical Journal* **572** (June, 2002) 944–949, [astro-ph/0111512].

[372] J. Casares, I. Negueruela, M. Ribó, I. Ribas, J. M. Paredes, A. Herrero et al., *A Be-type star with a black-hole companion*, *Nature* **505** (2014) 378–381, [1401.3711].

[373] A. Husseiniova, P. McGill, L. C. Smith and N. W. Evans, *A microlensing search of 700 million VVV light curves*, *Monthly Notices of the Royal Astronomical Society* **506** (Sept., 2021) 2482–2502, [2106.15617].

[374] A. C. Rodriguez, P. Mróz, S. R. Kulkarni, I. Andreoni, E. C. Bellm, R. Dekany et al., *Microlensing Events in the Galactic Plane Using the Zwicky Transient Facility*, *Astrophysical Journal* **927** (Mar., 2022) 150, [2112.07684].

[375] L. Wyrzykowski, J. Skowron, S. Kozłowski, A. Udalski, M. K. Szymański, M. Kubiak et al., *The OGLE view of microlensing towards the Magellanic Clouds – IV. OGLE-III SMC data and final conclusions on MACHOs**, *Monthly Notices of the Royal Astronomical Society* **416** (09, 2011) 2949–2961, [1106.2925].

[376] E. Kruse and E. Agol, *KOI-3278: A Self-Lensing Binary Star System*, *Science* **344** (2014) 275–277, [1404.4379].

[377] H. Kawahara, K. Masuda, M. MacLeod, D. W. Latham, A. Bieryla and O. Benomar, *Discovery of Three Self-lensing Binaries from Kepler*, *Astronomical Journal* **155** (Mar., 2018) 144, [1801.07874].

[378] K. Masuda, H. Kawahara, D. W. Latham, A. Bieryla, M. Kunitomo, M. MacLeod et al., *Self-lensing Discovery of a 0.2 $M_\odot$ White Dwarf in an Unusually Wide Orbit around a Sun-like Star*, *Astrophysical Journal Letters* **881** (Aug., 2019) L3, [1907.07656].

[379] J. Dexter and E. Agol, *A Fast New Public Code for Computing Photon Orbits in a Kerr Spacetime*, *The Astrophysical Journal* **696** (Apr, 2009) 1616–1629, [0903.0620].

[380] D. R. Mayerson, *Fuzzballs and observations*, *General Relativity and Gravitation* **52** (Dec., 2020) 115, [2010.09736].

[381] I. Bah, I. Bena, P. Heidmann, Y. Li and D. R. Mayerson, *Gravitational footprints of black holes and their microstate geometries*, *Journal of High Energy Physics* **2021** (Oct., 2021) 138, [2104.10686].

[382] LISA collaboration, K. G. Arun et al., *New horizons for fundamental physics with LISA*, *Living Rev. Rel.* **25** (2022) 4, [2205.01597].

[383] M. Sereno, *Gravitational lensing by stars with angular momentum*, *Monthly Notices of the Royal Astronomical Society* **344** (2003) 942–950, [astro-ph/0307243].

[384] V. Bozza, F. De Luca, G. Scarpetta and M. Sereno, *Analytic Kerr black hole lensing for equatorial observers in the strong deflection limit*, *Phys. Rev. D* **72** (Oct, 2005) 083003, [gr-qc/0507137].

[385] M. C. Werner and A. O. Petters, *Magnification relations for Kerr lensing and testing Cosmic Censorship*, *Phys. Rev. D* **76** (2007) 064024, [0706.0132].

[386] C. R. Keeton and A. O. Petters, *Formalism for testing theories of gravity using lensing by compact objects. III. Braneworld gravity*, *Phys. Rev. D* **73** (2006) 104032, [gr-qc/0603061].

[387] F. Eisenhauer, R. Genzel, T. Alexander, R. Abuter, T. Paumard, T. Ott et al., *SINFONI in the Galactic Center: Young Stars and Infrared Flares in the Central Light-Month*, *Astrophysical Journal* **628** (July, 2005) 246–259, [astro-ph/0502129].

[388] S. V. Iyer and E. C. Hansen, *Strong and Weak Deflection of Light in the Equatorial Plane of a Kerr Black Hole*, *arXiv e-prints* (Aug., 2009) , [0908.0085].

[389] A. B. Congdon, S. V. Iyer and C. R. Keeton, *Asymmetric Light Bending in the Equatorial Kerr Metric*, *arXiv e-prints* (July, 2022) , [2207.08987].

[390] J. Fuller and L. Ma, *Most Black Holes Are Born Very Slowly Rotating*, *Astrophysical Journal Letters* **881** (Aug., 2019) L1, [1907.03714].

[391] G. R. Ricker, J. N. Winn, R. Vanderspek, D. W. Latham, G. Á. Bakos, J. L. Bean et al., *Transiting Exoplanet Survey Satellite (TESS)*, *Journal of Astronomical Telescopes, Instruments, and Systems* **1** (Jan., 2015) 014003.

[392] H. Sana, S. E. de Mink, A. de Koter, N. Langer, C. J. Evans, M. Gieles et al., *Binary Interaction Dominates the Evolution of Massive Stars*, *Science* **337** (July, 2012) 444, [1207.6397].

[393] S. E. de Mink, H. Sana, N. Langer, R. G. Izzard and F. R. N. Schneider, *The Incidence of Stellar Mergers and Mass Gainers among Massive Stars*, *The Astrophysical Journal* **782** (Jan, 2014) 7, [1312.3650].

[394] J. E. McClintock, R. Shafee, R. Narayan, R. A. Remillard, S. W. Davis and L.-X. Li, *The Spin of the Near-Extreme Kerr Black Hole GRS 1915+105*, *The Astrophysical Journal* **652** (Nov, 2006) 518–539, [astro-ph/0606076].

[395] J. L. Blum, J. M. Miller, A. C. Fabian, M. C. Miller, J. Homan, M. van der Klis et al., *Measuring the Spin of GRS 1915+105 with Relativistic Disk Reflection*, *The Astrophysical Journal* **706** (oct, 2009) 60–66, [0909.5383].

[396] J. M. Miller, M. L. Parker, F. Fuerst, M. Bachetti, F. A. Harrison, D. Barret et al., *NuSTAR Spectroscopy of GRS 1915+105: Disk Reflection, Spin, and Connections to Jets*, *The Astrophysical Journal* **775** (Sep, 2013) L45, [1308.4669].

[397] L. Gou, J. E. McClintock, M. J. Reid, J. A. Orosz, J. F. Steiner, R. Narayan et al., *The Extreme Spin of the Black Hole in Cygnus X-1*, *The Astrophysical Journal* **742** (Nov, 2011) 85, [1106.3690].

[398] L. Gou, J. E. McClintock, R. A. Remillard, J. F. Steiner, M. J. Reid, J. A. Orosz et al., *Confirmation Via the Continuum-Fitting Method that the Spin of the Black Hole in Cygnus X-1 is Extreme*, *The Astrophysical Journal* **790** (Jun, 2014) 29, [1308.4760].

[399] H. J. Witt and S. Mao, *Can Lensed Stars Be Regarded as Pointlike for Microlensing by MACHOs?*, *Astrophysical Journal* **430** (Aug., 1994) 505.

[400] Z. Kopal, *Detailed effects of limb darkening upon light and velocity curves of close binary systems*, *Harvard College Observatory Circular* **454** (Jan., 1950) 1–12.

[401] J. Diaz-Cordoves and A. Gimenez, *A new nonlinear approximation to the limb-darkening of hot stars*, *Astronomy and Astrophysics* **259** (June, 1992) 227–231.

[402] D. A. Klinglesmith and S. Sobieski, *Nonlinear Limb Darkening for Early-Type Stars*, *Astronomical Journal* **75** (Mar., 1970) 175–182.

[403] A. Claret and P. H. Hauschildt, *The limb-darkening for spherically symmetric NextGen model atmospheres: A-G main-sequence and sub-giant stars*, *Astronomy and Astrophysics* **412** (Dec., 2003) 241–248.

[404] D. K. Sing, J. M. Désert, A. Lecavelier Des Etangs, G. E. Ballester, A. Vidal-Madjar, V. Parmentier et al., *Transit spectrophotometry of the exoplanet HD 189733b. I. Searching for water but finding haze with HST NICMOS*, *Astronomy and Astrophysics* **505** (Oct., 2009) 891–899, [0907.4991].

[405] A. Claret, *A new non-linear limb-darkening law for LTE stellar atmosphere models. Calculations for -5.0 <= log[M/H] <= +1, 2000 K <= T_{eff} <= 50000 K at several surface gravities*, *Astronomy and Astrophysics* **363** (Nov., 2000) 1081–1190.

[406] V. Bozza, F. D. Luca and G. Scarpetta, *Kerr black hole lensing for generic observers in the strong deflection limit*, *Physical Review D* **74** (2006) 063001, [gr-qc/0604093].

[407] T. Fragos and J. E. McClintock, *The Origin of Black Hole Spin in Galactic Low-mass X-Ray Binaries*, *Astrophysical Journal* **800** (Feb., 2015) 17, [1408.2661].

[408] J. W. T. Hessels, S. M. Ransom, I. H. Stairs, P. C. C. Freire, V. M. Kaspi and F. Camilo, *A Radio Pulsar Spinning at 716 Hz*, *Science* **311** (2006) 1901–1904, [astro-ph/0601337].

[409] K. Belczynski, A. Romagnolo, A. Olejak, J. Klencki, D. Chattopadhyay, S. Stevenson et al., *The Uncertain Future of Massive Binaries Obscures the Origin of LIGO/Virgo Sources*, *Astrophysical Journal* **925** (Jan., 2022) 69, [2108.10885].

[410] R. Brito, V. Cardoso and P. Pani, *Superradiance: New Frontiers in Black Hole*

Physics, *Lect. Notes Phys.* **906** (2015) pp.1–237, [1501.06570].

[411] R. Penrose, *Asymptotic Properties of Fields and Space-Times*, *Phys. Rev. Lett.* **10** (Jan, 1963) 66–68.

[412] J. Patera and H. Zassenhaus, *The Pauli matrices in n dimensions and finest gradings of simple Lie algebras of type A_{n-1}*, *Journal of Mathematical Physics* **29** (6, 1988) 665.

[413] D. Gottesman, A. Kitaev and J. Preskill, *Encoding a qubit in an oscillator*, *Phys. Rev. A* **64** (8, 2000) 123101–1231021, [quant-ph/0008040].

[414] S. D. Bartlett, H. de Guise and B. C. Sanders, *Quantum Encodings in Spin Systems and Harmonic Oscillators*, *Phys. Rev. A* **65** (9, 2001) 052316, [quant-ph/0109066].

[415] A. Ashikhmin and E. Knill, *Nonbinary Quantum Stabilizer Codes*, *IEEE Transactions on Information Theory* **47** (5, 2000) 3065–3072, [quant-ph/0005008].

[416] A. Ketkar, A. Klappenecker, S. Kumar and P. K. Sarvepalli, *Nonbinary stabilizer codes over finite fields*, *IEEE Transactions on Information Theory* **52** (8, 2005) 4892–4914, [quant-ph/0508070].

[417] M. Abramowitz, I. A. Stegun and R. H. Romer, *Handbook of Mathematical Functions with Formulas, Graphs, and Mathematical Tables*, *American Journal of Physics* **56** (1988) 958–958.